Title
Understanding and Controlling Nanoscale Morphology in Self-Assembled Semiconducting Materials

Author
Kang, Hyeyeon

Publication Date
2017

Peer reviewed|Thesis/dissertation

UNIVERSITY OF CALIFORNIA

Los Angeles

Understanding and Controlling Nanoscale Morphology in Self-Assembled Semiconducting Materials

A dissertation submitted in partial satisfaction of the requirements

for the degree Doctor of Philosophy in Chemistry

by

Hyeyeon Kang

2017

ABSTRACT OF THE DISSERTATION

Understanding and Controlling Nanoscale Morphology

in Self-Assembled Semiconducting Materials

by

Hyeyeon Kang

Doctor of Philosophy in Chemistry

University of California, Los Angeles, 2017

Professor Sarah H. Tolbert, Chair

Self-assembled semiconducting materials have been rapidly developed for a range of applications. This work aims to control the morphology of nanostructured semiconductors to understand how their functions arise from the structural properties.

The first part of this dissertation focuses on the formation of a bulk-heterojunction (BHJ) in the active layer of organic photovoltaics (OPV). A BHJ is a bicontinuous interpenetrating network of organic components. The phase separation of the electron donor and the acceptor is required to achieve a BHJ structure in the nanostructured morphology, which promotes an efficient charge

transportation. The use of solvent additive is one of the strategies to control the spontaneous phase separation during the film formation. Low vapor pressure solvent additives are introduced to a polymer casting solution in a sequentially processed OPV system, to study the swelling effect on the phase separation. In particular, the change in crystallinity and vertical mixing will be intensively studied upon polymer swelling. As another strategy, we introduce a molecular structure change to fullerene derivatives. A small structural variation leads to a large enough contrast of their surface energy, which is attributed to different vertical phase separation in the active layer. It eventually allows us to examine photovoltaic performance and device physics.

In the second part, mesoporous inorganic films are investigated by preparation from a nanocrystal solution or sol-gel precursors for solar energy applications. Mesoporous nanocrystal-based titania is synthesized for inorganic/organic hybrid solar cells. The effect of surface modification is examined by anchoring a fullerene derivative on to titania surface. 3D interconnected mesoporous tantalum nitride films are prepared via sol-gel method as photoanodes in solar water splitting. The simple synthetic method using polymer template enables us to successfully prepare nitride films with excellent pore periodicity. The porous tantalum nitride film is examined with photoelectrochemical measurement to investigate the correlation between nanostructuring and photocatalytic activity.

For the final part of this dissertation, porous cobalt ferrite and cadmium sulfide films are studied using ellipsometric porosimetry. Understanding the nature of their pores allows us to tune the intrinsic properties of the materials or prove the newly designed synthetic method.

This dissertation of Hyeyeon Kang is approved.

Xiangfeng Duan

Diana L. Huffaker

Sarah H. Tolbert, Committee Chair

University of California, Los Angeles

2017

CONTENTS

LIST OF FIGURES

Chapter 2

Chapter 3

Chapter 4

Chapter 5

Chapter 6

Chapter 7

LIST OF TABLES

Chapter 2

Chapter 3

Chapter 4

ACKNOWLEDGEMENTS

There are a number of the people who supported and believed in me for last 5 years. In particular, I could not have gone through this program without the endless support from my loving family: my grandma in Donam, my parents, my sisters and brother, my uncle and aunt in Paju and my lovely dog, Hongdol. I also would like to specially thank my other grandma, who passed away last October. Once I go back to Korea, I will visit where her soul is, and say I am terribly sorry for being late and I really missed her. Though my family and I lived apart halfway across the world, I always felt they were here for me. It is my great fortune to have such a wonderful family.

I also would like to thank my advisor, Professor Sarah Tolbert for guiding me to be a better scientist. I had not known how to troubleshoot when I encountered issues in research projects until I met her. She always welcomed me whenever I knocked her door, and taught me how to proceed forward on the projects by looking at the bigger picture and not being narrow-sighted. I feel all the time that she really cared for me, and tried to help me learn more through the program.

I want to thank my research group, Tolbies for being supportive in many ways beyond science. They are more than coworkers, and I enjoyed the easy-going vibe that I would never feel from other groups. I also thank all of my collaborators in solar cell group from the Schwartz group and the Rubin group. They are very helpful and knowledgeable and I could have learned so much by having countless discussions with them.

I would like to express my gratitude to my committee, Prof. Xiangfeng Duan and Prof. Diana L. Huffaker for their support. I also thank Prof. Richard Kaner for serving on my qualifying exam committee and being supportive for my fourth-year meeting.

I would like to thank Prof. Johnny Pang, whom I have worked for many times as a teaching assistant. He is always enthusiastic for his classes and considerate for all of his TAs. I could enjoy

teaching 14BL, 20L and 30AL labs, which reminded me of my college classes. It was a good opportunity for me to look into the general chemistry again.

I would like to acknowledge all the staff and officers in the Department of Chemistry and Biochemistry. This department would not function at all without their hard-work.

I was lucky to meet some amazing friends here at UCLA: Joan Valentine, Shauna Robbennolt, Abraham Buditama, Terri Lin, Ty Karaba, Dahee Jung and Yiyi Yao. They were my real friends here who made me laugh. The times that we spent together became a great memory to me, and I will remember them for a very long time. I knew they sincerely cared and supported me. There would be no way that I could survive in this jungle without these people.

Lastly, I want to thank my family-like old friends in South Korea. When I was frustrated for my research, the graduate school, other people, or just life in LA, they were always on the phone to listen to me even with the time difference between Korea and LA. I missed them so much and realized how awesome they are while living apart from them.

Much of the work here was supported by the U.S. Department of Energy, National Science Foundation (NSF), California NanoSystems Institute (CNSI) and University of California, Los Angeles Graduate Division. Much of the XRD presented here is performed at the Stanford Synchrotron Radiation Lightsource, a national user facility operated by Stanford University on behalf of the U.S. Department of Energy, Office of Basic Science. A portion of this research at ORNL's Spallation Neutron Source was sponsored by the Scientific User Facilities Division, Office of Basic Energy Sciences, U.S. Department of Energy.

Previous Publications and Contributions of Co-authors

Chapter 2 is a version of Hyeyeon Kang, Matthew T. Fontana, Patrick Yee, Steven A. Hawks, Zongwu Fan, Laura T. Schelhas, Sarah H. Tolbert, and Benjamin J. Schwartz, "Solvent Additives Function as Polymer Swelling Agents in Bulk Heterojunction Organic Photovoltaics." I did the measurement and analysis of ellipsometry and GIWAXS data. I also worked on Neutron Reflectivity data with Patrick. Matthew collected the *J-V* curves, and Laura collected XPS data. I and Matthew T. Fontana contributed equally collecting data, and editing the manuscript. Professor Sarah H. Tolbert and Benjamin J. Schwartz advised for troubleshooting the project and edited the manuscript. The manuscript will be submitted for publication shortly after filing this dissertation.

Chapter 3 is a version of Guangye Zhang, Shaohua Huang, Patrick Yee, Matthew T. Fontana, Hyeyeon Kang, Nicholas Knutson, Rachel C. Huber, Amy S. Ferreira, Yves F. Rubin, Sarah H. Tolbert, and Benjamin J. Schwartz, "Vertical Phase Segregation, Device Physics, and Surface Recombination in Polymer:Fullerene BHJ Solar Cells: The Role of Surface Energies". Guangye wrote the manuscript and collected the device data. Shaohua and Nick synthesized the fullerene derivatives. Patrick and I contributed collecting and editing Neutron Reflectivity data. Matthew assisted the device fabrication. Rachel and Amy collected GIWAXS data. Professor Sarah H. Tolbert, Benjamin J. Schwartz and Yves F. Rubin advised for troubleshooting the project and edited the manuscript. The manuscript will be submitted for publication shortly after filing this dissertation.

Chapter 4 is a version of Hyeyeon Kang, Robert Thomson, Matthew T. Fontana, Yves F. Rubin, Benjamin J. Schwartz and Sarah H. Tolbert, "Surface Modification of Mesoporous Titania Thin Films in Inorganic-Organic Hybrid Solar Cells". Robert Thomson synthesized PCBA, a fullerene derivative. Matthew helped collecting the device data. I did all the remaining work as

well as writing the manuscript. Professor Sarah H. Tolbert, Benjamin J. Schwartz and Yves F. Rubin advised for troubleshooting the project and edited the manuscript. The manuscript will be submitted for publication shortly after filing this dissertation.

Chapter 5 is a version of Hyeyeon Kang, Terri Lin, Yan Yan and Sarah H. Tolbert, "3D Interconnected Mesoporous Tantalum Nitride Film as a Photoanode for Efficient Solar Water Splitting". Terri contributed to the photoelectrochemical measurement and analysis, and edited the manuscript. Yan collected and analyzed XPS data. I contributed all the remaining work as well as writing the manuscript. Professor Sarah H. Tolbert advised for troubleshooting the project and edited the manuscript. The manuscript will be submitted for publication shortly after filing this dissertation.

Chapter 6 is a version of Justin C. Ondry, Shauna Robbennolt, Hyeyeon Kang, Yan Yan, and Sarah H. Tolbert, "Room-temperature, Solution Phase Method for the Synthesis of Mesoporous Metal Chalcogenide Nanocrystal-Based Thin Films with Precisely Controlled Grain Sizes" Chem. Mater. 2016, 28, 6105–6117 Copyright © 2016 American Chemical Society. I collected ellipsometic porosimetry data and edited the manuscript. Shauna collected TEM images, edited the manuscript and mentored Justin. Justin wrote the manuscript and did all the remaining work. Professor Sarah H. Tolbert advised for troubleshooting the project and edited the manuscript.

Chapter 7 is a version of Shauna Robbennolt, Hyeyeon Kang, Abraham N. Buditama, Paul Nordeen, Gregory P. Carman, Sarah H. Tolbert, "Fine Tuning the Magnetic Properties of Cobalt Ferrite Thin Films by Controlling Nanoscale Structure". I did the ellipsometric porosimetry measurements and analysis. Abraham N. Buditama fabricated some of the sol-gel derived films and participated in the magnetic characterization. Paul Nordeen helped to conduct all of the magnetometry measurements. Shauna contributed all the remaining data and analysis as well as

the manuscript writing. Professor Sarah Tolbert advised for troubleshooting the project and edited the manuscript. The manuscript will be submitted for publication shortly after filing this dissertation.

VITA

2005-2009	B.S in Chemistry and Life Science
	Ewha Womans University, Seoul, Republic of Korea
2008	Honor Scholarship awarded to Dean's List students
	Ewha Womans University, Seoul, Republic of Korea
2008-2009	Undergraduate Researcher in Center for Biomimetic System
	Ewha Womans University, Seoul, Republic of Korea
2009-2011	M.S in Chemistry and Nano Science
	Ewha Womans University, Seoul, Republic of Korea
2012-2014	Graduate Dean's Scholar Award
	University of California, Los Angeles
2012-2017	Teaching Assistant in Department of Chemistry and Biochemistry
	University of California, Los Angeles

SELECT PUBLICATIONS AND PRESENTATIONS

D. T. Scholes, P. Y. Yee, J. R. Lindemuth, **H. Kang**, J. Onorato, R. Ghosh, C. K. Luscombe, F. C. Spano, S. H. Tolbert, and B. J. Schwartz "The Effects of Crystallinity on Charge Transport and the Structure of Sequentially-Processed F4TCNQ-doped Conjugated Polymer Films" *Just accepted to Advance Functional Materials*.

D. Chien, A. Buditama, L. Schelhas, **H. Kang**, J. Chang, and S. H. Tolbert "Magnetoelectric Effect in Multiferroic Nanocomposites of Atomic Layer Deposition Pb(Zr,Ti)O3 Coupled with Templated Mesoporous $CoFe_2O_4$" *Appl. Phys. Lett*. 2016, 109, 112904.

J. Ondry, S. Robbennolt, **H. Kang**, and S. H. Tolbert "A room temperature, solution phase method for the synthesis of mesoporous metal chalcogenide nanocrystal based thin films with precisely controlled grain sizes" *Chem. Mater*. 2016, 28, 6105–6117.

G. Zhang, S. A. Hawks, C. Ngo, L. T. Schelhas, D. T. Scholes, **H. Kang**, J. C. Aguirre, S. H. Tolbert and B. J. Schwartz "Extensive penetration of evaporated electrode metals into fullerene

films : intercalated metal nanostructures and influence on device architecture" *ACS Appl. Mater. Interfaces*, 2015, 7, 25247-25258.

H.Y. Kang, J. Cho, L. V. Liu, R. Sarangi, E. Solomon and W. Nam "Mononuclear nickel(II)-superoxo and nickel(III)-peroxo complexes bearing a common macrocyclic TMC ligand" *Chem, Sci*. 2013, 4, 1502-1508.

J. Cho, R. Sarangi, **H.Y. Kang**, J.Y. Lee, M. Kubo, T. Ogura, E. Solomon and W. Nam "Synthesis, structural, and spectroscopic characterization and reactivities of mononuclear cobalt(III)-peroxo complexes" *J. Am. Chem. Soc*. 2010, 132, 16977-16986.

D. Kumar, L. Tahsini, S. de Visser, **H.Y. Kang**, S.J. Kim and W. Nam "Effect of porphyrin ligands on the regioselective dehydrogenation versus epoxidation of olefins by oxoiron(IV) mimics of cytochrome P450" *J. Phys. Chem. A* 2009, 113, 11713-11722.

S.J. Kim, R. Latifi, **H.Y. Kang**, W. Nam and S. de Visser "Activation of hydrocarbon C-H bonds by iodosylbenzene: how does it compare with iron(IV)-oxo oxidants?" *Chem. Commun*. 2009, 1562-1564.

03/2016	ACS 251st National Meeting & Exposition, San Diego, CA, USA. Poster presentation : 3-D interconnected mesoporous tantalum nitride as a novel water splitting photocatalyst
08/2011	ICBIC15 (15th International conference on Biological Inorganic Chemistry), Vancouver, CANADA. Poster presentation : Reactivity comparison of nickel-superoxo and –peroxo complexes with a tetraazamacrocyclic ligand
08/2010	Inorganic Chemistry Summer Symposium, Busan, KOREA. Oral presentation : Mononuclear cobalt(III)-peroxo complexes : structural and spectroscopic characterization and reactivity in O2-tranfer
07/2009	ICBIC14 (14th International conference on Biological Inorganic Chemistry), Nagoya, JAPAN. Poster presentation : An efficient oxygenation of hydrocarbons by diverse metal catalysts
11/2008	ASBIC IV (The 4th Asia Bioinorganic Chemistry Conference), Jeju, KOREA Poster presentation : An Efficient Oxygenation of Hydrocarbons Catalyzed by a Nonheme Manganese Complex

Chapter 1. Introduction

Self-assembly is one of the most promising strategies used to fabricate semiconducting materials in solution-phase. It allows us to develop a range of nanostructured systems composed of heterogeneous materials for various applications of electronic and energy-related devices. The morphology of nanostructured semiconductors needs to be deeply understood and precisely controlled because their functional characteristics are strongly dependent on the structural properties.

The goal of this work is to create nanostructured inorganic and organic materials with desired functional properties by controlling their morphology. This work is divided into three parts: the first parts presents the morphology controls of the bulk-heterojunction in organic photovoltaics; the second part focuses on developing mesoporous inorganic materials for solar energy applications; the final part involves the study of pore characteristics regarding their function properties and a new synthetic strategy.

The first part presents the formation of a bulk-heterojunction (BHJ) in the active layer of organic photovoltaics (OPV). OPVs have been developing rapidly due to their facile solution processability and low fabrication costs for the last three decades.[1,2] To achieve the photovoltaic effect, an electron-hole pair known as an exciton needs to promptly diffuse and reach an interface between an electron donor and acceptor.[3,4] Since the exciton diffusion length is typically 10-20nm,[5] it is necessary to optimize the morphology of the BHJ for high performing OPV devices. To achieve a BHJ structure, there are two methods: blend-casting (BC) and sequential processing (SqP). In the BC method, the polymer and fullerene are dissolved in solution, and spun down onto a substrate in one step. In the SqP method, the polymer and fullerene are dissolved in separate solutions. The polymer is casted on a substrate first and then a fullerene layer is deposited. In

chapter 2, SqP P3HT:PCBM solar cells are examined with the introduction of solvent additives that exhibit low vapor pressure. Because the additive is dissolved in a polymer casting solution, the interaction between additive and polymer can be isolated from the interaction between additive and fullerene. In this way, it enables us to elucidate the mechanism of polymer swelling, which influences crystallinity and vertical mixing. In chapter 4, we examine how the vertical phase separation (VPS) is affected by molecular structure in fullerene derivatives. A small molecular change of the structure influences the relative surface energy, which causes a completely different behavior of vertical phase separation. Understanding the correlation between VPS and the device physics allows us to select the appropriate device geometry to avoid undesirable surface recombination.

In the second part of this work, we synthesized mesoporous inorganic thin films using nanocrystals or sol-gel precursors. Evaporation Induced Self-Assembly (EISA) allows us to prepare porous film by simply mixing the precursor and an amphiphilic diblock copolymer, Poly(1,4-butadiene)-b-poly(ethylene oxide). [6,7] In chapter 4, mesoporous nanocrystal-based TiO_2 thin films are made for TiO_2:P3HT hybrid solar cells. A porous structure can provide a large interfacial contact between TiO_2 and P3HT, which reduces efficiency loss during charge separation and transportation. The challenges, however, for inorganic/organic composites, are intrinsic incompatibility and surface wetting.[8] To resolve these issues, [6, 6]-phenyl-C61-butyric acid (PCBA), a fullerene derivative with carboxylic acid, is introduced to modify the TiO_2 surface. PCBA acts as a mediator between TiO_2 and P3HT through chemical bond interactions. Since PCBA has a LUMO located between that of P3HT and TiO_2, it creates a cascade structure in energy levels, which allows us to expect facile charge transfer. In chapter 5, a mesoporous sol-gel based Ta_3N_5 film is prepared as a photoanode for photoelectrochemical water splitting. The

synthesis is processed in solution phase via simple two steps: EISA and nitridation. Mesoporous sol-gel Ta_2O_5 films are first synthesized and then converted to nitride with ammonia flow. The prepared porous Ta_3N_5 film shows excellent pore retention from the mother oxide film without severe grain growth or cracks even after heat treatment. In the photoelectrode performance, we explored the effect of nanostructuring by using porous and dense Ta_3N_5 film. The porous architecture creates a large interfacial contact between electrode and electrolyte, which promotes efficient charge transportation. The film morphology is further tuned by controlling film thickness and introducing cocatalysts, which affect photocatalytic activity.

In the last part, we investigated the nature of porous structures using ellipsometic porosimetry in newly synthesized metal oxide and metal chalcogenide films such as cobalt ferrite (CFO), cadmium sulfide (CdS), cadmium selenide (CdSe). In Chapter 6, we investigated a new synthetic method for mesoporous CdS and CdSe nanocrystals without thermal processing. Block copolymer templates usually require thermal degradation, which limits tuning the grain size and crystal structure.[9,10] Instead of thermal processing, we utilized bidentate ligands to bind the nanocrystals together, after which the polymer template is simply washed off. The prepared porous CdS and CdSe films show a homogenous porous architecture, which exhibits a great potential for the application of quantum confinement, which requires precise size control. In Chapter 7, porous CFO films are synthesized with two methods using nanocrystal and sol precursors. The synthetic method influences the pore characteristics of as-prepared films, which results in their coercivity. Thus, the magnetic properties can be tuned by controlling the synthetic precursor.

1.1 References

(1) He, Z.; Zhong, C.; Su, S.; Xu, M.; Wu, H.; Cao, Y. Enhanced Power-Conversion Efficiency in Polymer Solar Cells Using an Inverted Device Structure. *Nat. Photonics* **2012**, *6*, 591–595.

(2) Helgesen, M.; Søndergaard, R.; Krebs, F. C. Advanced Materials and Processes for Polymer Solar Cell Devices. *J. Mater. Chem*. **2010**, *20*, 36-60.

(3) Heeger, A. J. 25th Anniversary Article: Bulk Heterojunction Solar Cells: Understanding the Mechanism of Operation. *Adv. Mater*. **2014**, *26*, 10–28.

(4) Yu, G.; Gao, J.; Hummelen, J. C.; Wudl, F.; Heeger, A. J. Polymer Photovoltaic Cells: Enhanced Efficiencies via a Network of Internal Donor-Acceptor Heterojunctions. *Science* **1995**, *270*, 1789–1791.

(5) Piris, J.; Dykstra, T. E.; Bakulin, A. A.; Loosdrecht, P. H. M. Van; Knulst, W.; Trinh, M. T.; Schins, J. M.; Siebbeles, L. D. A. Photogeneration and Ultrafast Dynamics of Excitons and Charges in P3HT/PCBM Blends. *J. Phys. Chem. C* **2009**, *113*, 14500–14506.

(6) Zhao, D. Y.; Feng, J. L.; Huo, Q. S.; Melosh, N.; Fredrickson, G. H.; Chmelka, B. F.; Stucky, G. D. Triblock Copolymer Syntheses of Mesoporous Silica with Periodic 50 to 300 Angstrom Pores. *Science* **1998**, *279*, 548–552.

(7) Goltner, C. G.; Antonietti, M. Mesoporous Materials by Templating of Liquid Crystalline Phases. *Adv. Mater*. **1997**, *9*, 431–436.

(8) Fan, X.; Zhang, M.; Wang, X.; Yang, F.; Meng, X.; Recent Progress in Organic–Inorganic Hybrid Solar Cells. *J. Mater. Chem. A*, **2013**, *1*, 8694-8709.

(9) Rauda, I. E.; Saldarriaga-Lopez, L. C.; Helms, B. A.; Schelhas, L. T.; Membreno, D.; Milliron, D. J.; Tolbert, S. H. Nanoporous Semiconductors Synthesized through Polymer Templating of Ligand-Stripped CdSe Nanocrystals. *Adv. Mater*. **2013**, *25*, 1315−1322.

(10) Rivest, J. B.; Buonsanti, R.; Pick, T. E.; Zhu, L.; Lim, E.; Clavero, C.; Schaible, E.; Helms, B. A.; Milliron, D. J. Evolution of Ordered Metal Chalcogenide Architectures through Chemical Transformations. *J. Am. Chem. Soc*. **2013**, *135*, 7446−7449.

Chapter 2. Solvent Additives Function as Polymer Swelling Agents in Bulk Heterojunction.

2.1 Introduction

The formation of an ideal, well-mixed, nanometer-scale morphology is required for achieving a high power conversion efficiency (PCE) in organic bulk heterojunction (BHJ) photovoltaics. Although recent advances have pushed the efficiency of single-junction, polymer-fullerene BHJ solar cells near 12%,[1] attaining the ideal morphology for any given set of conjugated polymer and fullerene materials is quite challenging. In fact, most high-performing materials do not achieve ideal phase separation when they are simply mixed and cast into films, resulting in under-performing devices.[1–3] To address this issue, a variety of techniques have been developed to control polymer/fullerene phase separation, including thermal[4,5] and solvent annealing of already-cast BHJ films,[6,7] changing the host solvent from which the films are cast,[8] and the inclusion of small amounts of so-called solvent additives, such as 1,8-diiodooctane (DIO), 1,8-octanedithiol (ODT), or 1-chloronapthalene (CN), in the solution from which the films are cast.[1–3,9–22]

Unfortunately, none of these methods for improving BHJ morphology are effective without significant trial-and-error. For example, thermal annealing improves the morphology for semi-crystalline polymers such as poly(3-hexylthiophene-2,5-diyl) (P3HT) and is relatively straightforward in application, but the use of heat tends to degrade the performance of devices based on high-performance push-pull polymers.[23–26] The use of solvent additives in the casting solution has become perhaps the most widely used approach for tuning BHJ morphology,[2] but their effect is highly system specific. For example, BHJ systems that naturally form large polymer and fullerene domains require additives that can improve mixing and decrease domain size,[1,3,12–14,18,19,27–31] while BHJ systems that naturally over-mix require additives that can increase phase

separation.[9,10,20–22,32] The problem is, it is not always clear when a particular additive will increase or decrease the average domain size, or how much additive is necessary for optimal performance. This need for trial-and-error is a reflection of the fact that the method by which the additives function is not well understood; indeed, a recent review on additives calls for additional studies to investigate their mechanism of operation.[2]

In addition to the need for Edisonian optimization, the use of solvent additives is problematic on several other fronts: 1) In general, only very small amounts of additives are required for optimal performance. For example, 3% (v/v) additive is frequently reported as the optimal amount needed for many polymer BHJ systems,[2] while in small-molecule BHJ systems, changes in additive concentration of only 0.35% (v/v) from the optimal can cut device efficiency in half;[33] 2) The optimal amount of additive needed also changes upon scale-up.[34] Since most additives have high boiling points, they alter drying kinetics during film-formation, making it not surprising that large-scale fabrication methods, which have entirely different drying kinetics, require re-optimization; 3) The most widely used co-solvent, DIO, is both light- and air-reactive, making it of questionable use in any type of future commercial process. Moreover, it is well known that DIO tends to remain in BHJ films due to its low vapor pressure, requiring extra processing steps to ensure its removal to prevent device degradation upon exposure to light or air;[35–38] 4) Similar to solvent annealing, the time DIO resides within the film affects the morphology through 'additive annealing,' thereby requiring further optimization.[39]

One of the first and most widely used additives is DIO. Quite interestingly, DIO demonstrates high PCBM solubility of 120 mg/mL,[40] and because of this, many groups have postulated that the morphology control afforded by DIO is connected with differential solubility of the polymer and fullerene:[1,3,10,12,28,41] the idea is that additives help to suspend fullerenes in solution for greater

periods of time, which in turn effects the fullerene domain size as the film dries. This idea is not consistent, however, by the fact that molecules like ODT and CN are also commonly used as additives to favorably improves the BHJ morphology.[9,10,20,22,42] ODT has significantly less fullerene solubility (19 mg/mL)[43] than DIO, and CN affords little differential polymer/fullerene solubility.[44] This suggests the mechanism by which solvent additives operate to improve BHJ morphology depends on some property other than differential solubility.

In previous work, we proposed an alternate method for controlling BHJ morphology and fabricating high-performing solar cells based on a two-step fabrication process called sequential processing (SqP).[5,45,46] In SqP, a film of pure polymer is deposited first, and then the fullerene is intercalated to form a BHJ in a second step by casting from a quasi-orthogonal solvent that swells but does not dissolve the polymer underlayer. To ensure optimal BHJ formation, we showed that the solvent used in the fullerene-casting step must optimally swell the polymer underlayer.[45] If the fullerene-casting solvent insufficiently swells the polymer, then there will not be good penetration of the fullerene into the polymer to form the requisite BHJ. If the fullerene-casting solvent over-swells the polymer, it dissolves some of the polymer film away, again leading to poor BHJ formation. It is also important that the fullerene-casting solvent have a high enough fullerene solubility for mass action to drive fullerene into the properly swollen polymer underlayer.[45,47] We have demonstrated that solvent blends can be used to simultaneously optimize both polymer swelling and fullerene solubility, making rational BHJ construction tractable via SqP.[45,47]

In this paper, we take advantage of the fact that SqP decouples the polymer and fullerene components in BHJ formation to investigate the mechanism by which solvent additives improve BHJ morphology. We find that solvent additives function as swelling agents: additives alter polymer/fullerene mixing by swelling the polymer film, allowing fullerenes to remain mobile as

the BHJ is formed. Our evidence is based on experiments in which we add DIO, ODT, or CN to solutions of pure P3HT prior to casting P3HT films. We observe by spectroscopic ellipsometry that low vapor pressure additives such as DIO and ODT remain in the polymer film and significantly swell it, in agreement with previous in situ experiments on polymer/fullerene blend solutions.[48,49] We find by grazing-incidence wide-angle X-ray scattering (GIWAXS) that swelling of P3HT films by solvent additives is so great as to effectively destroy most of the polymer crystallinity; this suggests that additives act as 'secondary plasticizers', since the additive 'plasticizer' is expected to enter only the amorphous regions of the polymer film.[50] When we then spin-cast PCBM from dichloromethane (DCM) on top of either a pristine or additive-swollen P3HT film in a second SqP step, we find using X-ray photoelectron spectroscopy (XPS) and neutron reflectometry (NR) that the presence of the additive helps to produce complete mixing of P3HT and PCBM into a BHJ, whereas there is significantly less fullerene intercalation when no additive is present in the polymer underlayer. Moreover, the presence of the additive in the polymer underlayer leads to greatly improved sequentially-processed device performance. Therefore, similar to how solvent blends for fullerene solutions can be tuned to optimally swell a polymer film,[45] low vapor pressure solvent additives primary mechanism of operation is as co-solvents that swell polymer films. This conclusion should make it possible to rationally choose solvent additives as well as opening additional pathways for BHJ morphology improvement via SqP.

2.2 Results and Discussion

A. Exploring the Role of Solvent Additives by Sequential Processing

Detailing the solvent additive mechanism requires decoupling the additive from the active-layer components. Because most solar cells are fabricated via blend-casting, describing the additive's role is challenging. This is because additive-containing blends mix together the host solvent, polymer, fullerene, and additive into a single solution. Therefore, successful investigations into the additive mechanism must reply upon an alternative fabrication technique. Decoupling DIO from PCBM was first reported by Kong et al., where BHJ films are cast in the first step and optimized with DIO in the second step. In the second step, a dilute DIO solution is spun onto the solid BHJ film; this 'post-additive soaking' favorably reorganizes the donor and acceptor domains, resulting in significantly improved device efficiencies.[58] Since DIO was added to the film after BHJ formation, this two-step approach decouples DIO from PCBM, and further suggests the additive mechanism is independent of fullerene solubility.

Motivated by this result, we decided to investigate the solvent additive mechanism via sequential processing. Since SqP forms a BHJ in two sequential steps, SqP is the ideal processing technique for investigating the solvent additive mechanism.[45,46,59] Thus, we decided to fabricate solar cells by adding DIO to the P3HT solution. Since the first step in SqP spin-casts a polymer film, DIO is decoupled from PCBM. Figure 2.1 shows the *J-V* characteristics of SqP devices with 0, 3, and 7 % (v/v) DIO under AM-1.5 solar illumination; the plotted data is the average of approximately 9 separate devices. The detailed *J-V* parameters are presented in Table 2.1. Figure 2.1(a) shows that without DIO, the currents are quite low. However, with increasing percent DIO the currents increase significantly. Since DIO can only interact with P3HT, this results suggests

the DIO-P3HT interaction is responsible for device improvement. Since DIO has a very low vapor pressure,[60] DIO remains in the film and lowers the device efficiency due to its light reactivity and deleterious chemistry. Thus, we performed methanol washing experiments on films with DIO. Since methanol is known to remove DIO, we expect device improvement.[35–37,61] Methanol-washing occurred directly after P3HT film-formation and prior to PCBM spin-coating. Rather than increasing the device performance, we find that the currents for methanol-washed 3 and 7 % (v/v) DIO devices decrease. Furthermore, it is interesting to note that both methanol-washed devices have almost identical currents. This suggests that similar concentrations of DIO remain in the film after methanol washing, regardless of the initial % (v/v) DIO.

The *J-V* characteristics using different co-solvents are shown in Figure 2.1(b). DIO produces the best *J-V* characteristic and is quite comparable to ODT: we note that our P3HT:PCBM BC devices fabricated with DIO have similar photodiode characteristics to P3HT:PCBM BC devices fabricated with ODT. This suggests DIO and ODT share a similar interaction with P3HT. CN, on the other hand, demonstrates poor *J-V* characteristics and must interact differently. Therefore, the underlying question is the following: why do DIO and ODT significantly improve device performance, while CN does not. In the following sections, we present a series of structural measurements to answer this question and present an associated solvent additive mechanism.

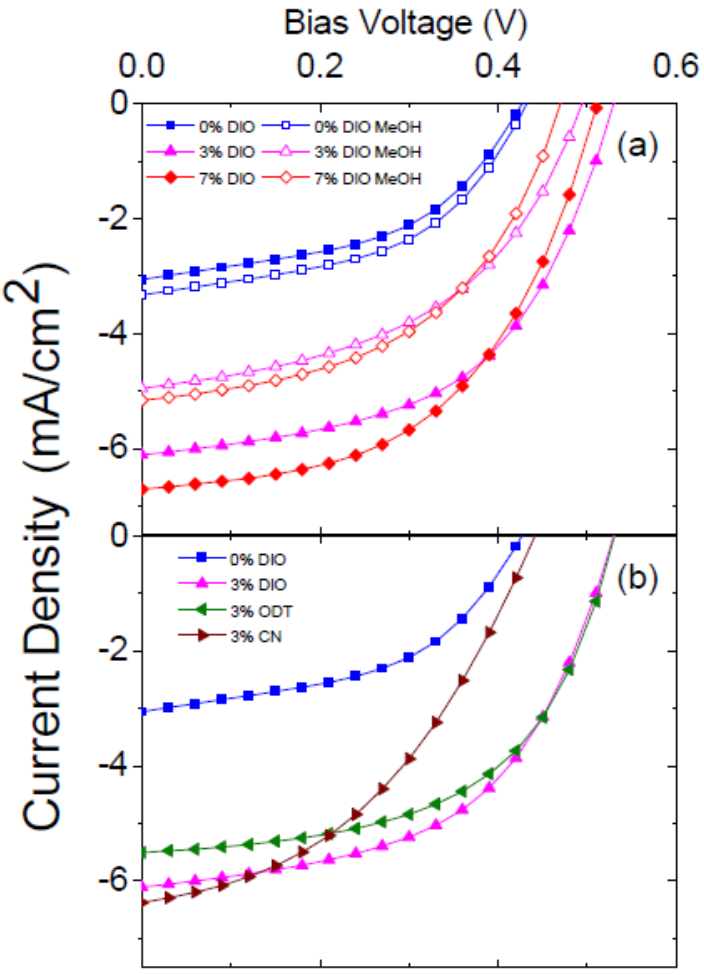

Figure 2.1. *J-V* measurements for sequentially processed devices. (a) *J-V* curves for sequentially processed ITO/PEDOT:PSS/P3HT(DIO)/PCBM/Ca/Al solar cells under AM-1.5 illumination. De-vices are fabricated with 0 % (v/v) DIO (blue squares), 3 % (v/v) DIO (purple up triangles), and 7(v/v) DIO (red diamonds) as well as methanol-washed for 0 % (v/v) DIO (hollow blue squares), 3 % (v/v) DIO (hollow purple up triangles), and 7 % (v/v) DIO (hollow red diamonds). (b) *J-V* curves for SqP devices processed with 0 % (v/v) DIO (blue squares), 3 % (v/v) DIO (purple up triangles), 3 % (v/v) ODT (green left triangles), and 3 % (v/v) CN (maroon right triangles).

Table 2.1. Summary of photovoltaic parameters.

	V_{oc} (V)	J_{sc} (mA/cm^2)	FF $(\%)$	PCE $(\%)$
0% Co-Solvent SqP	0.422 ± 0.026	3.10 ± 0.16	48.16 ± 3.88	0.63 ± 0.10
0% Co-Solvent MeOH SqP	0.430 ± 0.021	3.32 ± 0.11	49.82 ± 4.58	0.71 ± 0.08
0% Co-Solvent Annealed SqP	0.644 ± 0.001	6.34 ± 0.08	67.42 ± 1.29	2.76 ± 0.08
0% Co-Solvent BC	0.626 ± 0.002	7.05 ± 0.21	59.13 ± 0.37	2.61 ± 0.06
0% Co-Solvent Annealed BC	0.620 ± 0.002	8.16 ± 0.13	60.38 ± 3.23	3.06 ± 0.16
3% DIO SqP	0.531 ± 0.006	6.11 ± 0.29	53.58 ± 2.69	1.74 ± 0.15
3% DIO Annealed SqP	0.618 ± 0.002	6.16 ± 0.16	65.35 ± 1.13	2.48 ± 0.08
3% DIO BC	0.573 ± 0.001	9.05 ± 0.49	57.97 ± 0.42	3.00 ± 0.18
3% DIO Annealed BC	0.626 ± 0.002	8.35 ± 0.24	63.13 ± 0.63	3.30 ± 0.10
3% DIO MeOH SqP	0.495 ± 0.009	4.95 ± 0.15	47.72 ± 1.05	1.17 ± 0.06
7% DIO SqP	0.511 ± 0.007	7.15 ± 0.27	50.34 ± 1.32	1.84 ± 0.14
7% DIO MeOH SqP	0.475 ± 0.017	5.16 ± 0.48	48.78 ± 2.51	1.20 ± 0.13
7% DIO DCM SqP	0.545 ± 0.003	5.31 ± 0.12	51.53 ± 0.85	1.49 ± 0.03
3% ODT SqP	0.531 ± 0.011	5.51 ± 0.28	55.06 ± 1.11	1.65 ± 0.19
3% ODT Annealed SqP	0.599 ± 0.002	6.50 ± 0.20	65.62 ± 0.35	2.58 ± 0.04
3% CN SqP	0.441 ± 0.030	6.38 ± 0.50	42.30 ± 1.40	1.22 ± 0.23
3% CN Annealed SqP	0.623 ± 0.002	6.12 ± 0.07	67.47 ± 0.49	2.59 ± 0.06

B. Effect of Solvent Additives on Polymer Swelling and Crystallinity

1. Solvent Additive Swelling Properties

In prior work, we show that polymer swelling is responsible for SqP morphology control.[45] Spin-casting PCBM onto the polymer film during the second SqP step, the fullerene solution must optimally swell the polymer film. If the fullerene solution insufficiently swells the polymer film, poor mixing between donor and acceptor results in under-performing devices. Conversely, over-swelling dissolves the polymer film, again producing under-performing devices. With this swelling picture in mind, we investigated the swelling properties of DIO, ODT, and CN by spectroscopic ellipsometry. For the ellipsometry experiments, P3HT is spun onto Si from binary solutions of 1,2-dichlorobenzene (ODCB) and the respective additive. Figure 2.2 shows the thickness of P3HT films cast from the binary solution containing the additives and ODCB. Depending on the additive used, there is a substantial difference in thickness. Most additive-cast films are thicker than the control (ODCB), except CN film, and the thickest films are cast with the lowest vapor pressure (at 25 C) additive: DIO (0.04 Pa[60]) > ODT (1.60 Pa[62]) > CN (3.87 Pa[63]) > ODCB (181 Pa[64]). While all additives studied have lower vapor pressures than ODCB, DIO has a particularly low vapor pressure, which accounts for the greatest thickness. This indicates that low vapor pressure additives remain in the polymer film after ODCB evaporates and subsequently swell the polymer matrix.[48,49]

Since 7 % DIO produces the thickest film, we predict that higher concentrations of residual additive will most greatly swell P3HT. To test our swelling hypothesis, we predict that removing DIO from the swollen film with methanol will reduce the film thickness. After washing the film with methanol, both 3 % (v/v) and 7 % (v/v) DIO films experienced a significant thickness reduction, resulting in a final thickness that is similar to the pristine P3HT film. We note that the

thickness after washing is still slightly greater than the P3HT thickness because methanol does not fully remove DIO.[35]

While thickness measurements from ellipsometry strongly suggest that low vapor pressure additives swell polymer films, these results do not quantify the amount of additive present. This prevents a direct link between the amount of residual additive and the degree of polymer swelling. To quantify the amount of DIO remaining in both the 3 % (v/v) DIO and 7 % (v/v) DIO films after spin-coating, we applied the Bruggemann effective medium approximation (EMA). The Bruggemann effective medium approximation predicts the refractive index of the binary mixture using the known refractive indices of the film components.[65] When applied to the swollen P3HT system, the EMA quantifies the DIO volume fraction in the film.[45,66] Applying the EMA, DIO volume fractions are estimated as 27 % and 36 % for 3 % (v/v) DIO and 7 % (v/v) DIO films, respectively (Figure 2.2, red triangles). As the percent DIO increases, the sites for DIO-P3HT interaction are increasingly filled, which limits additional DIO incorporation within the film. After methanol washing, the DIO volume fraction drops below 5 % (v/v). Since the DIO volume fraction increases as the film thickness increases, we directly attribute P3HT swelling to the amount of residual additive. Furthermore, actively removing DIO reverses this process, highlighting the that residual additive is responsible for polymer swelling. We note that the EMA for 0 % DIO reads a non-zero value of 10 %. Due to organic solvents having similar index of refraction profiles, we attribute this non-zero EMA value to residual ODCB. We also find that the EMA value de-creases when placing the film under vacuum for at least 20 minutes, which supports the EMA measuring ODCB as DIO.

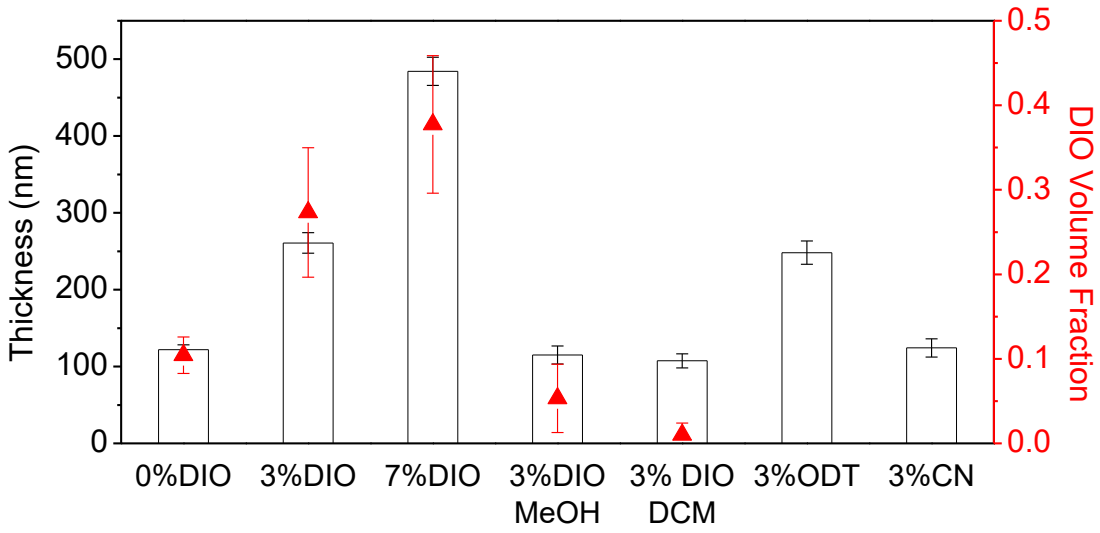

Figure 2.2. Thickness and DIO volume fraction of P3HT:PCBM films obtained by spectroscopic ellipsometry. (a) Thickness (measured directly after spin-casting) of pure P3HT and P3HT films cast with 3 % (v/v) DIO, 7 % (v/v) DIO, 3 % (v/v) DIO (methanol-washed), 3 % (v/v) DIO (dichloromethane-washed), 3 % (v/v) ODT, and 3 % (v/v) CN (white bars). The DIO volume fraction is shown by the red triangles. Swelling is greatest with more residual additive. The error bars represent one standard deviation obtained from averaging over at least three films.

We washed a 3 % (v/v) DIO film with DCM and find that the P3HT thickness decreases. Furthermore, the DIO volume fraction drops below 1 % (v/v). This shows that DCM, like methanol, removes DIO. Since PCBM is sequentially-processed from a DCM solution, SqP combines DIO removal and fullerene incorporation into a single step, thereby removing the need for a separate methanol washing step. Thus, not only is SqP a tractable route towards BHJ design, but simplifies the processing with DIO by combining DIO removal with PCBM deposition.

To further investigate how DIO changes the swelling properties of P3HT films, we studied the uptake of an external swelling solvent. For this experiment, we selected toluene due to its strong interactions with P3HT. P3HT films were swollen by toluene vapor in a home-built, customized vial. With this setup, the change in film thickness and refractive index were monitored by spectroscopic ellipsometry. Figure 2.3 shows that all the films increase in thickness upon solvent vapor uptake, either with or without DIO. Most notably, the thickness increase is largest for films with 3 % (v/v) and 7 % (v/v) DIO (250 nm to 397 nm and 482 nm to 627 nm, respectively). While the total toluene-swollen thickness for the 3 % (v/v) and 7 % (v/v) DIO films are different, the difference in thickness before and after toluene uptake is roughly equal (146 nm). This suggests that once swollen with a threshold level of DIO, a maximum amount of toluene penetrates into the swollen polymer matrix. In contrast, the difference in thickness before and after toluene uptake (127 nm to 194 nm) for the film without DIO is much less (67 nm increase). This result indicates that DIO significantly enhances the uptake of additional solvent, resulting in a significant volume expansion of P3HT. Thus, the presence of DIO not only swells the polymer film, but also increases the film's propensity to swell when put in the presence of other solvents.

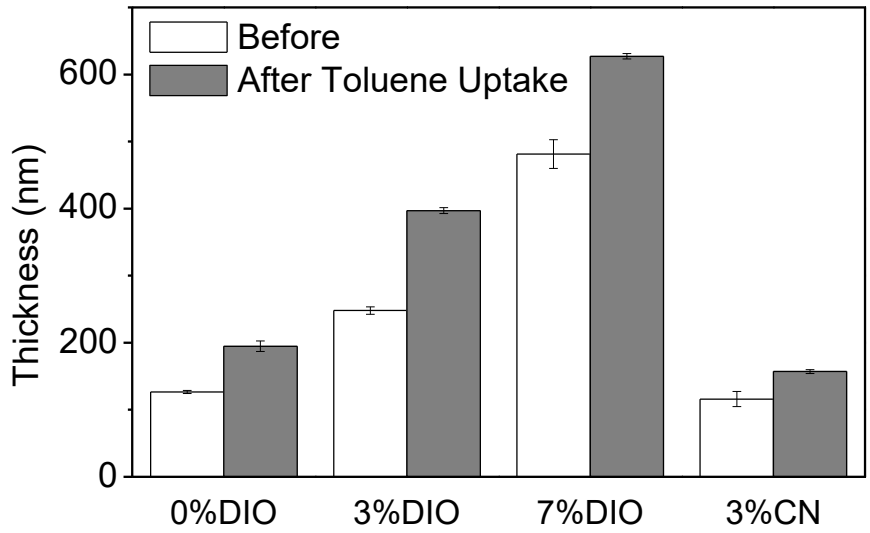

Figure 2.3. Thickness of P3HT films cast with 0 % (v/v) DIO, 3 % (v/v) DIO, and 3 % (v/v) CN before toluene uptake (white bars) and after toluene uptake (grey bars). The additional swelling by toluene for films with DIO demonstrates DIO ability to increase P3HT's propensity to swell compared to P3HT with 0 % (v/v) DIO and 3 % (v/v) CN. The error bars represent one standard deviation obtained from averaging over at least three films.

In contrast to DIO, upon exposure to toluene vapor the 3 % (v/v) CN film is appreciably less swollen. Because CN evaporates much faster than DIO during spin-coating, there is little CN remaining in the film. As we show in the following section, this increases P3HT crystallinity and limits polymer swelling.[67] Unfortunately, we were not able to obtain a steady-state thickness when performing the same measurement on a 3 % (v/v) ODT film of P3HT. We attribute this to the vapor pressure of ODT, which falls in-between DIO and CN; whereas DIO remains in the film for long times and CN evaporates during spin-coating, ODT evaporates during the measurement. This observation of additives delaying film-solidification is consistent with in-situ thickness measurements for doctor-bladed, blend-cast, BHJ films cast with DIO, ODT, and CN.[68,69]

Since we show that low vapor pressure additives remain in the film and delay film solidification, we propose that DIO and ODT are akin to a subset of external plasticizers, namely 'secondary plasticizers'.[50] Secondary plasticizers are known for their low vapor pressures, interaction with polymers via swelling, and ability to be removed. Furthermore, secondary plasticizers only penetrate the amorphous regions and do not dissolve or enter the crystalline regions. Since the sol-vent additive must swell the polymer film in the amorphous regions and act as a non-solvent, this provides the mechanistic origin for why many solvent additives are selected for their low polymer solubility. We propose that DIO and ODT swelling of P3HT operates by a similar mechanism to plasticization of the polymer polyvinyl chloride (PVC), which requires both polar and non-polar regions: non-polar regions ensure good compatibility with the polymer while polar regions inter-act with the polar regions of the crystallite to promote swelling.[70] Indeed, both DIO and ODT share this motif as both structures share non-polar alkyl chains and polar end groups. As such, this motif of high-performing systems requiring solvent additives with polar and non-polar regions is common among many polymer systems.[2,10,37,71,72]

2. Crystallinity Change of P3HT by Additives

As discussed in the previous section, P3HT films prepared with different additives show a large swelling range. It is well known that polymer crystallinity strongly affects swelling because sol-vent molecules cannot penetrate into highly crystalline regions.[45,73,74] To investigate the swelling effects on P3HT crystallites, we performed grazing incidence wide-angle X-ray scattering on films cast with DIO. In Figure 2.4(a)-(c), pristine P3HT shows the lamellar (100) and the p-p stacking peaks at q = 0.4 and 1.6 Å $^{-1}$, respectively. P3HT preserves a typical edge-on orientation showing an intense (100) and (010) peaks in the out-of- and in-plane, respectively. (Figure 2.5 (a) and (b)) With increasing percent DIO (v/v) the (100) peak area decreases as shown in Table 2.2, which is details significant structural changes. Therefore, DIO greatly inhibits P3HT crystallinity through polymer swelling. Swelling by DIO significantly disrupts the P3HT p-p stacking. For the (010) p-p stacking peak, DIO shifts the peak to lower q, which increases the (010) d-spacing from 2.8 Å (control) to 4.3 Å (7 % (v/v) DIO). Furthermore, widening of the (010) shoulder indicates a disordered π-π stacking, with a wider d-spacing distribution. We also note that the (010) peak in P3HT 7 % (v/v) DIO appears for both in- and out-of-plane with similar intensity, which demonstrates the π-π stacking becomes isotropic (Figure 2.5). Thus, the P3HT network containing DIO is less oriented. With residual DIO, the P3HT chain crystallinity is greatly inhibited because the film is swollen. Therefore, our crystallinity results agree with the swelling measurements since less crystalline films swell more.

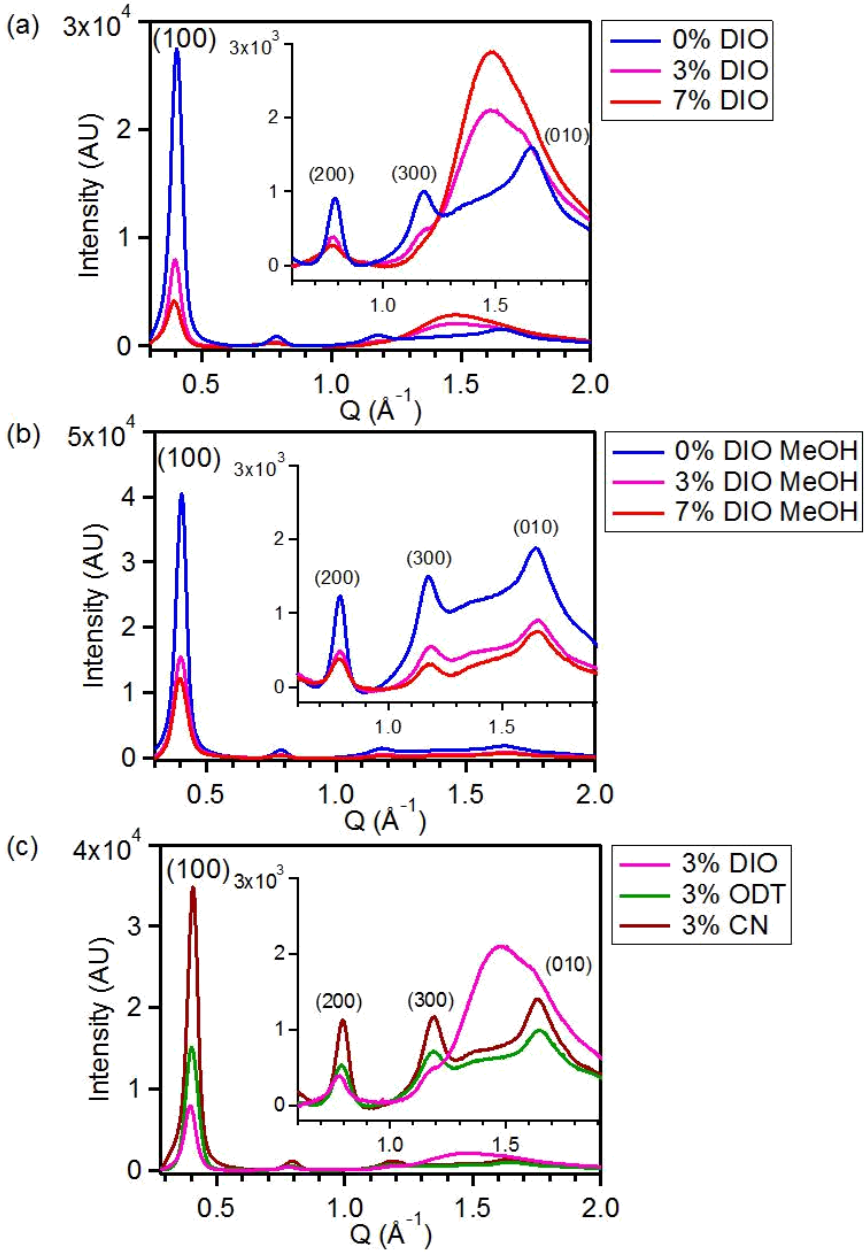

Figure 2.4. 2-D GIWAXS data for P3HT films cast with co-solvents and washed with methanol. (a) P3HT films cast with 0 % (v/v) additive (blue), 3 % (v/v) DIO (purple), and 7 % (v/v) DIO (red). (b) Methanol-washed films of P3HT cast with 0 % (v/v) co-solvent (blue), 3 % (v/v) DIO (purple), and 7 % (v/v) DIO (red). (c) P3HT films cast with 0 % (v/v) additive (blue), 3 % (v/v) DIO (purple), 3 % (v/v) ODT (green), and 3 % (v/v) CN (maroon). The insert in each panel is the high *q* region on an expanded vertical scale.

Table 2.2. (100) Integrated Peak Areas from Figure 2.4.

Film condition	(100) Peak Area (AU)
0% DIO	1621
3% DIO	482
7% DIO	295
0% DIO MeOH	2213
3% DIO MeOH	1069
7% DIO MeOH	842
3% ODT	942
3% CN	1917

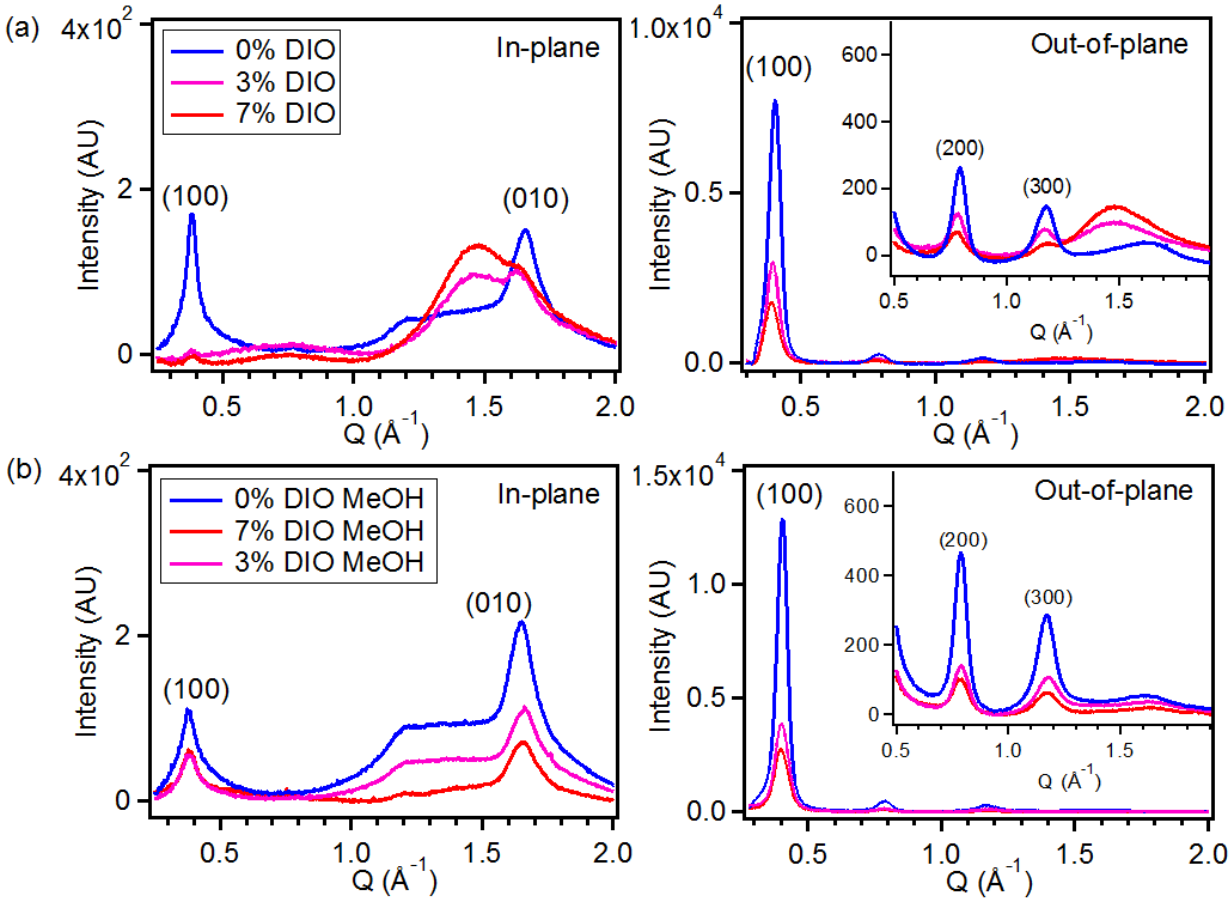

Figure 2.5. In-plane and out-of-plane integrated portion of 2D-GIWAXS films. (a) In-plane and out-of-plane of P3HT films with 0 % DIO (blue), 3 % DIO (purple), and 7 % DIO (red). (b) In-plane and (c) out-of-plane of P3HT films washed with methanol. The insets in out-of-plane show the high-q region on an expanded vertical scale.

As discussed in the ellipsometry section, methanol removes most residual DIO from the polymer film. Thus, we expect most of the DIO-associated structural changes to vanish or reduce upon DIO removal. As shown in Figure 2.4(b) methanol washing restores the P3HT crystallinity and orientation; the (100) peak is partially restored after methanol washing the 3 % (v/v) DIO and 7 % (v/v) DIO films and the (010) peak returns to the original q position. The disordered (010) peak also disappears upon methanol treatment. Although the 3 % (v/v) DIO MeOH and 7 % (v/v) DIO MeOH films show restored edge-on orientation, the P3HT chains are still less edge-on compared to the control P3HT film (Table 2.3). This agrees with the DIO volume fraction estimated by EMA model in Figure 2.2 and the inability of methanol to remove DIO completely.[35]

Table 2.3. Out-of-plane to in-plane ratio for the (100) and (010) peak area in the P3HT films after methanol washing.

	Integrated Peak Area Ratio	
	$(100)_{out\text{-}of\text{-}plane}/(100)_{in\text{-}plane}$	$(010)_{out\text{-}of\text{-}plane}/(010)_{in\text{-}plane}$
0% DIO MeOH	95.8	2.6
3% DIO MeOH	55.8	2.7
7% DIO MeOH	43.9	1.1

Figure 2.6 shows the change in crystallinity and orientation after PCBM deposition. It is interesting that both the (100) and (010) peaks become more intense as the amount of DIO is increased, which is opposite to the cases before PCBM deposition (Figure 2.4(a)) where additional DIO further inhibits P3HT crystallinity. This is because after PCBM deposition the film is fully solidified; for films with DIO the solidification process is longer. This is due to the lower vapor pressure of DIO, which extends the P3HT solidification time, thereby improving its crystallinity. This result agrees with in-situ grazing incidence X-ray scattering measurements on blend-cast films cast with ODT and CN.[48,49]

We note that the PCBM peak at q = 1.4 Å $^{-1}$ also increases with DIO content. This increase could be attributed to the following two factors. First, PCBM is known to preferentially penetrate into amorphous regions of polymer films, while leaving the crystalline region intact.[67] Since DIO lowers the polymer crystallinity, this presents an improved condition for PCBM inter-diffusion. Second, DIO molecules help PCBM diffuse into P3HT network due to the high solubility of PCBM in DIO. The optical density taken after dissolving the films also confirms the PCBM:P3HT mass ratio increases with increasing DIO. The mass ratio was determined by redissolving the polymer:fullerene film and collecting a UV-Visible spectrum of the redissolved solution.[46] The PCBM:P3HT mass ratio for 0, 3 and 7 % (v/v) DIO respectively are 0.80, 0.80, and 0.92 (Figure 2.7). Since the PCBM solutions are identical, the control over fullerene loading into the film is governed by swelling, as opposed to other avenues such as mass action[46] and fullerene solvent selection.[45,47]

To gain further insight on the action of different additives, we also compared the structural changes for P3HT films cast with DIO, ODT, and CN. In Figure 2.4(c), 3 % DIO (v/v) P3HT films show the smallest (100) peak. Since DIO's vapor pressure is very low, DIO remains in the polymer

film and inhibits crystallization by swelling. A similar observation holds for 3 % (v/v) ODT, except this effect is not as dramatic, owing to ODT's higher vapor pressure with respect to DIO; less ODT remains in the film and crystallization is not as strongly inhibited. In contrast to the other additives, the 3 % (v/v) CN P3HT system is the most crystalline. In fact, the (100) peak is higher for 3 % (v/v) CN than the P3HT control. This agrees with the swelling measurement shown in Figure 2.2. With a higher vapor pressure, CN mostly evaporates during spin-coating. However, its lower vapor pressure, with respect to the host solvent, extends the film-solidification time and enhances P3HT crystallinity.[49] Therefore, the vapor pressure of the additive strongly influences the degree of swelling, which directs polymer crystallinity. After PCBM deposition, the P3HT crystallinity trend for the various co-solvents is reversed (Figure 2.6). Similar to the 3 and 7 % (v/v) DIO case, additives with lower vapor pressures remain in the film longer and extend the film-solidification time. Thus, additives with the lowest vapor pressures will yield the most crystalline P3HT domains in the BHJ.

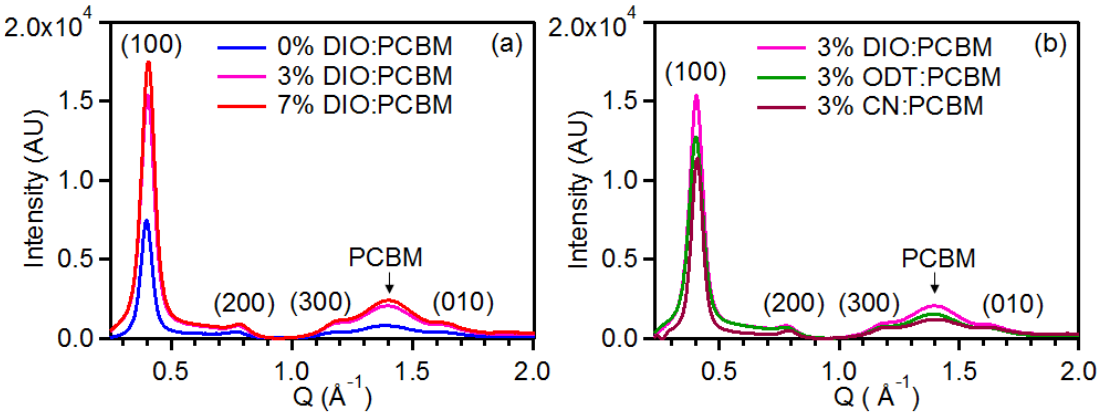

Figure 2.6. 2-D GIWAXS for sequentially processed active layer films. (a) P3HT(DIO):PCBM films with 0 % DIO (blue), 3 % DIO (purple), and 7 % DIO (red). The presence of DIO prior to removal by DCM, slows P3HT crystallization resulting in higher P3HT crystallinity after PCBM deposition. (b) P3HT(co-solvent):PCBM films with 3 % DIO (purple), 3 % ODT (green), and 3 % CN (maroon). The increase in P3HT crystallinity is directly related to the co-solvent vapor pressure: co-solvents with lower vapor pressures remain in the film longer and enhance P3HT crystallinity in the device.

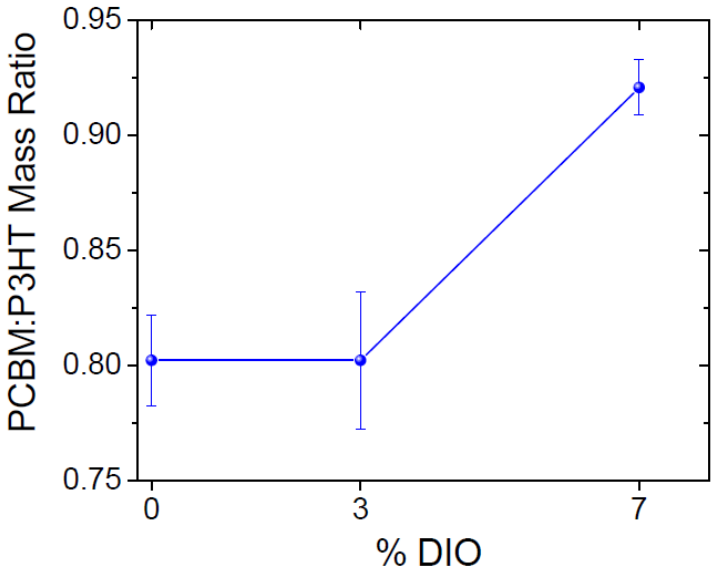

Figure 2.7. Redissolved sequentially processed P3HT(DIO):PCBM active layers. With higher % DIO (v/v), the PCBM:P3HT mass ratio increases. The error bars represent one standard deviation obtained from averaging over three films.

C. Improved Fullerene Mixing in P3HT/PCBM Films by DIO

For P3HT/PCBM sequentially-processed solar cells using DCM as the fullerene solvent, the top surface is enriched in PCBM.[56] With fewer donor-acceptor interfaces, this yields low device efficiencies: since DCM poorly swells P3HT, the high-surface-energy PCBM cannot diffuse toward the high-surface-energy bottom electrode.[45,56] However, annealing the BHJ adds enough thermal energy so that PCBM can diffuse towards the bottom electrode, which results in complete mixing in the vertical direction.[56,75,76] Since DIO swells P3HT and significantly improves the device performance, we investigated the vertical distribution of PCBM throughout the various active layers prepared with and without DIO. Furthermore, we expect PCBM to intercalate throughout the polymer film since DIO swells the polymer film. This increased diffusion of PCBM is consistent with DIO acting as a plasticizer and was observed in PTB7:$PC_{71}BM$ films.[77]

First, we probed the top surface composition of the SqP films by XPS. Measuring the sulfur-to-carbon (C/S) ratio, the surface composition is estimated since PCBM does not contain sulfur.[78–80] This ratio is determined by fitting the sulfur 2p and carbon 1s spectral lines (see Supporting Information for experimental and analysis details). Comparing the % S signal of a SqP film to a pure P3HT film, films with higher % S indicate fullerene intercalation since fullerene intercalation respectively enriches the top surface with P3HT. The XPS results in Figure 2.8 show that the presence of DIO increases the sulfur signal, which demonstrates that fullerene is driven into them film upon swelling. With just 3 % (v/v) DIO, the top surface is significantly enriched with P3HT. Upon additional swelling, PCBM is driven further into the film, further enriching the top surface with P3HT. In fact, 7 % (v/v) DIO swells the film so much that the top surface composition of the film is almost identical to a pure film of P3HT.

To characterize the extent of fullerene loading through the entire film thickness, we investigated the vertical phase segregation (VPS) of the films by neutron reflectometry (NR). NR serves as an excellent probe of vertical phase distribution along the perpendicular direction to the film plane.[56] The active layers measured were spin-coated onto PEDOT:PSS-coated Si substrates for the measurement. Additional details regarding the fitting is found in the Supporting Information.

The scattering length density (SLD) profiles shown in Figure 2.8 present the vertical distribution of P3HT and PCBM throughout the film and are in excellent agreement with our XPS results. Without DIO, a higher SLD value is obtained for the top surface, indicating a high PCBM con-centration. This effect is explained by three system properties. First, DCM weakly swells P3HT since P3HT's uniquely high crystallinity severely inhibits polymer-solvent interaction and therefore less PCBM interdiffusion.[45,67,73,81] Second, the high vapor pressure of DCM at 25 C (58,000 Pa[82]), limits fullerene intercalation, resulting in a fullerene-enriched top surface.[56,83–85] Third, the solubility of fullerene derivatives in DCM is poor.[47] Nonetheless, limited swelling of P3HT by DCM allows some PCBM to intercalate into the polymer network, establishing a limited mixed region.[56,75] However, this intercalation is not substantial throughout the entire film thickness, giving rise to a P3HT-rich region at the bottom. These distinct regions of pure material and limited mixing help explain the poor exciton splitting efficiency and low device currents in the absence of DIO. With 3 % (v/v) DIO, the NR SLD profile shows complete mixing throughout the entire film thickness, which agrees with DIO acting as a polymer sweller. The 7 % (v/v) DIO SLD profile also shows good mixing of P3HT and PCBM; the similarity of the 3 and 7 % (v/v) SLD depth profiles is supported by the similarity between the respective J V curves. However, the key difference between the two DIO films is the increased P3HT concentration near the top surface with 7 % (v/v) DIO. Since 7 % (v/v) DIO swells P3HT more than 3 % (v/v) DIO, and PCBM

favors the bottom surface based on surface energy, more PCBM intercalates within the polymer film with 7 % (v/v) DIO.[79] These XPS and NR results clearly demonstrate that by swelling the polymer film, DIO demonstrates great influence on the vertical mixing of PCBM and overall BHJ quality.

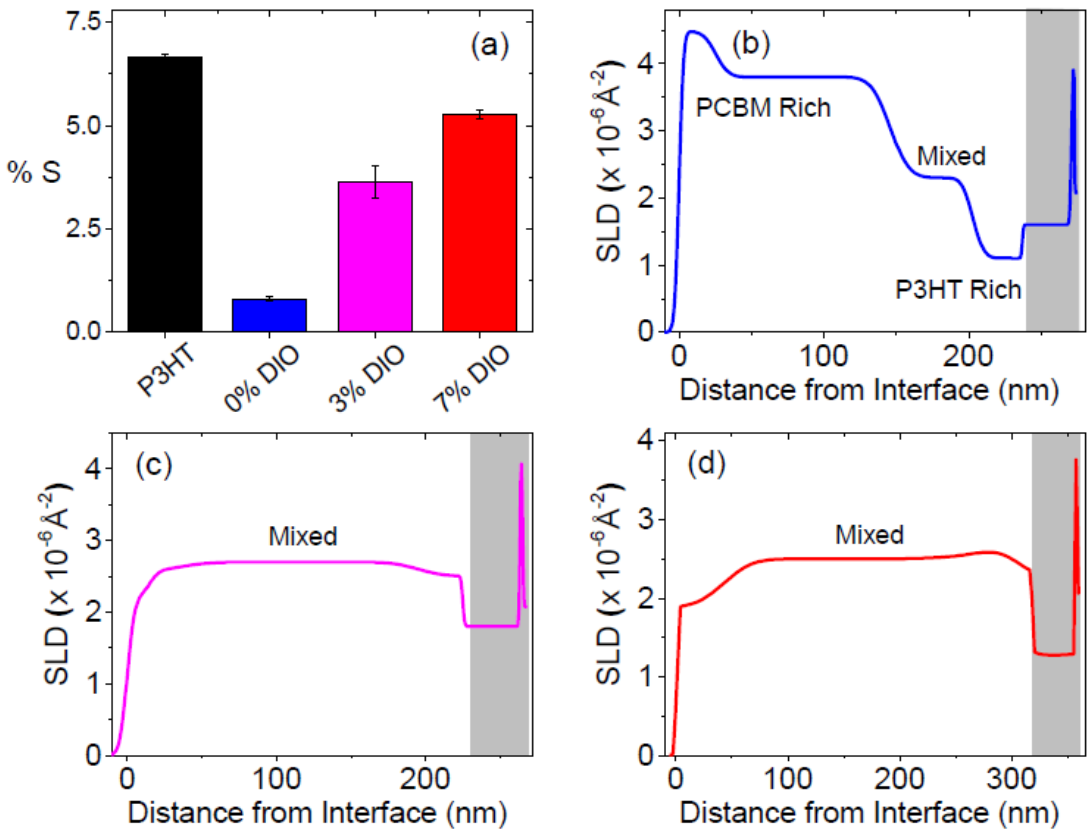

Figure 2.8. (a) Top-surface composition of P3HT:PCBM SqP films with 0 % DIO (blue), 3 % DIO (purple), and 7 % DIO (red) as measured by XPS. Shown for comparison is the film of pure P3HT (black), which is similar to the 7 % DIO film. The increase % S demonstrates increased fullerene intercalation upon swelling. The error bars represent one standard deviation for the average of at least three films. Neutron SLD depth profiles of P3HT:PCBM films obtained by fitting the NR data in Figure 2.9 of (b) 0 % (v/v) DIO (blue), (c) 3 % (v/v) DIO (purple), and (d) 7 % (v/v) DIO (red). Our model is constructed from multiple layer thicknesses, ensuring the active-layer/air interface is at the origin. Shown in gray is the PEDOT:PSS/Si interface. With increasing % (v/v) DIO, the PCBM concentration at the top surface decreases and becomes more homogeneously mixed throughout the vertical thickness of the device.

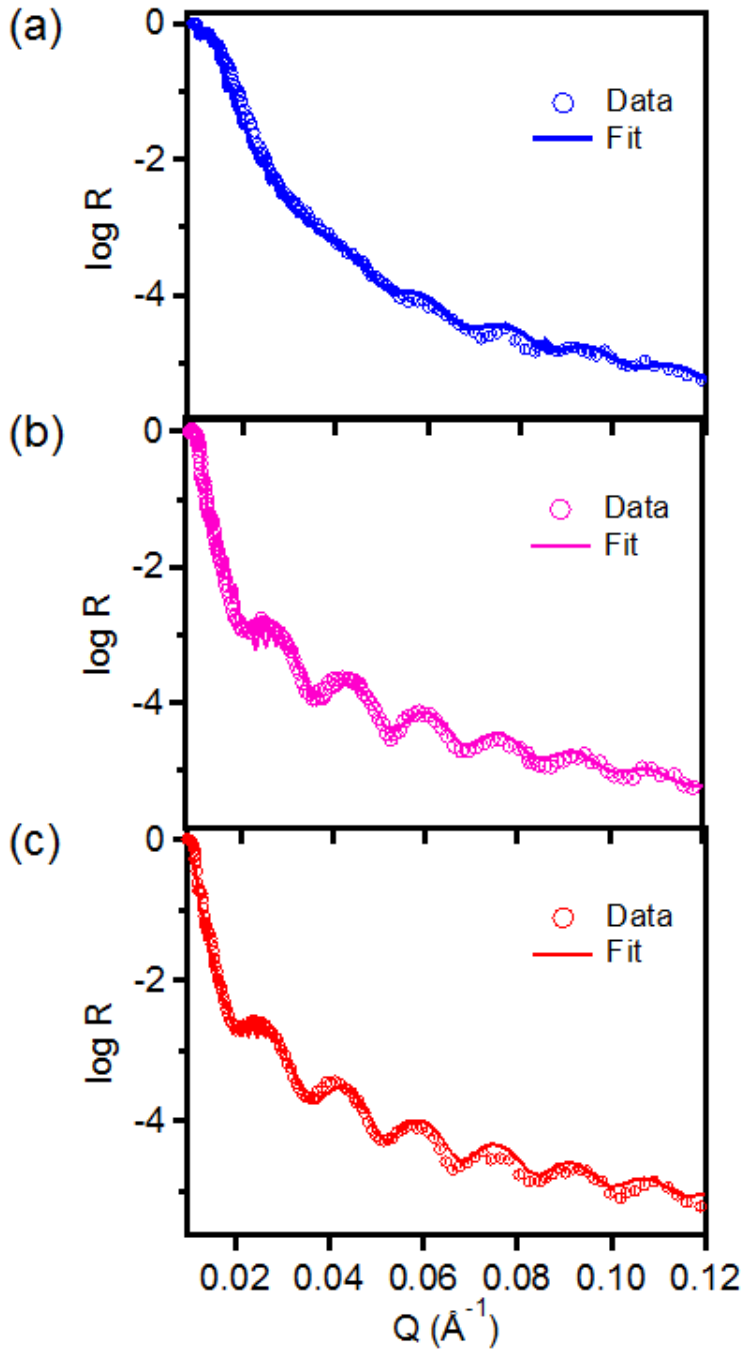

Figure 2.9. Neutron reflectivity data for SqP P3HT:PCBM films on Si with (a) 0 % DIO (blue), (b) 3 % DIO (purple), and (c) 7 % DIO (red). The solid lines are fits to the raw reflectivity data.

D. Solvent Additives are Co-Solvent Swelling Agents

We shave shown that low vapor pressure additives such as DIO and ODT swell P3HT films and almost entirely disrupt the crystallinity. Furthermore, this swelling or secondary plasticization facilitates complete mixing between P3HT and PCBM during the second SqP step. Thus, sol-vent additive function as co-solvent swelling agents. Since DIO and ODT swell the polymer film, this lowers the requirement for additional swelling power in the fullerene solvent. In this manner, swelling agents function identically to solvent blends.[45] Whereas swelling agents swell the polymer film once the film is cast, solvent blends swell the film in a secondary step. This affords additional routes toward tractable BHJ optimization via SqP. Not only can one swell the polymer film through solvent blends, but one can swell the polymer film with swelling agents in the polymer film or a combination of the two methods. In particular, a combination of the two methods is useful for polymers that are highly insoluble. In such cases, a greater fraction of swelling agent is required, which degrades the fullerene solvent quality and lowers device performance.[47] By swelling the polymer film directly, the fraction of fullerene solvent can be increased to produce an improved morphology.[45,47] Furthermore, our picture of solvent additives functioning as polymer swelling agents is supported by the post-additive soaking experiment. In these experiments, thicker BHJ films require increased % (v/v) DIO in the post-additive soaking to achieve optimal performance. This further agrees with our swelling mechanism since additional DIO must be present to swell a thicker film.[58]

Extending our SqP results to blend-cast systems, we arrive at the following picture: with polymer and fullerene co-dissolved in a binary solution of host solvent and swelling agent, the swelling agent swells the polymer and delays film solidification due to its low vapor pressure; swelling improves mixing and thus favorably decrease fullerene domain sizes. This mechanism

accounts for the majority of trends reported in the literature for high-performing push-pull polymers that over-aggregate.[1,3,12–14,18,19,27–31]

2.3 Conclusions

In summary, solvent additives are low vapor pressure polymer swelling agents. Fabricating films through sequential processing and adding the swelling agent to the P3HT solution, we observe significant structural changes. As verified by spectroscopic ellipsometry, swelling agents such as DIO or ODT swell P3HT and remain in the polymer film due to their low vapor pressures. With the pre-swollen polymer film, the fullerene solvent does not need to swell the polymer film as strongly; this makes DCM a good candidate for fullerene intercalation. CN, with its higher vapor pressure is not a swelling agent and does not remain in the polymer film after spin-coating. Since CN has a relatively lower vapor pressure than ODCB, CN extends film solidification and produces highly crystalline films that inhibit PCBM intercalation. Therefore, successful fullerene intercalation via sequential processing requires selecting a low vapor pressure swelling agent that remains in the film throughout fullerene spin-casting. Since DIO has a very low vapor pressure and swells the polymer film, DIO is the ideal candidate and functions as a secondary plasticizer.

This work demonstrates the importance of polymer swelling to ensure good mixing of both polymer donor and fullerene derivative acceptor materials. Furthermore, this approach is widely applicable to multiple polymer systems as the swelling agent is added directly to the polymer in solution. By directly swelling the polymer film with a low vapor pressure swelling agent, this makes sequential processing an even more tractable route towards optimal BHJ formation.

2.4 Experimental Methods

Solar Cell Materials

The materials used in this study were purchased commercially and used as received. P3HT was purchased from Rieke Metals. Inc. (Sepiolid P200) and PCBM was purchased from Nano-C. PEDOT:PSS (AI 4083) was purchased from Ossila.

Photovoltaic Device and Active Layer Fabrication Procedures

The first step in the P3HT:PCBM solar cell fabrication process is cleaning glass substrates prepatterned with tin-doped indium oxide (ITO; TFD Inc.). First, the ITO substrates are sonicated for approximately ten minutes in each cleaning solution (detergent, deionized water, acetone, and isopropanol). Following this, the ITO substrates are dried in vacuum for at least 30 min before treated with an air plasma (200 mTorr, 15 min). A thin layer of PEDOT:PSS is deposited by spincoating the PEDOT:PSS solution in air at 5000 rpm for 20 s. The PEDOT:PSS-covered substrates are then baked at 150 C for 20 min in air.

Sequentially processed active layers were prepared by spin-casting a P3HT solution onto a PEDOT:PSS-covered substrate. The P3HT solution was prepared by dissolving 20 mg P3HT in 1 mL o-dichlorobenzene and mixed at 55 ºC overnight. DIO, ODT or CN (typically 3 % by volume) is added directly to the polymer solution prior to heating. Before spinning, the solution cooled to room temperature. P3HT films were spin-cast in two successive steps (1000 rpm for 60 s; 3000 rpm for 5 s). If methanol washing was applied, methanol was deposited right after P3HT polymer film formation while the polymer film is still on the spin coater chuck. Methanol was spun onto the film with a speed of 2500 rpm for 40 s.

PCBM was deposited by spin-casting (4000 rpm for 5 s) a 1 % PCBM solution directly onto the P3HT film. The PCBM solution was prepared by dissolving 10 mg PCBM in 1 mL DCM and

mixed at room temperature for at least 20 minutes. Fullerene deposition occurred within one hour of casting the polymer film, and no vacuum step was applied between polymer and fullerene spinning. This ensured minimal co-solvent evaporated between polymer film preparation and fullerene deposition.

The P3HT:PCBM blend solutions were prepared by co-dissolving P3HT and PCBM with a weight ratio of 1:0.8 (P3HT:PCBM) in o-dichlorobenzene. The concentration, with respect to P3HT was 20 mg/mL and the solutions were stirred at 60 ºC overnight. After cooling to room temperature, the solution was spun in two successive steps (1160 rpm for 20 s; 3000 rpm for 5 s) onto the PEDOT:PSS-covered substrate. 3 % (v/v) DIO, ODT, or CN was directly added to the composite solution prior to heating.

For thermally annealed films, the annealing process occurred in an argon atmosphere, after BHJ formation. Sequentially processed films were annealed at 150 ºC for 15 min on a hot plate while blend cast films were annealed at 110 C for 20 minutes. Directly after annealing, the films were placed on the metal surface of the glove box for cooling.

For devices, electrodes were evaporated onto the active layers using a thermal evaporator (Angstrom Engineering). ~ 10 nm of Ca was evaporated at a rate of ~ 0.5 Å/s followed by evaporating ~ 70 nm Al at a rate of ~ 1 Å/s. Evaporation pressures were 10^{-7} Torr or less. The active areas of the resulting solar cells were 7.2 mm^2.

***J-V* Measurements**

J-V measurements were performed in an argon atmosphere using a Keithley 2400 source meter. A xenon arc lamp equipped with an AM-1.5 filter was used as the excitation source, with the intensity calibrated to match 1 sun. The *J-V* data the average of approximately 9 separate

devices and the error bars are ± 1 standard deviation. Dark *J-V* parameters are omitted from devices that do not perform as good diodes and therefore do not follow the diode equation.

Active-Layer Composition Analysis by the Redissolving Technique

The procedure for determining the active layer was performed on ITO/PEDOT/Active Layer/ substrates that were processed identically to the procedure above, except without evaporation of the Ca/Al top electrodes.[46] First, the outer edge (1-2 mm) of the active layer was removed with a razor blade, leaving the center portion of the film where the solar cells reside. This is because the outer edge can be anomalously rich in PCBM in SqP films, which is likely due to surface tension effects during the spin-coating deposition process.

The substrates were then cleaned with nitrogen and the active layer was redissolved by directly pipetting two to three drops of ODCB onto the active layer with a glass pipette. This results in instantaneous dissolution of the active layer, regardless of the processing condition. With ODCB still on the substrate, the active-layer-containing ODCB was drawn up into the pipette and redeposited onto the active layer a few times. Following this, the active layer solution was added to a 1 mm thick quartz cuvette. This entire process was repeated two to three additional times, each time using a clean glass pipette to redissolve the active layer. After transferring all of the dissolved active layer solution, the cuvette was vigorously shaken to yield a uniformly mixed and completely dissolved solution.

A UV-Visible spectrometer collected the absorbance spectrum of the redissolved film and the PCBM:P3HT ratio was determined by fitting the redissolved film's absorbance spectrum to a linear combination of the pure P3HT absorbance spectrum and the pure PCBM absorbance spectrum: $OD_{Soln}(\lambda) = A_{PCBM}OD_{PCBM}(\lambda) + A_{P3HT}OD_{P3HT}(\lambda)$

A_{PCBM} and A_{P3HT} are fitting coefficients that represent the amount of each material. Therefore, the PCBM:PCBM mass ratio is given by A_{PCBM}/A_{P3HT}.

Spectroscopic Ellipsometry Experiments and Analysis

For the solvent uptake experiments, spectroscopic ellipsometry was used to measure the film thickness. Each film was placed in a home-built customized vial, which is designed to contain a solvent (i.e. toluene). The film thickness in the vial is monitored until it reaches steady state while the P3HT film is exposed to toluene vapor in the vial. The relative solvent vapor pressure in the vial can reach up to p=p0 = 0.90. To determine this value, we first carried out the toluene adsorption using the ellipsometric porosimeter. It provided the swelling calibration curve with toluene, showing the change of film thickness as function of p=p0. Then, we mapped the thickness change of P3HT film collected from the vial onto the swelling calibration curve. To minimize the error, all the ellipsometric experiments were repeated three times and collected immediately after film-preparation. To ensure minimal co-solvent evaporated between film preparation and the measurement, all films were stored in sealed vials after spin-coating and were prepared less than one hour from the measurement time.

Grazing Incidence Wide-Angle X-ray Scattering (GIWAXS) Experiments and Analysis

2-D GIWAXS experiments were performed at the Stanford Synchrotron Radiation Lightsource on beam line 11-3 using a wavelength of 0.9742 Å . The beam spot is approximately 150 mm and a helium chamber was used to reduce the noise. Each data curve corresponds to the radially integrated pattern of the data from the full 2-D diffractogram and is the average of at least three different batches prepared under the same conditions. The 2-D images were collected on a plate with the detector 250 mm away from the center of the measured sample. The software package WxDiff was used to analyze the GIWAXS data. To ensure minimal co-solvent evaporated between

film preparation and the measurement, all films were stored in sealed vials after spin-coating and were prepared less than 24 hours from the measurement time.

X-ray Photoelectron Spectroscopy (XPS) Experiments and Analysis

X-ray photoelectron spectroscopy (XPS) experiments were performed on Si/active layer films using a Kratos Axis Ultra DLD with a monochromatic Ka radiation source. We did not use PEDOT:PSS/Si substrates since PEDOT:PSS contains sulfur, which can alter the S/C ratio. A charge neutralizer filament controlled for charging of the sample. For the beam, a 20 eV pass energy was used with a 0.05 eV step and scans were calibrated by shifting the C 1s peak to 284.8 eV. CasaXPS software integrated the peaks to find the respective peak areas in addition to determining atomic ratios. The Kratos library and Casa software provided the atomic sensitivity factors used.

Neutron Reflectometry Experiments and Analysis

Neutron reflectometry (NR) experiments were performed at Oak Ridge National Laboratory using the Magnetism Reflectometer at the Spallation Neutron Source using a neutron wavelength of 4.41 Å and an effective q-range of 0.008-0.153 $Å^{-1}$ ($q = 4\pi/\lambda sin\theta$, where λ is the neutron wavelength and q is the scattering angle). Motofit Software was used to determine the vertical distribution of the thin films by fitting the reflectivity.

The active layers measured were spin-coated onto PEDOT:PSS-coated Si substrates for the measurement. To obtain scattering length density (SLD) depth profiles, we calculated the reflectivity of a model SLD profile. SLD depth profiles were obtained by calculating the reflectivity of a model SLD profile, and iteratively refining the model until the calculated reflectivity profile matched the experimental reflectivity profile. Multiple layers compose depth profiles of the films, accounting for the 2 nm thermal oxide layer on the Si substrate, PEDOT:PSS

hole-transport layer, and active-layer. The SLD, thickness, and roughness of each layer are floating parameters in the fits. SLD values of pure P3HT and PCBM were obtained by fitting neutron reflectivity profiles of the pure components and determined to be $4.4 \times 10^{-6} Å^{-1}$ for PCBM and $0.6 \times 10^{-6} Å^{-1}$ for P3HT, which agrees with literature values.[54-56] Since the SLD contrast between P3HT and PCBM is sufficient, selective deuteration is not required.

2.5 References

(1) Zhao, J.; Li, Y.; Yang, G.; Jiang, K.; Lin, H.; Ade, H.; Wei, M.; Yan, H. Efficient Organic Solar Cells Processed from Hydrocarbon Solvents. *Nature Energy* **2016**, *1*, 15027.

(2) Kwon, S.; Kang, H.; Lee, J.-H.; Lee, J.; Hong, S.; Kim, H.; Lee, K. Effect of Processing Additives on Organic Photovoltaics: Recent Progress and Future Prospects. Advanced Energy Materials **2016**, *7*, 1601496.

(3) Liang, Y.; Xu, Z.; Xia, J.; Tsai, S.-T.; Wu, Y.; Li, G.; Ray, C.; Yu, L. For the Bright Future—Bulk Heterojunction Polymer Solar Cells with Power Conversion Efficiency of 7.4%. *Advanced Materials* **2010**, *22*, E135–E138.

(4) Ma, B. W.; Yang, C.; Gong, X.; Lee, K.; Heeger, A. J. Thermally Stable, Efficient Polymer Solar Cells with Nanoscale Control of the Interpenetrating Network Morphology. *Advanced Functional Materials* **2005**, *15*, 1617–1622.

(5) Ayzner, A. L.; Wanger, D. D.; Tassone, C. J.; Tolbert, S. H.; Schwartz, B. J. Room to Improve Conjugated Polymer-Based Solar Cells: Understanding How Thermal Annealing Affects the Fullerene Component of a Bulk Heterojunction Photovoltaic Device. *Journal of Physical Chemistry C Letters* **2008**, *112*, 18711–18716.

(6) Li, G.; Yao, Y.; Yang, H.; Shrotriya, V.; Yang, G.; Yang, Y. "Solvent Annealing" Effect in Polymer Solar Cells Based on Poly(3-hexylthiophene) and Methanofullerenes. *Advanced Functional Materials* **2007**, *17*, 1636–1644.

(7) Zhao, Y.; Xie, Z.; Qu, Y.; Geng, Y.; Wang, L.; Zhao, Y.; Xie, Z.; Qu, Y.; Geng, Y.; Wang, L. Solvent-vapor treatment induced performance enhancement of poly(3-hexylthiophene):methanofullerene bulk-heterojunction photovoltaic cells. *Applied Physics Letters* **2007**, *90*, 043504.

(8) Walker, B.; Tamayo, A.; Duong, D. T.; Dang, X.-D.; Kim, C.; Granstrom, J.; Nguyen, T.-Q. A Systematic Approach to Solvent Selection Based on Cohesive Energy Densities in a Molecular Bulk Heterojunction System. *Advanced Energy Materials* **2011**, *1*, 221–229.

(9) Peet, J.; Kim, J. Y.; Coates, N. E.; Ma, W. L.; Moses, D.; Heeger, A. J.; Bazan, G. C. Efficiency Enhancement in Low-Bandgap Polymer Solar Cells by Processing with Alkane Dithiols. *Nature Materials* **2007**, *6*, 497–500.

(10) Lee, J. K.; Ma, W. L.; Brabec, C. J.; Yuen, J.; Moon, J. S.; Kim, J. Y.; Lee, K.; Bazan, G. C.; Heeger, A. J. Processing Additives for Improved Efficiency from Bulk Heterojunction Solar Cells. *Journal of the American Chemical Society* **2008**, *130*, 3619–3623.

(11) Coffin, R. C.; Peet, J.; Rogers, J.; Bazan, G. C. Streamlined Microwave-Assisted Preparation of Narrow-Bandgap Conjugated Polymers for High-Performance Bulk Heterojunction Solar Cells. *Nature Chemistry* **2009**, *1*, 657–661.

(12) Bijleveld, J. C.; Gevaerts, V. S.; Nuzzo, D. D.; Turbiez, M.; Mathijssen, S. G. J.; de Leeuw, D. M.; Wienk, M. M.; Janssen, R. A. J. Efficient Solar Cells Based on an Easily Accessible Diketopyrrolopyrrole Polymer. *Advanced Materials* **2010**, *2*, E242–E246.

(13) Amb, C. M.; Chen, S.; Graham, K. R.; Subbiah, J.; Small, C. E.; So, F.; Reynolds, J. R. Dithienogermole as a Fused Electron Donor in Bulk Heterojunction Solar Cells. *Journal of the American Chemical Society* **2011**, *133*, 10062–10065.

(14) Guo, X.; Cui, C.; Zhang, M.; Huo, L.; Huang, Y.; Li, Y. High efficiency polymer solar cells based on poly(3-hexylthiophene)/indene-C70 bisadduct with solvent additive. *Energy and Environmental Science* **2012**, *5*, 7943–7949.

(15) Liu, Y.; Zhao, J.; Li, Z.; Mu, C.; Ma, W.; Hu, H.; Jiang, K.; Lin, H.; Ade, H.; Yan, H. Aggregation and Morphology Control Enables Multiple Cases of High-Efficiency Polymer Solar Cells. *Nature Communications* **2014**, *5*, 5293.

(16) Shao, M.; Keum, J. K.; Kumar, R.; Chen, J.; Browning, J. F.; Das, S.; Chen, W.; Hou, J.; Do, C.; Littrell, K. C.; Rondinone, A.; Geohegan, D. B.; Sumpter, B. G.; Xiao, K. Understanding How Processing Additives Tune the Nanoscale Morphology of High Efficiency Organic Photovoltaic Blends: From Casting Solution to Spun-Cast Thin Film. *Advanced Functional Materials* **2014**, *24*, 6647–6657.

(17) Chen, H.-Y.; Hou, J.; Zhang, S.; Liang, Y.; Yang, G.; Yang, Y. Polymer Solar Cells with Enhanced Open-Circuit Voltage and Efficiency. *Nature Photonics* **2009**, *3*, 649–653.

(18) Su, M.-S.; Kuo, C.-Y.; Yuan, M.-C.; Jeng, U.-S.; Su, C.-J.; Wei, K.-H. Improving Device Efficiency of Polymer/Fullerene Bulk Heterojunction Solar Cells Through Enhanced Crystallinity and Reduced Grain Boundaries Induced by Solvent Additives. *Advanced Materials* **2011**, *23*, 3315–3319.

(19) Zhang, Y.; Li, Z.; Wakim, S.; Alem, S.; Tsang, S.-W.; Lu, J.; Ding, J.; Tao, Y. Bulk Heterojunction Solar Cells Based on a New Low-Band-Gap Polymer: Morphology and Performance. *Organic Electronics* **2011**, *12*, 1211–1215.

(20) Chen, H.-Y.; Yang, H.; Yang, G.; Sista, S.; Zadoyan, R.; Li, G.; Yang, Y. Fast-Grown Interpenetrating Network in Poly(3-hexylthiophene): Methanofullerenes Solar Cells Processed with Additive. *Journal of Physical Chemistry C* **2009**, *113*, 7946–7953.

(21) Gu, Y.; Wang, C.; Russell, T. P. Multi-Length-Scale Morphologies in PCPDTBT/PCBM Bulk-Heterojunction Solar Cells. *Advanced Energy Materials* **2012**, *2*, 683–690.

(22) Schaffer, C. J.; Schlipf, J.; Dwi Indari, E.; Su, B.; Bernstorff, S.; Müller-Buschbaum, P. Effect of Blend Composition and Additives on the Morphology of PCPDTBT:PC71BM Thin Films for Organic Photovoltaics. *ACS Applied Materials and Interfaces* **2015**, *7*, 21347–21355.

(23) Liang, Y.; Yu, L. A New Class of Semiconducting Polymers for Bulk Heterojunction Solar Cells with Exceptionally High Performance. *Accounts of Chemical Research* **2010**, *43*, 1227–1236.

(24) Park, S. H.; Roy, A.; Beaupré, S.; Cho, S.; Coates, N.; Moon, J. S.; Moses, D.; Leclerec, M.; Lee, K.; Heeger, A. J. Bulk Heterojunction Solar Cells with Internal Quantum Efficiency Approaching 100%. *Nature Photonics* **2009**, *3*, 297–303.

(25) Chu, T.-Y.; Alem, S.; Tsang, S.-W.; Tse, S.-C.; Wakim, S.; Lu, J.; Dennler, G.; Gaudiana, R.; Tao, Y. Morphology Control in Polycarbazole Based Bulk Heterojunction Solar Cells and Its Impact on Device Performance. *Applied Physics Letters* **2011**, *98*, 253301.

(26) Bartelt, J. A.; Beiley, Z. M.; Hoke, E. T.; Mateker, W. R.; Douglas, J. D.; Collins, B. A.; Tumbleston, J. R.; Graham, K. R.; Amassian, A.; Ade, H.; Fréchet, J. M. J.; Toney, M. F.; McGehee, M. D. The Importance of Fullerene Percolation in the Mixed Regions of Polymer–Fullerene Bulk Heterojunction Solar Cells. *Advanced Energy Materials* **2013**, *3*, 364–374.

(27) Moon, J. S.; Takacs, C. J.; Cho, S.; Coffin, R. C.; Kim, H.; Bazan, G. C.; Heeger, A. J. Effect of Processing Additive on the Nanomorphology of a Bulk Heterojunction Material. *Nano letters* **2010**, *10*, 4005–4008.

(28) Zusan, A.; Zerson, M.; Dyakonov, V.; Magerle, R. The Effect of Diiodooctane on the Charge Carrier Generation in Organic Solar Cells Based on the Copolymer PBDTTT-C. *Scientific Reports* **2015**, *5*, 8286.

(29) Kwon, S.; Park, J. K.; Kim, G.; Kong, J.; Bazan, G. C.; Lee, K. Synergistic Effect of Processing Additives and Optical Spacers in Bulk-Heterojunction Solar Cells. *Advanced Energy Materials* **2012**, *2*, 1420–1424.

(30) Collins, B. A.; Li, Z.; Tumbleston, J. R.; Gann, E.; Mcneill, C. R.; Ade, H. Absolute Measurement of Domain Composition and Nanoscale Size Distribution Explains Performance in PTB7:PC71BM Solar Cells. *Advanced Energy Materials* **2013**, *3*, 65–74.

(31) Hoven, C. V.; Dang, X.-D.; Coffin, R. C.; Peet, J.; Nguyen, T.-Q.; Bazan, G. C. Improved Performance of Polymer Bulk Heterojunction Solar Cells Through the Reduction of Phase Separation via Solvent Additives. *Advanced Energy Materials* **2010**, *22*, 63–66.

(32) Pivrikas, A.; Stadler, P.; Neugebauer, H.; Sariciftci, N. S. Substituting the Postproduction Treatment for Bulk-Heterojunction Solar Cells using Chemical Additives. *Organic Electronics* **2008**, *9*, 775–782.

(33) Sun, Y.; Welch, G. C.; Leong, W. L.; Takacs, C. J.; Bazan, G. C.; Heeger, A. J. Solution-Processed Small-Molecule Solar Cells with 6.7% Efficiency. *Nature Materials* **2012**, *11*, 44–48.

(34) Cheng, P.; Lin, Y.; Zawacka, N. K.; Andersen, T. R.; Liu, W.; Bundgaard, E.; Jørgensen, M.; Chen, H.; Krebs, F. C.; Zhan, X. Comparison of Additive Amount Used in Spin-Coated and Roll-Coated Organic Solar Cells. *Journal of Materials Chemistry A* **2014**, *2*, 19542–19549.

(35) Tremolet de Villers, B. J.; Hara, K. A. O.; Ostrowski, D. P.; Biddle, P. H.; Shaheen, S. E.; Chabinyc, M. L.; Olson, D. C.; Kopidakis, N. Removal of Residual Diiodooctane Improves Photostability of High-Performance Organic Solar Cell Polymers. *Chemistry of Materials* **2016**, *28*, 876–884.

(36) Tournebize, A.; Rivaton, A.; Peisert, H.; Chassé, T. The Crucial Role of Confined Residual Additives on the Photostability of P3HT:PCBM Active Layers. *The Journal of Physical Chemistry C* **2015**, *119*, 9142–9148.

(37) Xie, Y.; Hu, X.; Yin, J.; Zhang, L.; Meng, X.; Xu, G.; Ai, Q.; Zhou,W.; Chen, Y. Butanedithiol Solvent Additive Extracting Fullerenes from Donor Phase To Improve Performance and Photostability in Polymer Solar Cells. *ACS Applied Materials and Interfaces* **2017**, *9*, 9918–9925.

(38) Reichenberger, M.; Baderschneider, S.; Kroh, D.; Grauf, S.; Köhler, J.; Hildner, R.; Köhler, Watching Paint Dry: The Impact of Diiodooctane on the Kinetics of Aggregate Formation in Thin Films of Poly(3-hexylthiophene). *Macromolecules* **2016**, *49*, 6420–6430.

(39) Li, L.; Xiao, L.; Qin, H.; Gao, K.; Peng, J.; Cao, Y.; Liu, F.; Russell, T. P.; Peng, X. High-Efficiency Small Molecule-Based Bulk-Heterojunction Solar Cells Enhanced by Additive Annealing. *ACS Applied Materials and Interfaces* **2015**, *7*, 21495–21502.

(40) Xiao, Z.; Yuan, Y.; Yang, B.; Vanderslice, J.; Chen, J.; Dyck, O. Universal Formation of Compositionally Graded Bulk Heterojunction for Efficiency Enhancement in Organic Photovoltaics. *Advanced Materials* **2014**, *26*, 3068–3075.

(41) Lou, S. J.; Szarko, J. M.; Xu, T.; Yu, L.; Marks, T. J.; Chen, L. X. Effects of Additives on the Morphology of Solution Phase Aggregates Formed by Active Layer Components of

High-Efficiency Organic Solar Cells. *Journal of the American Chemical Society* **2011**, *133*, 20661–20663.

(42) Liu, C.; Hu, X.; Zhong, C.; Huang, M.;Wang, K.; Zhang, Z.; Gong, X.; Cao, Y.; Heeger, A. J. The Influence of Binary Processing Additives on the Performance of Polymer Solar Cells. *Nanoscale* **2014**, *6*, 14297–14304.

(43) Yao, Y.; Hou, J.; Xu, Z.; Li, G.; Yang, Y. Effects of Solvent Mixtures on the Nanoscale Phase Separation in Polymer Solar Cells. *Advanced Functional Materials* **2008**, *18*, 1783–1789.

(44) Xie, L.; Lee, J. S.; Jang, Y.; Ahn, H.; Kim, Y.-h.; Kim, K. Organic Photovoltaics Utilizing a Polymer Nanofiber/Fullerene Interdigitated Bilayer Prepared by Sequential Solution Deposition. *The Journal of Physical Chemistry C* **2016**, *120*, 12933–12940.

(45) Aguirre, J. C.; Hawks, S. A.; Ferreira, A. S.; Yee, P.; Subramaniyan, S.; Jenekhe, S. A.; Tolbert, S. H.; Schwartz, B. J. Sequential Processing for Organic Photovoltaics: Design Rules for Morphology Control by Tailored Semi-Orthogonal Solvent Blends. *Advanced Energy Materials* **2015**, *5*, 1402020.

(46) Hawks, S. A.; Aguirre, J. C.; Schelhas, L. T.; Thompson, R. J.; Huber, R. C.; Ferreira, A. S.; Zhang, G.; Herzing, A. A.; Tolbert, S. H.; Schwartz, B. J. Comparing Matched Polymer:Fullerene Solar Cells Made by Solution-Sequential Processing and Traditional Blend Casting: Nanoscale Structure and Device Performance. *Journal of Physical Chemistry C* **2014**, *118*, 17413–17425.

(47) Van Franeker, J. J.; Kouijzer, S. ; Lou, X.; Turbiez, M.; Wienk, M. M.; Janssen, R. A. J. Depositing Fullerenes in Swollen Polymer Layers via Sequential Processing of Organic Solar Cells. *Advanced Energy Materials* **2015**, *5*, 1500464.

(48) Shin, N.; Richter, L. J.; Herzing, A. A.; Kline, R. J.; Delongchamp, D. M. Effect of Processing Additives on the Solidification of Blade-Coated Polymer/Fullerene Blend Films via In-Situ Structure Measurements. *Advanced Energy Materials* **2013**, *3*, 938–948.

(49) Richter, L. J.; Delongchamp, D. M.; Bokel, F. A.; Engmann, S.; Chou, K. W.; Amassian, A.; Schaible, E.; Hexemer, A. In Situ Morphology Studies of the Mechanism for Solution Additive Effects on the Formation of Bulk Heterojunction Films. *Advanced Energy Materials* **2015**, *5*, 1400975.

(50) Immergut, E. H.; Mark, H. F. Principles of Plasticization. *Advances in Chemistry* **1965**, *48*, 1–26.

(51) Papanu, J. S.; Hess, D.W.; Bell, A. T.; S, S. D. In Situ Ellipsometry to Monitor Swelling and Dissolution of Thin Polymer Films. *Journal of The Electrochemical Society* **1989**, *136*, 1195–1200.

(52) Ng, A.; Li, C. H.; Fung, M. K.; Djuriši´c, A. B.; Zapien, J. A.; Chan, W. K.; Cheung, K. Y.; Wong, W.-Y. Accurate Determination of the Index of Refraction of Polymer Blend Films by Spectroscopic Ellipsometry. *Journal of Physical Chemistry C* **2010**, *114*, 15094–15101.

(53) Campoy-Quiles, M.; Alonso, M. I.; Bradley, D. D. C.; Richter, L. J. Advanced Ellipsometric Characterization of Conjugated Polymer Films. *Advanced Functional Materials* **2014**, *24*, 2116–2134.

(54) Kiel, J. W.; Kirby, B. J.; Majkrzak, C. F.; Maranville, B.; Mackay, M. E. Nanoparticle Concentration Profile in Polymer-Based Solar Cells. *Soft Matter* **2010**, *6*, 641–646.

(55) Chen, H.; Hegde, R.; Browning, J.; Dadmun, M. D. The miscibility and depth profile of PCBM in P3HT: thermodynamic information to improve organic photovoltaics. *Physical Chemistry Chemical Physics* **2012**, *14*, 5635–5641.

(56) Lee, K. H.; Schwenn, P. E.; Smith, A. R. G.; Cavaye, H.; Shaw, P. E.; James, M.; Krueger, K. B.; Gentle, I. R.; Meredith, P.; Burn, P. L. Morphology of All-Solution-Processed "Bilayer" Organic Solar Cells. *Advanced Materials* **2011**, *23*, 766–770.

(57) Zhang, G.; Hawks, S. A.; Ngo, C.; Schelhas, L. T.; Scholes, D. T.; Kang, H.; Aguirre, J. C.; Tolbert, S. H.; Schwartz, B. J. Extensive Penetration of Evaporated Electrode Metals into Fullerene Films: Intercalated Metal Nanostructures and Influence on Device Architecture. *ACS Applied Materials and Interfaces* **2015**, *7*, 25247–25258.

(58) Kong, J.; Hwang, I.-W.; Lee, K. Top-Down Approach for Nanophase Reconstruction in Bulk Heterojunction Solar Cells. *Advanced Materials* **2014**, *26*, 6275–6283.

(59) Ayzner, A. L.; Tassone, C. J.; Tolbert, S. H.; Schwartz, B. J. Reappraising the Need for Bulk Heterojunctions in Polymer−Fullerene Photovoltaics: The Role of Carrier Transport in All-Solution-Processed P3HT/PCBM Bilayer Solar Cells. *Journal of Physical Chemistry C* **2009**, *113*, 20050–20060.

(60) Molebase, 1,8-Diiodooctane. 2017; http://www.molbase.com/en/properties{_}24772-63-2-moldata-48193.html.

(61) Ye, L.; Jing, Y.; Guo, X.; Sun, H.; Zhang, S.; Zhang, M.; Huo, L.; Hou, J. Remove the Residual Additives toward Enhanced Efficiency with Higher Reproducibility in Polymer Solar Cells. *Journal of Physical Chemistry C* **2013**, *117*, 14920–14928.

(62) Molebase, 1,8-Octanedithiol. 2017; http://www.molbase.com/en/1191-62-4-moldata-55275.html.

(63) PubChem, 1-Chloronaphthalene. 2017; https://pubchem.ncbi.nlm.nih.gov/compound/1-chloronaphthalene{\#}section=Top.

(64) PubChem, 1,2-Dichlorobenzene. 2017; https://pubchem.ncbi.nlm.nih.gov/compound/7239{\#}section=Top.

(65) Bruggeman, D. A. G. Berechnung verschiedener physikalischer Konstanten von heterogenen Substanzen. I. Dielektrizitätskonstanten und Leitfähigkeiten der Mischkörper aus isotropen Substanzen. *Annalen der Physik* **1935**, *416*, 665–679.

(66) Ogieglo,W.; van derWerf, H.; Tempelman, K.;Wormeester, H.;Wessling, M.; Nijmeijer, A.; Benes, N. E. n-Hexane Induced Wwelling of Thin PDMS Films under Non-Equilibrium Nanofiltration Permeation Conditions, Resolved by Spectroscopic Ellipsometry. *Journal of Membrane Science* **2013**, *431*, 233–243.

(67) Zhang, G.; Huber, R. C.; Ferreira, A. S.; Boyd, S. D.; Luscombe, C. K.; Tolbert, S. H.; Schwartz, B. J. Crystallinity Effects in Sequentially Processed and Blend-Cast Bulk-Heterojunction Polymer/Fullerene Photovoltaics. *The Journal of Physical Chemistry C* **2014**, *118*, 18424–18435.

(68) Engmann, S.; Bokel, F. A.; Herzing, A. A.; Ro, W.; Girotto, C.; Caputo, B.; Hoven, C. V.; Schaible, E.; Hexemer, A.; Delongchamp, M.; Richter, L. J. Real-time X-ray Scattering Studies of Film Evolution in High Performing Small-Molecule–Fullerene Organic Solar Cells. *Journal of Materials Chemistry A* **2015**, *3*, 8764–8771.

(69) Engmann, S.; Bokel, F. A.; Ro, H. W.; Delongchamp, D. M.; Richter, L. J. Real-Time Photoluminescence Studies of Structure Evolution in Organic Solar Cells. *Advanced Energy Materials* **2016**, *6*, 1502011.

(70) Krauskopf, L. G.; Godwin, A. Plasticizer. PVC Handbook; 2005; pp 173–193.

(71) Wan, Q.; Guo, X.;Wang, Z.; Li,W.; Guo, B.; Ma,W.; Zhang, M.; Li, Y. 10.8% Efficiency Polymer Solar Cells Based on PTB7-Th and $PC_{71}BM$ via Binary Solvent Additives Treatment. *Advanced Functional Materials* **2016**, *26*, 6635–6640.

(72) Jhuo, H.-J.; Liao, S.-H.; Li, Y.-L.; Yeh, P.-N.; Chen, S.-A.; Wu, W.-R.; Su, C.-J.; Lee, J.-J.; Yamada, N. L.; Jeng, U.-S. The Novel Additive 1-Naphthalenethiol Opens a New Processing Route to Efficiency-Enhanced Polymer Solar Cells. *Advanced Functional Materials* **2016**, *26*, 3094–3104.

(73) Rogers, C. E.; Stannett, V.; Szwarc, M. The Sorption of Organic Vapors by Polyethylene. *Journal of Physical Chemistry* **1959**, *63*, 1406–1413.

(74) Brown, H. R. Flory–Huggins–Rehner Theory and the Swelling of Semicrystalline Polymers by Organic Fluids. *Journal of Polymer Science: Polymer Physics Edition* **1978**, *16*, 1887–1889.

(75) Lee, K. H.; Zhang, Y.; Burn, P. L.; Gentle, I. R.; James, M.; Nelson, A.; Meredith, P. Correlation of Diffusion and Performance in Sequentially Processed P3HT/PCBM Heterojunction Films by Time-Resolved Neutron Reflectometry. *Journal of Materials Chemistry C* **2013**, *1*, 2593–2598.

(76) Tao, C.; Aljada, M.; Shaw, P. E.; Lee, K. H.; Cavaye, H.; Balfour, M. N.; Borthwick, R. J.; James, M.; Burn, P. L.; Gentle, I. R.; Meredith, P. Controlling Hierarchy in Solution-processed Polymer Solar Cells Based on Crosslinked P3HT. A*dvanced Energy Materials* **2013**, *3*, 105–112.

(77) Das, S.; Keum, J. K.; Browning, J. F.; Gu, G.; Yang, B.; Dyck, O.; Do, C.; Chen, W.; Chen, J.; Ivanov, I. N.; Hong, K.; Rondinone, A. J.; Joshi, P. C.; Geohegan, D. B.; Duscher, G.;

Xiao, K. Correlating High Power Conversion Efficiency of PTB7:$PC_{71}BM$ Inverted Organic Solar Cells with Nanoscale Structures. *Nanoscale* **2015**, *7*, 15576–15583.

(78) Ratcliff, E. L.; Jenkins, J. L.; Nebesny, K.; Armstrong, N. R. Electrodeposited, "Textured" Poly(3-hexyl-thiophene) (e-P3HT) Films for Photovoltaic Applications. *Chemistry of Materials* **2008**, *20*, 5796–5806.

(79) Xu, Z.; Chen, L.-M.; Yang, G.; Huang, C.-H.; Hou, J.; Wu, Y.; Li, G.; Hsu, C.-S.; Yang, Y. Vertical Phase Separation in Poly(3-hexylthiophene): Fullerene Derivative Blends and its Advantage for Inverted Structure Solar Cells. *Advanced Functional Materials* **2009**, *19*, 1227–1234.

(80) Orimo, A.; Masuda, K.; Honda, S.; Benten, H.; Ito, S.; Ohkita, H.; Tsuji, H. Surface Segregation at the Aluminum Interface of Poly(3-hexylthiophene)/Fullerene Solar Cells. *Applied Physics Letters* **2010**, *96*, 043305.

(81) Flory, P. J. Thermodynamics of High Polymer Solutions. *Journal of Chemical Physics* **1942**, *10*, 51–61.

(82) PubChem, Dichloromethane. 2017; https://pubchem.ncbi.nlm.nih.gov/compound/6344{\#}section=Density.

(83) Gevaerts, V. S.; Koster, L. J. A.; Wienk, M. M.; Janssen, R. A. J. Discriminating between Bilayer and Bulk Heterojunction Polymer:Fullerene Solar Cells Using the External Quantum Efficiency. *ACS Applied Materials &Interfaces* **2011**, *3*, 3252–3255.

(84) Moon, J. S.; Takacs, C. J.; Sun, Y.; Heeger, A. J. Spontaneous Formation of Bulk Heterojunction Nanostructures: Multiple Routes to Equivalent Morphologies. *Nano Letters* **2011**, *11*, 1036–1039.

(85) Nardes, A. M.; Ayzner, A. L.; Hammond, S. R.; Ferguson, A. J.; Schwartz, B. J.; Kopidakis, N. Photoinduced Charge Carrier Generation and Decay in Sequentially Deposited Polymer/Fullerene Layers: Bulk Heterojunction vs Planar Interface. *Journal of Physical Chemistry C* **2012**, *116*, 7293–7305.

Chapter 3. Vertical Phase Segregation and Surface Recombination in Polymer:Fullerene BHJ Solar Cells: The Role of Surface Energy

3.1 Introduction

Organic photovoltaics (OPVs) have been developing rapidly for the past decade. Their low-cost processability, flexibility and light weight provide them with extremely short energy payback time compared to most other PV techniques.[1–5] The highest-efficiency OPVs consist of blends of conjugated polymers as the electron donors and functionalized fullerenes as the electron-accepting species. The polymer and fullerene derivative active layer forms a bicontinuous interpenetrating network, which is called a bulk-heterojunciton (BHJ),[6,7] and serves as the key component of OPVs. Single-junction OPVs based on such BHJ structures have demonstrated power conversion efficiencies up to 10.8%.[8]

Due to the internal disorder of the organic materials and the complexity of the intermixed network by the donor and acceptor molecules, however, the underlying physical process governing OPV device performance is still not fully understood.[7] In particular, the spatial arrangement of the polymers and fullerene derivatives, which plays a major role in defining the morphology of the OPV active layer, is one of the most important factors that determines device efficiency.[9–16] The importance of the donor-acceptor morphology not only includes intermixing or demixing of the two components, but also their vertical phase segregation (VPS), i.e., the mass distribution of the two components in the direction perpendicular to the substrate. VPS has significant impact on device performance[17–21] because carrier movement parallel to the substrate plane does not result in charge collection by the electrode.

A variety of experiments have been carried out to characterize VPS in organic photovoltaic active layers. For example, X-ray photoelectron spectroscopy[17,22] can probe the surface properties

of polymer:fullerene BHJ films by quantifying the ratio between the polymer and fullerene near the surface, providing a way to estimate the VPS inside the active layer. Measuring the contact angle[18] serves a similar purpose for estimating the polymer-to-fullerene ratio at the surface. Neutron reflectometry takes advantage of the scattering contrast between fullerene derivatives and other organic materials to directly investigate the vertical distribution of the materials in the active layer;[23–28] Dynamic secondary ion mass spectrometry is a destructive technique that allows the depth-profiling of the organic layer by removing materials using continuous focused ion beam;[13,18,29,30] Spectroscopic ellipsometry can nondestructively study the dielectric properties of the active layer and estimate the degree of VPS through fitting experimental data using mathematical representations.[31–33]

The generally accepted picture based on a combination of these measurements is that for the classic polymer-based BHJ based on P3HT and PCBM, P3HT tends to segregate towards the organic/air interface (provided the substrate consists of a high surface energy material) and that PCBM prefers to segregate towards the bottom of the active layer.[21] Indeed, most substrates used for the fabrication or characterization of OPVs, such as Si/SiO_2,[34] PEDOT:PSS-coated ITO,[21] and ZnO nanoparticles coating ITO,[20] have high surface energies, so the fact that the polymer rises to the top of most active layers is a fairly general result. Moreover, thermal annealing has been demonstrated to further enhance VPS: more PCBM molecules are driven away from the top of the active layer after thermal annealing of an as-cast film.[21] Different research groups have attributed the reason for VPS to the relative surface energies of the polymer and fullerene:[17,21,34] PCBM is a higher surface energy material than P3HT, so it prefers the higher surface energy organic/substrate interface.

The reason VPS is important to understand is that in a 'normal' sandwich-structure device geometry, the top surface of the BHJ film will be in contact with the cathode, so VPS in the P3HT:PCBM system is detrimental for charge carrier collection. This is because the electrons in the PCBM network cannot be easily collected by the cathode and the holes on the polymer cannot be conducted to the anode to generate current. Indeed, poor device performance due to unfavorable vertical phase segregation in the P3HT:PCBM device has been reported by multiple groups.[19,31,35,36] It also has been shown that VPS can lead to an "S-shaped" *J-V* curve for the device with an extremely poor fill factor (*FF*), thereby reducing device efficiency.[35,37]

Considering the number of literature articles that report observations regarding the effect of VPS on device performance, it is surprising how few reports have investigated the precise way in which VPS affects the device physics, such as the nature of recombination. This is because device physics experiments usually measure contributions from both the bulk of the active layer and the interface between the active layer and the electrodes. To separate the effects from the bulk and the interface, one needs to find systems where the bulk and interfacial composition can be separately controlled. This requires more than one polymer:fullerene pair, some of which must have similar contributions from the bulk while the VPS is varied, and some of which must have similar VPS with different bulk properties.

In this work, we perform exactly this type of study by combining three different fullerene derivatives with two different conjugated polymers to systematically separate the device physics contributions of VPS from the bulk. Specifically, we utilized two novel 1,4-dibenzyl fullerene bisadducts (**2g** and **2h**) synthesized by our group (basic molecular properties in Chapter 3) together with PCBM as electron acceptors and P3HT and PTB7 as electron donors. Although **2g** and **2h** have very similar chemical structures, when combined with P3HT they show dramatically different

solar cell performance. In particular, fullerene **2g** shows similar J_{sc} and *FF* to devices built with PCBM, but devices built with **2g** have higher PCE than PCBM because the higher LUMO energy level of **2g** leads to an increased V_{oc}.

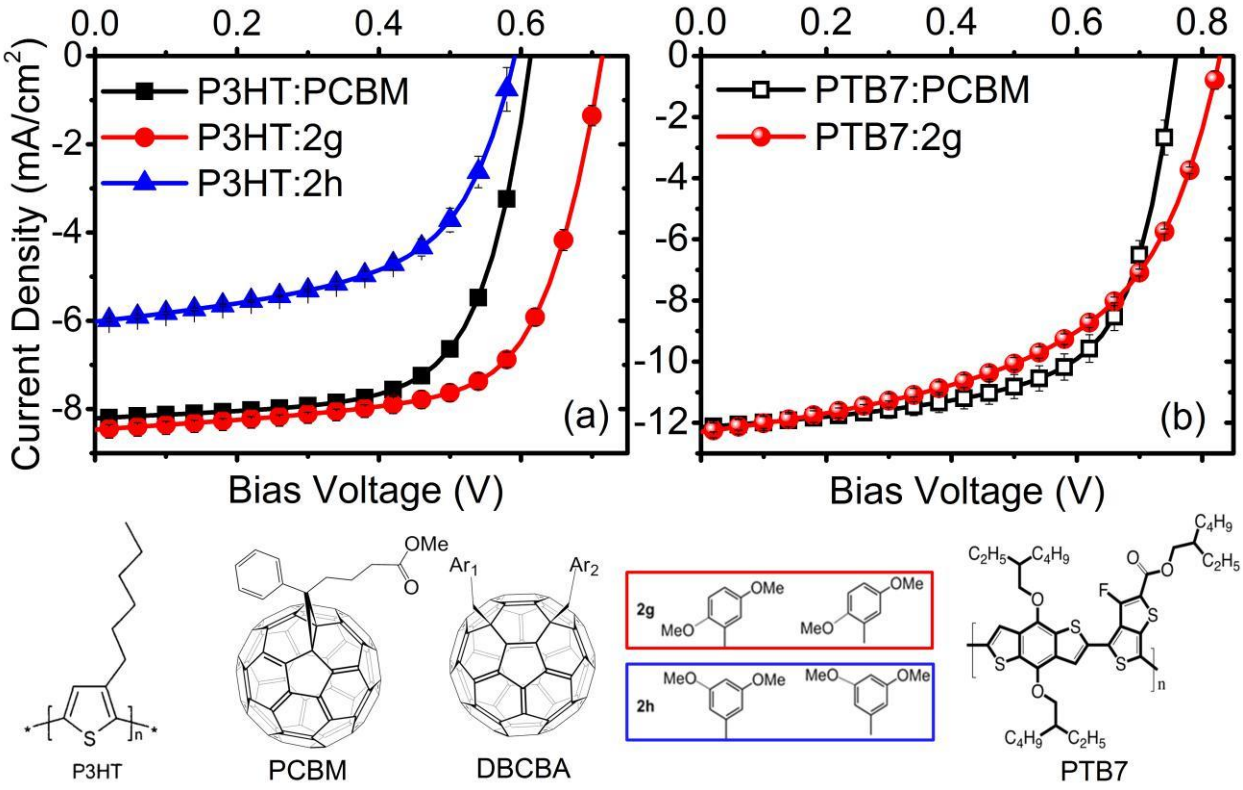

Figure 3.1 (a): *J-V* characteristics for solar cells with a structure of ITO/PEDOT:PSS/P3HT:Fullerene/Ca/Al under AM-1.5 solar illumination. All active layers were annealed at 150 ℃ for 20 min prior to the deposition of the cathode material. (b): *J-V* characteristics of PTB7:PCBM (black square) and PTB7:**2g** (red circle) photovoltaic devices under 1-sun with the same device structure as in (a). Below the *J-V* curves are the chemical structures for the polymers and fullerene derivatives used.

Our investigation begins by investigating the bulk morphology of our different polymer/fullerene pairs using grazing incidence wide angle X-ray scattering (GIWAXS), and the effects on device physics via photocurrent spectral response (PSR), transient photocurrent (TPC), transient photovoltage (TPV), and diode ideality factor analysis. We show that the main reason for the performance variation between devices with **2h** and the other fullerenes is that **2h** over phase separates from both polymers. In addition, **2h** produces a high defect state density inside the charge transfer bandgap that results in more trap-assisted recombination. In contrast, fullerene **2g** shows similar bulk device physics as devices built with PCBM. All of the analysis shows that the VPS between the devices with PCBM and the two fullerene bis-adducts are different, a result of the fact that the relative surface energies of the polymer and fullerene are reversed between PCBM and either **2g** or **2h**. This allows us to demonstrate that the interface effects caused by VPS dominate bulk effects in determining charge carrier density and lifetime. Taken together, this allows us to rationally select the best device architecture for different polymer:fullerene systems by simple surface energy measurements taken prior to device fabrication.

3.2 Results and Discussion

1. Structural Characterization of the Polymer:Fullerene Active Layer

To understand the dramatic difference in solar cell performance between **2h** and the other fullerenes seen in Figure 3.1, we first need to investigate the bulk morphology of the active layers. As discussed in previous chapters, GIWAXS is extremely useful for determining relative crystallinities as well as the average chain orientation of the polymers. We performed GIWAXS on our polymer:fullerene BHJ samples prepared on silicon substrates at the Stanford Synchrotron Radiation Light Source on beam line 11 – 3 using a wavelength of 0.9742 Å. The active layers were prepared under the exact same conditions using the same procedures as for device fabrication. The results are plotted in Figure 4.2. We find that compared to the thickness-matched pure P3HT sample, all of the BHJ samples blended with different fullerenes show less total polymer scattering; e.g., the intensities of the P3HT (200) peak at ~ 0.77 Å and the (010) peak at ~ 1.67 Å are weaker when fullerene derivatives are present. This makes physical sense since the fullerene derivatives in the BHJs can hinder crystalline growth of the polymer.[37] Thus, relative to the pure P3HT sample, the more the scattering peak area is reduced for the BHJ sample, the more intimately mixed are polymer and fullerene in the active layer.

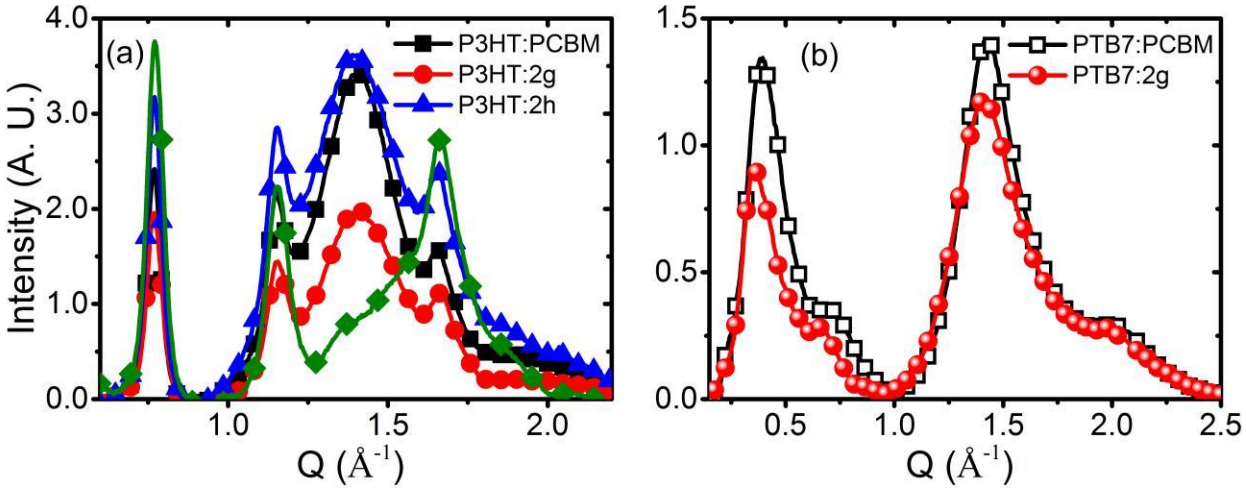

Figure 3.2 Radially integrated 2-D GIWAXS intensities for pure P3HT and three P3HT:fullerene BHJs (a) and two PTB7:fullerene BHJs (b) processed on silicon substrates. The polymer:fullerene active layers were prepared with the same method as used in device fabrication.

The P3HT:**2h** BHJ sample (blue up triangles, Figure 3.2 (a)) shows higher P3HT scattering intensity and integrated peak areas (i.e., higher overall polymer crystallinity) than the P3HT:PCBM sample (black squares), which in turn is higher than the P3HT:**2g** sample (red circles). The fullerene crystallinity/aggregation scattering band peaked at ~1.4 Å also has integrated areas that show the same trends. This indicates poor intermixing of the polymer and **2h**, suggesting that P3HT:**2h** samples are over phase separated. Indeed, photovoltaic devices based on P3HT:**2h** show both lower J_{sc}'s and *FF*'s than those based on P3HT:PCBM or P3HT:**2g**, consistent with non-ideal phase separation between the polymer and fullerene in active layers based on P3HT:**2h**.

In addition to the integrated area, the *Q* value of the scattering peak also contains useful information on the packing of the molecules.[42] The fullerene peak for P3HT:**2h** is positioned at 1.389 Å while the peaks for P3HT:PCBM and P3HT:**2g** are at 1.402 Å and 1.409 Å, respectively. This means the spacing between the **2h** fullerene derivatives is larger than the spacing between **2g** molecules or between PCBM molecules. Thus, the size and position of the side groups on the benzyl rings for the fullerene bisadducts have significant impact on the packing of the fullerene derivatives. Apparently, the methoxy groups on the benzyl rings of fullerene **2h**, which has a (3, 5, (3',5')) substitution pattern, hinders close packing of the fullerene molecules. Overall, the fact that local packing of **2h** is unfavorable, in combination with the fact that **2h** over phase separates from P3HT, explains the inferior solar cell performance for P3HT:**2h** based devices.

Figure 3.2(b) shows similar results for PTB7:PCBM and PTB7:**2g** BHJ samples. The overall trend of both the polymer and fullerene crystallinity is the same as that with P3HT: both the polymer and fullerene show lower crystallinity when **2g** is used relative to when PCBM is used. However, unlike P3HT, PTB7 is not a highly crystalline polymer.[29,43] Therefore, the **2g** molecule

may result in a slightly over-mixed morphology, inhibiting efficient charge transport in the PTB7 network, resulting the lower *FF* we observed in the PTB7:**2g** devices.

Our GIWAXS results suggest the nanoscale morphology of P3HT:**2h** active layers is markedly different from those of P3HT:PCBM and P3HT:**2g** active layers. The over phase separation in P3HT:**2h** BHJs and the relatively poor fullerene-fullerene contact of **2h** explain the poor device performance when this fullerene is used. In the next Section, we discuss how these factors affect the device physics, e.g., how they affect the electronic structure and change the mechanism of recombination within the device.

2. Interfacial States Measured by Photocurrent Spectral Response

Since the chemical structure of fullerene **2h** gives a different active layer BHJ morphology than standard fullerenes such as PCBM, we would like to investigate if this morphology gives a different electronic structure for the polymer:fullerene BHJs. To this end, we employed the photocurrent spectral response (PSR) technique to determine the polymer-fullerene interfacial density of states distribution. The PSR is a technique that measures the device photocurrent as a function of excitation energy. This provides a sensitive way to measure the optical absorption, so long as the absorption gives rise to mobile carriers. The PSR method is useful for revealing the electronic structure at the interface between the polymer and fullerene because it can detect not only the bulk absorption from the pure materials but also the lower-energy absorptions due to band-to-band charge-transfer (CT) or even excitations due to the localized states within the CT bandgap.

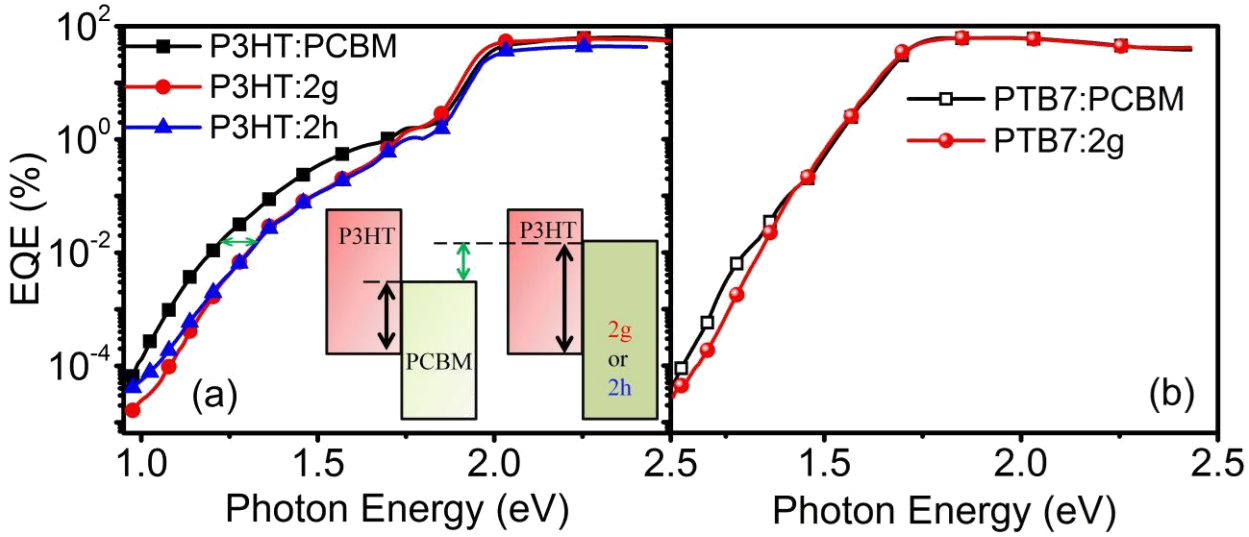

Figure 3.3 PSR spectra for the same P3HT:fullerene (a) and PTB7:fullerene (b) photovoltaic devices used in Figure 4.1. The horizontal difference (green arrow) between the spectra of devices with PCBM and **2g** (or **2h**) in the photon energy range of ~1.3 – 1.6 eV in (a) or ~1.2 – 1.4 eV in (b) is mainly ascribed as the LUMO level difference between PCBM and **2g** (or **2h**). The sub-gap EQE (<~1.3 eV) contains information on the interfacial transitions involving localized states within the CT bandgap. The device with **2h** clearly shows more localized density of states than those with **2g** or PCBM.

Figure 3.3 shows the PSR spectra we obtained for the photovoltaic devices whose *J*-*V* characteristics are shown in Figure 3.1. The PSR spectra can be typically divided into three main regions. Using the data in Figure 3.3(a) as an example, these regions include: (1) photons with energies higher than ~1.7 eV which mainly excite the bulk and cause absorption of individual materials. This region is the typically reported external quantum efficiency (EQE) spectrum that contributes to most of the photocurrent. The low spectral response for P3HT:**2h** device in this region agrees with the low J_{sc} from the *J*–*V* measurement; (2) photons with an energy between ~1.3 eV (depending on the bandgap of the materials) to ~1.7 eV, which measure the CT band-to-band excitation from the polymer HOMO to the fullerene LUMO. The increased LUMO energy of **2g** and **2h** relative to PCBM causes a horizontal shift of the PSR spectra towards higher photon energies,[46] as shown by the green arrows in Figure 3.3(a); (3) photons with energies lower than the CT band-to-band transition energy, which probe transitions involving localized states within the CT bandgap. The lower the photon energy, the deeper the localized states within the bandgap.[45]

Our results clearly show that devices based on P3HT:**2h** contain more deep states than devices based on P3HT:PCBM or P3HT:**2g**. These deep states clearly are traps for charge carriers and therefore can function as recombination centers. Since the CT band-to-band absorption of P3HT:**2h** (blue up triangles) and P3HT:**2g** (red circles) overlap, the main difference in the subgap electronic structure between them is the increased density of deep trap states for P3HT:**2h**. These trap states will give rise to more Shockley-Read-Hall (SRH) type recombination,[47–49] which also can be reflected in an increase in the dark diode ideality factor,[45] as discussed in details in the next section. The higher density of traps with **2h** is also consistent with the poor photovoltaic performance of devices based on this material.

We also obtained PSR spectra for PTB7:fullerene devices, as shown in Figure 3.3(b). The spectral responses of the two devices start to separate around 1.45 eV due to the LUMO level difference between the fullerenes. The response in the low photon energy region for both systems decay with a similar slope and show no clear signs of deep state traps for either fullerene.

3. Ideality Factor and Bulk Recombination

The diode ideality factor (n_{ideal}) reflects the dominant recombination mechanism of a photovoltaic device. For conjugated polymer-based solar cells, n_{ideal} typically ranges from 1 to 2. Diode theory tells us that n_{ideal} = 1 corresponds to the ideal band-to-band recombination. Larger values of n_{ideal} are consistent with localized state/trap-assisted recombination.[50] Based on the PSR spectra in the previous Section, we would expect higher n_{ideal} values for devices made with **2h** than those with **2g** or PCBM.

We measured n_{ideal} for our devices using two different methods. First we fit the exponential region of the dark *J*–*V* curve and obtained n_{ideal} using the maximum-slope differential method (Figure 4.4(a) and (b)).[54] Second, we measured V_{oc} as a function of illumination intensity (Figure 4.4(c) and (d)). This allowed us to calculate n_{ideal} at each light intensity using the linear dependence of the photocurrent density on light intensity:

$$n_{\mathrm{id,l}} = \frac{qV_{\mathrm{oc}}}{kT} / \{\ln\left(\frac{J_{\mathrm{ph}}}{J_{\mathrm{s}}} + 1\right)\} \quad (1)$$

where q is the elementary charge, k is the Boltzmann's constant, T is temperature, J_{ph} is the photocurrent density, and J_s is the saturation current.[54]

The solid lines in Figure 3.4(a) and (b) show the fits to the exponential regions of the dark *J*-*V* curve for each device. The n_{ideal} values shown next to the lines indeed confirm what we predicted

from the PSR measurements. P3HT:**2h** shows the highest ideality factor, n_{ideal} = 1.80, indicating that the dominant recombination mechanism for P3HT:**2h** devices is trap-assisted, or SRH type. The ideality factor of the P3HT:**2g** and P3HT:PCBM devices are much lower, with values of n_{ideal} = 1.32 and 1.34, respectively. This means there is more band-to-band recombination in these devices. Similarly, when PTB7 was used, the ideality factor for devices with **2g** and PCBM are indistinguishable with a value of n_{ideal} = 1.37. The data is again consistent with the PSR data, which showed that PTB7 devices with **2g** and PCBM had comparable localized state density distributions.

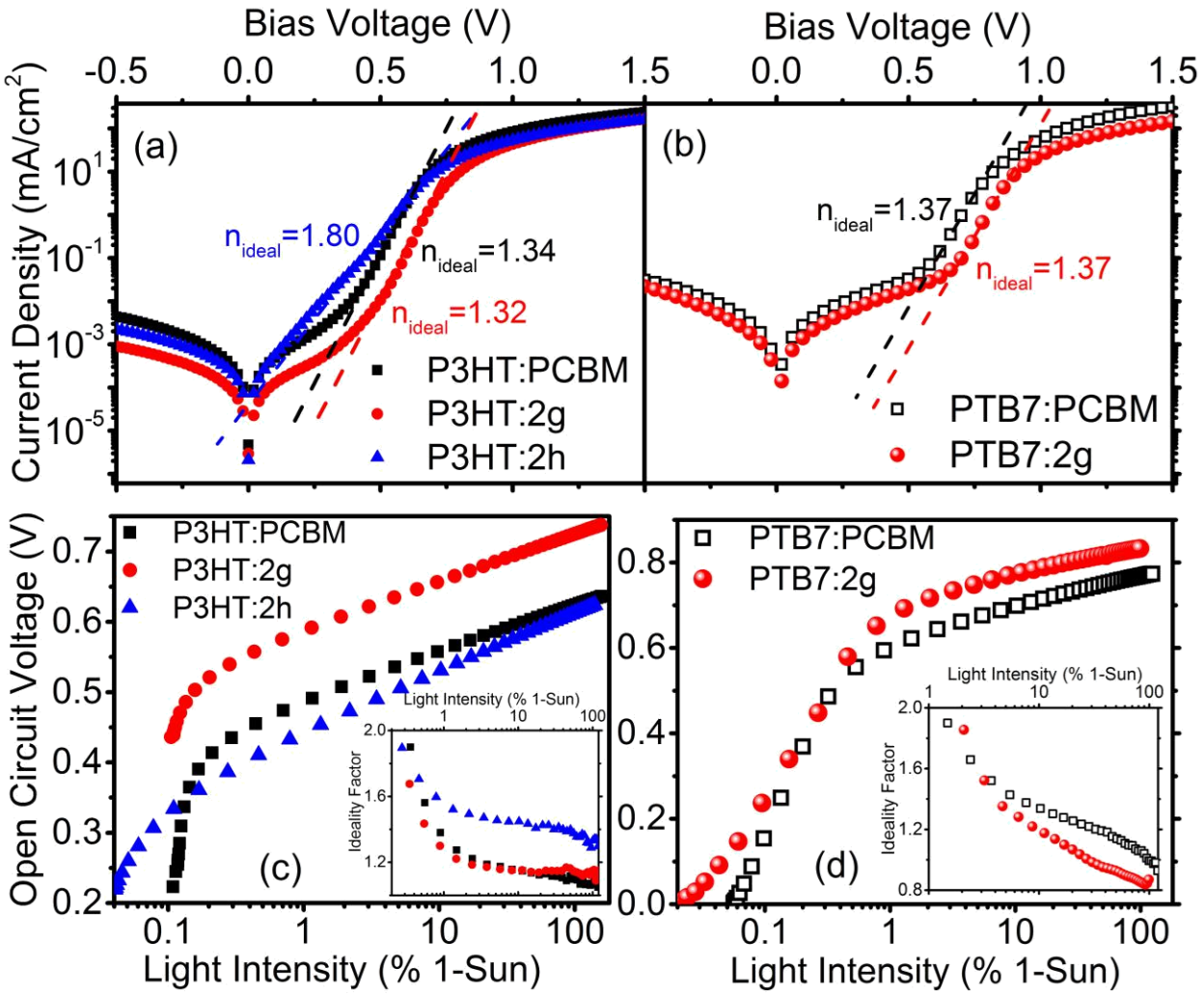

Figure 3.4 (a) and (b): Dark *J*-*V* curves for the same devices used in Figure 3.1. The dashed lines show the fitting region used to obtain the dark ideality factors. (c) and (d): The measured V_{oc} as a function of illumination intensity for the same devices. The insets show the corresponding differential ideality factors calculated using Eq. (1).

The trend of the $n_{ideal,light}$ values we obtained from measuring V_{oc} as a function of light intensity is the same as that obtained from the dark *J–V* curve fitting. The $n_{ideal,light}$ values we determined at a light intensity of 10% of 1-Sun were 1.45, 1.15 and 1.14 for P3HT:**2h**, P3HT:**2g** and P3HT:PCBM based devices, respectively. At that same intensity, the $n_{ideal,light}$ values for PTB7:**2g** and PTB7:PCBM are 1.19 and 1.34, respectively. The discrepancy between n_{ideal} and $n_{ideal,light}$ is mainly due to the fact that the dark ideality factor is affected by series resistance at low light intensities and shunt resistance at high light intensities.[50] Since the light ideality factor $n_{ideal,light}$ is obtained at open circuit, series resistance effects at high light intensities are eliminated. This makes light ideality factors easier to interpret and more representative of the underlying recombination mechanism at the typical intensities of solar cell operation.[50]

Despite these differences, both methods of measuring the ideality factor lead to the same conclusions. In P3HT:**2h** BHJ devices, the high density of states within the CT bandgap make bulk recombination trap-dominated. On the other hand, the ideality factors for devices with PCBM and **2g** are both similarly low, indicating more ideal band-to-band bulk recombination. Given the similar ideality factors and the similar J_{sc}'s and *FF*'s in their *J–V* curves, it is clear that the P3HT:**2g** and P3HT:PCBM systems provide two polymer:fullerene BHJs with distinct materials which have similar device physics in the bulk. Since our goal is to study the effect of vertical phase segregation (VPS) on device physics, our next task is to investigate to see whether or not the surface properties of these BHJs are different, and if so, to relate such differences to VPS in the active layers.

4.Vertical Phase Segregation and Surface Recombination

Our analysis of the V_{oc} as a function of light intensity experiment showed a particularly interesting feature: at high light intensities, $n_{ideal,light}$ for both the PTB7:PCBM and PTB7:**2g** BHJs dropped below unity. Moreover, for the P3HT-based devices, even though $n_{ideal,light}$ stayed above 1 at all intensities, the trend in the data makes clear sign that the light ideality factor would drop below 1 if we had continued to increase the illumination intensity. The observation of less than unity ideality factors has previously been described by Kirchartz *et al*.,[50] who attributed such below unity values to surface recombination. The argument is that once V_{oc} reaches the device's built-in voltage, it cannot increase further even if the light intensity is further increased because the device has lost its selectivity for charge carriers at this voltage. However, the charge carrier concentration will still increase as the light intensity increases. Consequently, the charge carriers will be extracted by the nearest electrode as there is no internal electric field to drive the carriers toward either the cathode or anode depending on the sign of the charge. Thus, based on Eq. (1), the light ideality factor calculated at sufficiently high light intensities can show values below 1.[50] These concepts are illustrated by the cartoon shown in Figure 3.5.

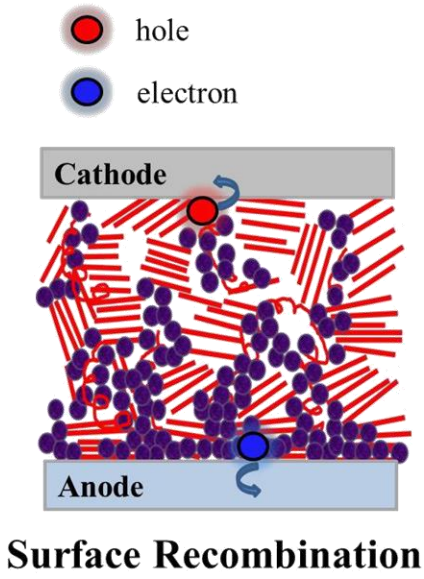

Figure 3.5 A cartoon illustrating the idea of surface recombination. The red solid lines represent the polymer and the purple circles represent the fullerene derivatives.

For the devices studied in the previous sections, $n_{ideal,light}$ decreased in P3HT:PCBM devices at high light intensities (inset of Figure 3.4(c)) but remained roughly constant in P3HT:**2g** devices at all light intensities. This indicates that in BHJ devices with P3HT as the donor, the use of PCBM as the acceptor leads to more surface recombination than the use of **2g**. This analysis is less clear for the devices made from P3HT:**2h**, as it is not straightforward to gain clues on surface recombination the light ideality factor due to the fact that the trap-assisted recombination dominates, making $n_{ideal,light}$ high even at high light intensities. When PTB7 is used as polymer donor, devices with both PCBM and **2g** show clear signatures of surface recombination (inset of Figure 3.4(d)). Since surface recombination involves charge carriers being collected by the "incorrect" electrode, more surface recombination means that more such carriers being generated near the "incorrect" electrode. To make this happen, the VPS of the active layer with more surface recombination must be such that more fullerene derivatives are near the anode and/or more polymers are near the cathode; after all, if there were only polymer located near the cathode or fullerene near the anode, it would be impossible for carriers to be collected by the 'wrong' electrode. Thus, a rough model for VPS for the different polymer:fullerene combinations based on the light ideality factor analysis can be summarized as follows. When used in combination with P3HT, PCBM tends to segregate towards the bottom of the active layer (near the anode). Bis-adduct **2g**, on the other hand, has a light ideality factor that becomes flat at higher light intensities, suggesting that it does not have a strong preference for the anode interface and therefore does not promote surface recombination. When used in combination with PTB7, in contrast, both PCBM and **2g** segregate towards the bottom of the active layer.

5. The Role of Surface Recombination in Charge Carrier Density and Lifetime

Given that we know that surface recombination is operative in all of our PV devices, it is logical to ask how surface recombination compares with bulk recombination in determining the overall recombination device recombination kinetics. For example, for fullerene derivatives **2g** and PCBM, which have similar bulk recombination in their devices when combined with P3HT, would differences in surface recombination give rise to any significant differences in carrier density or carrier lifetime? To answer this question, we employed transient photovoltage (TPV) and transient photocurrent (TPC) techniques.

TPV and TPC techniques have been widely applied in OPVs to study the excess charge carrier densities and their decay dynamics in working photovoltaic devices under standard operating conditions with regard to bias voltage and illumination intensity. In TPV measurements, the cell is held at V_{oc} under continuous illumination and then a weak, perturbative ns-duration laser pulse is applied to the device. The excess charge carriers generated by the laser pulse will decay with time only through recombination. Fitting the decay of the transient photovoltage produced by these excess carriers provides a measurement of the total carrier lifetime, $\tau(n)$. TPC is used in conjunction with TPV to obtain the excess charge carrier density in the device. In TPC measurements, the same weak perturbative laser pulse is applied to the device at the same background illumination intensity as used in TPV, but this time the device is operated under short circuit conditions. By analyzing the current transients generated by the excess carriers using the differential capacitance method, we were able to calculate the average excess charge carrier densities n.[22,39]

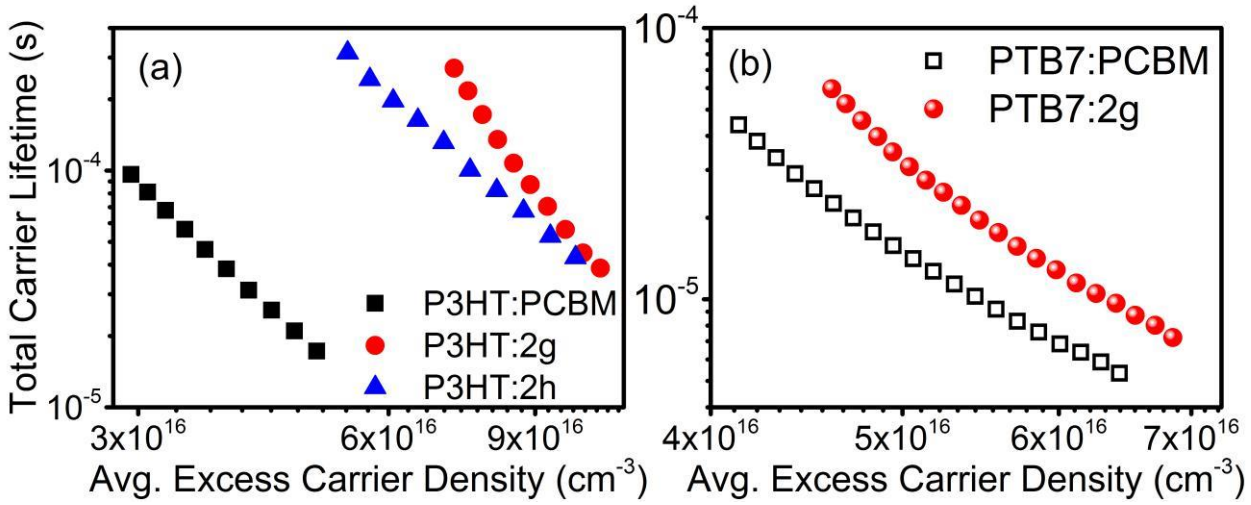

Figure 3.6 Total carrier lifetime versus average excess carrier density for the same P3HT:fullerene (a) and PTB7:fullerene (b) devices used in Figure 3.1. The total carrier lifetime and average excess charge carrier density are obtained from TPV and TPC measurements, respectively. Each data set represents the average of at least two devices.

The results from TPV/TPC measurements on the same devices used above are plotted in Figure 3.6. Each of the polymer:fullerene BHJ devices demonstrate a power-law-like behavior with $\tau(n) \sim n^{-\lambda}$ with $\lambda > 1$, indicating the existence of trap-assisted recombination.[39,53] The order of the power law (λ) varies slightly between different material systems.[53] More importantly, however, is that Figure 3.6(a) shows that the absolute total carrier lifetime for P3HT:fullerene samples at the same carrier density varies by over an order of magnitude: devices with the fullerene bisadducts **2g** and **2h** show carrier lifetimes more than an order of magnitude greater than those with PCBM as acceptors. Or, expressed another way, the carrier densities at the same lifetime for devices with **2g** or **2h** are ~3 times higher than those with PCBM.

These differences in recombination kinetics are surprising, particularly given that the bulk recombination in these devices is described by a similar ideality factor, as discussed above. This suggests that the differences in recombination kinetics are almost entirely the result of surface recombination, so that active layers with similar bulk morphologies have significantly different VPS. For P3HT:PCBM BHJ devices, unfavorable VPS that places P3HT near the cathode and PCBM near the anode causes more surface recombination, which decreases both the average carrier density and carrier lifetime. In P3HT:**2g** devices, the VPS is reversed with respect to the P3HT:PCBM, leading to favorable VPS that causes the carriers generated in the active layer to recombine more through the internal BHJ polymer:fullerene interface rather than through the organic/electrode interfaces. The large difference in kinetics we observe between **2g** and PCBM thus indicate that the effect of the surface recombination can overwhelm that of the bulk recombination in determining the overall device recombination properties. This is highlighted by the behavior of the P3HT:**2h** device, whose carrier density and lifetime were comparable to

P3HT**:2g** device, even though these two derivatives have vastly different amounts of bulk recombination.

For PTB7, the recombination properties between devices made with PCBM and **2g** do not differ the way they do in P3HT-based devices, though the PTB7 device with **2g** still shows higher carrier lifetimes. Since the $n_{ideal,light}$ vs. light intensity data indicates both PTB7:PCBM and PTB7:**2g** devices have strong surface recombination, the relatively small difference between their carrier lifetimes is perhaps not unexpected.

The observation of huge variations in the carrier lifetimes at the same carrier density also has also been reported by other groups. Credgington *et al*.[53] reported devices with carrier lifetime varied over orders of magnitude when different polymer donors were applied in combination of PCBM or its C_{70} analog. Ryan *et al*.[58] reported a study of recombination in a squaraine donor/C_{60} acceptor bilayer system. They found by increasing the squaraine layer thickness, they could reduce the number of surface recombination sites between C_{60} and the anode, which led to enhanced carrier densities and increased in carrier lifetimes at the same carrier density. All of this work is in agreement with our results that surface recombination can dramatically alter carrier recombination properties.

6. Using the VPS Model to Explain Device Physics: Dark Carriers Measured by CELIV

In the previous section, we argued that differences in VPS could explain the different device recombination properties of polymer:PCBM and polymer**:2g** active layers. Our TPV/TPC results suggested that P3HT:2h and P3HT:**2g** have a similar degree active layer VPS, and that the VPS was reversed with P3HT:PCBM. To further investigate this conclusion, we employed the charge extraction by linear increasing voltage (CELIV) technique.[57] We have previously reported that

when a cathode metal such as Ca was evaporated onto the active layer, the device with fullerene derivative molecules segregated towards the top of the active layer showed carriers that could be extracted in a CELIV experiment in the dark.[22] Here, we take advantage of the conclusion that extracted dark carriers correspond to an active layer that has VPS enriched in fullerene at the top. The idea is that when a linear voltage ramp is applied to a PV device in the dark at voltages where carriers are not injected, the device behaves as a capacitor and the resulting current transient is constant in time. If excess carriers are presented in the sample, these carriers are swept out when the voltage ramp is applied, leading to a 'bump' in the current transient whose integral is proportional to the number of excess carriers.

Figure 3.7 shows the dark CELIV data taken on the same devices studied in this work. In Figure 3.7(a), the noticeable bumps in the CELIV transients are signatures of dark carriers present in the devices.[22] For P3HT:**2g** and P3HT:**2h** devices, the number of dark carriers is much greater than the negligable amount of dark carriers seen in the P3HT:PCBM device, indicating that the top surface of the active layer is predominantly composed **of 2g** or **2h**, while devices made with PCBM have primarily P3HT at the top interface. We observed no dark carriers in our PTB7:fullerene devices, suggesting that no significant amount of fullerene is present at the top of the active layer. All of these results are consistent with our general picture of VPS in these systems.

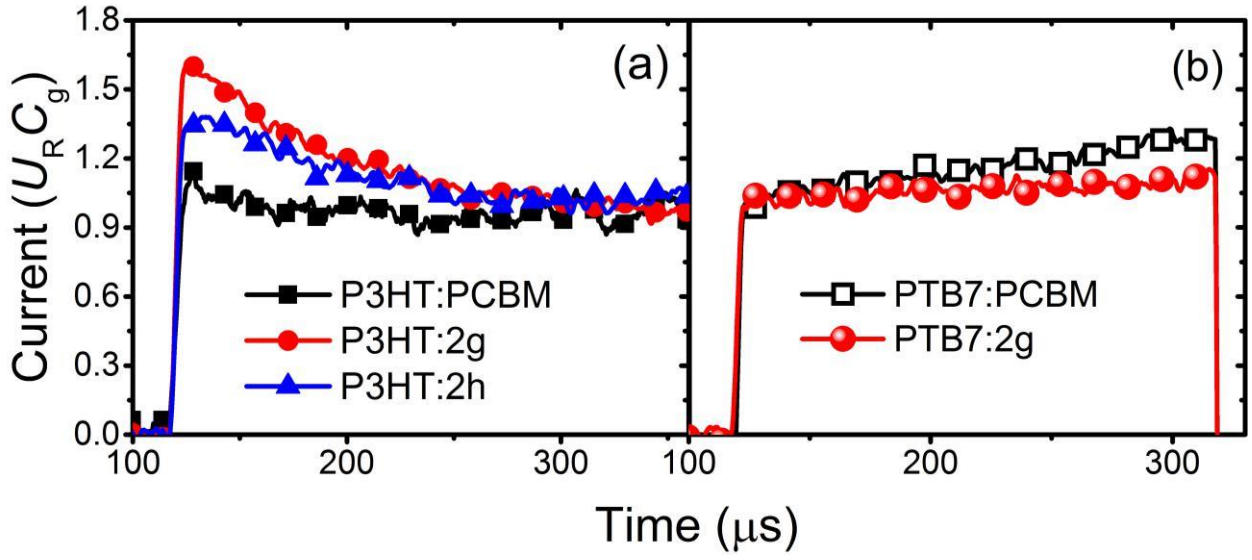

Figure 3.7 Dark CELIV current transients on diodes with P3HT:fullerene (a) and PTB7:fullerene (b). All curves were divided by the product of their geometric capacitance (C_g) and CELIV ramp rate (U_R).

7. Using Vertical Phase Separation to Understand the Difference Between V_{oc} and E_{ct}

The VPS that causes surface recombination also affects the open circuit voltage of polymer solar cells. In Figure 4.8 we plot the V_{oc} of the devices obtained from the *J*–*V* measurements of Figure 4.1 versus the CT bandgap obtained by fitting the PSR spectra (section 4.3.2) using the model by Vandewal, K. R. *et al.*[60–62] The solid line indicates the typical energy loss between the CT state energy and the measured V_{oc} (multiplied by the elementary charge) for OPVs.[63] All of the data points for the devices we made, except for P3HT:**2h**, are above the solid line; the difference between qV_{oc} and E_{ct} for these devices is in the range of 0.5 – 0.6 eV, indicating that the energy loss due to recombination in these devices is above the OPV average. For the P3HT:**2h** devices, the E_{ct} is similar to P3HT:**2g**, as expected since the LUMO level of these two fullerene bisadducts does not differ significantly (see Chapter 3). However, since trap-assisted recombination is dominant in the bulk of the P3HT:**2h** BHJ device, the data point in Figure 4.8 is far below the solid line. This again suggests that the V_{oc} of the P3HT:**2h** device is governed primarily by the poor morphology of its active layer.

Further examination of Figure 3.8 shows a variation in the V_{oc} differences between polymer:PCBM and polymer:**2g** devices when the two different polymers were used. The V_{oc} difference between devices with P3HT:PCBM and P3HT:**2g** is ~101 mV, but this difference becomes only ~70 mV when PTB7 is used. The V_{oc} of an OPV device depends on the energy gap between acceptor LUMO and donor HOMO, E_{ct}, and the nature of the carrier recombination in the cell.[53] The right side in Figure 4.8 shows an energy level diagram illustrating that even when the polymer energy levels are different, differences in E_{ct} with different fullerenes should stay constant, equal to the LUMO level differences between the fullerenes. However, our PSR

data shows that the difference in E_{ct} with different fullerenes is not constant when different polymers are used: E_{ct} (P3HT:PCBM) – E_{ct} (P3HT:2g) = ~109 meV, and E_{ct} (PTB7:PCBM) – E_{ct} (PTB7:2g) = ~ 73 meV. This change in the E_{ct} difference is roughly equal to the change in V_{oc} difference, which says that the CT bandgap energy change is the main contribution to the variation in V_{oc}.

If the change in V_{oc} does arise from a change in CT energy, this suggests that the energy level of either the polymer HOMO or the fullerene LUMO is changed in at least one of the polymer:fullerene systems. We attribute this to the change in the LUMO of **2g** when used in combination with P3HT in 'normal' structure PV devices for the following reason: as we show in the following section (3.3.8), we made 'inverted' devices we found that the variation in V_{oc} difference between devices with different polymers no longer exists: i.e., the V_{oc} difference for devices with **2g** and PCBM is independent of the polymer was used. The main change between the normal vs. inverted structure was a decrease of V_{oc} for P3HT:**2g** inverted device, which gave V_{oc} (P3HT:2g) – V_{oc} (P3HT:PCBM) ≈ V_{oc} (PTB7:2g) – V_{oc} (PTB7:PCBM). The V_{oc}'s for the other inverted devices were almost identical to the normal structure. Thus, the change had to come from a shift in the **2g** LUMO level in the P3HT:2g BHJ 'normal' device.

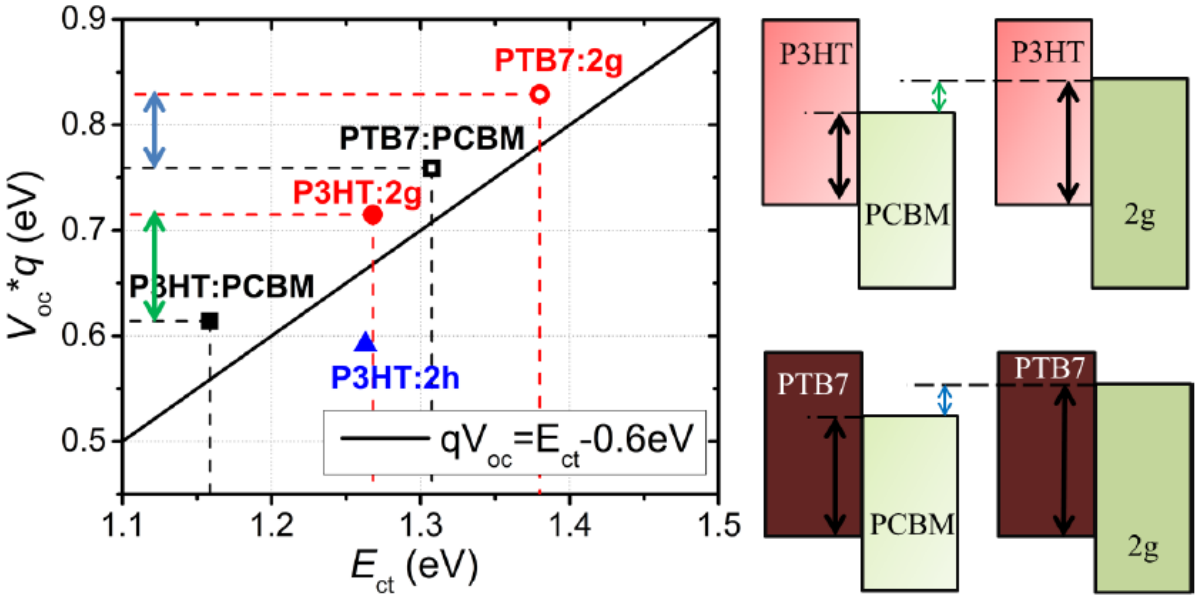

Figure 3.8 Plot of Voc*q versus charge transfer state energy for the five polymer:fullerene BHJ systems. The solid line in the left plot represents the typical difference between Voc and Ect for OPVs, which is about 0.6 eV. All of our devices are above the line except for the P3HT:2h device due to its non-ideal bulk recombination. The arrows in the left plot show the difference.

8. Understanding Vertical Phase Segregation by Measuring Surface Energies via Contact Angle

Overall, many experimental results can be explained by the idea that VPS is different for different fullerene derivatives in different polymers. In this section, we investigate the fundamental molecular properties that cause VPS to differ so dramatically.

Surface energy is the excess energy at the surface of a material compared to the bulk. In the OPV community, the surface energy of organic materials has been considered the reason behind VPS in BHJ solar cells.[17,20,21,34] If we consider a device with a structure of Electrode A/Polymer:Fullerene/Electrode B, where the surface energy of electrode A is larger than that of electrode B, then the organic material with the lower surface energy prefers to segregate towards B while that with the higher surface energy prefers to segregate towards A. Most substrates used in fabricating OPV devices consist of high surface energy materials, so the organic material with the higher surface energy usually spontaneously segregates towards the bottom of the film.

In addition to the surface energies of the electrodes, different processing also can enhance or hinder VPS. For example, thermal annealing can enhance the natural VPS that occurs due to electrode surface energies,[19] whereas the use of solvent additives can alter the direction of VPS.[64] There also are claims that surface energies are important for determining the bulk morphology of polymer/fullerene BHJs: in other words, that the degree of phase separation is related to the difference in surface energies between the two materials.[65]

To evaluate the surface energies of the polymers and fullerene derivatives used in this study, we performed contact angle measurements on thin films of each pure organic material. We used two different liquids, water and ethylene glycol (EG), to obtain pairs of contact angles for each material and then calculated the surface energy of each pure material via: where is the contact angle, is the solid/vapor surface energy, is the liquid/vapor surface energy.[66] The images used to

measure the contact angle with water for P3HT, PTB7, PCBM, **2g** and **2h**, are shown in Figure 3.9. The surface energies determined from the contact angles for both water and EG, determined via Eq. 2 using literature values for ,[67] are summarized in Table 3.1. The small discrepancies between the surface energies obtained using different solvents is mainly due to the difference in polarity of different liquids, as has been discussed elsewhere.[66] For our purposes, however, only on the relative surface energies of the polymers and fullerenes are important for understanding VPS, and indeed the ordering of the surface energies for the five different materials stays the same between different liquids.

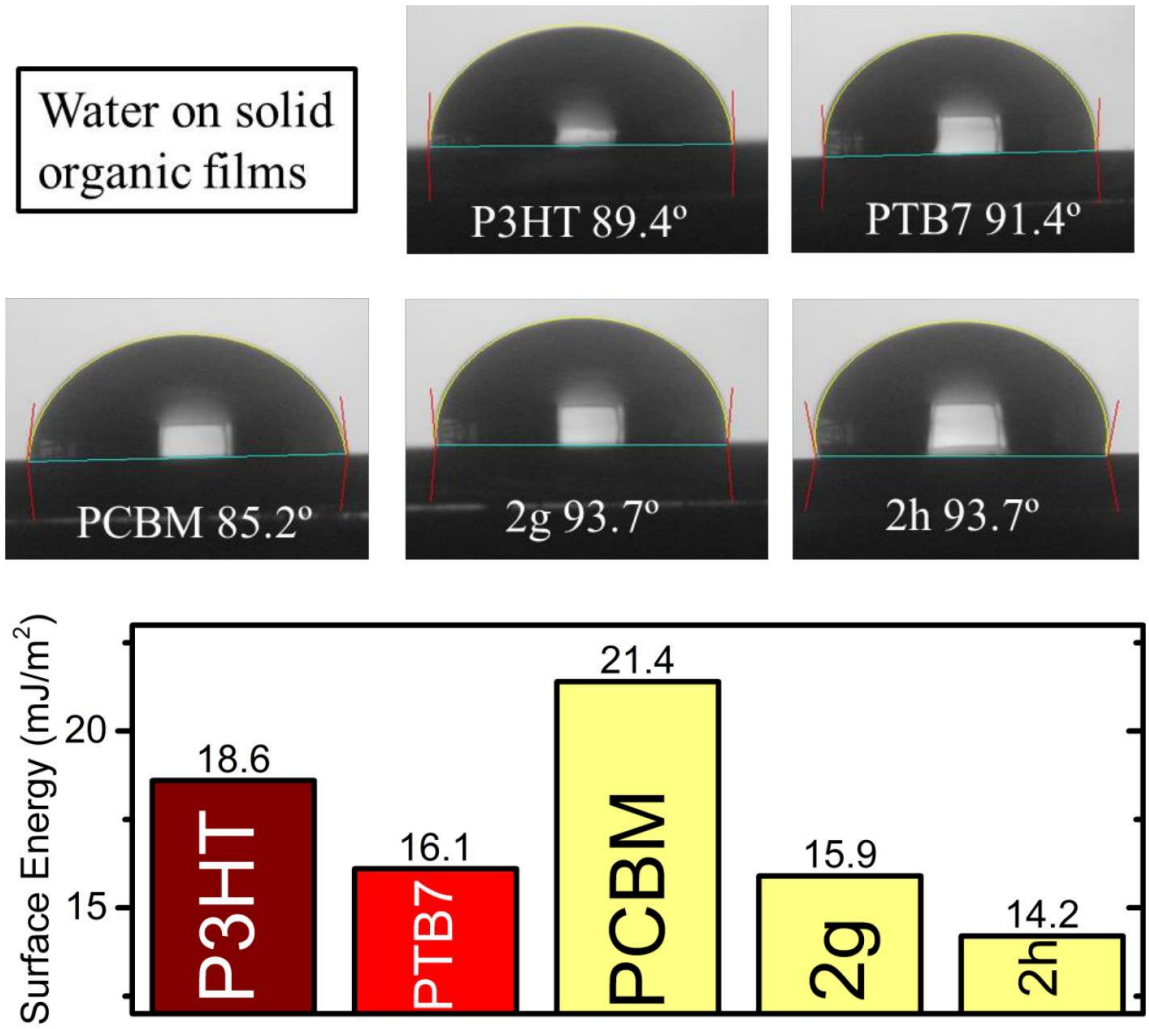

Figure 3.9 Top: Contact angle images taken on liquid water/thin films (<100 nm) consisted of pure organic material. Bottom: Bar graphs for the calculated surface energies for pure polymers or fullerene derivatives from water contact angle measurements.

Table 3.1 Summary of measured contact angles and the calculated surface energies.

Organic Layer	*Contact Angle Water* (degree)	*Contact Angle EG* (degree)	*Surface Energy Water* (mN/m)	*Surface Energy EG* (mN/m)
P3HT	89.4	63.5	18.6	25.0
PTB7	93.4	66.0	16.1	23.9
PCBM	85.2	54.5	21.4	28.7
2g	93.7	65.4	15.9	23.9
2h	96.6	69.7	14.2	21.6

For either liquid, the surface energies we obtained have the following order: **2h** < **2g** ≈ PTB7 < P3HT < PCBM. This result is important for understanding VPS when fabricating active layers from blends of these materials. First, the 1,4-dibenzyl fullerene bisadducts **2g** and **2h** have much lower surface energy than PCBM. In fact, their surface energies are even lower than that of P3HT. This implies that both **2g** and **2h** will prefer to reside near the top interface of the active layer. In contrast, PCBM will tend to segregate towards the bottom of the active since its surface energy is higher than that of the polymer. For PTB7:**2g** BHJs, the polymer and fullerene are expected to form a well-mixed active layer with little VPS due to the fact that **2g** and PTB7 have almost identical surface energies. The results in Table 3.1, taken together, allow us to build an expectation for the VPS in each of our polymer/fullerene combinations that is summarized in Figure 3.10. The surface energy analysis provides us with the fundamental reason for explaining the observed the changes in the device physics such as the TPV/TPC results and the excess carriers measured by CELIV.

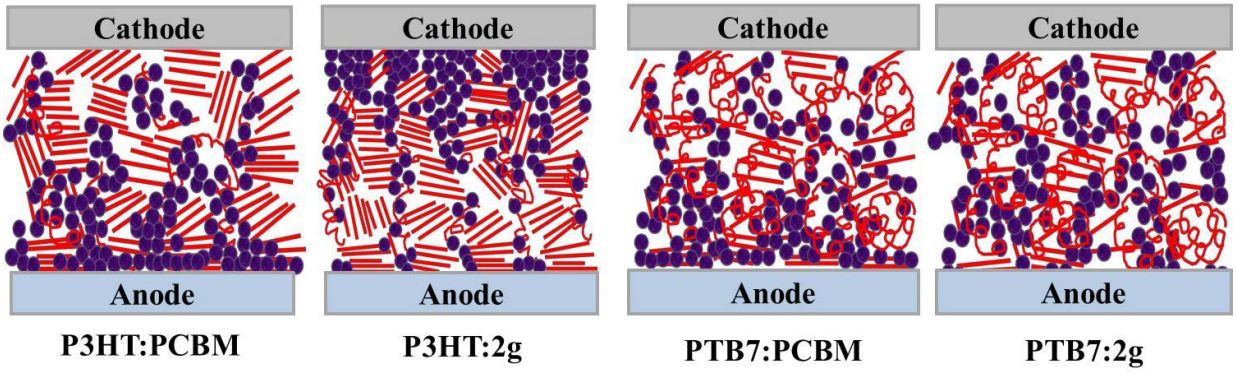

Figure 3.10 Cartoons illustrating different vertical phase segregation in different polymer:fullerene systems, based on the relative surface energies of the different polymers and fullerenes summarized in Table 3.1.

9. Using Surface Energies to Understand the Operation of Normal vs. Inverted Device

As mentioned in the Introduction, several methods have been developed to try to control VPS during or after the formation of the active layer to improve device performance.[19,28,64,68,69] If VPS is unfavorable, however, the most common way to improve device performance is to invert the structure of the solar cell by making the anode on the top and cathode on the bottom, so that the originally unfavorable VPS becomes favorable in the inverted device structure. The inverted structure also provides more favorable light management in most polymer/fullerene solar cells, leading to improved J_{sc}'s.[70,71]

Based on the relative surface energies in Table 3.1/Figure 3.10, we can predict which device structure should be optimal for a given a polymer:fullerene combination. For example, we would predict the inverted structure is better for P3HT:PCBM than the normal structure since PCBM molecules tend to segregate towards the bottom; in contrast, inverted devices would be predicted to be less ideal for P3HT:**2g** since the relative surface energies are opposite those of P3HT:PCBM. Similarly, for PTB7:PCBM, the inverted structure should be a better choice, while for PTB7:**2g**, since there is no obvious preference for VPS, inverted and normal device geometries should give comparable performance.

To verify these predictions, we fabricated inverted devices with a structure of ITO/ZnO/Polymer:Fullerene/MoO_3/Ag for all of the materials combinations studied above. The inverted device *J*–*V* curves are plotted in Figure 3.11, together with the results of the normal device shown in Figure 3.1 for ease of comparison; the results confirm what we predicted from the surface energy measurements.

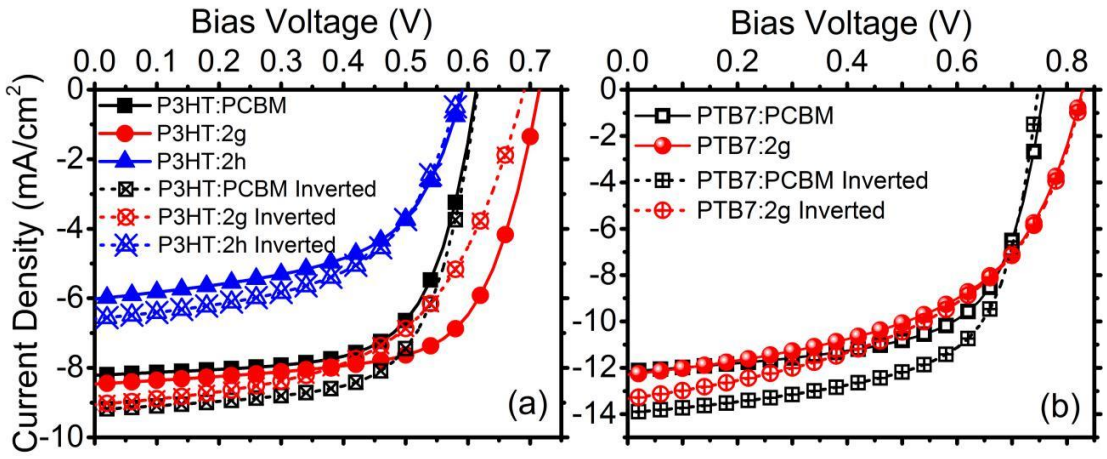

Figure 3.11 "Normal" versus "Inverted" devices using the same polymer:fullerene active layers where (a) is P3HT:fullerene and (b) is PTB7:fullerene. The "normal" devices' *J-V* curves are reprinted results from Figure 4.1 for ease of comparison. The "normal" device has a structure of ITO/PEDOT:PSS/Polymer:Fullerene/Ca/Al while the "inverted" device has a structure of ITO/ZnO/Polymer:Fullerene/MoO_3/Ag. The error bars are omitted in the figure for clarity but the standard deviations are included in Table 3.2.

Table 3.2 Summary of photovoltaic device parameters[a]

	Voc (mV)	*Jsc* (mA/cm^2)	*FF* *(%)*	*PCE* *(%)*
P3HT:PCBM	613 ±2	8.2 ±0.2	66.6 ±0.4	3.4 ±0.1
P3HT:2g	715 ±1	8.5 ±0.2	66.3 ±0.7	3.9 ±0.1
P3HT:2h	588 ±5	6.0 ±0.1	55.4 ±1.3	2.0 ±0.1
P3HT:PCBM inverted	616 ±4	9.2 ±0.1	65.8 ±0.6	3.7 ±0.1
P3HT:2g inverted	691 ±6	9.1 ±0.2	54.2 ±1.6	3.4 ±0.2
P3HT:2h inverted	588 ±3	6.7 ±0.1	54.8 ±0.7	2.1 ±0.1
PTB7:PCBM	760 ±1	12.1 ±0.2	64.4 ±0.1	5.9 ±0.2
PTB7:2g	825 ±9	12.3 ±0.2	53.3 ±0.1	5.4 ±0.1
PTB7:PCBM inverted	747 ±3	13.9 ±0.7	64.4 ±1.8	6.7 ±0.3
PTB7:2g inverted	830 ±4	13.3 ±0.2	50.0 ±0.8	5.5 ±0.1

[a] The standard deviation is based on measurements over at least three independent devices.

For the P3HT:PCBM-based devices, the inverted structure provides the better PCE of 3.7% compared to only 3.4% for the normal device structure. When **2g** is used as acceptor with P3HT, the inverted device shows an efficiency of 3.4%, comparable to that of PCBM, yet the normal structure device has a significantly higher efficiency (3.9%) due to improvements in both the V_{oc} and *FF*. Most of the improvement of the J_{sc} for the inverted polymer:fullerene combinations is likely due to the light management, but some may also result from more favorable VPS. The poor device performance of P3HT:**2h** is governed by its overly phase separated active layer morphology and unfavorable bulk recombination, so the structure of the device contributes little to the efficiency.

For PTB7-based devices, the trend with device structure also confirms our predications based on surface energies. With PCBM, the inverted devices (PCE=6.7%) show a particularly large increase in PCE compared to the normal structure (PCE=5.9%), most likely due to the fact that PTB7 and PCBM have the largest surface energy difference of the materials studied in this work. When PTB7 is used in combination with **2g**, however, there is no clear performance trend between the normal (PCE=5.4%) and inverted structures (PCE=5.5%), consistent with the comparable surface energies of these two materials.

3.3 Conclusions

In conclusion, we have employed two novel fullerene bisadducts together with PCBM and two polymers, P3HT and PTB7, to build a system of five different polymer:fullerene combinations that allows us to separate the effects of the bulk BHJ morphology from that of the interface caused by vertical phase segregation on device performance and device physics. We found that the bulk recombination is the dominant factor for determining the overall device efficiency. Devices with the largest degree of phase separation showed the highest trap-state density. This led to a dominant trap-assisted recombination in the bulk and inferior device performance. For devices with similar bulk recombination, surface recombination, determined primarily by VPS, plays the most important role in device physics, including determining the charge carrier density and lifetime. We found that surface recombination could make the light ideality factors go below unity. We found that the surface energies of the fullerene bisadducts studied in this work were comparable to or lower than those of the polymers used, which were in turn lower than that of PCBM. This resulted in a reversal of the vertical phase segregation between devices with PCBM and those with the fullerene bisadducts. By comparing the surface energy of the pure materials, we were able to successfully predict the trend in device performance when changing the device structure from normal to inverted. Thus, our work shows that simple contact angle measurements can offer deep insights in how to select the best device structure for a given material system.

3.4 Experimental Methods

Device Fabrication

The 1,4-dibenzyl [60] fullerene bisadducts, **2g** and **2h**, were previously synthesized.[75] PCBM, P3HT and PTB7 were commercially available materials. We fabricated polymer:fullerene BHJ solar cells by starting with cleaning pre-patterned tin-doped indium oxide (ITO; TFD Inc.) coated substrates with four successive sonication steps: detergent solution, deionized water, acetone and isopropanol for approximately 10 min each. The ITO substrates were treated with an air plasma (200 mTorr, 15 min) after drying in vacuum for at least 30 min. We then deposited a thin layer of PEDOT:PSS by spin-coating the solution in air at 5000 rpm for 20 s. The PEDOT:PSS-covered substrates were then baked at 150 ℃ for 20 min in air.

The P3HT:fullerene blend solutions were prepared by dissolving P3HT and the fullerene derivatives with a weight ratio of 1:0.8 in *o*-dichlorobenzene. The concentration with respect to P3HT was 20 mg/mL. The solutions were stirred at 60 ℃ overnight before being cooled to room temperature and spun onto the PEDOT:PSS-covered substrates at a spin speed of 1160 rpm for 20 s. The active layers were still wet when the samples were taken off from the spin-coater. After about 2 min in the nitrogen glovebox, the active layers were dry. All of the films were then thermally annealed at 150 ℃ for 20 min on a hot plate under an argon atmosphere. Film thicknesses were measured with a Dektak 150 Stylus Surface Profiler.

The PTB7:fullerene solutions were prepared by dissolving PTB7 and the fullerene derivatives in a mixture of 95% chlorobenzene/5% diiodooctane with a polymer:fullerene weight ratio of 1:1.5 for the fullerene bisadducts and 1:1.34 for PCBM (the change in weight ratio accounts for molecular weight differences to ensure that the blends were equimolar). The solutions were stirred at 55 ℃ on a hot plate overnight prior to being spun at 1000 rpm for 60 s onto the PEDOT:PSS-

covered substrates. The films were then transferred to the antechamber of the glovebox and held under vacuum for ~1 hr. Then pure methanol was spun onto the films at a speed of 2500 rpm for 40 s. No further treatments were performed after this step before the deposition of the metal cathode.

For normal geometry devices, cathode deposition consisted of ~10 nm of Ca evaporated at a rate of ~0.5 Å/s followed by evaporation of 70 nm of Al at ~1 Å/s. The active areas of the resulting cells were 7.2 mm^2. For inverted geometry devices, the active layers were fabricated with the same methods. The cathode was a thin layer formed by spin-coating a ZnO nanoparticle solution, prepared following literature procedures,[72,73] at 4000 rpm for 20 s. The anode layer consisted of 15 nm of MoO_3 evaporated at a rate of ~ 0.5 Å/s followed by 70 nm of Ag evaporated at a rate of 1 Å/s. For the P3HT:fullerene devices, thermal annealing was performed before the deposition of MoO_3/Ag.

The *J*-*V* measurements were performed in an argon atmosphere using a Keithley 2400 source meter. We used a xenon arc lamp and an AM-1.5 filter as the excitation source, with the intensity calibrated to match 1 sun. For the inverted geometry devices, we performed a UV lamp treatment for at least 5 min before *J*–*V* testing.[74]

GIWAXS

2-D GIWAXS experiments were performed at the Stanford Synchrotron Radiation Lightsource on beamline 11-3 using a wavelength of 0.9742 Å. Figure 4.2 in the main text corresponds to the radially integrated pattern of the data from the full 2-D diffractogram. Each data curve in Figure 4.2 is the average of at least three different samples prepared under the same conditions. The 2-D images were collected on a plate with the detector 400 mm away from the

center of the measured sample. The beam spot had a width of ~150 μm. A helium chamber was used to reduce the noise. The software package WxDiff was used to analyze the GIWAXS data.

Optoelectronic Measurements and CELIV

EQE, PSR, TPV/TPC and dark CELIV measurements were taken using the approach detailed in previous publications by our group.[22]

Contact Angle and Surface Energy Analysis

The surface energy analysis based on Eq. 2 in the main text comes from combining three well known relations:[66]

Young Equation: $$\gamma_{sv} - \gamma_{sl} = \gamma_{lv}\cos\theta \quad (3)$$

Dupre Equation: $$\gamma_{sl} = \gamma_{lv} + \gamma_{sv} - W_{sl} \quad (4)$$

Fowkes Equation: $$W_{sl} = 2\sqrt{\gamma_{lv} \times \gamma_{sv}} \quad (5)$$

which lead directly to Eq. 2 upon substitution.

3.5 References

(1) Deibel, C.; Dyakonov, V. Polymer–Fullerene Bulk Heterojunction Solar Cells. *Rep. Prog. Phys* **2010**, *73*, 096401.

(2) Jørgensen, M.; Carlé, J. E.; Søndergaard, R. R.; Lauritzen, M.; Dagnæs-Hansen, N. A.; Byskov, S. L.; Andersen, T. R.; Larsen-Olsen, T. T.; Böttiger, A. P. L.; Andreasen, B.; et al. The State of Organic Solar cells—A Meta Analysis. *Sol. Energy Mater. Sol. Cells* **2013**, *119*, 84–93.

(3) Søndergaard, R. R.; Hösel, M.; Krebs, F. C. Roll-to-Roll Fabrication of Large Area Functional Organic Materials. *J. Polym. Sci. Part B Polym. Phys.* **2013**, *51*, 16–34.

(4) Scharber, M. C.; Sariciftci, N. S. Efficiency of Bulk-Heterojunction Organic Solar Cells. *Prog. Polym. Sci.* **2013**, *38*, 1929–1940.

(5) Krebs, F. C.; Espinosa, N.; Hösel, M.; Søndergaard, R. R.; Jørgensen, M. 25th Anniversary Article: Rise to Power - OPV-Based Solar Parks. *Adv. Mater.* **2014**, *26*, 29–39.

(6) Yu, G.; Gao, J.; Hummelen, J. C.; Wudl, F.; Heeger, A. J. Polymer Photovoltaic Cells: Enhanced Efficiencies via a Network of Internal Donor-Acceptor Heterojunctions. *Science* **1995**, *270*, 1789–1791.

(7) Heeger, A. J. 25th Anniversary Article: Bulk Heterojunction Solar Cells: Understanding the Mechanism of Operation. *Adv. Mater.* **2014**, *26*, 10–27.

(8) Liu, Y.; Zhao, J.; Li, Z.; Mu, C.; Ma, W.; Hu, H.; Jiang, K.; Lin, H.; Ade, H.; Yan, H. Aggregation and Morphology Control Enables Multiple Cases of High-Efficiency Polymer Solar Cells. *Nat. Commun.* **2014**, *5*, 5293.

(9) Kim, Y.; Choulis, S. A.; Nelson, J.; Bradley, D. D. C.; Cook, S.; Durrant, J. R. Device Annealing Effect in Organic Solar Cells with Blends of Regioregular poly(3-Hexylthiophene) and Soluble Fullerene. *Appl. Phys. Lett.* **2005**, *86*, 63502.

(10) Ayzner, A. L.; Wanger, D. D.; Tassone, C. J.; Tolbert, S. H.; Schwartz, B. J. Room to Improve Conjugated Polymer-Based Solar Cells: Understanding How Thermal Annealing Affects the Fullerene Component of a Bulk Heterojunction Photovoltaic Device. *J. Phys. Chem. C* **2008**, *112*, 18711–18716.

(11) Collins, B. A.; Tumbleston, J. R.; Ade, H. Miscibility, Crystallinity, and Phase Development in P3HT/PCBM Solar Cells: Toward an Enlightened Understanding of Device Morphology and Stability. *J. Phys. Chem. Lett.* **2011**, *2*, 3135–3145.

(12) Parnell, A. J.; Cadby, A. J.; Mykhaylyk, O. O.; Dunbar, A. D. F.; Hopkinson, P. E.; Donald, A. M.; Jones, R. A. L. Nanoscale Phase Separation of P3HT PCBM Thick Films As Measured by Small-Angle X-Ray Scattering. *Macromolecules* **2011**, *44*, 6503–6508.

(13) Chen, D.; Nakahara, A.; Wei, D.; Nordlund, D.; Russell, T. P. P3HT/PCBM Bulk Heterojunction Organic Photovoltaics: Correlating Efficiency and Morphology. *Nano Lett.* **2011**, *11*, 561–567.

(14) Shoaee, S.; Subramaniyan, S.; Xin, H.; Keiderling, C.; Tuladhar, P. S.; Jamieson, F.; Jenekhe, S. A.; Durrant, J. R. Charge Photogeneration for a Series of Thiazolo-Thiazole Donor Polymers Blended with the Fullerene Electron Acceptors PCBM and ICBA. *Adv. Funct. Mater.* **2013**, *23*, 3286–3298.

(15) Westacott, P.; Tumbleston, J. R.; Shoaee, S.; Fearn, S.; Bannock, J. H.; Gilchrist, J. B.; Heutz, S.; DeMello, J.; Heeney, M.; Ade, H.; et al. On the Role of Intermixed Phases in Organic Photovoltaic Blends. *Energy Environ. Sci.* **2013**, *6*, 2756–2764.

(16) Zhang, G.; Huber, R. C.; Ferreira, A. S.; Boyd, S. D.; Luscombe, C. K.; Tolbert, S. H.; Schwartz, B. J. Crystallinity Effects in Sequentially Processed and Blend-Cast Bulk-Heterojunction Polymer/Fullerene Photovoltaics. *J. Phys. Chem. C* **2014**, *118*, 18424–18435.

(17) Orimo, A.; Masuda, K.; Honda, S.; Benten, H.; Ito, S.; Ohkita, H.; Tsuji, H. Surface Segregation at the Aluminum Interface of poly(3-Hexylthiophene)/fullerene Solar Cells. *Appl. Phys. Lett.* **2010**, *96*, 43305.

(18) Lu, H.; Akgun, B.; Russell, T. P. Morphological Characterization of a Low-Bandgap Crystalline Polymer:PCBM Bulk Heterojunction Solar Cells. *Adv. Energy Mater.* **2011**, *1*, 870–878.

(19) Xu, Z.; Chen, L.-M.; Yang, G.; Huang, C.-H.; Hou, J.; Wu, Y.; Li, G.; Hsu, C.-S.; Yang, Y. Vertical Phase Separation in Poly(3-Hexylthiophene): Fullerene Derivative Blends and Its Advantage for Inverted Structure Solar Cells. *Adv. Funct. Mater.* **2009**, *19*, 1227–1234.

(20) Ibrahem, M. A.; Wei, H.-Y.; Tsai, M.-H.; Ho, K.-C.; Shyue, J.-J.; Chu, C. W. Solution-Processed Zinc Oxide Nanoparticles as Interlayer Materials for Inverted Organic Solar Cells. *Sol. Energy Mater. Sol. Cells* **2013**, *108*, 156–163.

(21) Mauger, S. A.; Chang, L.; Friedrich, S.; Rochester, C. W.; Huang, D. M.; Wang, P.; Moulé, A. J. Self-Assembly of Selective Interfaces in Organic Photovoltaics. *Adv. Funct. Mater.* **2013**, *23*, 1935–1946.

(22) Hawks, S. A.; Aguirre, J. C.; Schelhas, L. T.; Thompson, R. J.; Huber, R. C.; Ferreira, A. S.; Zhang, G.; Herzing, A. A.; Tolbert, S. H.; Schwartz, B. J. Comparing Matched Polymer:Fullerene Solar Cells Made by Solution-Sequential Processing and Traditional

Blend Casting: Nanoscale Structure and Device Performance. *J. Phys. Chem. C* **2014**, *118*, 17413–17425.

(23) Kiel, J. W.; Kirby, B. J.; Majkrzak, C. F.; Maranville, B. B.; Mackay, M. E. Nanoparticle Concentration Profile in Polymer-Based Solar Cells. *Soft Matter* **2010**, *6*, 641.

(24) Parnell, A. J.; Dunbar, A. D. F.; Pearson, A. J.; Staniec, P. a; Dennison, A. J. C.; Hamamatsu, H.; Skoda, M. W. A.; Lidzey, D. G.; Jones, R. A. L. Depletion of PCBM at the Cathode Interface in P3HT/PCBM Thin Films as Quantified via Neutron Reflectivity Measurements. *Adv. Mater.* **2010**, *22*, 2444–2447.

(25) Kirschner, S. B.; Smith, N. P.; Wepasnick, K. a.; Katz, H. E.; Kirby, B. J.; Borchers, J. a.; Reich, D. H. X-Ray and Neutron Reflectivity and Electronic Properties of PCBM-Poly(bromo)styrene Blends and Bilayers with poly(3-Hexylthiophene). *J. Mater. Chem.* **2012**, *22*, 4364.

(26) Lee, K. H.; Zhang, Y.; Burn, P. L.; Gentle, I. R.; James, M.; Nelson, A.; Meredith, P. Correlation of Diffusion and Performance in Sequentially Processed P3HT/PCBM Heterojunction Films by Time-Resolved Neutron Reflectometry. *J. Mater. Chem. C* **2013**, *1*, 2593–2598.

(27) Chen, H.; Hegde, R.; Browning, J.; Dadmun, M. D. The Miscibility and Depth Profile of PCBM in P3HT: Thermodynamic Information to Improve Organic Photovoltaics. *Phys. Chem. Chem. Phys.* **2012**, *14*, 5635–5641.

(28) Chen, H.; Hu, S.; Zang, H.; Hu, B.; Dadmun, M. Precise Structural Development and Its Correlation to Function in Conjugated Polymer: Fullerene Thin Films by Controlled Solvent Annealing. *Adv. Funct. Mater.* **2013**, *23*, 1701–1710.

(29) Liu, F.; Zhao, W.; Tumbleston, J. R.; Wang, C.; Gu, Y.; Wang, D.; Briseno, A. L.; Ade, H.; Russell, T. P. Understanding the Morphology of PTB7:PCBM Blends in Organic Photovoltaics. *Adv. Energy Mater.* **2014**, *4*, 1301377.

(30) Welch, G. C.; Perez, L. A.; Hoven, C. V.; Zhang, Y.; Dang, X.-D.; Sharenko, A.; Toney, M. F.; Kramer, E. J.; Nguyen, T.-Q.; Bazan, G. C. A Modular Molecular Framework for Utility in Small-Molecule Solution-Processed Organic Photovoltaic Devices. *J. Mater. Chem.* **2011**, *21*, 12700.

(31) Campoy-Quiles, M.; Ferenczi, T.; Agostinelli, T.; Etchegoin, P. G.; Kim, Y.; Anthopoulos, T. D.; Stavrinou, P. N.; Bradley, D. D. C.; Nelson, J. Morphology Evolution via Self-Organization and Lateral and Vertical Diffusion in Polymer:fullerene Solar Cell Blends. *Nat. Mater.* **2008**, *7*, 158–164.

(32) Campoy-Quiles, M.; Alonso, M. I.; Bradley, D. D. C.; Richter, L. J. Advanced Ellipsometric Characterization of Conjugated Polymer Films. *Adv. Funct. Mater.* **2014**, *24*, 2116–2134.

(33) Madsen, M. V.; Sylvester-Hvid, K. O.; Dastmalchi, B.; Hingerl, K.; Norrman, K.; Tromholt, T.; Manceau, M.; Angmo, D.; Krebs, F. C. Ellipsometry as a Nondestructive Depth Profiling Tool for Roll-to-Roll Manufactured Flexible Solar Cells. *J. Phys. Chem. C* **2011**, *115*, 10817–10822.

(34) Germack, D. S.; Chan, C. K.; Hamadani, B. H.; Richter, L. J.; Fischer, D. A.; Gundlach, D. J.; DeLongchamp, D. M. Substrate-Dependent Interface Composition and Charge Transport in Films for Organic Photovoltaics. *Appl. Phys. Lett.* **2009**, *94*, 233303.

(35) Tremolet de Villers, B.; Tassone, C. J.; Tolbert, S. H.; Schwartz, B. J. Improving the Reproducibility of P3HT:PCBM Solar Cells by Controlling the PCBM/Cathode Interface. *J. Phys. Chem. C* **2009**, *113*, 18978–18982.

(36) Li, G.; Chu, C.-W.; Shrotriya, V.; Huang, J.; Yang, Y. Efficient Inverted Polymer Solar Cells. *Appl. Phys. Lett.* **2006**, *88*, 253503.

(37) Finck, B. Y.; Schwartz, B. J. Understanding the Origin of the S-Curve in Conjugated Polymer/fullerene Photovoltaics from Drift-Diffusion Simulations. *Appl. Phys. Lett.* **2013**, *103*, 53304–53306.

(38) Street, R. A.; Song, K. W.; Northrup, J. E.; Cowan, S. Photoconductivity Measurements of the Electronic Structure of Organic Solar Cells. *Phys. Rev. B* **2011**, *83*, 165207.

(39) Shuttle, C. G.; Maurano, a.; Hamilton, R.; O'Regan, B.; de Mello, J. C.; Durrant, J. R. Charge Extraction Analysis of Charge Carrier Densities in a Polythiophene/fullerene Solar Cell: Analysis of the Origin of the Device Dark Current. *Appl. Phys. Lett.* **2008**, *93*, 183501.

(40) Maurano, A.; Hamilton, R.; Shuttle, C. G.; Ballantyne, A. M.; Nelson, J.; O'Regan, B.; Zhang, W.; McCulloch, I.; Azimi, H.; Morana, M.; et al. Recombination Dynamics as a Key Determinant of Open Circuit Voltage in Organic Bulk Heterojunction Solar Cells: A Comparison of Four Different Donor Polymers. *Adv. Mater.* **2010**, *22*, 4987–4992.

(41) Juska, G.; Arlauskas, K.; Viliunas, M.; Kocka, J. Extraction Current Transients : New Method of Study of Charge Transport in Microcrystalline Silicon. *Phys. Rev. Lett.* **2000**, *84*, 4946–4949.

(42) Kim, Y.; Cook, S.; Tuladhar, S. M.; Choulis, S. A.; Nelson, J.; Durrant, J. R.; Bradley, D. D. C.; Giles, M.; McCulloch, I.; Ha, C.-S.; et al. A Strong Regioregularity Effect in Self-

Organizing Conjugated Polymer Films and High-Efficiency Polythiophene:fullerene Solar Cells. *Nat. Mater.* **2006**, *5*, 197–203.

(43) Collins, B. A.; Li, Z.; Tumbleston, J. R.; Gann, E.; McNeill, C. R.; Ade, H. Absolute Measurement of Domain Composition and Nanoscale Size Distribution Explains Performance in PTB7:PC71BM Solar Cells. *Adv. Energy Mater.* **2013**, *3*, 65–74.

(44) Street, R. A.; Schoendorf, M.; Roy, A.; Lee, J. H. Interface State Recombination in Organic Solar Cells. *Phys. Rev. B* **2010**, *81*, 205307.

(45) Street, R. A.; Krakaris, A.; Cowan, S. R. Recombination Through Different Types of Localized States in Organic Solar Cells. *Adv. Funct. Mater.* **2012**, *22*, 4608–4619.

(46) Street, R. A.; Davies, D.; Khlyabich, P. P.; Burkhart, B.; Thompson, B. C. Origin of the Tunable Open-Circuit Voltage in Ternary Blend Bulk Heterojunction Organic Solar Cells. *J. Am. Chem. Soc.* **2013**, *135*, 986–989.

(47) Shockley, W.; Jr, W. R. Statistics of the Recombinations of Holes and Electrons. *Phys. Rev.* **1952**, *87*, 835–842.

(48) Cowan, S. R.; Roy, A.; Heeger, A. J. Recombination in Polymer-Fullerene Bulk Heterojunction Solar Cells. *Phys. Rev. B* **2010**, *82*, 245207.

(49) Tzabari, L.; Tessler, N. Shockley–Read–Hall Recombination in P3HT:PCBM Solar Cells as Observed under Ultralow Light Intensities. *J. Appl. Phys.* **2011**, *109*, 064501.

(50) Kirchartz, T.; Deledalle, F.; Tuladhar, P. S.; Durrant, J. R.; Nelson, J. On the Differences between Dark and Light Ideality Factor in Polymer: Fullerene Solar Cells. *J. Phys. Chem. Lett.* **2013**, *4*, 2371–2376.

(51) Kirchartz, T.; Pieters, B. E.; Kirkpatrick, J.; Rau, U.; Nelson, J. Recombination via Tail States in Polythiophene:fullerene Solar Cells. *Phys. Rev. B* **2011**, *83*, 115209.

(52) Foertig, A.; Rauh, J.; Dyakonov, V.; Deibel, C. Shockley Equation Parameters of P3HT:PCBM Solar Cells Determined by Transient Techniques. *Phys. Rev. B* **2012**, *86*, 115302.

(53) Credgington, D.; Durrant, J. R. Insights from Transient Optoelectronic Analyses on the Open-Circuit Voltage of Organic Solar Cells. *J. Phys. Chem. Lett.* **2012**, *3*, 1465–1478.

(54) Wetzelaer, G. A. H.; Kuik, M.; Lenes, M.; Blom, P. W. M. Origin of the Dark-Current Ideality Factor in Polymer:fullerene Bulk Heterojunction Solar Cells. *Appl. Phys. Lett.* **2011**, *99*, 153506.

(55) Shuttle, C. G.; O'Regan, B.; Ballantyne, A. M.; Nelson, J.; Bradley, D. D. C.; de Mello, J.; Durrant, J. R. Experimental Determination of the Rate Law for Charge Carrier Decay in a Polythiophene: Fullerene Solar Cell. *Appl. Phys. Lett.* **2008**, *92*, 93311–93313.

(56) Ballantyne, A. M.; Ferenczi, T. a. M.; Campoy-Quiles, M.; Clarke, T. M.; Maurano, A.; Wong, K. H.; Zhang, W.; Stingelin-Stutzmann, N.; Kim, J.-S.; Bradley, D. D. C.; et al. Understanding the Influence of Morphology on Poly(3-hexylselenothiophene):PCBM Solar Cells. *Macromolecules* **2010**, *43*, 1169–1174.

(57) Maurano, A.; Shuttle, C. G.; Hamilton, R.; Ballantyne, A. M.; Nelson, J.; Zhang, W.; Heeney, M.; Durrant, J. R. Transient Optoelectronic Analysis of Charge Carrier Losses in a Selenophene/Fullerene Blend Solar Cell. *J. Phys. Chem. C* **2011**, *115*, 5947–5957.

(59) Ryan, J. W.; Kirchartz, T.; Viterisi, A.; Nelson, J.; Palomares, E. Understanding the Effect of Donor Layer Thickness and a MoO3 Hole Transport Layer on the Open-Circuit Voltage in Squaraine/C60 Bilayer Solar Cells. *J. Phys. Chem. C* **2013**, *117*, 19866–19874.

(60) Dibb, G. F. a.; Kirchartz, T.; Credgington, D.; Durrant, J. R.; Nelson, J. Analysis of the Relationship between Linearity of Corrected Photocurrent and the Order of Recombination in Organic Solar Cells. *J. Phys. Chem. Lett.* **2011**, *2*, 2407–2411.

(61) Vandewal, K.; Tvingstedt, K.; Gadisa, A.; Inganäs, O.; Manca, J. V. Relating the Open-Circuit Voltage to Interface Molecular Properties of Donor:Acceptor Bulk Heterojunction Solar Cells. *Phys. Rev. B* **2010**, *81*, 125204.

(62) Graham, K. R.; Erwin, P.; Nordlund, D.; Vandewal, K.; Li, R.; Ngongang Ndjawa, G. O.; Hoke, E. T.; Salleo, A.; Thompson, M. E.; McGehee, M. D.; et al. Re-Evaluating the Role of Sterics and Electronic Coupling in Determining the Open-Circuit Voltage of Organic Solar Cells. *Adv. Mater.* **2013**, *25*, 6076–6082.

(63) Vandewal, K.; Oosterbaan, W. D.; Bertho, S.; Vrindts, V.; Gadisa, A.; Lutsen, L.; Vanderzande, D.; Manca, J. V. Varying Polymer Crystallinity in Nanofiber poly(3-Alkylthiophene): PCBM Solar Cells: Influence on Charge-Transfer State Energy and Open-Circuit Voltage. *Appl. Phys. Lett.* **2009**, *95*, 123303.

(64) Graham, K.; Amassian, A.; Erwin, P.; Thompson, M.; Nordlund, D.; Vandewal, K.; Hoke, E.; Salleo, A.; Mcgehee, M.; Lee, R.; et al. Charge-Transfer State Energy Determines Open-Circuit Voltage in Organic Photovoltaics. *SPIE Newsroom* **2013**, DOI: 10.1117/2.1201309.005006.

(65) Kong, J.; Hwang, I.-W.; Lee, K. Top-down Approach for Nanophase Reconstruction in Bulk Heterojunction Solar Cells. *Adv. Mater.* **2014**, *26*, 6275–6283.

(65) Huang, J.-H.; Hsiao, Y.-S.; Richard, E.; Chen, C.-C.; Chen, P.; Li, G.; Chu, C.-W.; Yang, Y. The Investigation of Donor-Acceptor Compatibility in Bulk-Heterojunction Polymer Systems. *Appl. Phys. Lett.* **2013**, *103*, 043304.

(66) Carré, A. Polar Interactions at Liquid/polymer Interfaces. *J. Adhes. Sci. Technol.* **2007**, *21*, 961–981.

(67) Janssen, D.; De Palma, R.; Verlaak, S.; Heremans, P.; Dehaen, W. Static Solvent Contact Angle Measurements, Surface Free Energy and Wettability Determination of Various Self-Assembled Monolayers on Silicon Dioxide. *Thin Solid Films* **2006**, *515*, 1433–1438.

(68) Zhao, Y.; Xie, Z.; Qu, Y.; Geng, Y.; Wang, L. Solvent-Vapor Treatment Induced Performance Enhancement of poly(3-Hexylthiophene):methanofullerene Bulk-Heterojunction Photovoltaic Cells. *Appl. Phys. Lett.* **2007**, *90*, 43503–43504.

(69) Chambon, S.; Derue, L.; Lahaye, M.; Pavageau, B.; Hirsch, L.; Wantz, G. MoO_3 Thickness, Thermal Annealing and Solvent Annealing Effects on Inverted and Direct Polymer Photovoltaic Solar Cells. *Materials (Basel).* **2012**, *5*, 2521–2536.

(70) Hadipour, A.; Cheyns, D.; Heremans, P.; Rand, B. P. Electrode Considerations for the Optical Enhancement of Organic Bulk Heterojunction Solar Cells. *Adv. Energy Mater.* **2011**, *1*, 930–935.

(71) Yip, H.-L.; Jen, A. K. Y. Recent Advances in Solution-Processed Interfacial Materials for Efficient and Stable Polymer Solar Cells. *Energy Environ. Sci.* **2012**, *5*, 5994–6011.

(72) Beek, W. J. E.; Wienk, M. M.; Kemerink, M.; Yang, X.; Janssen, R. A. J. Hybrid Zinc Oxide Conjugated Polymer Bulk Heterojunction Solar Cells. *J. Phys. Chem. B* **2005**, *109*, 9505–9516.

(73) Sun, B.; Sirringhaus, H. Solution-Processed Zinc Oxide Field-Effect Transistors Based on Self-Assembly of Colloidal Nanorods. *Nano Lett.* **2005**, *5*, 2408–2413.

(74) Kuwabara, T.; Tamai, C.; Omura, Y.; Yamaguchi, T.; Taima, T.; Takahashi, K. Effect of UV Light Irradiation on Photovoltaic Characteristics of Inverted Polymer Solar Cells

Containing Sol–gel Zinc Oxide Electron Collection Layer. *Org. Electron.* **2013**, *14*, 649–656.

(75) S. Huang, G. Zhang, N. S. Knutson, M. T. Fontana, R. C. Huber, A. S. Ferreira, S. H. Tolbert, B. J. Schwartz, Y. Rubin, *J. Mater. Chem. A*. **2016**, *4*, 416-424.

Chapter 4. Surface Modification of Mesoporous Titania Thin Films in Inorganic-Organic Hybrid Solar Cells

4.1 Introduction

Since the silicon solar cell was invented in the 1940's,[1] photovoltaic system has been improving to increase power conversion efficiencies (PCE) and decrease production costs. For the last three decades, solar cells based on small organic molecules and conjugated polymers have been intensively studied due to their enhanced light absorption over a wide range of wavelengths, facile solution processability and low fabrication costs.[2,3] Most organic photovoltaics consist of semiconducting polymer and fullerene derivative as electron donor (D) and acceptor(A), respectively. To achieve high performing photovoltaics, a bulk-heterojunction (BHJ) structure needs to be formed in the active layer. [4] When the incident photon energy is larger than the band gap of the organic semiconductors, excitons are generated upon the electron excitation from the valence band to the conduction band. They subsequently diffuse to an interface where they split into free charge carriers, and then are collected at their respective electrodes. Therefore, it is important to have the ideally mixed donor and acceptor to create a large interfacial area and a good charge transport pathway. In particular, the exciton diffusion length in semiconducting polymers is very short (10-20 nm),[5-7] indicating that the only excitons generated at the D/A interface can have an effective charge separation. The morphology in nanoscale organic components is, however, very difficult to precisely control, which remains the challenge for charge carriers to participate in the photocurrent generation.[8-11] In particular, even a small modification to chemical structure in organic components causes a significant change in the device performance, which also lowers the reproducibility.[12]

Inorganic/organic hybrid solar cells have been given attention because they potentially have the advantages of both inorganic and organic components.[13,14] Nanostructured inorganics offer a high charge carrier mobility and stability as well as controllable morphologies, which is expected to resolve the intrinsic issues from organic solar cells.[15-17] McGehee *et. al*. reported the hybrid solar cells consisting of porous TiO_2 and Poly(3-hexylthiophene) (P3HT).[18-19] In the external quantum efficiency (EQE) measurement, the porous TiO_2 device showed 3 times higher efficiency at 514 nm than that of the dense TiO_2 device. This is attributed to the larger interface area provided by the porous structure, which could lower charge recombination. Their devices, however, still suffered from a low power conversion efficiency of 0.45 % under AM 1.5 condition. This can be due to the incompatibility of inorganic and organic components, which need to be resolved for further development of hybrid solar cells.

In this work, we have investigated mesoporous nanocrystal-based TiO_2:P3HT hybrid solar cells. Mesoporous TiO_2 films are prepared using as-synthesized TiO_2 nanocrystals and amphiphilic diblock copolymer, Poly(1,4-butadiene)-b-poly(ethylene oxide). To improve photovoltaic performance, it is necessary to create a better contact between porous TiO_2 and P3HT via interfacial modification and efficient infiltration of P3HT into the pores. Here, the porous TiO_2 surface is modified by a fullerene derivative, [6, 6]-phenyl-C61-butyric acid (PCBA) to resolve the incompatibility between hydrophilic TiO_2 and hydrophobic P3HT. Different infiltration methods have been studied to incorporate P3HT into the porous architecture, which is required to achieve efficient charge transfer. We utilized PL spectra and the SEM image to determine the efficient pore filling methods. Lastly, we examined the device performance by collecting *J*-*V* curves to investigate the surface modification effect.

4.2 Results and Discussion

We synthesized TiO_2 nanocrystals using $TiCl_4$ and benzyl alcohol. The synthetic method was previously reported,[20] and can be found in the section of Experimental Methods. Mesoporous TiO_2 film (mp- TiO_2) is prepared from as-synthesized TiO_2 nanocrystals using an amphilphlic diblock copolymer, Poly(1,4-butadiene)-b-poly(ethylene oxide) via Evaporation Induced Self-Assembly (EISA).[21-23] A clearly dissolved diblock copolymer solution, PB-b-PEO is added to the TiO_2 nanocrystals at 60 ºC. Once the solution is homogenous, the film is deposited via dip-coating then calcined at 600 ºC to remove the polymer template. Figure 4.1 shows the XRD pattern of drop-casted TiO_2 nanocrystals (a) and mesoporous TiO_2 film (b). We observed well-matching distinctive peaks at 25º, 37º and 48º in 2θ from both (a) and (b), which corresponds to (101), (004), and (200) of (hkl) in tetragonal anatase TiO_2 (JCPDS No. 00-021-1272). Figure 4.2 (a) and (b) present the top-view and cross-section SEM images for mesoporous TiO_2 film after calcination. The open pores are clearly observed from the top surface, and the pore architecture forms across the entire film. To get further insight on the nature of porous structure, we performed ellipsometric porosimetry on mp-TiO_2 film. The porosity and pore size distribution are obtained by measuring toluene adsorption-desorption isotherm. In Figure 4.3 (a) and (b), mp-TiO_2 film shows 56% of porosity, and its pore and neck diameter are calculated to 14 nm and 9 nm, respectively.

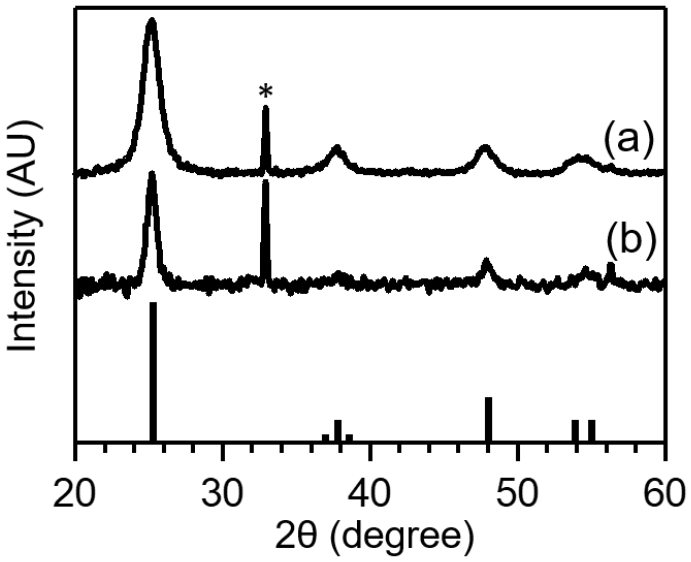

Figure 4.1. X-ray diffraction of drop-casted TiO_2 nanocrystals (a) and mp-TiO_2 (b). The stick pattern corresponds to tetragonal anatase TiO_2. (JCPDS No. 00-021-1272) (* peak indicates Si substrate.)

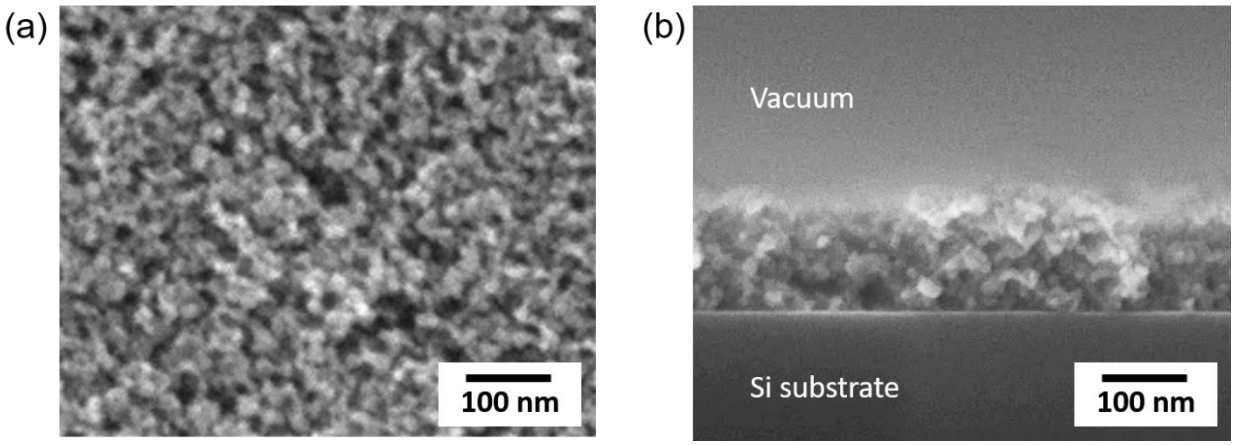

Figure 4.2 SEM images of mp-TiO_2 film in top-view (a) and cross section (b).

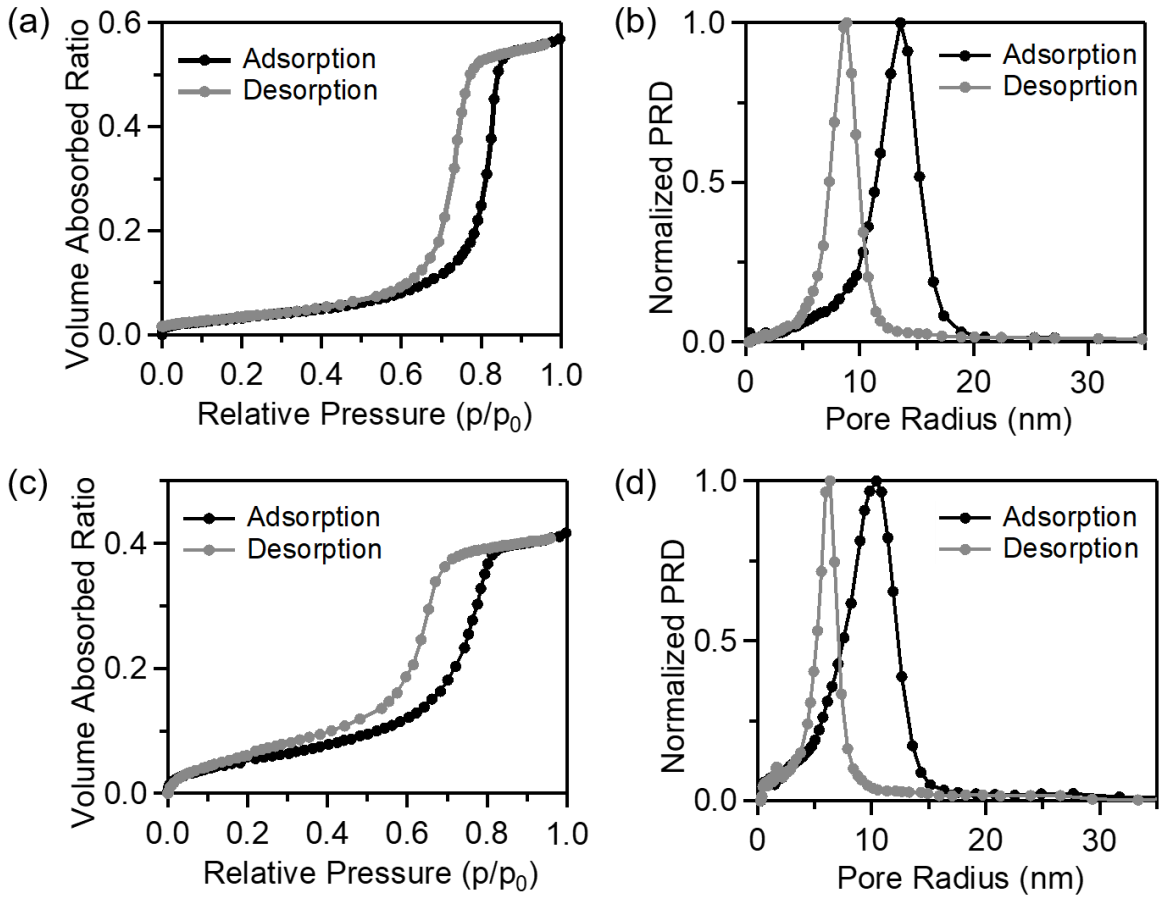

Figure 4.3 Toluene adsorption-desorption isotherms showing characteristic mesoporous behavior for mp-TiO_2 (a) and for surface-modified mp-TiO_2 (c). The calculated pore size distribution using the isotherm for mp-TiO_2 (b) and for surface-modified mp-TiO_2 (d).

In hybrid solar cells, one of the biggest challenges is the poor interaction between inorganic and organic components that has limited the device efficiency. Therefore, it is important to resolve incompatibility between hydrophilic TiO_2 surface and hydrophobic P3HT to achieve efficient device performances. Manthiram *et. al*. introduced a single carboxylic ending group into P3HT to improve the interaction between P3HT and TiO_2.[24] The replacement of P3HT with P3HT-COOH increased open-circuit voltage (V_{oc}) and decreased charge traps. The –COOH group acts as an anchoring group on the surface of TiO_2, which leads to reduced charge recombination and enhanced charge transportation. Based on this idea, we introduced a fullerene derivative, [6, 6]-phenyl-C61-butyric acid (PCBA) onto mp-TiO_2 as a surface mediator. As shown in Figure 4. 4 (a), the carboxylic acid group of PCBA is likely to form covalent bonds on –OH groups of hydrophilic TiO_2 surface to promote a well-connected inorganic/organic structure. The C_{60} ball of PCBA is able to interact with P3HT via π-π interactions. The hydrophilic TiO_2 surface is modified by being soaked in PCBA/pyridine solution. The binding of the PCBA to the mp-TiO_2 is observed by a slight change in UV-visible absorption spectra. (Figure 4.5) Further evidence for the PCBA anchoring is shown in the ellipsometric porosimetry analysis. (Figure 4.3 (c) and (d)) After PCBA soaking, the porosity is reduced to 41%, and the pore and neck diameter also decreased to 11 nm 7 nm, respectively. Considering that PCBM (Phenyl-C61-butyric acid methyl ester), a similar fullerene derivative, is approximately 10-20 nm in size,[25] the pore diameter reduction from 14 to 11 nm implies a little aggregation of PCBM rather than the formation of PCBA monolayer. Another advantage that we can expect from the surface modification is a cascade structure in the energy band diagram. As shown in Figure 4.4 (b), the LUMO energy level of PCBA is -3.7 eV,[26, 27] which is in between that of P3HT and TiO_2. There is no energy barrier for electrons and holes to move toward each electrode, and the offset between the energy levels is larger than the exciton

binding energy (a few meV to 100 meV).[28] Therfore, efficient charge carrier transfer can be driven upon the surface modification.

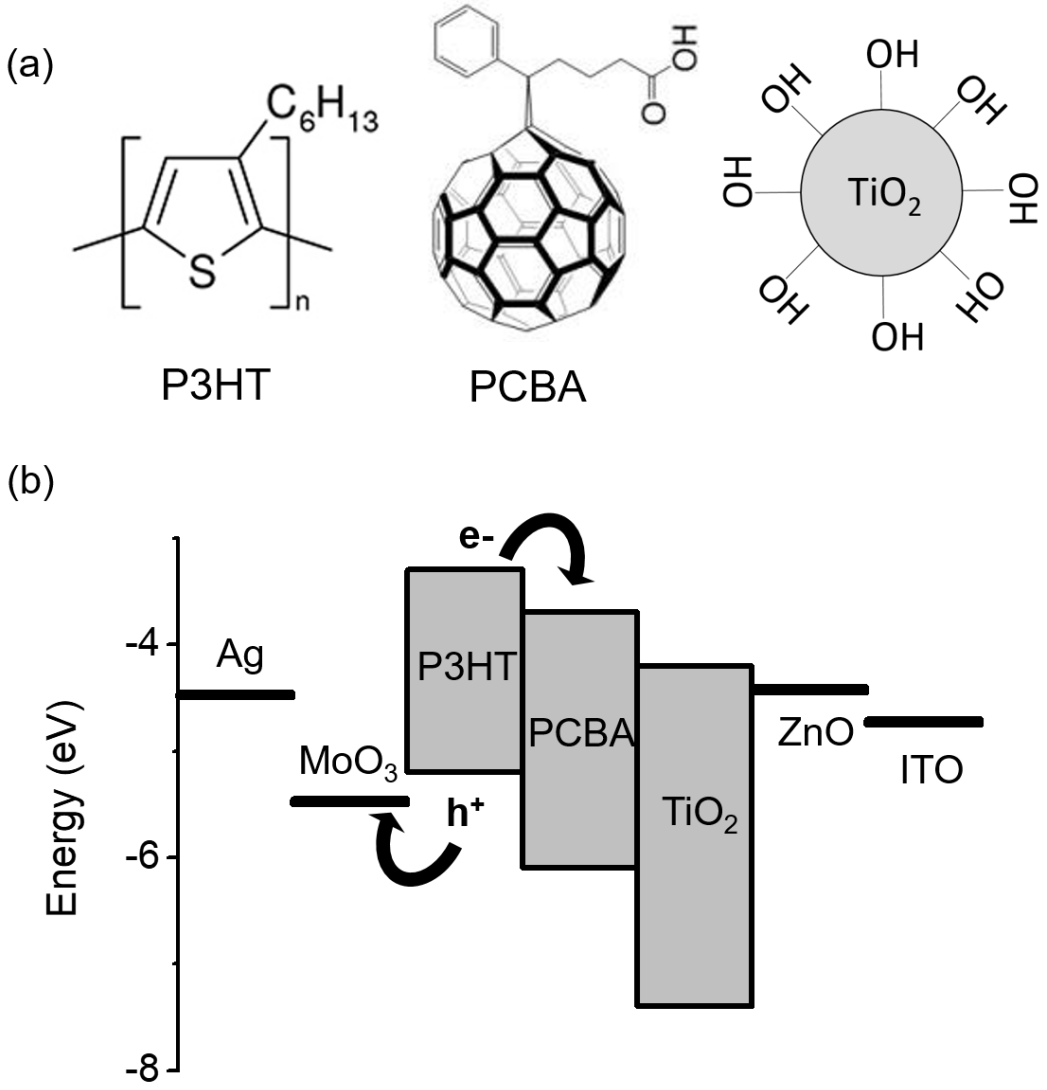

Figure 4.4 (a) Chemical structures of the light absorber, Poly(3-hexylthiophene) (P3HT) and the surface mediator, [6, 6]-phenyl-C61-butyric acid (PCBA). The carboxylic group of PCBA is covalently bonded to hydroxo groups on TiO_2. (b) Schematic energy level of the inverted solar cell with a cascade structure. The energy levels are extracted from ref (26), (33) and (34).

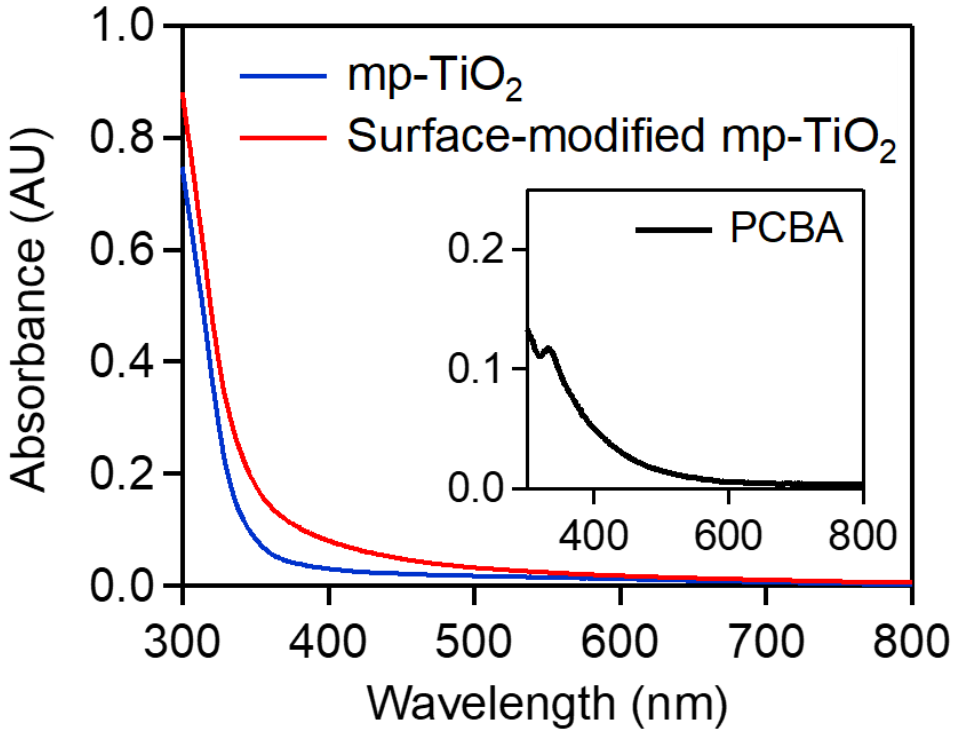

Figure 4.5. UV-visible absorption spectra of mp-TiO_2 (blue) and surface-modified mp-TiO_2 (red) films on glass. The subtraction of the two spectra provides the absorption spectrum of PCBA shown in the inset.

We next investigated multiple ways to infiltrate P3HT into the pores of TiO_2 film. The pore filling ratio directly influences the formation of intimate contacts, which results in the improved solar cell performance.[18,19,29,30] Figure 4.6 (a) represents the cross section SEM image after a P3HT solution is spun down onto mp-TiO_2 film without post-treatment. Most P3HT stays in the overlayer on the top of TiO_2 leaving the majority of pores unfilled. To achieve a better pore filling, we have attempted the multiple ways such as solvent-drop, slow drying, solvent-vapor, heating at 140 ºC and heating at 230 ºC. Solvent-drop method is that a very small amount of the pure solvent (*o*-dichlorobenzene) is added onto the top surface of the film after P3HT is spun down. Since mp-TiO_2 film is pre-soaked in the pure solvent (See the Experimental Methods for details), it may help P3HT move easily and get into the pores. Slow-drying method is that P3HT solution is spun down for a shorter time, and the wet P3HT layer is slowly dried out. It allows P3HT chain to infiltrate into the pores for a longer time. Solvent-vapor method is that mp-TiO_2:P3HT film after spin-coating is exposed to the pure solvent vapor in a sealable container. Heating methods involve heating themp-TiO_2:P3HT film on a hot plate at a designated temperature, 140 ºC or 230 ºC after spin-coating. Figure 4.6 (b)-(f) represents the cross section SEM images of mp-TiO_2:P3HT prepared by different infiltration methods. We noticed that solvent-drop and slow drying methods lead to very poor pore filling (Figure 4.6 (b) and (c), respectively). In solvent-drop method, the top surface of TiO_2 film is not completely covered, implying the polymer dissolution. In slow-drying method, P3HT sits on top of mp-TiO_2 as the overlayer, and it rarely fills the pores like as-cast film. For solvent vapor and heating methods, we observed some pores filled as well as the overlayer in the SEM images. In particular, heating at 230 ºC looked a very promising in terms of showing improved pore filling. PL spectra is obtained from the solvent-vapor and heating methods to investigate charge transfer trend regarding P3HT infiltration. If efficient pore filling is achieved,

PL intensity is substantially decreased due to better charge extraction. Figure 4.7 (a) represents the PL emission of surface-modified mp-TiO_2:P3HT prepared by different infiltration methods. As we expected from the SEM images, heating at 230 ºC showed the highest quenching efficiency indicating the most efficient charge transfer. The fact that the melting point of P3HT crystallites is 233 ºC,[31] allows us to speculate that P3HT chains are more likely to experience the morphology conformation, which might lead to a facile infiltration.[19] We also performed PL measurement on mp-TiO_2:P3HT prepared by heating at 230 ºC as to compare to the quenching behavior of surface-modified mp-TiO_2:P3HT. As shown in Figure 4.7 (b), mp-TiO_2:P3HT shows fluorescence emission with much higher intensity than that of Surface-modified mp-TiO_2:P3HT. This the surface modification by PCBA contributes to improved charge transfer.

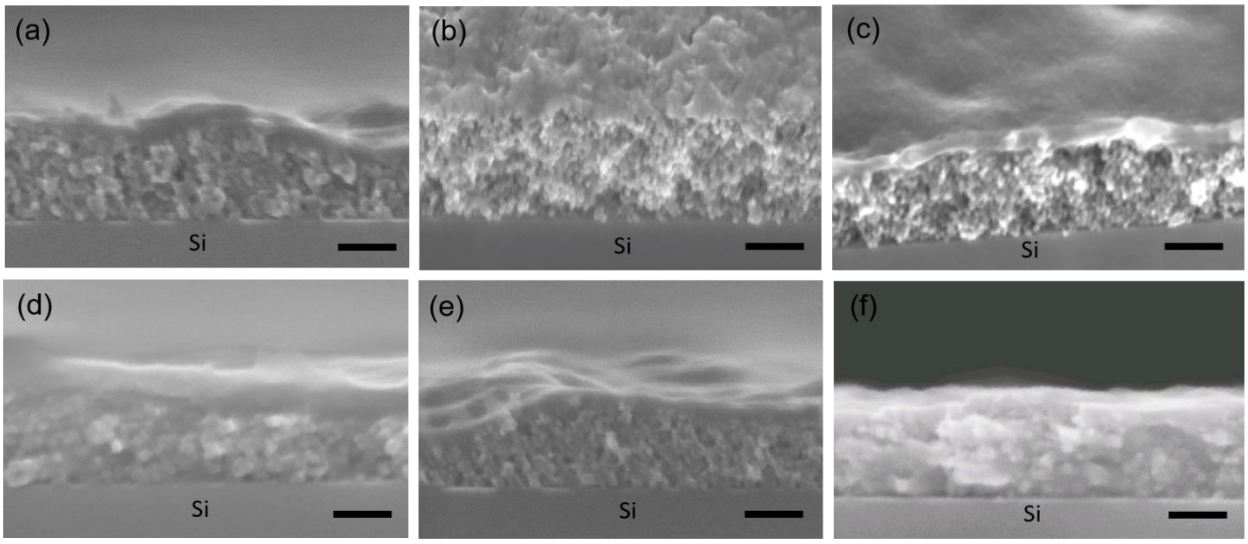

Figure 4.6. Cross section SEM images on P3HT infiltrated mp-TiO_2 film by different infiltration methods. (a) as-cast (no treatment after P3HT spin-coating), (b) solvent-drop, (c) slow drying, (d) solvent vapor, (e) heating at 140 ºC and (f) heating at 230 ºC.

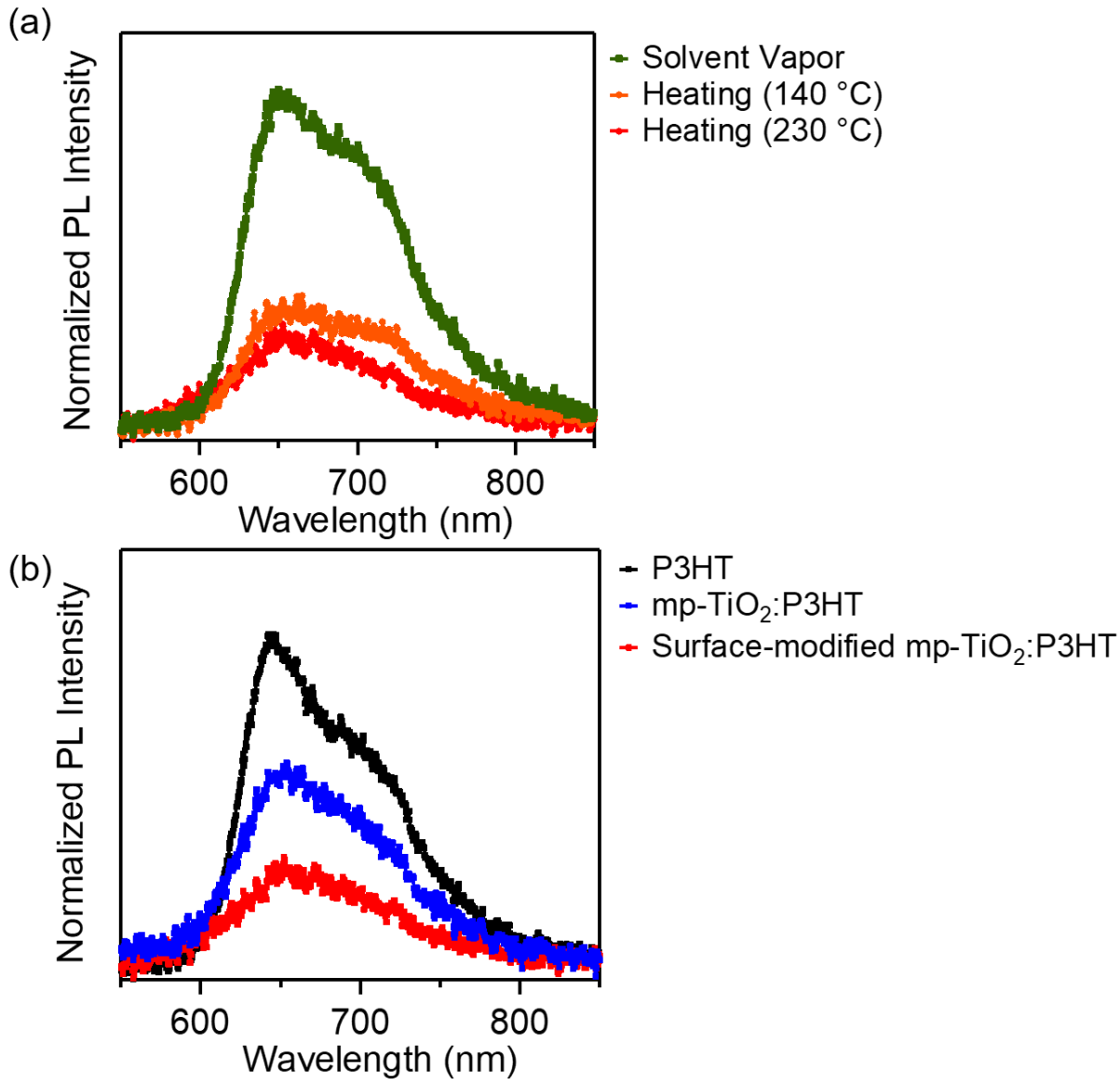

Figure 4.7. (a) Photoluminescence (PL) spectra of Surface-modified mp-TiO_2:P3HT films with different infiltration methods: Solvent-vapor infiltration (green), heating at 140 ºC (orange) and heating at 230 ºC (red). (b) Photoluminescence (PL) spectra of pure P3HT (black), mp-TiO_2:P3HT (blue), and Surface-modified mp-TiO_2:P3HT (red) films. All the PL intensity are normalized by the absorbance at λ_{ex} = 514 nm.

Figure 4.8 and Table 4.1 display the current density-voltage curves and photovoltaic parameters of the devices with mp-TiO_2:P3HT and Surface-modified mp-TiO_2:P3HT, respectively. The increased open-circuit voltage (V_{oc}) of 0.33 V is due to the higher LUMO energy level of PCBA as we discussed earlier. (Figure 4.4 (b)). We observed that the Power Conversion Efficiency (PCE) is slightly increased upon the surface modification from 0.049 % to 0.053%. Such a small improvement in PCE (%) is highly associated with the reduced short-circuit current density (J_{sc}) for Surface-modified mp-TiO_2:P3HT device. We earlier observed the decrease in the pore size due to possible PCBA aggregation after surface modification. (Figure 4.3 (d)) Based on this, we speculate the PCBA aggregation acts as a recombination site. In addition, we noted that both devices performed poorly regardless of the surface modification. It might be related to the undesired overlayer of P3HT, which limits the device efficiency due to increased serial resistance and the low short-circuit current density. The fact that PL of Surface-modified TiO_2:P3HT is not completely quenched, enables us to speculate that exciton generated in P3HT might experience radiative deactivation before reaching the TiO_2 surface.[32]

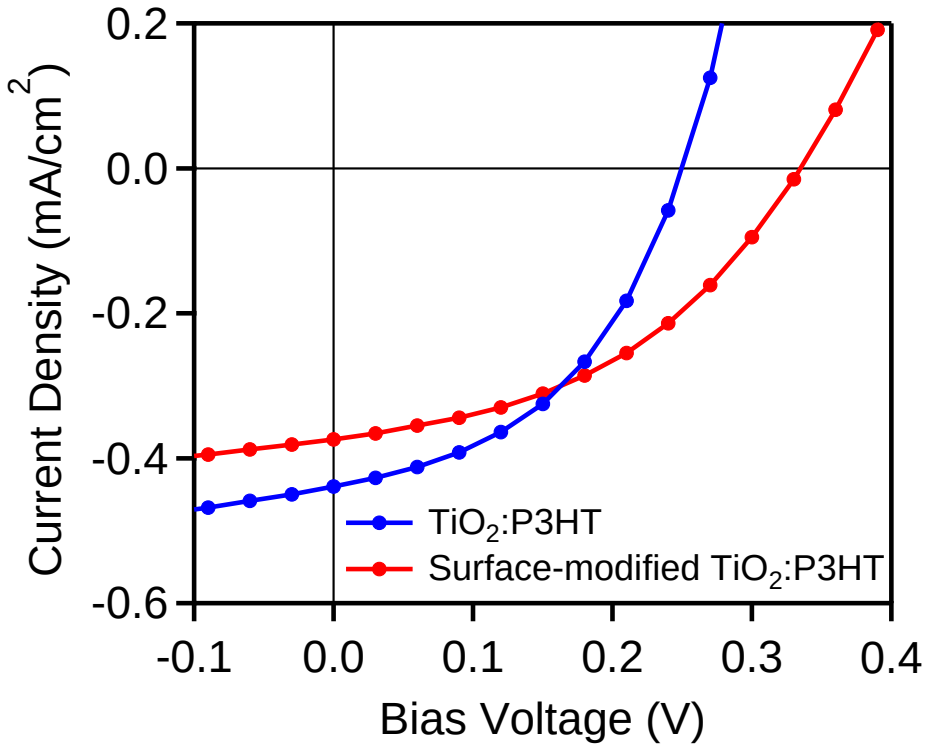

Figure 4.8. *J-V* characteristics of devices from surface-modified mp-TiO_2:P3HT (red) and mp-TiO_2:P3HT (blue). The photovoltaic parameters are shown in Table 4.1.

Table 4.1. Photovoltaic parameters of surface-modified mp-TiO_2:P3HT and mp-TiO_2:P3HT solar cells.

	Surface-modified mp-TiO_2:P3HT	mp-TiO_2:P3HT
OC Voltage (V)	0.33	0.25
Current Density (mA/cm^2)	-0.38	-0.44
Fill Factor (%)	41.6	44.4
Efficiency (%)	0.053	0.049

4.3 Conclusions

Here, we have prepared mesoporous nanocrystal-based TiO_2 thin films for use in hybrid solar cells using the amphiphilic block copolymer, PB-b-PEO. A surface mediator, PCBA, is anchored on the hydrophilic titania surface leading to better compatibility between TiO_2 and P3HT. As confirmed in PL spectra and the SEM images, the most efficient pore filling is achieved when P3HT is infiltrated by heating at 230 ºC. The device shows the increased open-circuit voltage of 0.33 V and power conversion efficiency of 0.053 % with the surface modification by PCBA. Such improvement is explained by the synergetic effect of porous structure, surface modification and efficient pore filling to create a large and intimate interface between electron donor and acceptor. However, there still remain challenges such as the overall low PCE and reduced short-circuit current density upon the surface modification. For improved photovoltaic performance, further investigation is required to optimize the thickness of P3HT overlayer, and control the PCBA aggregation for a lower series resistance and higher shunt resistance.

4.4 Experimental Methods

Materials

$TiCl_4$ (99.0%) and anhydrous benzyl alcohol (99.8%) were purchased from Sigma-Aldrich. Poly(1,4-butadiene)-b-poly(ethylene oxide) (PB-b-PEO) was purchased from Polymer Source Inc. The Polydispersity Index (PDI) is 1.04, and the number average molecular weight (Mn) is PB(4800)-b-PEO(5800). P3HT was purchased from Rieke Metals. Inc. (Sepiolid P200)

Synthesis of Anatase TiO_2 Nanocrystals.

The synthesis of anatase TiO_2 nanocrystals and mesoporous TiO_2 film were previously reported.[20] 0.5 mL of $TiCl_4$ is slowly added to 2 mL of anhydrous EtOH and then combined with 10 mL of anhydrous benzyl alcohol. The solution in the vial is loosely sealed and heated at 80 ℃ for 9 h. To isolate the nanocrystalline particles, 1 mL of the suspension is precipitated in 12 mL of diethyl ether and centrifuged at 5000 rpm. The obtained white powder is then dispersed in 3 mL of EtOH and sonicated for 2 h, yielding a transparent sol.

Synthesis of Mesoporous Nanocrystal-Based TiO_2 Films.

40 mg of PB(4800)-b-PEO(5800) dissolved in 0.5 mL of EtOH is added to 3 mL of the anatase nanoparticle sol (content: 15 mg/mL). Once the solution is homogeneous, 0.2 mL of double distilled H_2O is added right before dip-coating. Thin films are produced via dip-coating at 30% relative humidity. Calcination of the composite to fully remove the polymer template is done using a 2 h ramp up to 600 ℃, followed by a 1 h soak. The thickness of a templated film is only about 150 nm (as-synthesized) due to the relatively low TiO_2 nanoparticle content in the sol.

Synthesis of [6, 6]-phenyl-C61-butyric acid (PCBA).

PCBA is prepared according to the literature procedure[35] and the UV-vis absorption spectrum matched the reported values.

Surface modification of TiO_2 film with PCBA.

TiO_2 film is first kept in a furnace at 150 ℃ to get rid of moisture in the pores. The film is placed in a sealable container wrapped with aluminum foil, and PCBA/pyridine solution (1.6 mg/mL) is added to the film at 60 ℃. The film is soaked overnight, and washed with 1,2-dichlorobenzene and pentane.

P3HT deposition for as-cast.

A P3HT solution in o-dichlorobenzene (20 mg/mL) is spun coated (at 1000 rpm for 120 s unless described separately) onto porous TiO_2 films after soaking in pure solvent to remove air bubbles. Different infiltration methods are carried out for improved pore filling by **1) solvent-drop**: A drop of o-dichlorobenzene is added on to as-cast film, and let the film dried at ambient atmosphere, **2) slow-drying** : P3HT is spun down at 1000 rpm for 20 s. The wet P3HT is slowly dried at ambient atmosphere. **3) solvent-vapor** : As-cast film is kept in a sealed container filled with chlorobenzene at 80℃ for 4 hours. **4) heating at 140 ℃** : As-cast film is heated on a hot plate at 140 ℃ for 20 min. **5) heating 230 ℃** : As-cast film is heated on a hot plate at 230 ℃ for 4 hours.

Device fabrication.

ZnO nanocrystals are synthesized in the solution phase according to the literature method.[33] As prepared ZnO is spun down onto cleaned glass substrates pre-patterned with tin-doped indium oxide (ITO; TFD Inc.). Each active layer, mp-TiO_2:P3HT and surface-modified mp-TiO_2:P3HT, was prepared on top of ZnO layer, which acts as an electron transport layer. 15nm of MoO_3 (hole transport layer) and 60nm of Ag (electrode) were evaporated at a rate < 2 Å /s onto the active layers using a thermal evaporator (Angstrom Engineering). Evaporation pressures were 10^{-7} Torr or less. The active areas of the resulting solar cells were 7.2 mm^2.

Characterizations.

A JEOL JSM-6700F field emission scanning electron microscope (FE-SEM) was used to characterize the microstructure of the films. Ellipsometric porosimetry was performed on a PS-1100 instrument from Semilab using toluene as the adsorbate at room temperature. A UV-visible CCD detector adapted to a grating spectrograph analyzes the signal reflected by the sample. The light source is a 75-W Hamamatsu Xenon lamp and measurements were performed in the spectral range from 1.24–4.5 eV. Data analysis was performed using the associated SEA software.

Photoluminescence (PL) Quenching Experiments.

Photoluminescence was measured using a Coherent Innova argon ion laser (514 nm) as an excitation source. Fluorescence spectra were collected using an Ocean Optics SD 2000 fiberoptic spectrometer, with a linear CCD. For all measurements the slit widths and integrations were held constant, and the sample was positioned at 45 degrees with respect to the excitation axis. The emission spectra were normalized by the absorption at 514 nm.

***J-V* Measurements.**

J-V measurements were performed in an argon atmosphere using a Keithley 2400 source meter. A xenon arc lamp equipped with an AM-1.5 filter was used as the excitation source.

4.5 References

(1) Ohl, R. S. Light-Sensitive Electric Device, U.S. Patent, No.2, 402, 622, 1941.

(2) Li, S.; Chen, C. Polymer–metal-oxide Hybrid Solar Cells. *J. Mater. Chem. A*, **2013**, *1*, 10574–10591.

(3) Spanggaard, H.; Krebs, F. C. A Brief History of the Development of Organic and Polymeric Photovoltaics. *Solar Energy Materials & Solar Cells* **2004**, *83*, 125–146.

(4) Friend, R. H.; Denton, G. J.; Halls, J. J. M.; Harrison, N. T.; Holmes, A. B.; Kohler, A.; Lux, A.; Moratti, S. C.; Pichler, K.; Tessler, N.; Towns, K.; Wittmann, H. F. Electronic Excitations in Luminescent Conjugated Polymers. *Solid State Commun.* **1997**, 102, 249-258.

(5) Shaw, P. E.; Ruseckas, A.; Samuel, I. D. W. Exciton Diffusion Measurements in Poly(3-hexylthiophene). *Adv. Mater*. **2008**, *20*, 3516–3520.

(6) Savenije, T. J.; Warman, J. M.; Goossens, A. Visible Light Sensitisation of Titanium Dioxide Using a Phenylene Vinylene Polymer. *Chem. Phys. Lett*. **1998**, *287*, 148-153.

(7) Arango, A. C.; Johnson, L. R.; Bliznyuk, V. N.; Schlesinger, Z.; Carter, S. A.; Horhold, H. H. Efficient Titanium Oxide/Conjugated Polymer Photovoltaics for Solar Energy Conversion. *Adv. Mater*. **2000**, *12*, 1689-1692.

(8) Shaheen, S. E.; Brabec, C. J.; Sariciftci, N. S.; Padinger, P.; Fromherz, T.; Hummelen, J. C. 2.5% efficient organic plastic solar cells. *Appl. Phys. Lett*. 2001, 78, 841-843.

(9) Padinger, F.; Rittberger, R.S; Sariciftci, N. S. Effects of Postproduction Treatment on Plastic Solar Cells *Adv. Funct. Mater*. **2003**, *13*, 85-88.

(10) Peet, J.; Kim, J. Y.; Coates, N. E.; Ma, W. L.; Moses, D.; Heeger, A. J.; Bazan, G. C. Efficiency Enhancement in Low-Bandgap Polymer Solar Cells by Processing with Alkane Dithiols. *Nat. Mater*. **2007**, *6*, 497-500.

(11) Liao, W.-P.; Hsu, S.-C.; Lin, Wu, W.-H. Hierarchical TiO_2 Nanostructured Array/P3HT Hybrid Solar Cells with Interfacial Modification. *J. Phys. Chem. C* **2012**, *116*, 15938−15945.

(12) Scharber, M. C.; Koppe, M.; Gao, J.; Cordella, F.; Loi, M. A.; Denk, P.; Morana, M.; Egelhaaf, H.-J.; Forberich, K.; Dennler, G.; Gaudiana, R.; Waller, D.; Zhu, Z.; Shi, X.; Brabec, C. J. Influence of the Bridging Atom on the Performance of a Low-Bandgap Bulk Heterojunction Solar Cell. *Adv. Mater*. **2010**, *22*, 367-370.

(13) Fan, X.; Zhang, M.; Wang, X.; Yang, F.; Meng, X. Recent Progress in Organic–Inorganic Hybrid Solar Cells. *J. Mater. Chem. A*, **2013**, *1*, 8694–8709.

(14) Sanchez, C.; Julia´n, B.; Belleville, P.; Popall, M. Applications of Hybrid Organic–Inorganic Nanocomposites. *J. Mater. Chem.* **2005**, *15*, 3559–3592.

(15) Mayer, A. C.; Scully, S. R.; Hardin, B. E.; Rowell, M. W.; McGehee, M. D. Polymer-Based Solar Cells. *Mater. Today* **2007**, *10*, 28−33.

(16) Tepavcevic, S.; Darling, S. B.; Dimitrijevic, N. M.; Rajh, T.; Sibener, S. J. Improved Hybrid Solar Cells via in situ UV Polymerization. *Small* **2009**, *5*, 1776−1783.

(17) Weickert, J.; Dunbar, R. B.; Hesse, H. C.; Wiedemann, W.; Schmidt-Mende, L.; Nanostructured Organic and Hybrid Solar Cells. *Adv. Mater*. **2011**, *23*, 1810−1828.

(18) Coakley, K. M.; McGehee, M. D. Photovoltaic cells made from conjugated polymers infiltrated into mesoporous titania. *Applied Physics Letters*, **2003**, *83*, 3380-3382.

(19) Coakley, K. M.; Liu, Y.; McGehee, M. D.; Frindell, K. L.; Stucky, G. D. Infiltrating Semiconducting Polymers into Self-Assembled Mesoporous Titania Films for Photovoltaic Applications. *Adv. Funct. Mater*. **2003**, *13*, 301-306.

(20) Brezesinski, T.; Wang, J.; Polleux, J.; Dunn, B.; Tolbert, S. H Templated Nanocrystal-Based Porous TiO_2 Films for Next-Generation Electrochemical Capacitors. *J. Am. Chem. Soc*. **2009**, *131*, 1802–1809.

(21) Brinker, C. J.; Lu, Y. F.; Sellinger, A.; Fan, H. Evaporation-Induced Self-Assembly: Nanostructures Made Easy. *Adv. Mater*. **1999**, *11*, 579–585.

(22) Zhao, D. Y.; Feng, J. L.; Huo, Q. S.; Melosh, N.; Fredrickson, G. H.; Chmelka, B. F.; Stucky, G. D. Triblock Copolymer Syntheses of Mesoporous Silica with Periodic 50 to 300 Angstrom Pores. *Science* **1998**, *279*, 548–552.

(23) Goltner, C. G.; Antonietti, M. Mesoporous Materials by Templating of Liquid Crystalline Phases. *Adv. Mater*. **1997**, *9*, 431–436.

(24) Reeja-Jayan, B.; Adachi, T.; Ono, R. J.; Vanden Bout, D. A.; Bielawskib, C. W.; Manthiram, A. Effect of Interfacial Dipoles on Charge Traps in Organic–Inorganic Hybrid Solar Cells. *J. Mater. Chem. A*. **2013**, *1*, 3258-3262.

(25) Casalegno, M.; Zanardi, S.; Frigerio, F.; Po, R.; Carbonera, C.; Marra, G.; Nicolini, T.; Raos, G.; Meille, S. V. Solvent-Free Phenyl-C61-Butyric Acid Methyl Ester (PCBM) from Clathrates: Insights for Organic Photovoltaics from Crystal Structures and Molecular Dynamics. *Chem. Commun*. **2013**, *49*, 4525-4527.

(26) Li, Z.; Zhang, X.; Lu, G. Dipole-Assisted Charge Separation in Organic−Inorganic Hybrid Photovoltaic Heterojunctions: Insight from First-Principles Simulations. *J. Phys. Chem. C* **2012**, *116*, 9845−9851.

(27) Cho, E.-C.; Ciou, J.-H.; Zheng, J.-H.; Pan, J.; Hsiao, Y.-S.; Lee, K.-C.; Huang, J.-H. Fullerene C70 Decorated TiO_2 Nanowires for Visible-Light-Responsive Photocatalyst. *Applied Surface Science* **2015**, *355*, 536–546.

(28) Feron, K.; Cave, J. M.; Thameel, M. N.; O'Sullivan, C.; Kroon, R.; Andersson, M. R.; Zhou, X.; Fell, C. J.; Belcher, W. J.; Walker, A. B.; Dastoor, P. C. Utilizing Energy Transfer in Binary and Ternary Bulk Heterojunction Organic Solar Cells. *ACS Appl. Mater. Interfaces* **2016**, *8*, 20928−20937.

(29) Schmidt-Mende, L.; Grätzel, M. TiO_2 Pore-Filling and Its Effect on the Efficiency of Solid-State Dye-Sensitized Solar Cells. *Thin Solid Films* **2006**, *500*, 296-301.

(30) Rawolle, M.; Sarkar, K.; Niedermeier, M. A.; Schindler, M.; Lellig, P.; Gutmann, J.; Moulin, J.-F.; Haese-Seiller, M.; Wochnik, A. S.; Scheu, C.; Müller-Buschbaum. P. Infiltration of Polymer Hole-Conductor into Mesoporous Titania Structures for Solid-State Dye-Sensitized Solar Cells. *ACS Appl. Mater. Interfaces* **2013**, *5*, 719-729.

(31) Ngo, T. T.; Nguyen, D. N.; Nguyen, V. T. Glass Transition of PCBM, P3HT and Their Blends in Quenched State. *Adv. Nat. Sci.: Nanosci. Nanotechnol*. **2012**, *3*, 045001.

(32) Wang, Y.; Ohkita, H.; Benten, H.; Ito, S. Highly efficient exciton harvesting and charge transport in ternary blend solar cells based on wide- and low-bandgap polymers. *Phys. Chem. Chem. Phys*. **2015**, *17*, 27217-27224.

(33) Sun, B.; Sirringhaus, H. Solution-Processed Zinc Oxide Field-Effect Transistors Based on Self-Assembly of Colloidal Nanorods. *Nano Lett.*, **2005**, *5*, 2408-2413.

(34) Wang, J.; Qin, M.; Tao, H.; Ke, W.; Chen, Z.; Wan, J.; Qin, P.; Xiong, L.; Lei, H.; Yu, H.; Fang, G. Performance Enhancement of Perovskite Solar Cells with Mg-Doped TiO_2 Compact Film as The Hole-Blocking Layer. *Appl. Phys. Lett*. **2015**, *106*,121104.

(35) Hummelen, J. C.; Knight, B. W.; LePeq, F.; Wudl, F.; Yao, J.; Wilkins, C. L. Prepration and Characterizaiton of Fulleroid and Methanofullerene Derivatives. *J. Org. Chem*. **1995**, *60*, 532-538.

Chapter 5. 3D Interconnected Mesoporous Tantalum Nitride Film as a Photoanode for Efficient Solar Water Splitting

5.1 Introduction

Recently, hydrogen has gained tremendous attention as a promising clean fuel in replacement of fossil fuel. The majority of the commercial hydrogen, however, is produced by hydrocarbon reformation. Since the reaction is accompanied by the formation of carbon monoxide and dioxide, the hydrogen is produced via an unclean process.[1] To avoid greenhouse gas emission, water electrolysis is one of the alternatives to produce hydrogen cleanly. However, hydrogen generation from water can only produce 4% of the entire hydrogen production up to present, because the current technology for water splitting requires four times more energy than other hydrogen sources.[2-3]

Since the photocatalytic activity of TiO_2 has been reported by Fujishima and Honda in 1972,[4] metal oxide semiconductors have been studied for photoelectrochemical(PEC) water splitting. Utilizing both external bias and solar energy can make water oxidation/reduction more efficient than photocatalytic water splitting, which is driven by solar energy only. Based on thermodynamic, a minimum bandgap of 1.23 eV is required for photocatalysts to split water into H_2 and O_2. When the photocatalyst absorbs photon energy, which is larger than its bandgap, electrons from the conduction band is excited to the valence band. After the photoexcitation, the charge carriers (electron-hole pairs) are then generated. The charge carriers are separated and transferred to the surface active sites where they can participate in water redox reactions as described in equation (1-3).

$$2\,H_2O \longrightarrow 4\,H^+ + 4\,e^- + O_2 \quad \text{Water oxidation} \quad (1)$$

$$4\,H^+ + 4\,e^- \longrightarrow 2\,H_2 \quad \text{Water Reduction} \quad (2)$$

$$2\,H_2O \longrightarrow 2\,H_2 + O_2 \quad \text{Water Splitting} \quad (3)$$

The bandgap of a photocatalyst is critical to achieve a high performance in PEC water splitting. Li *et al* reported that the theoretical maximum solar-to-hydrogen (STH) efficiency and the photocurrent density can be increased to 17.8% and 14.5 mA/cm^2 with the bandgap of 2.0 eV.[5] Thus, it is inevitable to utilize a highly visible-light active material because visible region accounts for more than 50% of the total solar energy.[6] Non-oxide semiconductors have narrower bandgaps in comparison to metal-oxide semiconductors. In the case of nitride and sulfide, since the valence band consists of N 2p or S 2p orbitals in nitride or sulfide, their lower electronegativity causes the valence band to shift negatively.[7]

Water oxidation reaction is considered as the biggest challenge in the overall water splitting process because it is a four electrons and a four protons process (equation (1)). Since the activation energy of water oxidation reaction is dominant in the activation energy of overall water splitting, it is necessary to development an efficient photoanode material or an oxygen evolution reaction photocatalyst to build up high performing solar water splitting system.[23] Tantalum nitride (Ta_3N_5) is one of the promising candidates for a photoanode in PEC water splitting due to its high visible light activity.[8-12] The possible theoretical maximum STH efficiency for Ta_3N_5 is estimated to be 15.9%, which is attributed to its narrow band gap (~2.1 eV).[13,14] Beside the bandgap, its conduction/valence band positions are appropriate to drive overall water splitting. Despite of its great potential, challenges such as unfavorable oxidative decomposition with accumulated holes,

poor photocurrent stability and fast charge recombination still need to be further improved in order to realize its full potential.[15,16]

Regarding the aforementioned issues, many efforts have been made to develop nanostructured Ta_3N_5 in the form of nanorods, nanoparticles, nanotubes, micro/nanopores.[17-19] The introduction of nanostructuring is known to improve light absorption, reduce charge transportation pathway, and increase reaction sites. Though many studies have been done on powder forms of Ta_3N_5, only a few studies have been reported for Ta_3N_5 films. The reactive ballistic deposition (RBD) or anodization are utilized to synthesize nanostructured films .[15,18,20] These methods are, however, very limited due to difficulty to precisely control the nanoscale morphology, elevated cost, and violent chemical reactions with the concentrated HF.[21,22] To further improve the efficiency of these semiconducting photocatalyst, most system requires the use of cocatalysts that suppress charge carrier recombination and increase stability to overcome slow kinetic and self-decomposition.[23] Noble metals such as Pt, Rh, Ir, Au and their oxides (RuO_2 and IrO_2) have been commonly used to enhance H_2/O_2 evolution activity.[24] Anyhow, for large-scale production, cost-effective cocatalysts need to be developed using earth-abundant element such as copper, nickel, cobalt. Recently, cobalt-based cocatalysts (i.e. CoO_x, Co-Pi, Co_3O_4, $Co(OH)_x$)[20,25-27] have been reported to increase the stability of photoanode by acting as hole scavengers. With the presence of those cocatalysts, increased photocurrent and reduced onset potential are observed due to improved charge carrier lifetime.[28,29]

In this work, 3D interconnected mesoporous Ta_3N_5 thin film is fabricated in solution phase via a simple two steps synthesis: Evaporation-Induced Self-Assembly (EISA) follow by nitridation. Crystalline sol-gel Ta_2O_5 film is deposited directly on a conductive substrate. A highly-ordered mesoporous structure is obtained using an amphiphilic diblock copolymer as the pore template.

Upon nitridation using ammonia, as-prepared Ta_2O_5 is converted to Ta_3N_5 with excellent pore periodicity. To investigate the nanostructuring effect on the water splitting performance, we tested mesoporousTa_3N_5 (mp-Ta_3N_5) and dense Ta_3N_5 (d-Ta_3N_5) films as photoanodes in PEC measurements. We further investigated the correlation between the morphology and photocatalytic activity by studying the optimal film thickness and modifying the surface with a cocatalyst, $Co(OH)_x$. The most improved photocurrent density is observed in $Co(OH)_x$ modified mp-Ta_3N_5 film, which supports the synergetic effect of nanostructuring and surface modification by the cocatalyst.

5.2 Results and Discussion

The synthesis of mesoporous sol-gel Ta_2O_5 via EISA (Evaporation-induced Self-Assembly) has been reported previously.[30] We used the conductive substrate, Ti(3nm)/Pt(150nm)/Ti(3nm)/SiO2(150nm)/Si to provide electron transport pathway toward the counter electrode in PEC measurement.[31] The amphiphilic diblock copolymer, Poly(1,4-butadiene)-*b*-poly(ethylene oxide), forms micelles when tantalum precursor sol is dried after dip-coating. The film was slowly heated up to 180 ºC in multiple steps then aged for 12 hours, which improves the robustness of the porous structure without cracks. By heating it up to 750 ºC, crystalline sol-gel Ta_2O_5 film was prepared. Figure 5.1 (a) represents GIWAXS (Grazing Incident Wide Angle X-ray Scattering) analysis on Ta_2O_5 film. The distinctive crystalline peaks appear at Q = 1.62, 1.99, 2.57 $Å^{-1}$ (2θ = 22.9°, 28.3°, and 36.7°) corresponding to (0 0 1), (1 11 0) and (1 11 1). Based on the XRD pattern, as-synthesized Ta_2O_5 film is confirmed to be in orthorhombic β-Ta_2O_5 phase (JCPDS no. 00-025-0922). The UV-vis absorption spectrum also verifies a wide bandgap (4.0 eV) of Ta_2O_5 from the absorption edge near 310 nm. (Figure 5.2, blue) This is comparable to the reported value, 3.9 eV from electrochemical and UPS measurement.[7]

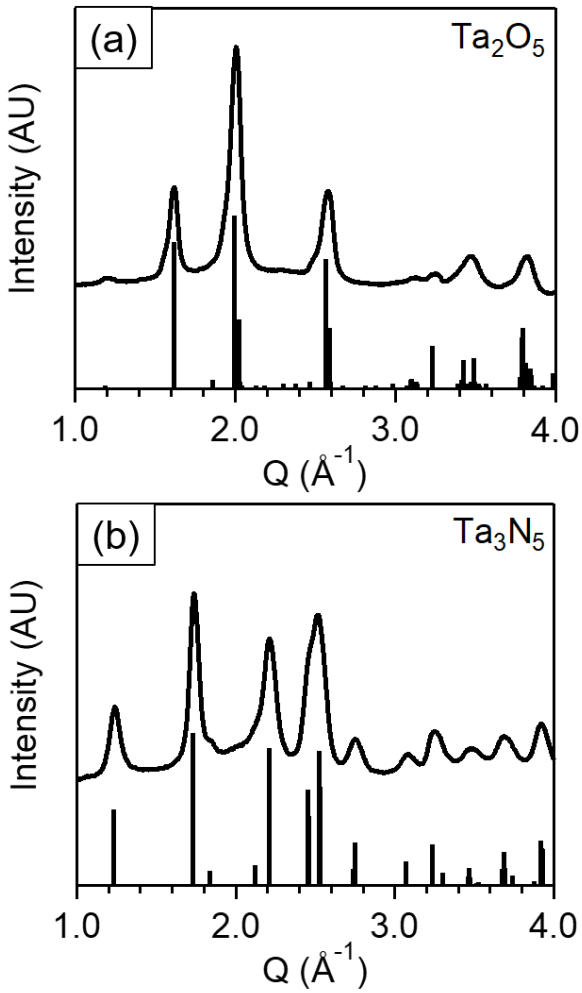

Figure 5.1 (a) XRD patterns obtained by integrating two-dimensional (2D) WAXS patterns of mp-Ta_2O_5 film. The stick pattern corresponds to orthogonal Ta_2O_5(JCPDS No.00-025-0922). (b) XRD patterns obtained by integrating 2D WAXS patterns of mp-Ta_3N_5 film after nitridation. The stick pattern corresponds to orthogonal Ta_3N_5 (JCPDS No. 01-079-1533).

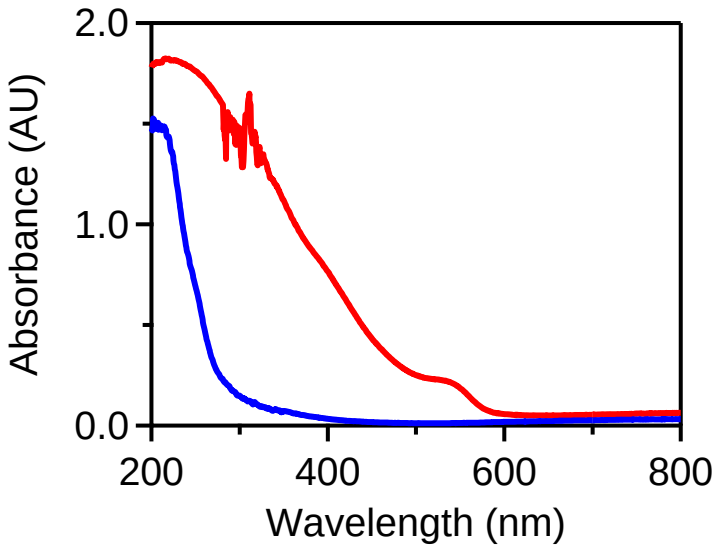

Figure 5.2 UV-visible absorption spectra of mp-Ta_2O_5 (blue) and mp-Ta_3N_5 (red) films deposited on fused SiO_2. Blank fused SiO_2 absorption was subtracted from each sample spectra.

For the morphology characterization, we performed scanning emission microscope (SEM) on as-synthesized Ta_2O_5 film. The top view SEM images show highly-ordered open pores and the pore size is approximately 10-20 nm in diameter. (Figure 5.3 (a)) To investigate the pore periodicity in a long range, GISAXS (Grazing Incident Small Angle X-ray Scattering) was performed. A pair of the long arc appears at $Q_{xy} = 0.18$ nm^{-1} when $Q_z = 0$ indicating the excellent periodicity along the xy plane of the substrate. (Figure 5.3 (c)) The pore-to-pore repeat distance is around 35 nm, which corresponds to the top-view SEM image shown in Figure 5.3 (a). To get further insight on the nature of porosity, the sample was analyzed using toluene vapor from ellipsoemetric porosimeter. As shown in Figure 5.4 (a), Ta_2O_5 film exhibits 34% of the porosity with the distinctive hysteresis loop, which is indicative of mesopores.[32] The pore radius distribution is obtained from the isotherm of adsorption/desorption using Kelvin equation,[33] resulting in 14 and 7 nm in pore and neck diameter, respectively. (Figure 5.4 (c)) This is also in agreement with the estimated pore diameter shown the SEM image (Figure 5.3 (a)).

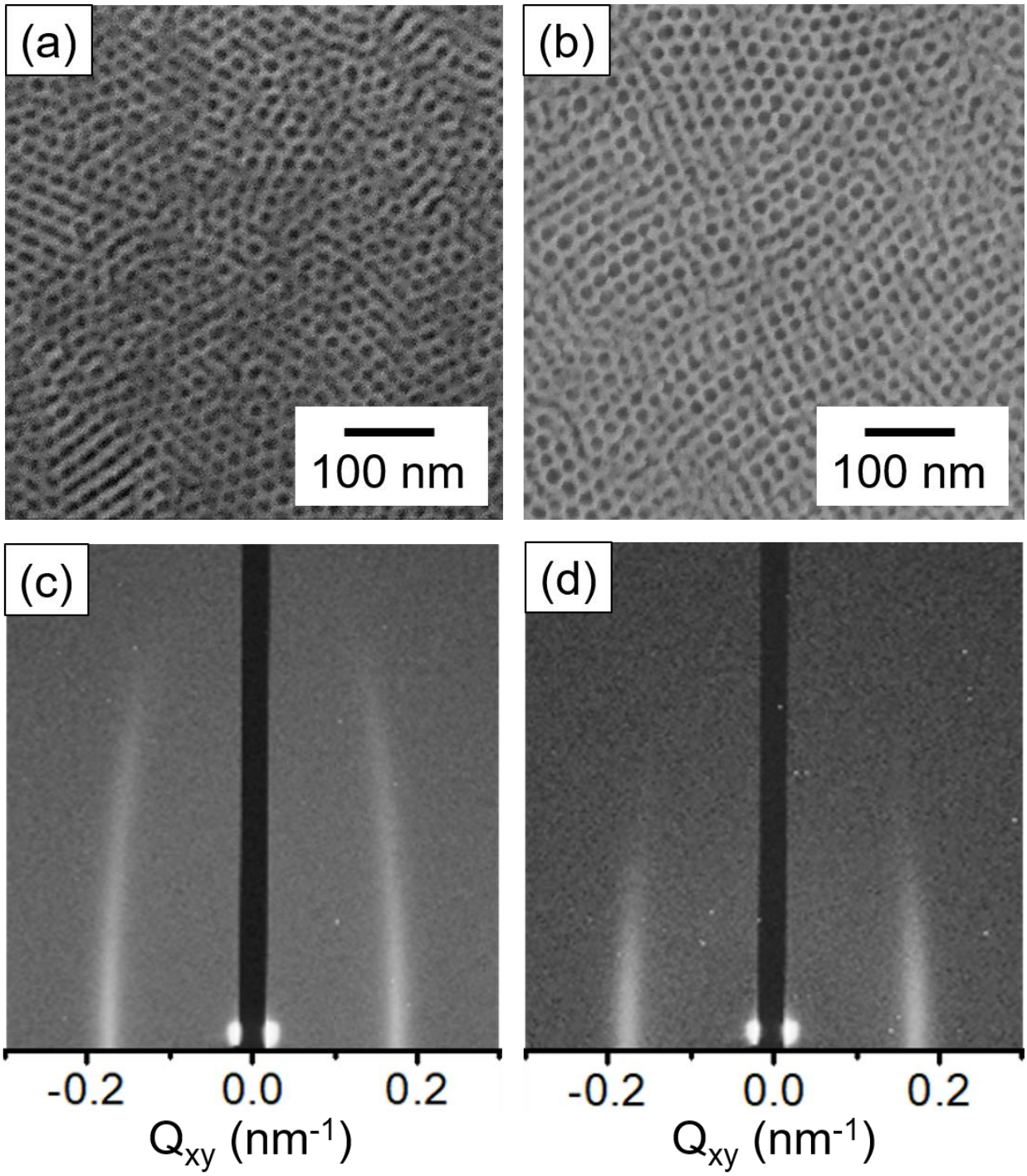

Figure 5.3 Top-view SEM of (a) mp-Ta_2O_5 film and (b) mp-Ta_3N_5 film. GISAXS pattern of (c) mp-Ta_2O_5 film and (d) mp-Ta_3N_5 film. Excellent retention of the ordered mesoporous structure is observed after nitridation.

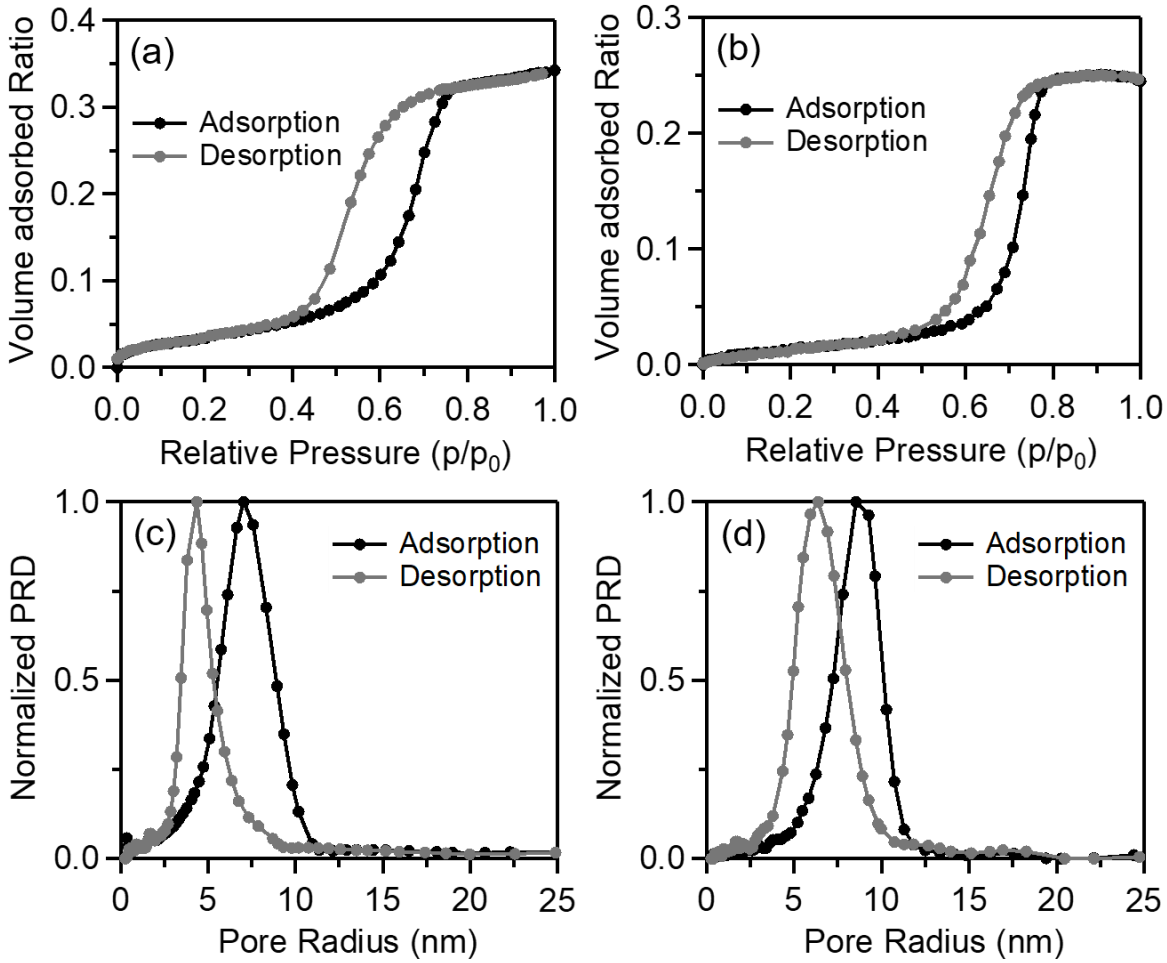

Figure 5.4 Characterization of porous structure using ellipsometric porosimetry. Toluene adsorption-desorption isotherms and pore size distributions are presented for mp-Ta_2O_5 thin film in (a) and (c), and for mp-Ta_3N_5 films in (b) and (d), respectively.

After a thorough characterization of mesoporous-Ta_2O_5 (mp-Ta_2O_5) thin film, the oxide film is converted to tantalum nitride, Ta_3N_5, by flowing vaporized liquid ammonia at 850 ºC. GIWAXS pattern proves that Ta_2O_5 has been successfully converted to Ta_3N_5 after nitridation (Figure 5.1 (b)). The distinctive peaks at Q = 1.22, 1.72, 2.2 and 2.5 $Å^{-1}$ clearly match the reference pattern (JCPDS no. 01-079-1533), indicating orthorhombic Ta_3N_5. The conversion from oxide to nitride causes the bandgap to decrease due to the incorporation of nitrogen atom into the oxide lattice.[13] UV-vis spectrum in Figure 5.2 (red) shows the shifted absorption edge from 310nm to 610 nm, which corresponds to the 2,1 eV bandgap of Ta_3N_5.

Figure 5.3 (b) shows the top-view SEM image of Ta_3N_5 film after nitridation. We noted that the overall porous structure from mp-Ta_2O_5 is still retained without severe grain growth or cracks. It is interesting that the pore periodicity of mp-Ta_2O_5 is also preserved in Ta_3N_5 film showing the scattering peak near Q = 0.18 nm^{-1} in GISAXS pattern. (Figure 5.3 (d)). In combination with the SEM image, it strongly proves a highly ordered mp-Ta_3N_5 with excellent retention. Ellipsometric porosimetry is performed on mp-Ta_3N_5 for the porosity and pore size analysis. (Figure 5.4 (b) and (d)) The porosity is slightly reduced to 25% for mp-Ta_3N_5 with an increase in the pore and neck diameter 17 nm and 12 nm, respectively. The heat treatment required for nitridation might cause some collapse on the porous structure resulting in the slight reduction of porosity. In addition, higher density of Ta_3N_5 with respect to Ta_2O_5 may cause the pore wall shrinkage upon the conversion. Despite the slight difference from mp-Ta_2O_5, this synthetic route is an easy and simple way to fabricate highly ordered porous Ta_3N_5 film.

We next examined the PEC performance of the Ta_3N_5 film as a photoanode in 0.1 M aqueous Na_2SO_4 (pH = 6) electrolyte using chopped light from AM 1.5G solar simulator at 100 mW/cm^2.

Since the film is directly deposited on the conductive substrate, it eliminates the additional step for electrode fabrication, which is normally required for photocatalyst synthesized in powder form. The applied bias is cathodically swept to avoid an undesired oxidation associated with the cocatalyst, Co(OH).[34,35] From the PEC measurement, we aimed to study 1) optimal film thickness, 2) nanostructuring effect arisen from the porous structure, and 3) surface modification effect by the cocatalyst, $Co(OH)_x$. The generated charge carriers need to be separated and transported promptly before unfavorable charge recombinations occur. If the photoelectrode film is too thin, the light absorption is insufficient in a given photon energy, resulting in limited number of photogenerated charge carriers. If the film is too thick, the generated charge carriers encounter serious charge recombinations because the exciton diffusion length is very short (10-20 nm).[25] Only with an optimal thickness, light absorption can be maximized and charge carriers can participate the water splitting reaction successfully. To study the effect of the previously mentioned factors on efficiency, we prepared both mesoporous and dense films with different thickness by controlling the number of dip-coating. The surface modification with the cocatalyst is intentionally excluded from this measurement to only focus on the nanostructuring effect. Figure 5.5 (a) and (b) shows photocurrent density-potential curves of dense-Ta_3N_5(d-Ta_3N_5) and porous Ta_3N_5 (mp-Ta_3N_5) films, respectively with 140 nm in thickness. The photocurrent density of 0.012 mA/cm^2 is measured at 1.23 V_{RHE} for mp-Ta_3N_5, which is 3 times higher than that of d-Ta_3N_5. This result clearly supports nanostructuring effect in that porous structure provides a large surface area between Ta_3N_5 electrode and the electrolyte interface, promoting facile hole transportation, in particular.[36] In addition, the porous structure may decrease light loss caused by reflection and scattering on smooth surfaces.[37, 38]

We noted that 140 nm film produces the photocurrent density 4 times higher than 70 nm film in the case of mp-Ta_3N_5. (Figure 5.5 (b) and (d)). 140 nm film exhibits a much higher optical density (green line) in Figure 5.6, which proves enhanced photon absorption as the film thickness increases. Interestingly, for d-Ta_3N_5, the 70 nm film has a slightly higher photocurrent density. (Figure 5.5 (a) and (c)). Though 70 nm film absorbs less photon energy than 140 nm film, the charge carriers need to travel only a smaller distance in continuous thin film to reach the reaction sites resulting in a facile chare transportation

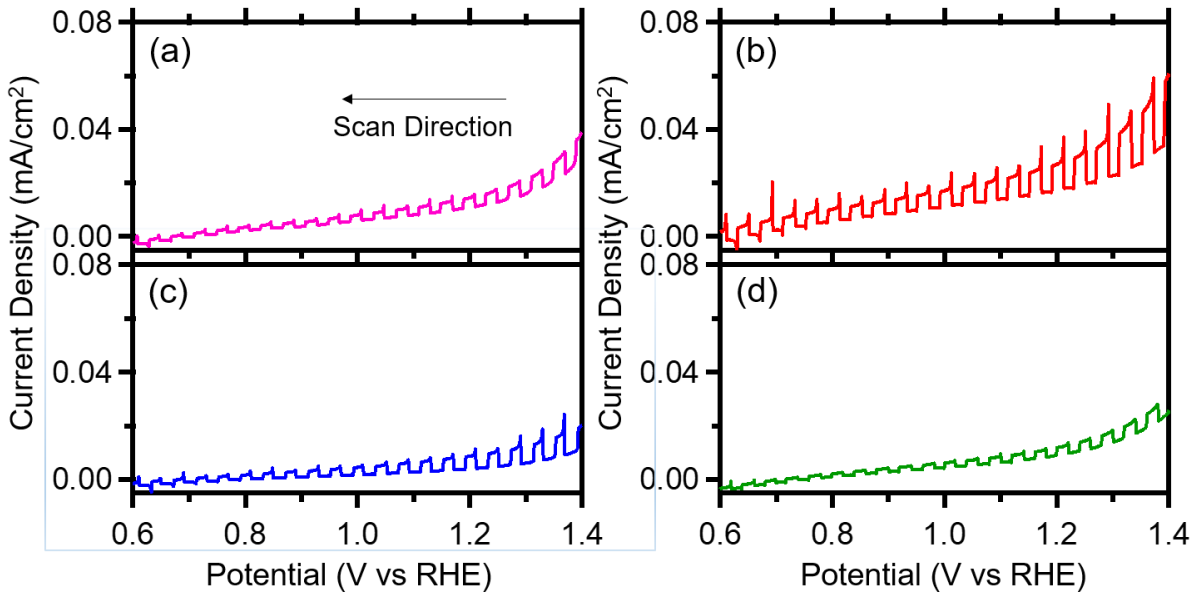

Figure 5.5 Chopped light PEC performance of d-Ta_3N_5 in (a), (c), and mp-Ta_3N_5 (b), (d) in 0.1 M Na_2SO_4 (pH=6) electrolyte using AM 1.5G solar simulator at 100 mW/cm^2. The film thickness obtained from ellipsometry are 140 nm for (a) and (b), 70 nm for (c) and (d).

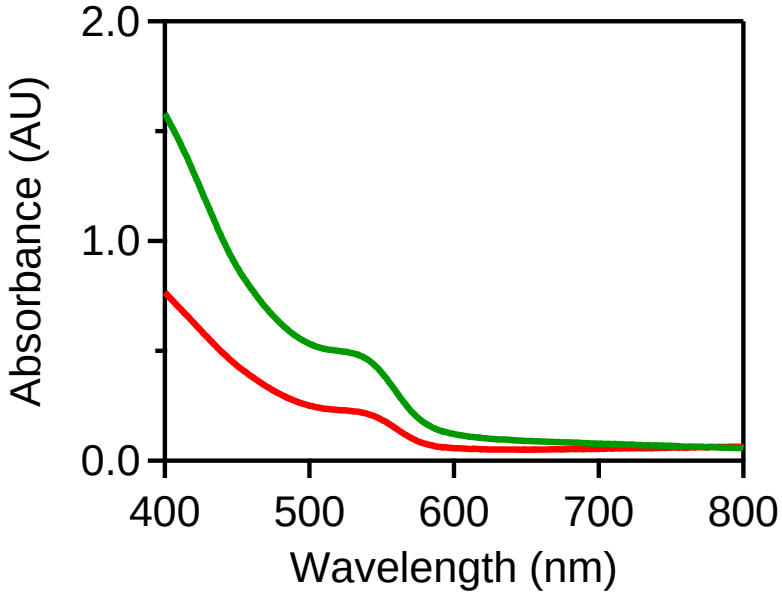

Figure 5.6 Visible light absorption on mp-Ta_3N_5 film with thickness of 140 nm (Green) and 70 nm (red).

Although 140nm mp-Ta_3N_5 film (Figure 5.5 (b)) produced the highest photocurrent, the general PEC performance is still very poor. It is highly associated with bad photocurrent stability for nitride semiconductors due to an undesired hole oxidation reaction.[11,13] The surface modification with cocatalysts can be an avenue to increase the photocatalyst stability. In particular, a number of cobalt-based cocatalysts have been received much attention due to their excellent performance and low cost. Liao *et al* reported that the photocurrent density and stability are much improved for $Co(OH)_x$ modified Ta_3N_5 electrode with respect to bare Ta_3N_5 electrode.[16]

We examined PEC performance of $Co(OH)_x$ modified d-Ta_3N_5 and mp-Ta_3N_5 in Figure 5.7 (a) and (b), respectively. $Co(OH)_x$ is deposited onto 140 nm d- and mp-Ta_3N_5 films using a successive ionic layer adsorption.[17] Upon the surface modification of $Co(OH)_x$, we observed an improvement in photocurrent density for both d-Ta_3N_5 (0.020 mA/cm^2) and mp-Ta_3N_5 (0.050 mA/cm^2) at V_{RHE} = 1.23. These values are 5 times higher than those of non-modified d- and mp-Ta_3N_5 films, respectively. Moreover, with the presence of $Co(OH)_x$, higher photocurrent density is also observed in mp-Ta_3N_5, which indicates the importance of nanostructuring effect in order to achieve a high performing photoelectrode.

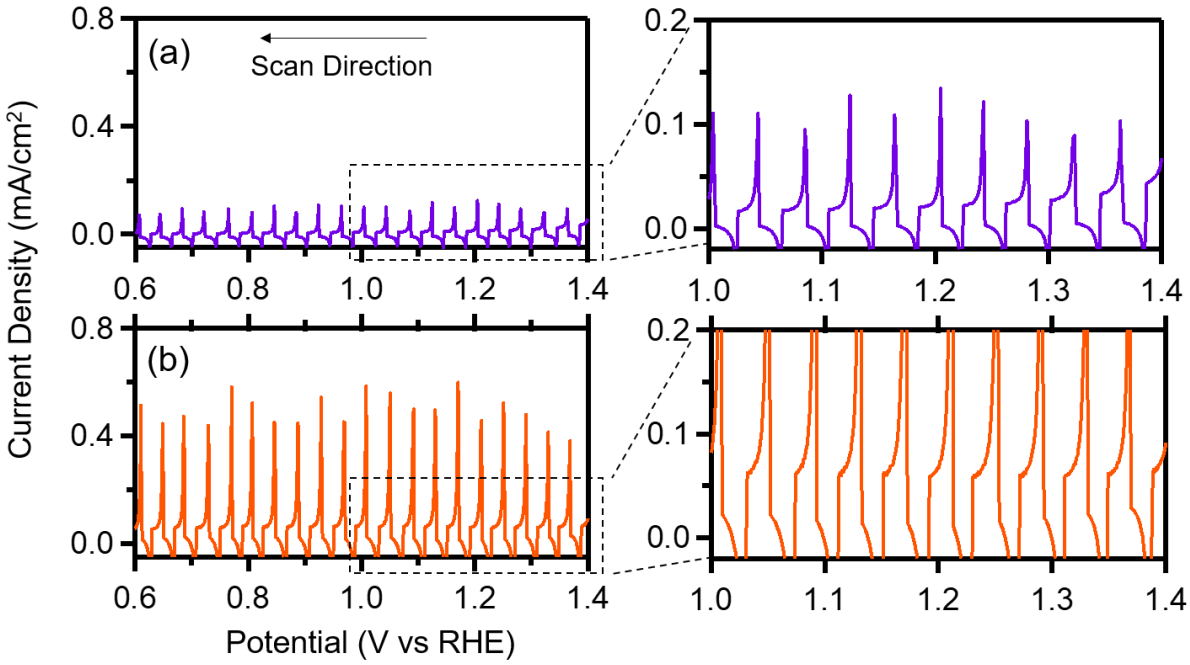

Figure 5.7 Chopped light PEC performance of $Co(OH)_x$ modified d-Ta_3N_5 (a) and mp-Ta_3N_5 (b) using 0.1 M NA_2SO_4 electrolyte (pH=6) using AM 1.5G solar simulator at 100 mW/cm^2. Both dense and porous films are 140 nm in thickness. The voltage is swept cathodically to avoid of unfavorable oxidations associated with $Co(OH)_x$.

The *J-V* curves in Figure 5.7 show a large initial spike followed by an exponential decrease in photocurrent density. The capacitance characteristic may cause such a high initial spike, and the reduced photocurrent density may be attributed to poor photocurrent stability.[17] Since $Co(OH)_x$ colloids are expected to form a protection layer over Ta_3N_5 film, we investigated the vertical distribution of $Co(OH)_x$ across mp-Ta_3N_5 film. XPS etching analysis shows the atomic ratio of Co relative to Ta in Figure 5.8 (a). The film is etched with the argon beam before and after the PEC measurement along the vertical direction to the film. Before the PEC test, 58% of cobalt was detected from the top surface (etch number '0'). At every etching cycle, the Co atomic ratio drastically decreases, and only 26% of Co exists after the fifth etching. After the PEC measurement, all the Co atomic ratio reduced about 30-45 % with respect to each ratio obtained before the PEC measurement. Since the porous films are exposed to the electrolyte in a larger area, homogenous $Co(OH)_x$ deposition is significant in order to create an even protection layer over the entire porous architecture. This is in agreement with the weaker initial spikes appeared in $Co(OH)_x$ modified d-Ta_3N_5 in Figure 5.7 (a) because only the top surface is in contact with electrolyte. The XPS analysis tells us there is more room for improvement on our cocatalyst deposition method to achieve even $Co(OH)_x$ distribution across the entire film. Another interesting result is that the porous architecture of mp-Ta_3N_5 film remains almost identical even after the PEC measurement as shown in Figure 5.8 (b). There is no sign of collapse or disorder on the film surface, which indicates the enhanced robustness of photoelectrode. It shows the potential of our 3D interconnected mp-Ta_3N_5 films as a reusable photoelectrode.

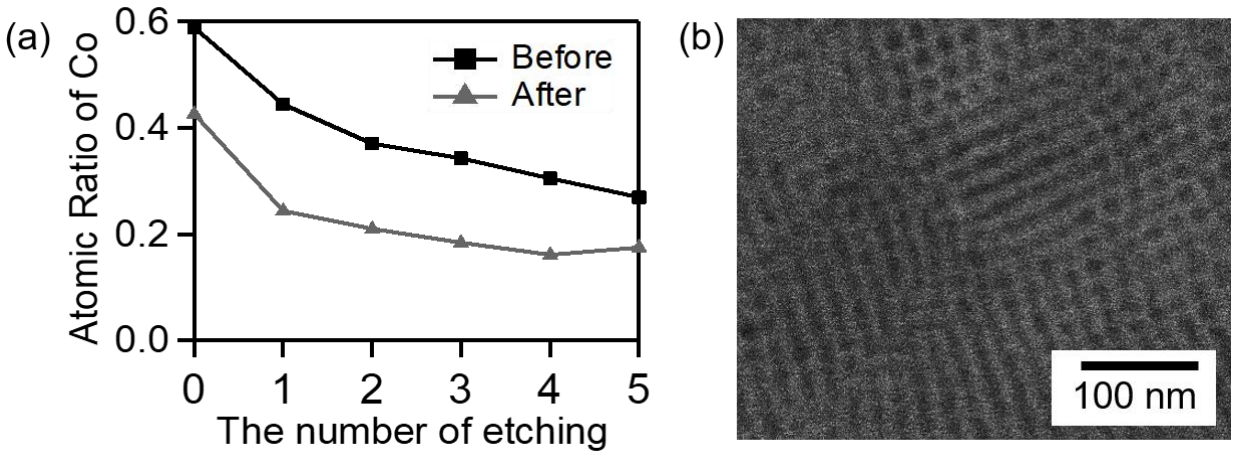

Figure 5.8 (a) The atomic ratio of cobalt on mp-Ta_3N_5 upon XPS etching in vertical direction to the films. The black line with square indicates the cobalt atomic ratio before the PEC measurement, and the grey line with triangle represents the cobalt atomic ratio after the PEC measurement. The sample is being etched for 60s each cycle using the argon beam (4 keV). (b) The top-view SEM image on mp-Ta_3N_5 film after the PEC measurement. The open porous structure is still maintained.

5.3 Conclusions

In summary, we have demonstrated the potential of the 3D interconnected mesoporous Ta_3N_5 (mp-Ta_3N_5) film as a photoanode for water splitting through a simple synthesis, EISA followed by nitridation. The mp-Ta_3N_5 film retained the highly ordered porous structure from mp-Ta_2O_5 film without cracks or severe grain growth. In the PEC performance, nanostructuring effect is clearly observed for mp-Ta_3N_5 and $Co(OH)_x$ modified mp-Ta_3N_5 photoanode. Without $Co(OH)_x$, mp-Ta_3N_5 generates the photocurrent density of 0.012 mA/cm^2 at V_{RHE} = 1.23 V, which is 4 times higher than d-Ta_3N_5. With surface modification by $Co(OH)_x$, mp-Ta_3N_5 shows the photocurrent density of 0.050 mA/cm^2 at V_{RHE} = 1.23 V, which is 2.5 times higher than d-Ta_3N_5. Thus, regardless of surface modification, the porous structure contributes to improved photoelectrode performance due to a lager interfacial contact between the electrode and the electrolyte as well as enhanced photon absorption. Even after the PEC measurement, the original porous structure of mp-Ta_3N_5 film is retained, indicating the robust nanoscale architecture. With the development of the cocatalyst deposition method, a further improvement can be achieved for mp-Ta_3N_5 as an efficient photoelectrode in the PEC water splitting.

5.4 Experimental Methods

Material.

$Ta(OC_2H_5)_5$ (99.99+%) was purchased from Strem Chemicals, and Poly(1,4-butadiene)-b-poly(ethylene oxide) was purchased from Polymer Source Inc. The Polydispersity Index (PDI) is 1.04, and the number average molecular weight (M_n) is PE(4800)-b-EO(5800). Cobalt(II) acetate tetrahydrate was purchased from Sigma-Aldrich. All the chemicals were used without further purification.

Synthesis of sol-gel derived mesoporous and dense-Ta_2O_5 thin films.

The synthesis of sol-gel mp-Ta_2O_5 thin film was previously reported.[30] 0.12 mL of $Ta(OC_2H_5)_5$ and 0.2 mL of HCl were added to 2.5 mL of ethanol, and the solution was stirred for 1 hour at 60 ^oC. For porous films, 0.040g of the diblock copolymer, PB-b-PEO, was dissolved in 0.5 mL of ethanol at 60 ^oC. The clearly dissolved diblock copolymer solution was added to the ethanol-based precursor sol, and stirred for another 1 hour at 60 ^oC. Both dense and porous films were deposited via dip-coating directly onto conductive substrate, Ti(3nm)/Pt(150nm)/Ti(3nm)/SiO_2(150nm)/Si. The films were dried with the relative humidity of <15%, and aged at 180 ^oC for 12 hours to preserve porous structure during calcination and crystallization. Subsequently, the films are annealed at 750 ^oC for 5 minutes to remove the polymer template and complete the crystallization. The film thickness is controllable by multiple dip-coating, and the concentration of sol precursor.

Synthesis of mesoporous and dense Ta_3N_5 thin films

The synthesized Ta_2O_5 thin films were converted to Ta_3N_5 via nitridation using anhydrous liquid NH_3. The reaction is carried out in a tube furnace at 850 ^oC under flowing NH_3 gas (flow rate 35 mL min^{-1}) for 3 hours. $Co(OH)_x$ was deposited on both mesoporous and dense Ta_3N_5 films via successive ionic layer adsorption and reaction (SILAR).[40] The porous Ta_3N_5 film was

successively immersed in an aqueous solution of $Co(CH_3COO)_2$ (0.05 M), deionized water, an aqueous solution of NaOH (0.1 M) and deionized water. The amount of $Co(OH)_x$ nanoparticles deposited was controlled by the immersing time and the number of reaction cycle.

Characterization

A JEOL JSM-6700F field emission scanning electron microscope (FE-SEM) was used to characterize the microstructure of the films. Ellipsometric porosimetry was performed on a PS-1100 instrument from Semilab using toluene as the adsorbate at room temperature. A UV-visible CCD detector adapted to a grating spectrograph analyzes the signal reflected by the sample. The light source is a 75-W Hamamatsu Xenon lamp and measurements were performed in the spectral range from 1.24–4.5 eV. Data analysis was performed using the associated SEA software.

XPS analysis was performed using a Kratos Axis Ultra DLD with a monochromatic Al Kα radiation source. The charge neutralizer filament was used to control charging of the sample, a 20 eV pass energy was used with a 0.1 eV step size, and scans were calibrated using the C 1s peak shifted to 284.8 eV. The integrated area of the peaks was found using the CasaXPS software, and atomic ratios were also found using this software. The atomic sensitivity factors used were from the Kratos library within the Casa software.

2D grazing incident wide angle and small angle X-ray scattering (GIWAXS and GISAXS, respectively) were collected at the Stanford Synchrotron Lightsource (SSRL) using beamlines 11-3 and 1-5, respectively. Beamline 11-3 was operated at 12700 eV, and the beam spot is approximately 3 mm x 0.15 mm. A helium chamber was used to reduce the noise. Each data curve corresponds to the radially integrated pattern of the data from the full 2D diffractogram. The 2D images were collected on a plate with the detector 250 mm away from the center of the measured sample. The software package WxDiff was used to analyze the GIWAXS data. Beamline 1-5 was

operated at 12.5 keV using Rayonix 165 CCD detector. The beam spot is approximately 300 μm x 300 μm. The sample-to-detector distance was 3 meter and the software Scatter was used for analysis.

Photoelectrochemical measurement

Photoelectrochemical measurement was carried out using the conventional three electrode system, which consists of the prepared Ta_3N_5 film (working electrode), Pt foil (counter electrode, Alfa Aesar), and Ag/AgCl (reference electrode, CH instruments). These three electrodes were immersed in 0.1 M aqueous Na_2SO_4 electrolyte (pH = 6) and irradiated by chopped light from AM 1.5G solar simulator at 100 mW/cm^2 (ABET technologies). Linear sweep voltammograms (LSVs) was performed using a VSP potentiostat/galvanostat (Bio-Logic). The potential range is calculated using the Nernst equation ($E_{RHE} = E_{Ag/AgCl} + 0.059pH + 0.196$). For all the photochemical measurements, the potential was swept cathodically at a scan rate of 10 mV/s at 298 K while the electrolyte was being stirred.

5.5 References

(1) Abbasi, T.; Abbasi S.A. 'Renewable' Hydrogen: Prospects and Challenges, *Renewable and Sustainable Energy Reviews* **2011**, *15*, 3034-3040.

(2) Weissermel, K.; Arpe,H. J. *Industrial Organic Chemistry*, 4th ed.; Wiley-VCH: Weinheim, 2003.

(3) Chiarello, G. L.; Aguirre, M. H.; Selli, E. Hydrogen Production by Photocatalytic Steam Reforming of Methanol on Noble Metal-Modified TiO_2. *Journal of Catalysis* **2010**, *273*, 182-190.

(4) Fujishima. A.; Honda, K. Electrochemical Photolysis of Water at a Semiconductor Electrode. *Nature* **1972**, *238*, 37-38.

(5) Li, J.; Wu, N. Semiconductor-Based Photocatalysts and Photoelectrochemical Cells for Solar Fuel Generation: A Review. *Catal. Sci. Technol.* **2015**, *5*, 1360–1384.

(6) Hisatomi, T.; Kubota, J.; Domen, K. Recent Advances in Semiconductors for Photocatalytic and Photoelectrochemical Water Splitting. *Chem. Soc. Rev*. **2014**, *43*, 7520-7535.

(7) Chun, W; Ishikawa, A.; Fujisawa, H.; Takata, T; Kondo, J. N.; Hara, M.; Kawai, M.; Matsumoto, Y.; Domen, K. Conduction and Valence Band Positions of Ta_2O_5, TaON, and Ta_3N_5 by UPS and Electrochemical Methods. *J. Phys. Chem. B* **2003**, *107*, 1798-1803.

(8) Salamat, A.; Woodhead, K.; Shah, S. I. U.; Hector, A. L.; McMillan, P. F. Synthesis of U_3Se_5 and U_3Te_5 Type Polymorphs of Ta_3N_5 by Combining High Pressure–Temperature Pathways with a Chemical Precursor Approach. *Chem. Commun.* **2014**, *50*, 10041-10044.

(9) Luo, Y.; Liu, X.; Tang, X.; Luo, Y.; Zeng, Q.; Ding, S.; Sun, Y. Gold Nanoparticles Embedded in Ta_2O_5/Ta_3N_5 as Active Visible-Light Plasmonic Photocatalysts for Solar Hydrogen Evolution. *J. Mater. Chem. A* **2014**, *2*, 14927-14939.

(10) Cui, L.; Wang, M.; Wang, Y. X. Nitrogen Vacancies and Oxygen Substitution of Ta_3N_5: First-Principles Investigation. *J. Phys. Soc. Jpn.* **2014**, *83*, 114707.

(11) Pinaud, B. A.; Vailionis, A.; Jaramillo, T. F. Controlling the Structural and Optical Properties of Ta_3N_5 Films through Nitridation Temperature and the Nature of the Ta Metal. *Chem. Mater.* **2014**, *26*, 1576-1582.

(12) Nurlaela, E.; Ould-Chikh, S.; Harb, M.; Gobbo, S. D.; Aouine, M.; Puzenat, E.; Sautet, P.; Domen, K.; Basset, J.-M.; Takanabe, K. Critical Role of the Semiconductor–Electrolyte Interface in Photocatalytic Performance for Water-Splitting Reactions Using Ta_3N_5 Particles. *Chem. Mater.* **2014**, *26*, 4812-4825.

(13) Murphy, A. B.; Barnes, P. R. F.; Randeniya, L. K.; Plumb, I. C.; Grey, I. E.; Horne, M. D.; Glasscock, J. A. Efficiency of Solar Water Splitting using Semiconductor Electrodes. *Int. J. Hydrogen Energy* **2006**, *31*, 1999-2017.

(14) Ziani, A.; Nurlaela, E.; Dhawale, D. S.; Silva, D. A.; Alarousu, E.; Mohammed, O. F.; Takanabe, K. Carrier Dynamics of a Visible-light Responsive Ta_3N_5 Photoanode for Water Oxidation. *Phys. Chem. Chem. Phys*. **2015**, *17*, 2670−2677.

(15) Yokoyama, D.; Hashiguchi, H.; Maeda, K.; Minegishi, T.; Takata, T.; Abe, R.; Kubota, J.; Domen, K. Ta_3N_5 Photoanodes for Water Splitting Prepared by Sputtering. *Thin Solid Films* **2011**, *519*, 2087-2092.

(16) Liao, M.; Feng, J.; Luo, W.; Wang, Z.; Zhang, J.; Li, Z.; Yu, T.; Zou, Z. Co_3O_4 Nanoparticles as Robust Water Oxidation Catalysts Towards Remarkably Enhanced Photostability of a Ta_3N_5 Photoanode. *Adv. Funct. Mater*. **2012**, *22*, 3066-3074.

(17) Zhen, C.; Wang, L.; Liu, G.; Lu, G. Q.; Cheng, H.-M.; Template-Free Synthesis of Ta_3N_5 Nanorod Arrays for Efficient Photoelectrochemical Water Splitting. *Chem. Commun*. **2013**, *49*, 3019-3021.

(18) Dang, H. X.; Hahn, N. T.; Park, H. S.; Bard, A. J.; Mullins, C. B. Nanostructured Ta_3N_5 Films as Visible-Light Active Photoanodes for Water Oxidation. *J. Phys. Chem. C* **2012**, *116*, 19225−19232.

(19) Ito, S.; Thampi, K. R.; Comte, P.; Liska, P.; Gra¨tzel, M. Highly Active Meso–Microporous TaON Photocatalyst Driven by Visible Light. *Chem. Commun*. **2005**, 268–270.

(20) Cong, Y.; Park, H. S.; Wang, S.; Dang, H. X.; Fan, F. R. F.; Mullins, C. B.; Bard, A. J. Synthesis of Ta_3N_5 Nanotube Arrays Modified with Electrocatalysts for Photoelectrochemical Water Oxidation. *J. Phys. Chem. C* **2012**, *116*, 14541-14550.

(21) Xinjian Feng†, Thomas J. LaTempa‡, James I. Basham‡, Gopal K. Mor†, Oomman K. Varghese† and Craig A. Grimes. Ta_3N_5 Nanotube Arrays for Visible Light Water Photoelectrolysis. *Nano Lett*. **2010**, *10*, 948–952) Photocatalytic Semiconductors: Synthesis, Characterization, and ...edited by Aracely Hernández-Ramírez, Iliana Medina-Ramírez,

(22) Wang, L.; Zhou, X.; Nguyen, N. T.; Hwang, I.; Schmuki, P. Strongly Enhanced Water Splitting Performance of Ta_3N_5 Nanotube Photoanodes with Subnitrides. *Adv. Mater*. **2016**, *28*, 2432–2438.

(23) Yang, J.; Wang, D.; Han, H.; Li, C. Roles of Cocatalysts in Photocatalysis and Photoelectrocatalysis. *Accounts of chemical research* **2013**, *46*, 1900-1909.

(24) Ran, J.; Zhang, J.; Yu, J.; Jaroniecc, M.; Qiao, S. Z. Earth-Abundant Cocatalysts for Semiconductor-Based Photocatalytic Water Splitting. *Chem. Soc. Rev*. **2014**, *43*, 7787-7812.

(25) Liu, Y.; Wang, H.; Wang, Y. C.; Xu, H. M.; Li, M.; Shen, H. Substrate-Free, Large-Scale, Free-Standing and Two-Side Oriented Single Crystal TiO_2 Nanorod Array Films with Photocatalytic Properties. *Chem. Commun*. **2011**, *47*, 3790-3792.

(26) Chen, H. M.; Chen, C. K.; Liu, R. S.; Zhang, L.; Zhang, J. J.; Wilkinson, D. P.; Nano-Architecture and Material Designs for Water Splitting Photoelectrodes. *Chem. Soc. Rev*. **2012**, *41*, 5654-5671.

(27) Higashi, M.; Domen, K.; Abe, R. Fabrication of Efficient TaON and Ta_3N_5 Photoanodes for Water Splitting under Visible Light Irradiation. *Energy Environ. Sci*. **2011**, *4*, 4138-4147.

(28) Zhang, F.; Yamakata, A.; Maeda, K.; Moriya, Y.; Takata, T.; Kubota, J.; Teshima, K.; Oishi, S.; Domen, K. Cobalt-Modified Porous Single-Crystalline $LaTiO_2N$ for Highly Efficient Water Oxidation under Visible Light. *J. Am. Chem. Soc*. **2012**, *134*, 8348-8351.

(29) Lee, R.-L.; Tran, P. D.; Pramana, S. S.; Chiam, S. Y.; Ren, Y.; Meng, S. Y.; Wong, L. H.; Barber, J. Assembling Graphitic-Carbon-Nitride with Cobalt-Oxide-Phosphate to Construct an Efficient Hybrid Photocatalyst for Water Splitting Application. *Catal. Sci. Technol*. **2013**, *3*, 1694-1698.

(30) Brezesinski, K.; Wang, J.; Haetge, J.; Reitz, C.; Steinmueller, S. O.; Tolbert, S. H.; Smarsly, B. M.; Dunn, B.; Brezesinski, T. Pseudocapacitive Contributions to Charge Storage in Highly Ordered Mesoporous Group V Transition Metal Oxides with Iso-Oriented Layered Nanocrystalline Domains. *J. Am. Chem. Soc.* **2010**, *132*, 6982–6990.

(31) Chen, Z.; Dinh, H. N.; Miller, E. *Photoelectrochemical Water Splitting: Standard, Experimental Methods, and Protocols*. Springer Briefs in Energy, 2003.

(32) Sing, K. S.; Everett, D. H.; Haul, R. A.; Mouscou, L.; Pierotti, R. A.; Rouquerol, J.; Simieniewska, T. Reporting Physisorption Data for Gas/Solid Systems with Special

Reference to the Determination of Surface Area and Porosity. *Pure Appl. Chem*. **1985**, *57*, 603-619.

(33) Lowell, S.; Shields, J.; Thomas, M. A.; Thommes, M. *Characterization of Porous Solids and Powders: Surface Area. Porosity and Density*, Springer, 2004

(34) Higashi, M.; Domen, K.; Abe, R. Highly Stable Water Splitting on Oxynitride TaON Photoanode System under Visible Light Irradiation. *J. Am. Chem. Soc*. **2012**, *134*, 6968-6971.

(35) Seo, J.; Takata, T.; Nakabayashi, M.; Hisatomi, T.; Shibata N.; Minegishi, T.; Domen K. Mg−Zr Cosubstituted Ta_3N_5 Photoanode for Lower-Onset-Potential Solar-Driven Photoelectrochemical Water Splitting. *J. Am. Chem. Soc*. **2015**, *137*, 12780−12783.

(36) Pinaud, B. A.; Vesborg, P. C. K.; Jaramillo, T. F. Effect of Film Morphology and Thickness on Charge Transport in Ta_3N_5/Ta Photoanodes for Solar Water Splitting. *J. Phys. Chem. C* **2012**, *116*, 15918−15924.

(37) Boettcher, S. W.; Warren, E. L.; Putnam, M. C.; Santori, E. A.; Turner-Evans, D.; Kelzenberg, M. D.; Walter, M. G.; McKone, J. R.; Brunschwig, B. S.; Atwater, H. A.; Lewis, N. S. Photoelectrochemical Hydrogen Evolution Using Si Microwire Arrays. *J. Am. Chem. Soc*. **2011**, *133*, 1216-1219.

(38) Kelzenberg, M. D.; Boettcher, S. W.; Petykiewicz, J. A.; Turner-Evans, D. B.; Putnam, M. C.; Warren, E. L.; Spurgeon, J. M.; Briggs, R. M.; Lewis, N. S.; Atwater, H. A. Enhanced Absorption and Carrier Collection in Si Wire Arrays for Photovoltaic Applications. *Nat. Mater*. **2010**, *9*, 239-244.

(39) Osterloh, F. E. Inorganic Nanostructures for Photoelectrochemical and Photocatalytic Water Splitting. *Chem. Soc. Rev*. **2013**, *42*, 2294-2320.

(40) Sun, K.; Su, Z.; Yan, C.; Liu, F.; Cui, H.; Jiang, L.; Shen, Y.; Hao, X.; Liu, Y. Flexible Cu_2ZnSnS_4 Solar Cells Based on Successive Ionic Layer Adsorption and Reaction Method. *RSC Adv*. **2014**, *4*, 17703-17708.

Chapter 6. A Room-Temperature, Solution Phase Method for the Synthesis of Mesoporous Metal Chalcogenide Nanocrystal-Based Thin Films with Precisely Controlled Grain Sizes

6.1 Introduction

The overarching goal of nanoscience research has been to precisely control the unique size-dependent properties of nanomaterials. More specifically, preserving the inherent properties of the materials such as grain size, crystallinity and composition, while being able to precisely control nanoscale architecture, is necessary for many applications. Nanomaterials with precisely controlled properties and architecture could lead to improvements in applications ranging from catalysis,[1] photocatalysis,[2–5] and electrochemical charge storage[6] to photovoltaics.[7–9]

Semiconductor nanocrystals, or quantum dots, make up a particularly interesting class of materials for a wide variety of applications.[8,10–17] For example, tunable band gaps[18,19] and the capacity for barrier-less carrier multiplication[20–23] could revolutionize photovoltaics, among other fields. While the size-dependent optical properties provide a wealth of tunability, the small size also depresses the melting point in nanocrystals compared to those of their bulk counterparts, which limits temperatures at which nanocrystal-based devices can be processed while still maintaining their favorable size-dependent properties.[24]

For many applications, precise control over both film morphology and the properties of the individual nanocrystals is necessary. For example, there is a double necessity to maintain precisely controlled small size and narrow nanocrystal size distributions for applications in quantum dot photovoltaics. In other applications, it has been shown that decreasing the size of nanocrystals improves the thermoelectric properties of semiconducting nanocrystal-based films. Thus, the ability to precisely control both film morphology and nanocrystal size could lead to improved devices.

Synthetic methods for producing a variety of semiconductor nanocrystals with precise control over size, composition, crystal structure, and shape have been previously developed; here we include only a small subset of the many available synthetic methods.[28−36] A majority of these syntheses leave long organic ligands on the nanocrystal surface to control kinetics during nanocrystal growth, prevent nanocrystal aggregation, and maintain colloid stability. These ligands have limited the use of these nanocrystals in electronic devices, mostly because of their insulating nature and the fact that they keep the nanocrystals fairly far apart. It has been shown, however, that small bidentate ligands can replace the long aliphatic ligands to shorten interparticle spacing and improve the electrical conductivity in nanocrystal films, allowing for their expanded use in device applications.[15,37 −45] Ligand exchange generally results in a volume contraction, however, so repeated multilayer deposition is required to produce homogeneous films using these methods.

Given that our goal is to control both size and mesoscale architecture in semiconductor nanocrystal assemblies, we need a method for controlling nanocrystal size, assembly, and connectivity in nanocrystal-derived solids. Recently, some beautiful sol−gel methods for assembling semiconductor nanocrystals into porous aerogels with retention of their quantum confined properties have been developed.[46−50] While these materials have a large surface area and connected porosity, in general they are characterized by a broad pore size distribution that ranges from mesopores to macropores (∼2− 120 nm). Although these methods provide precise control over nanocrystal size, and thus optical properties, a method for the assembly of semiconductor nanocrystals with smaller, more homogeneous porosity, ideally in the thin film format, is desirable.

To accomplish this goal, we build upon recent progress in the field of assembling nanocrystals into porous thin films using block copolymers as a template.[51− 61] Most of the more recent papers

in this field take advantage of synthetic advances that have led to the development of ligand-stripped or "bare" nanocrystals.[62–65] In these methods, a reactive molecule interacts with anionic surface ligands, causing them to desorb from the surface; this leaves uncompensated cationic sites on the nanocrystal surfaces that are charge balanced by some anionic component of the reactive stripping agent. Despite the absence of ligands, the nanocrystals do not aggregate because of electrostatic repulsion between individual charged nanocrystals. To make these nanocrystals into mesoporous films, amphiphilic diblock copolymers are dissolved in polar solvents where they form micelles and are combined with ligand-stripped nanocrystals. Upon deposition onto a substrate and solvent evaporation, the ligand-stripped nanocrystals co-assemble with the polymer micelles. Typically, the films are then heated to remove the polymer template, leaving behind an open porous network of the inorganic material. Partial sintering of the nanocrystals during thermal processing provides mechanical robustness, which prevents the porous structure from collapsing. This method is very robust and allows for the synthesis of materials with large pore volume fractions from a broad range of materials.[51–53]

While the current method for producing mesoporous films from nanocrystals can provide exquisite control of film morphology, the effects of thermal processing can be detrimental to other material properties, such as grain size. Previously, we used thermal processing to remove the polymer template from mesoporous CdSe.[51] X-ray diffraction (XRD) showed the presence of ~5 nm grains, which corresponds to the size of an individual nanocrystal, as well as larger 18 nm grains in these films after thermal processing. This grain growth caused the loss of a well-defined first excitation peak in the UV−visible absorption spectrum, which is indicative of a loss of well-defined nanocrystal size. A red shift of the absorption onset was also observed, again caused by

the grain growth. Milliron and co-workers also used heat treatment to remove the polymer template from their mesoporous CdSe and observed similar trends.[53] Unfortunately, the current copolymers used to template semiconductor nanocrystals need to be heated to ~400 °C to be completely thermally degraded and produce open pores.[51,53] As a result, the deleterious effects on the nanocrystals' grain size and the template removal cannot be separated if thermal processing is used.

Despite its detrimental effects, thermal processing has previously been necessary because it both fuses nanocrystals, giving the film mechanical rigidity, and removes the polymer template.[51,52] As previously discussed, small bidentate ligands have been used to decrease interparticle spacing, showing that they can strongly bind the particles together.[15,39] This makes small molecule cross-linking agents a promising alternative to thermal treatments to form a robust nanocrystal network. If nanocrystals can be well cross-linked using bidentate ligands, then the polymer template can be removed by simply washing it out of the pores.[5] In our case, the distance between two nanoparticles is already small because of the ligand stripping treatments. Thus, upon treatment with small bidentate ligands, there should be negligible volume contraction. The flexibility of nanoporous networks is also likely to help accommodate any volume change that does occur upon cross-linking.[66]

The cadmium chalcogenide nanocrystals investigated by the porous materials community so far provide a good model system for developing new methods for assembling nanocrystals into porous structures because of their impressive chemical stability toward different ligand treatments and their well-studied, size-dependent optical properties. The lead chalcogenides (PbS and PbSe) are also of great interest for applications such as solar energy harvesting because of their much smaller bulk band gaps and large Bohr exciton radii, which subsequently allow for a size tunable

bandgap throughout the near-infrared (NIR) region.[67] Despite these attractive advantages, these Pb-based nanocrystals do not have the same chemical stability that the cadmium chalcogenides exhibit. Indeed, in many of the reported methods developed to produce cationic, "naked" nanocrystals, the lead chalcogenides were not explored or it was reported that the methods failed to produce stable colloidal dispersions for the lead chalcogenides.[62,63,65] One recent exception stands out; researchers used Lewis acid− base adducts of BF_3 to produce stable, ligand-stripped, dispersions of ∼6 nm PbSe nanocrystals.[64] This advance provides a path forward for preparing open, mesoporous films of NIR PbX-based nanocrystals. Gentle cross-linking and template removal likely will be necessary for the fabrication of these sensitive materials.

In this work, we thus show that ethanedithiol and 3-mercaptopropionic acid, two standard bidentate nanocrystal cross-linkers, can be used to cross-link both CdS and CdSe nanocrystals using both ether- and acrylamide-based block copolymer templates. After cross-linking, we show that the polymer template can be removed by soaking the films in appropriate solvents. Because no thermal processing is used, the size-dependent optical properties of the original nanocryst-als are well maintained. Further, we show that this method can be expanded to sensitive NIR active PbS/CdS core/shell nanocrystals. We thus present a method for organizing nanocrystals into porous networks while fully preserving quantum confinement effects.

6.2 Result and Discussion

In this work, our goal was to mitigate the negative effects of thermal processing on nanocrystal properties by removing the need for heat treatments during the synthesis of mesoporous films made from nanocrystals. Scheme 1 gives an overview of our method for porous film formation. First, ligand-stripped nanocrystal solutions were combined with amphiphilic diblock copolymer solutions. Films were deposited by spin coating onto suitable substrates where the nanocrystals co-assembled with polymer micelles to form organic/inorganic composites. The resulting films were then soaked in solutions of bidentate cross-linking ligands to bind the nanocrystals together. The cross-linking solutions used were much more concentrated than those used for layer-by-layer deposition of dense nanocrystal solids.[39,40] To preserve the porous structure of the films, the rate of nanocrystal cross-linking must be faster than the rate of polymer template diffusion out of the film, so more concentrated solutions of the cross-linking molecules were used to accelerate the cross-linking kinetics. In addition, the solvent used for the cross-linking was specifically chosen to dissolve the cross-linking agent, while having minimal nanocrystal and polymer solubility. The films were soaked in the solution of cross-linking molecules for 24 h to ensure complete cross-linking of the nanocrystals. After cross-linking, the polymer template was removed by soaking the resulting films for 48 h in a good solvent for the polymer template. In both cases, the time the films were soaked was chosen to ensure completeness of reaction; the reactions could proceed much faster, but shorter times were not investigated.

The most direct evidence of the porous structure of our films comes from top view SEM images. Figure 6.1 presents top view SEM images of mesoporous films of cross-linked nanocrystals made using different cross-linkers, different polymer templates, and different nanocrystal building blocks. Despite the lack of thermal processing, it is difficult to see individual

nanocrystals in the pore walls because the organic cross-linkers coat the nanocrystals. However, in all cases, we observe disordered but homogeneous porosity. The disorder is likely a combination of disorder in the initial polymer/nanocrystal composite and disorder introduced during cross-linking and polymer removal. Unfortunately, we were unable to observe any long-range order by small angle X-ray scattering. Other polymers specifically designed to produce more ordered pore structures with non-oxide nanocrystals could be used to achieve more ordered mesopores.[53]

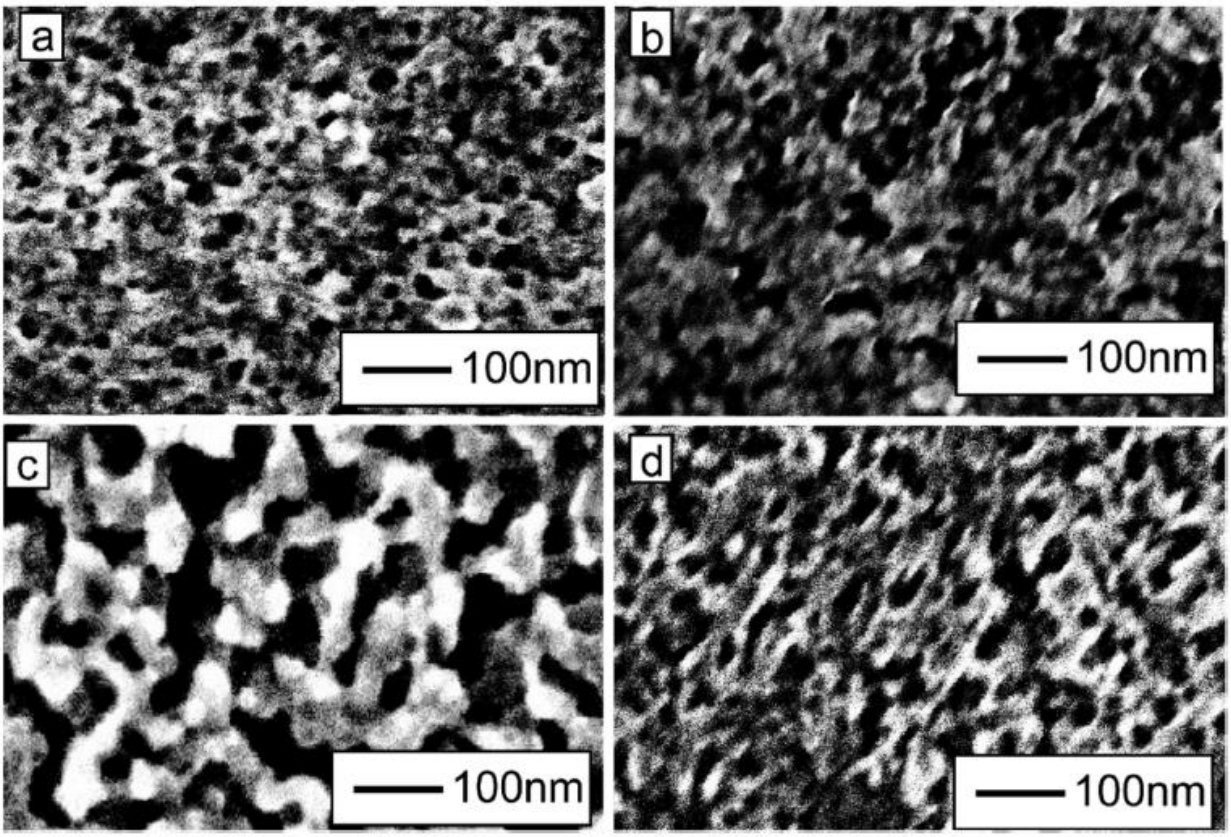

Figure 6.1 Top view SEM images of spin-coated porous films of nanocrystals using different polymers and cross-linkers. (a and b) PEO-b-PBO template ~5 nm CdS nanocrystals cross-linked with EDT and MPA, respectively. (c) CdS nanocrystals (~5 nm) templated with PS-b-PDMA and cross-linked with MPA. (d) CdSe nanocrystals (~4 nm) templated with PEO-b-PBO and cross-linked with EDT

To understand the effect of different cross-linking ligands, we prepared identical PEO-b-PBO-templated films and treated them with either 3-mercaptopropionic acid (MPA) or 1,2-ethanedithiol (EDT) in methanol and washed out the polymer template using ethanol. Figure 6.1(a) shows a top view SEM image of an MPA cross-linked film made from ~5 nm CdS nanocrystals, and Figure 6.1(b) shows a top view image of an EDT cross-linked film made using the same nanocrystals.

Qualitatively, there are minimal differences in the film morphology between the two different cross-linkers used. Observation of the bound thiolate by XPS (Figure 6.2) shows that the cross-linking ligands remain bound after the procedure to wash out the polymer template. Because the morphology appears to be independent of cross-linker and the linking molecules remain bound, our method could be general to many bidentate small molecule cross-linkers, including hydrazine, ethylenediamine, and diacids. Importantly, these different small molecules can be used to tune electronic properties of nanocrystal solids.[37–39,45]

While SEM provides evidence of the mesoscale structure, it does not provide any information about the internal three-dimensional structure of the nanocrystal assemblies, and importantly, it does not prove removal of the polymer template. To address this, we analyzed the mesoporosity using ellipsometric porosimetry with toluene as the adsorbate.[71] Figure 6.3(a) shows an adsorption isotherm for PEO-b-PBO-templated CdS. This sample shows ~20% solvent accessible pore volume, which is in reasonable agreement with SEM images (Figure 6.1(a)). The pore radius distribution (Figure 6.3(b)) was determined from a Kelvin model fit of the adsorption data. The average pore radius measured was ~9 nm, which is in good agreement with SEM images for this sample (Figure 6.1(a)). Similar results were seen for mesoporous CdSe (Figure 6.3 (c),(d)); however, in this case, a larger solvent accessible pore volume (~30%) was observed, along with a slightly larger average pore radius (~12 nm). These results are again in good agreement with SEM

images, where the CdSe films (Figure 6.1(d)) show an average pore size slightly larger than that of the CdS films (Figure 6.1(a)).

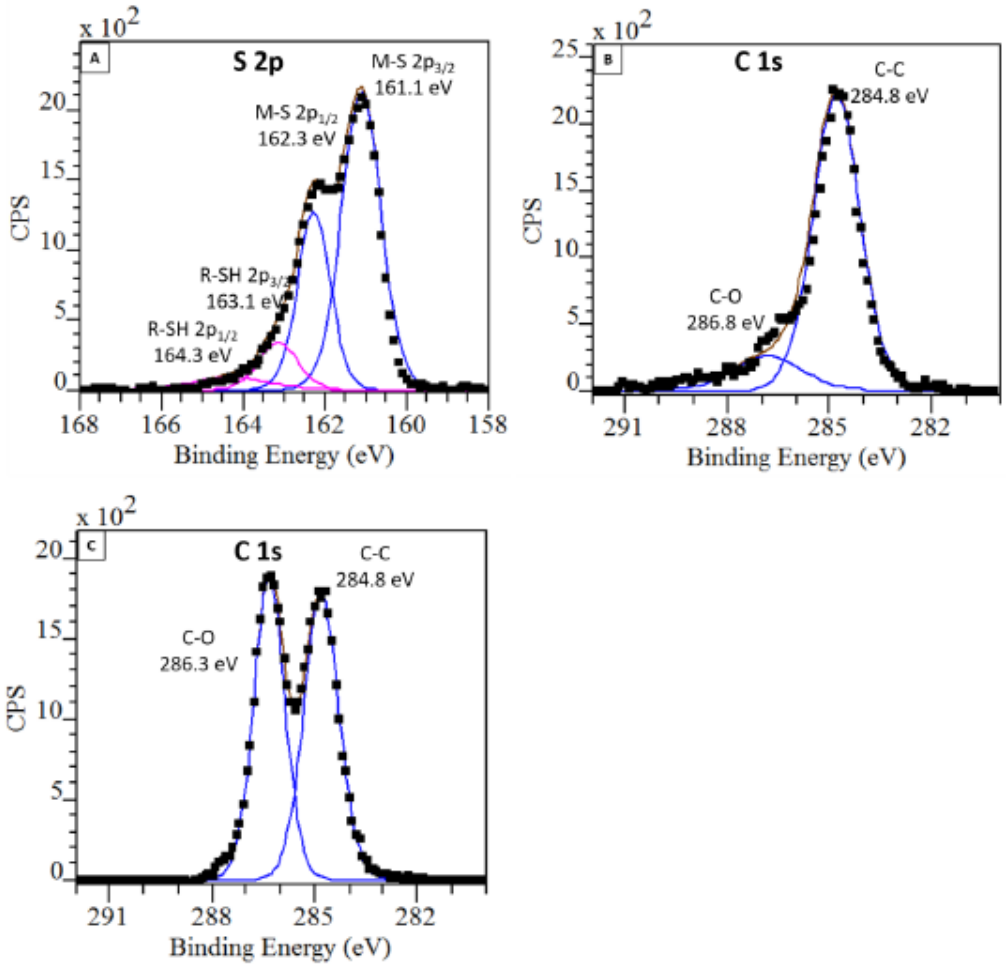

Figure 6.2 (A) Sulfur 2p XPS from a mesoporous film of EDT cross linked PbS/CdS core shell nanocrystals showing the presence of sulfur signal arising from the metal sulfide nanocrystals and the bound thiolate arising from the EDT bound to the surface. (B) Carbon 1s XPS from a mesoporous film of EDT cross linked PbS/CdS core shell nanocrystals showing minimal signal from C-O, which comes from the ethers present in the PEO-b-PBO polymer template. The data thus indicates removal of the majority of the polymer template. (C) C 1s XPS from pure PEO-b-PBO showing a large C-O signal, as expected from a poly-ether based polymer, along with significant C-C signal.

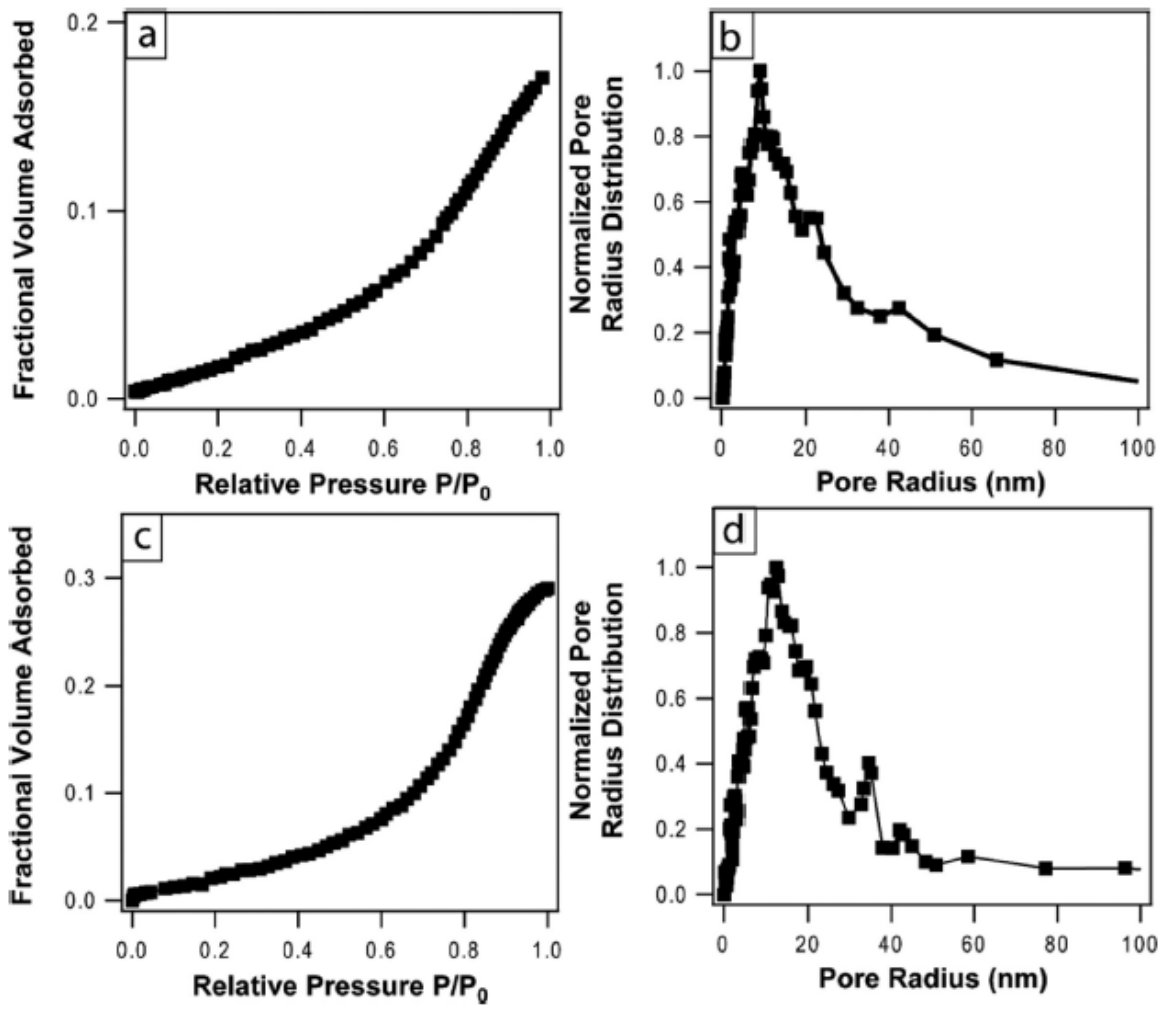

Figure 6.3 Toluene adsorption isotherms for (a) CdS and (c) CdSe templated with PEO-b-PBO and cross-linked with EDT. Corresponding pore radius distributions for (b) CdS and (d) CdSe calculated from a Kelvin model fit for mesopores. CdS data correspond to the SEM image in Figure 1a and CdSe data to the SEM image in Figure 6.1(d).

The differences in porosity between these two samples are attributed to different polymer template:nanocrystal ratios used in the synthesis of these specific samples (0.5 mg of polymer/ mg of as-synthesized nanocrystals for the CdS samples vs 0.7 mg of polymer for the CdSe sample). The variation in pore size is in good agreement with previous examples of polymer-templated nanocrystal films where the polymer:nanocrystal ratio was systematically explored.[54] The SEM images and the porosimetry together provide strong evidence of the existence of homogeneous, nanoscale porosity of our films. These data thus indicate that the polymer template was indeed successfully removed using our solution phase methods. While our films show good porosity, it is lower than the highest values of 50% solvent accessible porosity we have achieved using thermal decomposition of the same polymer template.[51] In the case of thermal decomposition, the total porosity is a combination of mesopores resulting from the polymer template and micro-pores stemming from spaces between individual nanocrystals. In this case, the spaces between individual nanocrystals are occupied with cross-linking molecules and therefore cannot be accessed by adsorbate molecules, which could partly account for the smaller solvent accessible pore volume. Other differences could arise from variations in the nanocrystal:template ratio.

Further evidence of the removal of the polymer template comes from evaluation of C 1s signals from XPS. Because PEO-b-PBO contains many ether linkages, the intensity of the C−O signal with a binding energy of 286.3 eV can be used to probe the amount of remaining polymer template. A C 1s XPS spectrum for an EDT cross-linked film of PbS/CdS nanocrystals (Figure 6. 2(a)) shows signal primarily from C−C species that could arise from both contamination of the sample with adventitious carbon from the atmosphere and carbon in the dithiol. A small shoulder attributed to C−O species that we attribute to small amounts of residual polymer is also observed. By comparing this signal to the C−O signal from a sample of pure PEO-b-PBO (Figure 6.2(c)), it is

easy to see that the ratio of C−O carbon to C−C carbon is much higher in the pure polymer sample than in our films. This qualitatively shows that most of the polymer template is removed. We then quantified the amount of remaining polymer by determining the atom percent of C−O carbon and comparing it to the atom percent of sulfur from the XPS data. On the basis of the unique distribution of aliphatic and C−O carbons in PEO-b-PBO, we calculated the mass of polymer from the C−O signal and compared it to the mass of metal sulfide nanocrystals calculated from the atom percent of sulfur. Through this analysis, we determine there is ∼0.1 wt % polymer remaining in our samples, compared to ∼30 wt % in the as-formed films, indicating that the polymer template is thoroughly removed.

We next examined the structure of the films using wide angle X-ray scattering (WAXS) and optical absorption spectroscopy. WAXS was used to determine the crystal structure and average crystallite size of freshly ligand-stripped nanocrystals and of the nanocrystals in the porous films. Figure 6.4(A) shows WAXS patterns for CdS nanocrystals in different environments. Part a shows WAXS patterns for ligand-stripped CdS nanocrystals that can be indexed to zinc blende CdS. Wurtzite CdS could give a very similar pattern; however, the peak at 1.86 $Å^{-1}$ would be a convolution of three peaks and would thus be broader than the peak seen at 3.1 $Å^{-1}$. Also, wurtzite CdS shows a peak at 2.6 $Å^{-1}$, which is not seen in our patterns. The diffraction patterns show broad peaks consistent with their small crystallite size. We found that by fitting the peaks and applying the Scherrer equation modified for q space and assuming spherical crystallites,[72] we determined a crystallite size of ∼4.1 nm. Porous films cross-linked with EDT were prepared from the same nanocrystal batch. WAXS patterns for the film (panel A, part b) shows an identical pattern with minimal changes to the peak broadening or peak positions, which indicates essentially no changes to the crystal structure and crystallite size due to oxidation, etching, or sintering. EDT-derived

porous films showed a Scherrer crystallite size of 4.1 nm, in excellent agreement with that of the isolated nanocrystals. In the case of CdS nanocrystals cross-linked with MPA, we calculate a Scherrer size of 4.2 nm, which further indicates the retention of size throughout processing with different ligands. Any variations in size are well within the uncertainty of the measurement. CdSe nanocrystals (Figure 6.4(B)) showed similar trends. In this case, we calculated a Scherrer size of 3.3 nm for the ligand-stripped CdSe and a size of 3.2 nm for CdSe cross-linked with EDT. On the basis of WAXS, we thus conclude that there is no measurable change in the crystal structure or size of the nanocrystals during formation of the mesoporous network. By avoiding heat treatments in this method for making mesoporous films, we fully preserve the crystallite size in the resulting film.

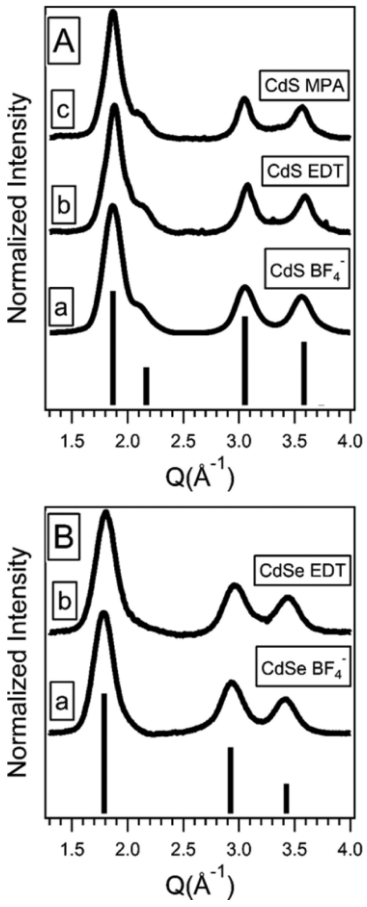

Figure 6.4 (A) Wide angle XRD patterns obtained by integrating two-dimensional (2D) WAXS patterns of CdS nanocrystals after different ligand treatments: (a) ligand-stripped CdS nanocrystals, (b) template CdS nanocrystal film cross-linked with EDT, and (c) templated CdS nanocrystal film cross-linked with MPA. The stick pattern corresponds to zinc blende CdS (JCPDS Card 00-010-0454). (B) Wide angle XRD patterns obtained by integrating 2D WAXS patterns of CdSe nanocrystals after different ligand treatments: (a) ligand-stripped CdS nanocrystals and (b) templated CdS nanocrystal film cross-linked with EDT. The stick pattern corresponds to zinc blende CdSe (JCPDS Card 00-019-0191). Good nanocrystal size retention is observed for all samples across all processing conditions.

UV−visible absorption spectroscopy was employed to investigate the effects of film processing on the nanocrystal optical properties. Absorption is also highly sensitive to changes in nanocrystal size, so it is a good double check of the conclusion from WAXS. On the basis of the preservation of nanocrystal size, we expect to see minimal differences between the optical absorption of the as-synthesized nanocrystals and the optical absorption of those in the porous films due to nanocrystal size effects. However, the optical absorption, and in particular the position of the first exciton peak, of nanocrystals is also affected by other factors such as the surface ligands and the spacing between the individual nanocrystals, which can change the dielectric environment surrounding the nanocrystals and causes coupling between quantum dots. In this system, the ligand environment changes from the oleic acid ligands used in the synthesis to a charge stabilization and finally to a thiol ligand bound to the surface.

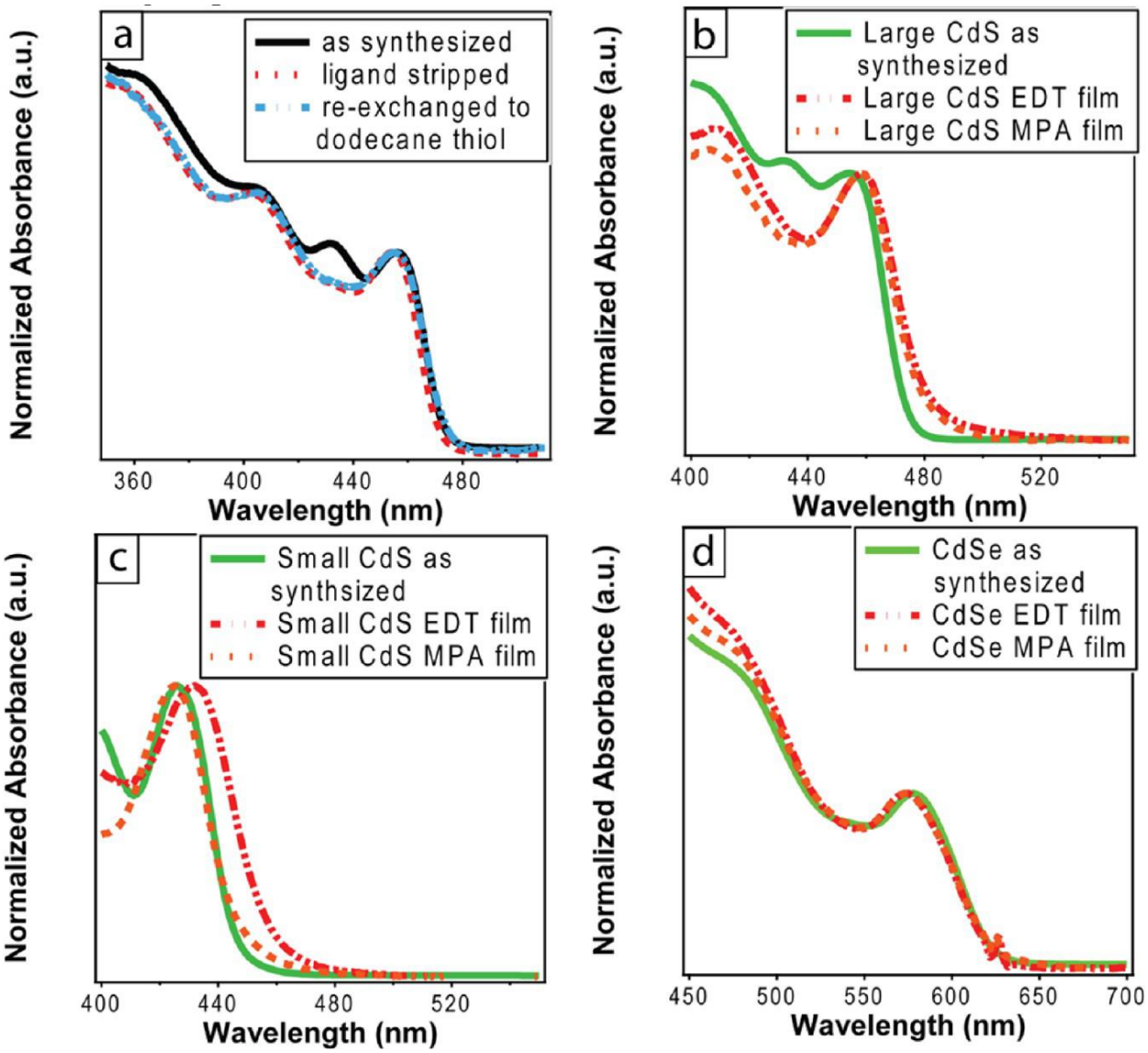

Figure 6.5 (a) Solution phase optical absorption for CdS nanocrystals with different capping ligands. (b and c) Absorption for large (~5 nm) and small (~3 nm) CdS, respectively, templated into porous films and cross-linked with different molecules. (d) Absorption for CdSe-based porous films cross-linked with different molecules. As-synthesized traces correspond to solution phase absorption of nanocrystals homogeneously dissolved in hexanes.

To understand the ligand effects, we first prepared multiple solutions of CdS nanocrystals from the same batch with different surface ligands. We specifically examined nanocrystals with oleic acid ligands, as charge-stabilized nanocrystals in DMF, and with dodecanethiol ligands to mimic the surface effect of EDT or MPA. We then performed solution phase absorption measurements to remove electronic coupling effects. UV−vis absorption (Figure 6.5(a)) shows a blue shift of 2 nm in wavelength from the nanocrystals with the native ligands to ligand-stripped nanocrystals. This could result from either a negative solvatochromatic shift due to the higher dielectric constant of DMF compared to that of hexanes or an altered spherical potential confining the exciton wave function due to ligand effects. Upon conversion from charge-stabilized nano-crystals to thiol-capped nanocrystals, there is a 1 nm red shift. The addition of a sulfur from the thiol to the surface of the nanocrystals will slightly increase the size of the nanocrystal, which could explain the red shift. One peculiarity of the absorption spectra is the decreased intensity of the second absorption peak for ligand-stripped and thiol-capped nano-crystals. This effect was also seen in other nanocrystal surface treatments using inorganic ligands as the capping agents[65,73] but has not been fully explained. We suspect that this mode has significant p character; thus, its oscillator strength will be more influenced by surface modifications.[74,75] Overall, while some changes in absorption spectra do occur with different ligand environments, the effect is weak.

For porous nanocrystal films treated with bidentate ligands, the small shifts due to changes in the ligand environment will be superimposed with the effects from decreasing the interparticle spacing. Figure 6.5(b) shows UV−vis absorption for large (∼5 nm) nanocrystals with oleic acid ligands in hexanes, and for porous films templated with PEO-b-PBO and treated with MPA and EDT. The absorption spectra for the films were corrected for a small scattering background due to film imperfections to facilitate comparison. There is an ∼5 nm red shift from the as-synthesized

nanocrystals going to the cross-linked porous films. Similar trends are seen for smaller CdS (~4 nm) for EDT-cross-linked films (Figure 6.5(c)). However, the same trend is not seen for MPA-cross-linked films for the smaller nanocrystals.

To understand the cause of the red shift in EDT-treated films, we consider related systems. PbSe nanocrystals cross-linked with EDT show a similar red shift, and it has been suggested that this red shift arises from a combination of changes to (i) the dielectric constant at the surface of the nanocrystals, (ii) radiative electronic coupling, and (iii) increased wave function overlap.[39] More recent work has shown that the red shift is predominantly a result of changes to the dielectric environment surrounding each quantum dot (~88%), with a smaller contribution from electronic or transition dipole coupling.[76] The effects of the increased dielectric constant may be stronger for PbSe than for CdSe or CdS because of the larger Bohr exciton radius of PbSe, meaning the exciton will be located closer to the nanocrystal surface for PbSe and subsequently be more sensitive to surface effects.[77] Nonetheless, red shifts of the absorption peak in close-packed films of CdSe nanocrystals capped with tributyl phosphine/ tributyl phosphine oxide (TBP/TBPO) ligands have been observed and attributed to changes to the dielectric environ-ment around the nanocrystals.[78] However, in this case, shifts were smaller than the ones we observe here because the TBP/ TBPO ligands are much larger than EDT.[78] We thus conclude that the red shifts observed in our samples are a result of decreased interparticle spacing, which predominantly changes the dielectric environment of the nanocrystals, thus causing their absorption to red shift.

We also looked at the absorption of porous CdSe films cross-linked with both EDT and MPA (Figure 6.5(d)). Here, there is no red shift in the cross-linked films. However, CdSe is more sensitive to oxidation than CdS, especially when both are ligand-stripped. Any oxidation of the nanocrystals will blue shift the absorption, so the effects due to oxidation and coupling have

opposite effects on the position of the first excitation peak and could cancel out.[77] In support of this idea, CdSe-based films made in air showed clearly observable blue shifts (data not shown), confirming that the presence of air can blue shift the position of the first excitation peak. We note that while some measurable changes in our optical absorption spectra of both CdS and CdSe can be observed, all changes are small compared to the changes previously observed using thermal treatments, where red shifts of up to 100 nm were observed.[51] Others have used less aggressive thermal treatments and saw smaller red shifts (~15 nm), but even those changes are much more significant than the ones shown here.[53] While those less aggressive thermal treatments mitigated some of the effects of grain growth, it is unclear whether the polymer template was fully removed and a truly open porosity was achieved at those more modest temperatures, as porosimetry was not used to confirm an open pore volume and the temperature was somewhat lower than the polymer decomposition temper-ature.[53] This discussion serves to emphasize that the methods presented here allow for precise control over the optical properties of porous films, combined with fully accessible porosity.

In addition to information about the size of the nanocrystals, optical absorption can also provide information about the size distribution of the nanocrystals in a sample. The right half-width at half-maximum (RHWHM) of the first exciton peak has been used to quantify the size distribution of quantum dot samples in solution.[19,79] Because the position of this peak is dependent on size, absorption from nanocrystals larger and smaller than the average will broaden the absorption peak in a polydisperse sample. The RHWHM values of the first excitation peak for the as-synthesized nanocrystals in solution and for the porous films were measured, and in the case of the ~5 nm diameter CdS nanocrystals, we found the RHWHM values to be 12.8, 12.6, and 12.8 nm for as-synthesized nanocrystals, EDT-cross-linked porous films, and MPA-cross-linked porous

films, respectively. Similar trends were observed for the smaller ~4 nm CdS. One might expect some broadening due to wave function overlap, but as discussed above, the dominant optical changes resulting from nanocrystal assembly are dielectric changes; therefore, the effect of wave function overlap is expected to be small. We note that similar trends (i.e., a red shift in peak position but no peak broadening) have also been observed for dense EDT-cross-linked PbSe films.[39] The minimal changes to the RHWHM of the first exciton peak show that there are minimal changes to the size distribution of the nanocrystals in our samples, which is important for many optoelectronic applications.[25]

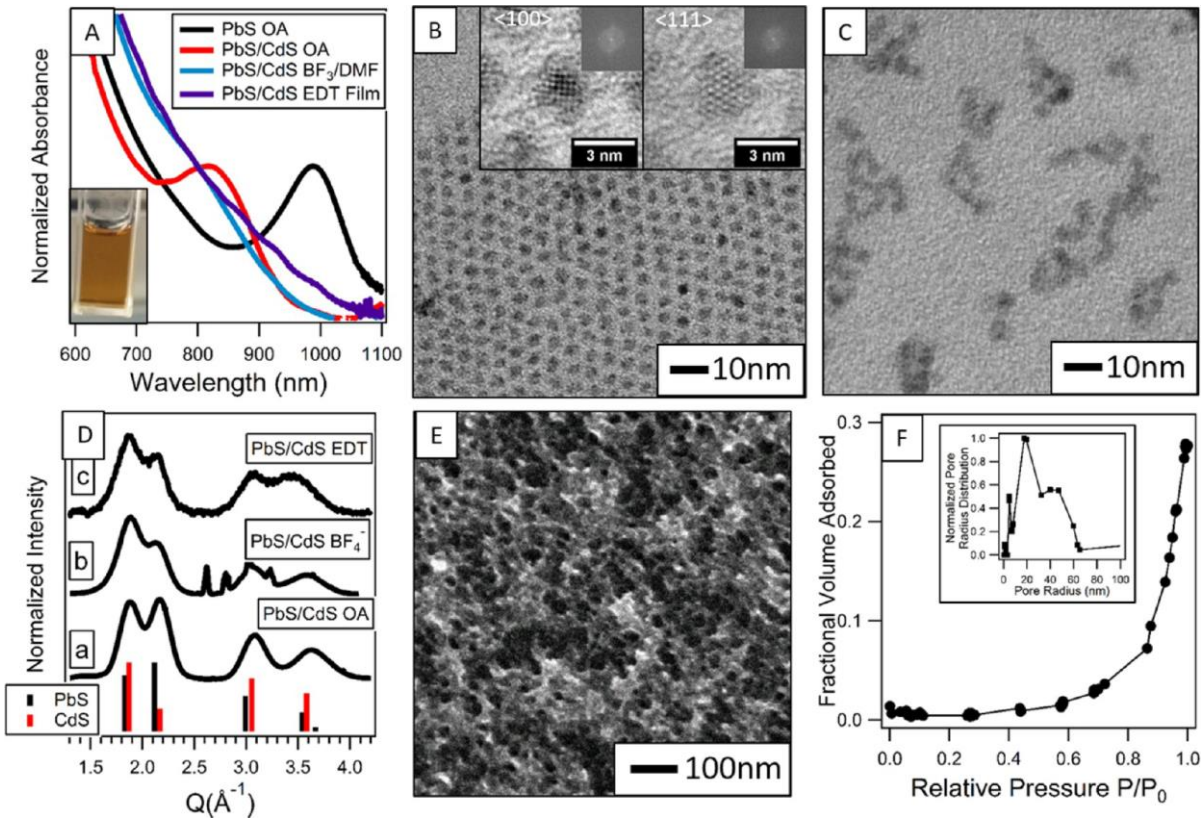

Figure 6.6 (A) Visible−NIR absorption of PbS and PbS/CdS core/shell nanocrystals in different ligand environments. The difference in the position of the first excition peak between the PbS and PbS/CdS nanocrystals is used to estimate the shell thickness. All spectra except those of the PbS/CdS EDT film were recorded in dilute solution. Because of the lack of distinct excitonic features for the PbS/CdS BF4 and PbS/CdS EDT samples, spectra were normalized at 800 nm. The inset is a photograph of the clear solution of ligand-stripped PbS/CdS core/shell nanocrystals in DMF. (B) Low-magnification TEM image of PbS/CdS core/shell particles with oleate ligands. Inset are HRTEM images and corresponding FFTs of particles along the 100 and 111 zone axes. (C) Low-magnification TEM image after treatment with BF3− in DMF. (D) Wide angle XRD patterns obtained by integrating 2D WAXS patterns of PbS/CdS core/shell nanocrystals with

different ligand environments: (a) as-synthesized PbS/CdS core/shell nanocrystals, (b) nanocrystals from the same batch after treatment with BF_3 in DMF, and (c) a porous film of PbS/CdS nanocrystals after treatment with EDT. (E) Top view SEM image of PbS/CdS core/shell nanocrystals assembled into an open porous structure using PEO-b-PBO as the pore template. (F) Toluene adsorption isotherms for a porous PbS/CdS nanocrystal film cross-linked with EDT and (inset) the corresponding pore radius distribution. This data was collected on films made in the same batch as the sample shown in panel E.

Next we wanted to expand out method to more sensitive NIR particles to take advantage of the gentle process we have developed. While the "gentle" BF_3 ligand stripping procedure developed by Helms and co-workers is a synthetic break-through and could guide the development of new strategies for producing naked nanocrystals, it was only verified for large PbSe nanocrystals.[64] Large PbSe nanocrystals have a band gap that is too small for use in solar energy harvesting because of the limited open circuit voltage. When we used small (~3 nm) PbS nanocrystals, which have ideal band gaps for use in single-junction solar cells, we were unable to obtain stable colloidal dispersions. We suspect that the smaller sized nanocrystals have much higher surface energies and cannot accommodate a ligand free, naked surface. To address this problem, we hypothesized that a thin cadmium sulfide shell on the surface of the PbS nanocrystals would stabilize the surface and allow us to obtain stable dispersions of PbS nanocrystals. We thus synthesized PbS/CdS core/shell nanocrystals using a partial cation exchange approach that has been fully characterized elsewhere.[69] In these nanocrystals, the shell is grown by replacement of Pb^{2+} with Cd^{2+} on the surface. Thus, the effective size of the PbS core decreases as the shell grows. Because the position of the first excition peak is determined by the size of the PbS core, the shell thickness can be calculated on the basis of the blue shift of the first exciton peak using the empirical fit for the size dependence of the exciton peak.[18] On the basis of the blue shift observed for our PbS nanocrystals after shell growth (Figure 6.6(A), black and red traces), we estimate a shell thickness of 0.3 nm. We targeted 0.3 nm thick CdS shells to ensure complete coverage of CdS on the surface, but at the same time keeping the shell thin enough for charge transport between nanocrystals to be possible.

TEM of the PbS/CdS core/shell particles (Figure 6.6(B)) shows a narrow size distribution after the shell growth reactions. Because of the thin nature of the shell and the nearly indistinguishable lattice parameters of PbS and CdS, determin-ing the shell thickness of the particles by HRTEM is

difficult. However, the different crystal structures (rock salt vs zinc blende) of the core and shell materials allow for the visualization of the two domains based on the symmetry of HRTEM lattice fringes and the coherent alignment of the two materials.[80] On the basis of this, along the 100 zone axis, both PbS and CdS are expected to have square lattices that are offset by 45° with a lattice spacing of 2.96 Å for the (200) planes of the PbS and 2.05 Å for the (220) planes of the CdS shell. In our HRTEM image along the 100 zone axis (Figure 6.6(B)), left inset), we observe well-defined fringes of the PbS core that do not extend to the edge of the particle. We assign the diffuse shell, which can be easily distinguished from the low-background graphene support, to the CdS layer on the surface.

We suspect the lattice fringes from the shell cannot be resolved because of its thin nature and the small lattice fringe spacing, which is approaching the resolution limit of the TEM used. Along the 111 zone axis, PbS and CdS have the same projection; thus, we should expect lattice fringes to extend to the surface of the nanocrystal, which is what we observe by HRTEM (Figure 6.6(B), right inset). Additional TEM images and visualization of the core and shell crystal structures viewed down different zone axes are shown in Figure 6.7. We note that not all of the particles observed by HRTEM were defect free (Figure 6.8) like the ones shown in Figure 6.6(A). It is unclear if this is expected for these types of particles because papers reporting their synthesis show HRTEM from only a few particles.[69] While TEM can provide detailed information about individual particles, it is difficult to extract information from the "average" nanocrystal. Optical methods are thus more reliable for determining average shell thickness.[69]

We then stripped the oleic acid ligands off the nanocrystal surface using the BF_3/DMF Lewis acid−base adducts discussed above.[64] Using this method, we were able to obtain dispersions of ligand-stripped PbS/CdS core/shell nanocrystals in DMF (inset of Figure 6.6(A)) that did not

scatter light and were stable for several days in a nitrogen-filled glovebox. Optical absorption from the ligand-stripped PbS/CdS nanocrystals (Figure 6.6(A), blue trace) shows that the well-defined excitonic features are lost upon ligand stripping, indicating more polydisperse samples. In agreement with this fact, TEM also shows a broader size distribution for ligand-stripped nanocrystals (Figure 6.6(C)).

Comparing the WAXS patterns for the as-synthesized PbS/ CdS core/shell nanocrystals and the ligand-stripped nanocrystals (Figure 6.6(D), traces a and b, respectively) shows a decrease in the intensity of the peak at ~2.2 q after ligand stripping. The close proximity of the PbS and CdS causes constructive interference between the core and shell materials, which makes the diffraction patterns appear as a weighted average of the two reference patterns, in agreement with the results of XRD simulation presented elsewhere.[69] On this basis, we can use the intensity of the (002) reflection (peak at ~2.2 q) as a way to determine the relative amounts of the two materials because the CdS phase has a much lower intensity for that reflection; the loss of intensity suggests a loss of Pb^{2+} from the system. We suspect the sharp peaks from 2.5 q to 3.5 q are from residual Lewis acid−base adducts of BF_3, which are a byproduct of the reaction. We were not able to match them with any known reference patterns, however. The changes to the optical properties and the possible loss of lead could come from etching of the nanocrystals by trace amounts of HBF_4, a byproduct of ligand stripping if trace amounts of water are available.[64] We note that there are no data available in the literature on the optical properties of ligand-stripped PbSe or PbS, so it is not possible to tell if these dramatic changes in optical absorption are expected upon ligand stripping.

While ligand stripping causes changes to the structural and optical properties of the nanocrystals, the goal of this paper is to develop new methods of processing nanocrystals into porous structures without altering their properties. In comparing the vis−NIR absorption of the

ligand-stripped nanocrystals with that of a porous film of nanocrystals (Figure 6.6(A)) treated with EDT, we find that minimal changes are seen, indicating the optical properties of the nanocrystals are maintained. There is a slight red shift of the absorption onset that is expected on the basis of the increased dielectric constant surrounding the nanocrystals when they are incorporated into a film.[76] Furthermore, we do not observe any changes to the wide angle diffraction during the processing used to make porous films of nanocrystals (Figure 6.6(D), traces b and c). This evidence further shows that our process for making porous films of nanocrystals can be expanded to other, less well-behaved, systems while still maintaining the properties of the ligand-stripped nanocrystal building blocks. Further work still needs to be done, however, to develop general methods for synthesizing ligand free "naked" nanocrystals for these highly reactive systems without altering their delicate optical and electronic properties.

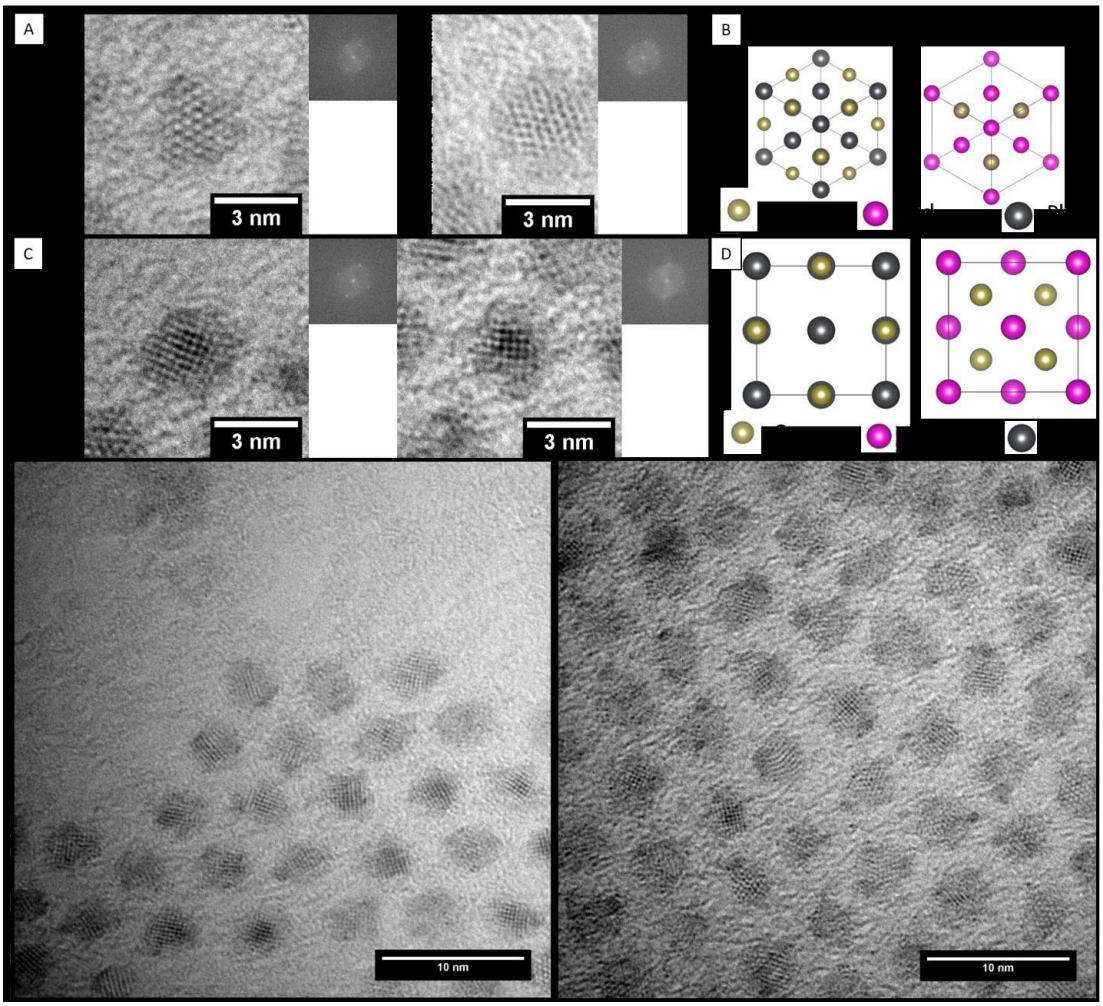

Figure 6.7: (A) HRTEM images of PbS/CdS particles viewed down the <111> zone axis. (B) Visulization of the PbS and CdS lattices when viewed down the <111> zone axis. (C) HRTEM Images of PbS/CdS particles viewed down the <100> zone axis. (D) Visulization of the PbS and CdS lattices when viewed down the <100> zone axis. (E) and (F) wide field HRTEM images of several PbS/CdS nanocrystals showing the diversity of structures that are observed.

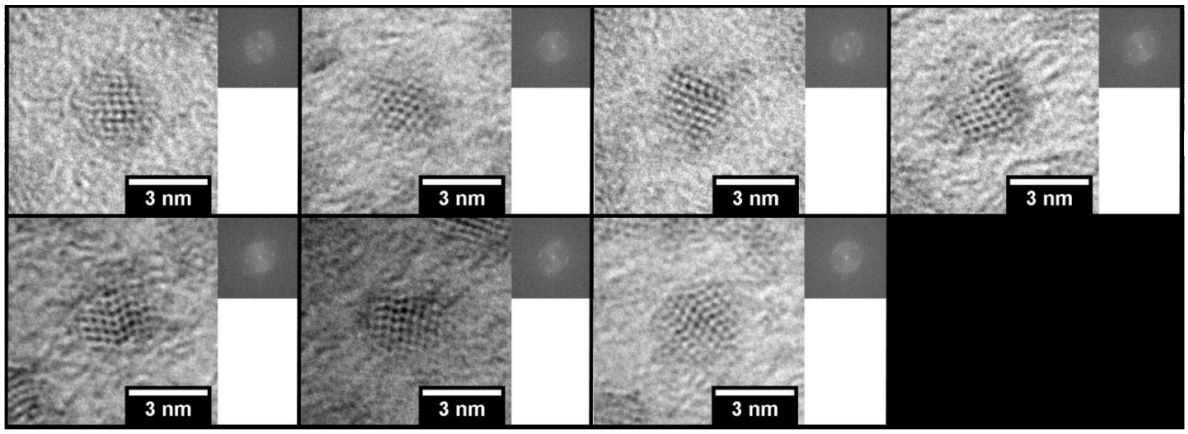

Figure 6.8: HRTEM images of PbS/CdS core shell particles that contain stacking faults and other defects.

The pore structure of the films made with PbS/CdS core/ shell nanocrystals shows structures similar to those made with cadmium chalcogenide nanocrystals. A top view SEM image (Figure 6.6(E)) of a porous PbS/CdS core/shell nanocrystal-based film templated with PEO-b-PBO shows a homogeneous pore size that is comparable to those made with CdS or CdSe nanocrystals. This indicates that the pore structure and material comprising the pore wall can be independently changed by using the appropriate choice of nanocrystal building blocks. Furthermore, porosimetry (Figure 6.6(F)) shows a 28% solvent accessible pore volume, confirming the pores are open and interconnected. The pore radius distribution determined by a Kelvin model fit (inset of F)) shows a peak at 20 nm and a relatively broad distribution that corresponds well with the pore sizes observed by SEM (Figure 6.6(E)). To the best of our knowledge, this is the first example of a film made from NIR active lead chalcogenide nanocrystals with interconnected, solvent accessible mesoporosity. These open pores could be filled with an acceptor material, which could lead to advances in quantum dot photovoltaics by allowing intimate mixing of donor and acceptor materials. This, in turn, would limit the distance excitons must diffuse before being separated at a heterojunction, while maintaining connected pathways to both electrodes.

6.3 Conclusions

In this work, we have developed a new technique for making porous films of nanocrystals without thermal treatments using block copolymer templating. We employ bidentate ligands to bind the nanocrystals together and simple washing to remove the polymer template. Our films show disordered but homogeneous porosity by SEM and good pore accessibility using ellipsometric porosimetry. In addition, WAXS and absorption spectroscopy show there is no change in the size of the nanocrystals constituting the film throughout the synthesis process. Our method thus provides a route to simultaneous control of the mesoscale architecture and the electronic properties of the nanocrystal building blocks that has not been achieved using thermal treatments. The generality of the method is demonstrated here using three different types of nanocrystals (CdS, CdSe, and PbS/CdS core/shell nanocryst-als), two different block copolymers (PEO-b-PBO and PS-b-PDMA), and two different cross-linking agents (MPA and EDT).

To appreciate the potential impact of these methods, it is interesting to consider the fantastic array of kinetically trapped nanocrystals that have been synthesized, including core/shell particles,[81] graded alloys,[82] metastable crystal structures,[83,84] and highly anisotropic shapes,[85–87] many of which exhibit interesting and useful properties. Unfortunately, these kinetically trapped materials often convert to the thermodynamic products upon mild heat treatment.[87,88] Using the methods described here, open porous networks of these nanocrystals can potentially be made at room temperature, allowing metastable nanocrystals to be assembled into porous architectures. The only requirements are that a suitable surface treatment must be available to disperse the nanocrystals as ligand free charge-stabilized colloids in polar solvents, and finding an appropriate bidentate ligand for the given nanocrystal. While these constraints are significant, the method offers interesting possibilities for making novel photovoltaic, thermoelectric, electrochemical, and

catalytic materials for which precise control over the mesoscale structure and nanocrystal properties are needed.

6.4 Experimental methods

Materials.

The following chemicals were used as received: tetraethylthiuram disulfide (97%, Alfa Aesar), 2,2′-dithiobis-(benzothiazole) (99%, Aldrich), tetradecanoic acid (98%, Alfa Aesar), cadmium acetate dihydrate (98%, Alfa Aesar), cadmium oxide (99%, Strem),sulfur powder (99.5%, Alfa Aesar), selenium powder (99.5%, Strem), oleic acid (90%, Fischer), 1-ocadecene (90%, Acros), trioctylphosphine (90%, Aldrich), 1,2-ethanedithiol (95%, Acros), and 3-mercaptopropionic acid (>99%, Acros). Poly(ethylene oxide)-block-poly(butylene oxide) with a PEO(6500)-b-PBO(5000) mass ratio and a PDI of 1.09 was purchased from Advanced Polymer Materials Inc. Polystyrene-block-poly(dimethyacrylamide) with a PS(51000)-b-PDMA(8500) mass ratio and a PDI of 1.3 was purchased from Polymer Source Inc.

Nanocrystal synthesis.

CdS nanocrystals were synthesized using slight modifications to literature procedures.[31] Briefly, cadmium acetate dihydrate (1 mmol, 269 mg), sulfur (0.5 mmol, 16 mg), tetradecanoic acid (2 mmol, 451 mg), and tetraethylthiuram disulfide (TETD) (0.06 mmol, 17 mg) were added to a three-neck flask. Next, 2,2′-dithiobis(benzothiazole) (DTBT) was added, and the amount of DTBT was used to control the size of the nanocrystals. A 1:3 TETD:DTBT molar ratio was used for larger (∼5 nm) CdS nanocrystals, and a 2:1 ratio was used for smaller (∼3 nm) CdS nanocrystals. This reaction mixture was dissolved in 50 mL of octadecene and stirred at 120 °C under flowing argon for 2 h. The temperature was increased to 240 °C with a ramp rate of ∼10 °C/min and held for an additional 2.5 h under flowing argon. After cooling to room temperature, the nanocrystals were collected by centrifugation at 4000 rpm for 10 min. It was found that the nanocrystals were not dispersible with the native tetradecanoic acid ligands; however, adding

excess oleic acid to the pelleted solid followed by sonication brought the nanocrystals into solution, and the nanocrystals were then purified by three cycles of dissolution in hexanes, followed by precipitation using ethanol. CdSe nanocrystals were synthesized according to reported procedures, and the only modifications were that the reaction was performed under argon protection and the reaction was scaled up 5-fold.[68] PbS/CdS core/shell nanocrystals were synthesized according to reported procedures.[69]

Ligand Stripping.

For CdS and CdSe nanocrystals, organic ligands were stripped from the nanocrystal surfaces using Me_3OBF_4 or Et_3OBF_4 (Meerwein's salts) according to recently reported proce-dures.[63] Typically, half the products from a CdS synthesis dispersed in ~15 mg/mL hexanes were mixed with a 40 mg/mL solution of Meerwein's salt dissolved in acetonitrile. The Meerwein's salt solution was added until the nanocrystals precipitated from the solution (~0.5 mL). Chloroform was added, and the nanocrystals were pelleted by centrifugation. The supernatant was discarded, and the nanocrystals were dissolved in 2 mL of DMF for subsequent use. We found that the nanocrystals were more easily degraded by an excessive stripping agent when using Me_3OBF_4; however, both reagents were used to prepare ligand-stripped nanocrystals for this work. Native ligands were stripped from the PbS/CdS core/shell nanocrystals under equilibrium conditions by Lewis acid−base adducts of born trifluoride using the methods recently developed by Helms and co-workers.[64] After removal of the organic ligands, the nanocrystals were dissolved in DMF with a concentration of ~20 mg/mL.

Nanocrystals with dodecanethiol ligands for optical absorption studies were prepared by exposing ligand-stripped nanocrystals in DMF to a solution of dodecanethiol dissolved in hexanes. The resulting biphasic mixture was vigorously stirred until the nanocrystals were transferred to the

hexanes, as indicated by a color change in the hexane layer from clear to yellow. The hexane layer was isolated, and the nanocrystals were purified by precipitation with ethanol followed by resuspension in hexanes to remove excess dodecanethiol.

Film Synthesis.

In a typical synthesis of a mesoporous film, 5 mg of PEO-b-PBO was dissolved in ~0.2 mL of ethanol with gentle heating and sonication. Next, 0.8 mL of ~5 nm diameter ligand-stripped nanocrystals in DMF (described above) was added to the polymer solution. After being stirred for ~1 h, followed by brief sonication, this solution was used to deposit films via spin coating at 1000 rpm for 90 s onto oxygen plasma-cleaned (100) silicon substrates for diffraction, ellipsometric porosimetry, X-ray photoelectron spec-troscopy (XPS), or electron microscopy, or onto clean glass slides for optical absorption measurements. After spin coating, the films were quickly placed in a septum-capped vial and purged with argon. A 10% (v/v) solution of either ethanedithiol (EDT) or 3-mercaptopropionic acid (MPA) in methanol was then added to the vial. Approximately 2 mL of the bidentate ligand solutions was used for a 1 cm^2 film. Caution: Ethanedithiol is highly toxic. The films were allowed to soak in this solution for 24 h without stirring or agitation. After being soaked in the cross-linking solution, the films were washed twice with ethanol by gently flowing ethanol over the film and soaked in ethanol for an additional 48 h to remove the polymer template. The films were then dried and stored in septa-capped vials flushed with argon. These films were used without further processing for all subsequent characterization. The procedures for synthesizing films templated using PS-b-PDMA were similar to the descriptions included above, with the exception that the polymer was dissolved in DMF initially rather than ethanol. In addition, 0.2 mL of N-methyl-2-pyrrolidone (NMP) was added to the polymer/nanocrystal solution to facilitate better wetting of the solution on the substrates. Cross-linking with MPA and EDT was

performed as described above; however, the template was removed by soaking the films in DMF because of the low solubility of PS-b-PDMA in ethanol. Films for UV−visible absorption spectroscopy and wide angle X-ray scattering (WAXS) and those made with PbS/CdS core/shell nanocrystals were prepared under air free conditions by spin coating the samples in a nitrogen atmosphere glovebox and sealing them in septa vials. The vials were removed from the glovebox where the cross-linking solutions were added and removed using septa syringe techniques under a dry argon flow. In most cases, some optimization of nanocrystal:polymer template ratios was needed to produce films with homogeneous porosity because other factors, such as the size of nanocrystals, can affect the ideal ratio.

Characterization.

Scanning electron microscopy (SEM) images were obtained using a JEOL model 6700F electron microscope with an accelerating voltage of 5 kV. Transmission electron microscopy (TEM) and high-resolution transmission electron microscopy (HRTEM) micrographs of the PbS/CdS core/shell particles were collected using an FEI Tecnai T20 G2 S-TWIN TEM instrument operating at 200 kV. To improve contrast, samples were supported on three- to five-layer graphene-spanning holes in Quantifoil R1.2/1.3 holey carbon grids. These grids were prepared using the direct transfer method.[70] TEM micrographs of the ligand-stripped particles were collected using an FEI T12 TEM instrument operating at 120 kV. Two-dimensional (2D) WAXS data were collected at the Stanford Synchrotron Radiation Lightsource (SSRL) using beamline 11-3. Measurements were taken in reflection mode with the incoming beam near grazing incidence and an X-ray energy of 1.27 keV. Transmission absorbance spectra were recorded on an Agilent HP 8452A UV−vis spectrophotometer. Ellipsometric porosimetry was performed on a PS-1000 instrument from Semilab using toluene as the adsorbate. A UV− visible CCD detector adapted to

a grating spectrograph analyzed the signal reflected by the sample. The light source was a 75 W Hamamatsu xenon lamp, and measurements were taken in the spectral range from 1.24 to 4.5 eV with an angle of incidence of 60°. Data analysis was performed using the associated WinElli II software with the assumption of cylindrical pores. XPS analysis was performed using a Kratos Axis Ultra DLD instrument with a monochromatic Al Kα radiation source. The charge neutralizer filament was used to control charging of the sample; a 20 eV pass energy was used with a 0.1 eV step size for high-resolution scans, and scans were calibrated using the C 1s peak shifted to 284.8 eV.

6.5 References

(1) Zaera, F. Nanostructured Materials for Applications in Heterogeneous Catalysis. *Chem. Soc. Rev.* **2013**, *42*, 2746−2762.

(2) Liu, C.; Dasgupta, N.; Yang, P. Semiconductor Nanowires for Artificial Photosynthesis. *Chem. Mater*. **2014**, *26*, 415−422.

(3) Zhang, Y.; Yuwono, A. H.; Wang, J.; Li, J. Enhanced Photocatalysis by Doping Cerium into Mesoporous Titania Thin Films. *J. Phys. Chem. C* **2009**, *113*, 21406−21412.

(4) Sreethawong, T.; Suzuki, Y.; Yoshikawa, S. Photocatalytic Evolution of Hydrogen over Mesoporous Supported NiO Photo-catalyst Prepared by Single-Step Sol−gel Process with Surfactant Template. *Int. J. Hydrogen Energy* **2005**, *30*, 1053−1062.

(5) Vamvasakis, I.; Subrahmanyam, K. S.; Kanatzidis, M. G.; Armatas, G. S. Template-Directed Assembly of Metal-Chalcogenide Nanocrystals into Ordered Mesoporous Networks. *ACS Nano* **2015**, *9*, 4419− 4426.

(6) Rauda, I. E.; Augustyn, V.; Dunn, B.; Tolbert, S. H. Enhancing Pseudocapacitive Charge Storage in Polymer Templated Mesoporous Materials. *Acc. Chem. Res*. **2013**, *46*, 1113−1124.

(7) Zhang, Y.; Xie, Z.; Wang, J. Supramolecular-Templated Thick Mesoporous Titania Films for Dye-Sensitized Solar Cells: Effect of Morphology on Performance. *ACS Appl. Mater. Interfaces* **2009**, *1*, 2789−2795.

(8) Kamat, P. V. Quantum Dot Solar Cells. The Next Big Thing in Photovoltaics. *J. Phys. Chem. Lett*. **2013**, *4*, 908−918.

(9) Nozik, A. J. Nanoscience and Nanostructures for Photovoltaics and Solar Fuels. *Nano Lett.* **2010**, *10*, 2735−2741.

(10) Alivisatos, A. Perspectives on the Physical Chemistry of Semiconductor Nanocrystals. *J. Phys. Chem*. **1996**, *100*, 13226−13239.

(11) Kamat, P. V. Quantum Dot Solar Cells. Semiconductor Nanocrystals as Light Harvesters. *J. Phys. Chem. C* **2008**, *112*, 18737−18753.

(12) Nozik, a J.; Beard, M. C.; Luther, J. M.; Law, M.; Ellingson, R. J.; Johnson, J. C. Semiconductor Quantum Dots and Quantum Dot Arrays and Applications of Multiple Exciton Generation to Third-Generation Photovoltaic Solar Cells. *Chem. Rev*. **2010**, *110*, 6873− 6890.

(13) Maraghechi, P.; Labelle, A. J.; Kirmani, A. R.; Lan, X.; Adachi, M. M.; Thon, S. M.; Hoogland, S.; Lee, A.; Ning, Z.; Fischer, A.; et al. The Donor-Supply Electrode Enhances Performance in Colloidal Quantum Dot Solar Cells. *ACS Nano* **2013**, *7*, 6111−6116.

(14) Kramer, I.; Sargent, E. Colloidal Quantum Dot Photovoltaics: A Path Forward. *ACS Nano* **2011**, *5*, 8506−8514.

(15) Ip, A. H.; Thon, S. M.; Hoogland, S.; Voznyy, O.; Zhitomirsky, D.; Debnath, R.; Levina, L.; Rollny, L. R.; Carey, G. H.; Fischer, A.; et al. Hybrid Passivated Colloidal Quantum Dot Solids. *Nat. Nanotechnol*. **2012**, *7*, 577−582.

(16) Talapin, D. V.; Lee, J.-S.; Kovalenko, M. V.; Shevchenko, E. V. Prospects of Colloidal Nanocrystals for Electronic and Optoelectronic Applications. *Chem. Rev*. **2010**, *110*, 389−458.

(17) Kovalenko, M. V.; Manna, L.; Cabot, A.; Hens, Z.; Talapin, D. V.; Kagan, C. R.; Klimov, X. V. I; Rogach, A. L.; Reiss, P.; Milliron, D. J.; et al. Prospects of Nanoscience with Nanocrystals. *ACS Nano* **2015**, *9*, 1012−1057.

(18) Moreels, I.; Lambert, K.; Smeets, D.; De Muynck, D.; Nollet, T.; Martins, J. C.; Vanhaecke, F.; Vantomme, A.; Delerue, C.; Allan, G.; et al. Size-Dependent Optical Properties of Colloidal PbS Quantum Dots. *ACS Nano* **2009**, *3*, 3023−3030.

(19) Yu, W. W.; Qu, L.; Guo, W.; Peng, X. Experimental Determination of the Extinction Coefficient of CdTe, CdSe, and CdS Nanocrystals. *Chem. Mater*. **2003**, *15*, 2854−2860.

(20) Pietryga, J.; Zhuravlev, K.; Whitehead, M.; Klimov, V.; Schaller, R. Evidence for Barrierless Auger Recombination in PbSe Nanocryst-als: A Pressure-Dependent Study of Transient Optical Absorption. *Phys. Rev. Lett*. **2008**, *101*, 217401.

(21) Padilha, L. a; Stewart, J. T.; Sandberg, R. L.; Bae, W. K.; Koh, W.-K.; Pietryga, J. M.; Klimov, V. I. Carrier Multiplication in Semiconductor Nanocrystals: Influence of Size, Shape, and Composition. *Acc. Chem. Res*. **2013**, *46*, 1261−1269.

(22) Nootz, G.; Padilha, L. a.; Levina, L.; Sukhovatkin, V.; Webster, S.; Brzozowski, L.; Sargent, E. H.; Hagan, D. J.; Van Stryland, E. W. Size Dependence of Carrier Dynamics and Carrier Multiplication in PbS Quantum Dots. *Phys. Rev. B: Condens. Matter Mater. Phys*. **2011**, *83*, 155302.

(23) Sandberg, R. L.; Padilha, L. a; Qazilbash, M. M.; Bae, W. K.; Schaller, R. D.; Pietryga, J. M.; Stevens, M. J.; Baek, B.; Nam, S. W.; Klimov, V. I. Multiexciton Dynamics in Infrared-Emitting Colloidal Nanostructures Probed by a Superconducting Nanowire Single-Photon Detector. *ACS Nano* **2012**, 6, 9532−9540.

(24) Goldstein, A. N.; Echer, C. M.; Alivisatos, A. P. Melting in Semiconductor Nanocrystals. *Science* (Washington, DC, U. S.) **1992**, *256*, 1425−1427.

(25) Zhitomirsky, D.; Kramer, I. J.; Labelle, A. J.; Fischer, A.; Debnath, R.; Pan, J.; Bakr, O. M.; Sargent, E. H. Colloidal Quantum Dot Photovoltaics: The Effect of Polydispersity. *Nano Lett.* **2012**, *12*, 1007−1012.

(26) Son, J. S.; Park, K.; Han, M.-K.; Kang, C.; Park, S.-G.; Kim, J.-H.; Kim, W.; Kim, S.-J.; Hyeon, T. Large-Scale Synthesis and Characterization of the Size-Dependent Thermoelectric Properties of Uniformly Sized Bismuth Nanocrystals. *Angew. Chem*. **2011**, *123*, 1399−1402.

(27) Wang, R. Y.; Feser, J. P.; Lee, J.-S.; Talapin, D. V.; Segalman, R.; Majumdar, A. Enhanced Thermopower in PbSe Nanocrystal Quantum Dot Superlattices. *Nano Lett*. **2008**, *8*, 2283−2288.

(28) Yu, W. W.; Peng, X. Formation of High-Quality CdS and Other II ± VI Semiconductor Nanocrystals in Noncoordinating Solvent-s:Tunable Reactivity of Monomers. *Angew. Chem., Int. Ed*. **2002**, *41*, 2368−2371.

(29) Hines, M. A.; Scholes, G. D. Colloidal PbS Nanocrystals with Size-Tunable Near-Infrared Emission: Observation of Post-Synthesis Self-Narrowing of the Particle Size Distribution. *Adv. Mater*. **2003**, *15*, 1844−1849.

(30) Joo, J.; Na, H.; Yu, T.; Yu, J.; Kim, Y.; Wu, F.; Zhang, J. Z.; Hyeon, T. Generalized and Facile Synthesis of Semiconducting Metal Sulfide Nanocrystals. *J. Am. Chem. Soc*. **2003**, *125*, 11100−11105.

(31) Cao, Y. C.; Wang, J. One-Pot Synthesis of High-Quality Zinc-Blende CdS Nanocrystals. *J. Am. Chem. Soc*. **2004**, *126*, 14336−14337.

(32) Yin, Y.; Alivisatos, A. P. Colloidal Nanocrystal Synthesis and the Organic-Inorganic Interface. *Nature* **2005**, *437*, 664−670.

(33) Wang, X.; Zhuang, J.; Peng, Q.; Li, Y. A General Strategy for Nanocrystal Synthesis. *Nature* **2005**, *437*, 121−124.

(34) Regulacio, M. D.; Han, M.-Y. Composition-Tunable Alloyed Semiconductor Nanocrystals. *Acc. Chem. Res*. **2010**, *43*, 621−630.

(35) Peng, Z.; Peng, X. Mechanisms of the Shape Evolution of CdSe Nanocrystals. *J. Am. Chem. Soc*. **2001**, *123*, 1389−1395.

(36) Zou, Y.; Li, D.; Yang, D. Single Step Synthesis of CdSeS Nanorods with Chemical Composition Gradients. *J. Cryst. Growth* **2010**, *312*, 3406−3409.

(37) Law, M.; Luther, J. M.; Song, Q.; Hughes, B. K.; Perkins, C. L.; Nozik, A. J. Structural, Optical, and Electrical Properties of PbSe Nanocrystal Solids Treated Thermally or with Simple Amines. *J. Am. Chem. Soc*. **2008**, *130*, 5974−5985.

(38) Zarghami, M. H.; Liu, Y.; Gibbs, M.; Gebremichael, E.; Webster, C.; Law, M. P-Type PbSe and PbS Quantum Dot Solids Prepared with Short-Chain Acids and Diacids. *ACS Nano* **2010**, *4*, 2475−2485.

(39) Luther, J. M.; Law, M.; Song, Q.; Perkins, C. L.; Beard, M. C.; Nozik, A. J. Structural, Optical, and Electrical Properties of Self-Assembled Films of PbSe Nanocrystals Treated with 1,2-Ethanedithiol. *ACS Nano* **2008**, *2*, 271−280.

(40) Klem, E. J. D.; MacNeil, D. D.; Cyr, P. W.; Levina, L.; Sargent, E. H. Efficient Solution-Processed Infrared Photovoltaic Cells: Planarized All-Inorganic Bulk Heterojunction Devices via Inter-Quantum-Dot Bridging during Growth from Solution. *Appl. Phys. Lett*. **2007**, *90*, 183113.

(41) Klem, E. J. D.; Shukla, H.; Hinds, S.; MacNeil, D. D.; Levina, L.; Sargent, E. H. Impact of Dithiol Treatment and Air Annealing on the Conductivity, Mobility, and Hole Density in PbS Colloidal Quantum Dot Solids. *Appl. Phys. Lett*. **2008**, *92*, 212105.

(42) Tang, J.; Wang, X.; Brzozowski, L.; Barkhouse, D. A. R.; Debnath, R.; Levina, L.; Sargent, E. H. Schottky Quantum Dot Solar Cells Stable in Air under Solar Illumination. *Adv. Mater*. **2010**, *22*, 1398−1402.

(43) Luther, J. M.; Gao, J.; Lloyd, M. T.; Semonin, O. E.; Beard, M. C.; Nozik, A. J. Stability Assessment on a 3% Bilayer PbS/ZnO Quantum Dot Heterojunction Solar Cell. *Adv. Mater*. **2010**, *22*, 3704− 3707.

(44) Choi, J. J.; Lim, Y.-F.; Santiago-Berrios, M. B.; Oh, M.; Hyun, B.-R.; Sun, L.; Bartnik, A. C.; Goedhart, A.; Malliaras, G. G.; Abruña, H. D.; et al. PbSe Nanocrystal Excitonic Solar Cells. *Nano Lett*. **2009**, *9*, 3749−3755.

(45) Liu, Y.; Gibbs, M.; Puthussery, J.; Gaik, S.; Ihly, R.; Hillhouse, H. W.; Law, M. Dependence of Carrier Mobility on Nanocrystal Size and Ligand Length in PbSe Nanocrystal Solids. *Nano Lett*. **2010**, *10*, 1960−1969.

(46) Yao, Q.; Arachchige, I. U.; Brock, S. L. Expanding the Repertoire of Chalcogenide Nanocrystal Networks: Ag 2Se Gels and Aerogels by Cation Exchange Reactions. *J. Am. Chem. Soc*. **2009**, *131*, 2800−2801.

(47) Yao, Q.; Brock, S. L. Porous CdTe Nanocrystal Assemblies: Ligation Effects on the Gelation Process and the Properties of Resultant Aerogels. *Inorg. Chem*. **2011**, *50*, 9985−9992.

(48) Mohanan, J. L.; Arachchige, I. U.; Brock, S. L. Porous Semiconductor Chalcogenide Aerogels. *Science* **2005**, *307*, 397−400.

(49) Yu, H.; Bellair, R.; Kannan, R. M.; Brock, S. L. Engineering Strength, Porosity, and Emission Intensity of Nanostructured CdSe Networks by Altering the Building-Block Shape. *J. Am. Chem. Soc*. **2008**, *130*, 5054−5055.

(50) Hitihami-Mudiyanselage, A.; Senevirathne, K.; Brock, S. L. Assembly of Phosphide Nanocrystals into Porous Networks: Formation of InP Gels and Aerogels. *ACS Nano* **2013**, *7*, 1163−1170.

(51) Rauda, I. E.; Saldarriaga-Lopez, L. C.; Helms, B. A.; Schelhas, L. T.; Membreno, D.; Milliron, D. J.; Tolbert, S. H. Nanoporous Semiconductors Synthesized through Polymer Templating of Ligand-Stripped CdSe Nanocrystals. *Adv. Mater*. **2013**, *25*, 1315−1322.

(52) Rauda, I. E.; Buonsanti, R.; Saldarriaga-lopez, L. C.; Benjauthrit, K.; Schelhas, L. T.; Stefik, M.; Augustyn, V.; Ko, J.; Dunn, B.; Wiesner, U.; et al. General Method for the Synthesis of Hierarchical Nanocrystal-Based Mesoporous Materials. *ACS Nano* **2012**, *6*, 6386−6399.

(53) Rivest, J. B.; Buonsanti, R.; Pick, T. E.; Zhu, L.; Lim, E.; Clavero, C.; Schaible, E.; Helms, B. A.; Milliron, D. J. Evolution of Ordered Metal Chalcogenide Architectures through Chemical Transformations. *J. Am. Chem. Soc*. **2013**, *135*, 7446−7449.

(54) Buonsanti, R.; Pick, T. E.; Krins, N.; Richardson, T. J.; Helms, B. A.; Milliron, D. J. Assembly of Ligand-Stripped Nanocrystals into Precisely Controlled Mesoporous Architectures. *Nano Lett*. **2012**, *12*, 3872−3877.

(55) Warren, S. C.; Messina, L. C.; Slaughter, L. S.; Kamperman, M.; Zhou, Q.; Gruner, S. M.; DiSalvo, F. J.; Wiesner, U. Ordered Mesoporous Materials from Metal Nanoparticle-Block Copolymer Self-Assembly. *Science* **2008**, *320*, 1748−1752.

(56) Corma, A.; Atienzar, P.; García, H.; Chane-Ching, J.-Y. Hierarchically Mesostructured Doped CeO2 with Potential for Solar-Cell Use. *Nat. Mater*. **2004**, *3*, 394−397.

(57) Ba, J.; Polleux, J.; Antonietti, M.; Niederberger, M. Non-Aqueous Synthesis of Tin Oxide Nanocrystals and Their Assembly into Ordered Porous Mesostructures. *Adv. Mater*. **2005**, *17*, 2509− 2512.

(58) Brezesinski, T.; Wang, J.; Polleux, J.; Dunn, B.; Tolbert, S. H. Templated Nanocrystal-Based Porous TiO2 Films for next-Generation Electrochemical Capacitors. *J. Am. Chem. Soc*. **2009**, *131*, 1802−1809.

(59) Szeifert, J. M.; Feckl, J. M.; Fattakhova-Rohlfing, D.; Liu, Y.; Kalousek, V.; Rathousky, J.; Bein, T. Ultrasmall Titania Nanocrystals and Their Direct Assembly into Mesoporous Structures Showing Fast Lithium Insertion. *J. Am. Chem. Soc*. **2010**, *132*, 12605−12611.

(60) Stefik, M.; Wang, S.; Hovden, R.; Sai, H.; Tate, M. W.; Muller, D. a.; Steiner, U.; Gruner, S. M.; Wiesner, U. Networked and Chiral Nanocomposites from ABC Triblock Terpolymer Coassembly with Transition Metal Oxide Nanoparticles. *J. Mater. Chem*. **2012**, *22*, 1078−1087.

(61) Papadas, I. T.; Vamvasakis, I.; Tamiolakis, I.; Armatas, G. S. Templated Self-Assembly of Colloidal Nanocrystals into Three-Dimensional Mesoscopic Structures: A Perspective on Synthesis and Catalytic Prospects. *Chem. Mater*. **2016**, *28*, 2886−2896.

(62) Dong, A.; Ye, X.; Chen, J.; Kang, Y.; Gordon, T.; Kikkawa, J. M.; Murray, C. B. A Generalized Ligand-Exchange Strategy Enabling Sequential Surface Functionalization of Colloidal Nanocrystals. *J. Am. Chem. Soc*. **2011**, *133*, 998−1006.

(63) Rosen, E. L.; Buonsanti, R.; Llordes, A.; Sawvel, A. M.; Milliron, D. J.; Helms, B. A. Exceptionally Mild Reactive Stripping of Native Ligands from Nanocrystal Surfaces by Using Meerwein's Salt. *Angew. Chem., Int. Ed.* **2012**, *51*, 684−689.

(64) Doris, S. E.; Lynch, J. J.; Li, C.; Wills, A. W.; Urban, J. J.; Helms, B. A. Mechanistic Insight into the Formation of Cationic Naked Nanocrystals Generated under Equilibrium Control. *J. Am. Chem. Soc*. **2014**, *136*, 15702−15710.

(65) Nag, A.; Kovalenko, M. V.; Lee, J.; Liu, W.; Spokoyny, B.; Talapin, D. V. Metal-Free Inorganic Ligands for Colloidal Nanocryst-als: S2-, HS-, Se2-, HSe-, Te2-, HTe-, OH-, and NH2- as Surface Ligands. *J. Am. Chem. Soc*. **2011**, *133*, 10612−10620.

(66) Kirsch, B. L.; Chen, X.; Richman, E. K.; Gupta, V.; Tolbert, S. H. Probing the Effects of Nanoscale Architecture on the Mechanical Properties of Hexagonal Silica/polymer Composite Thin Films. *Adv. Funct. Mater*. **2005**, *15*, 1319−1327.

(67) Debnath, R.; Bakr, O.; Sargent, E. H. Solution-Processed Colloidal Quantum Dot Photovoltaics: A Perspective. *Energy Environ. Sci*. **2011**, *4*, 4870−4881.

(68) Nordell, K. J.; Boatman, E. M.; Lisensky, G. C. A Safer, Easier, Faster Synthesis for CdSe Quantum Dot Nanocrystals. *J. Chem. Educ*. **2005**, *82*, 1697.

(69) Neo, D. C. J.; Cheng, C.; Stranks, S. D.; Fairclough, S. M.; Kim, J. S.; Kirkland, A. I.; Smith, J. M.; Snaith, H. J.; Assender, H. E.; Watt, A. A. R. Influence of Shell Thickness and Surface Passivation on PbS/ CdS Core/Shell Colloidal Quantum Dot Solar Cells. *Chem. Mater*. **2014**, *26*, 4004−4013.

(70) Regan, W.; Alem, N.; Aleman,́B.; Geng, B.; Girit, Ç.;Maserati, L.; Wang, F.; Crommie, M.; Zettl, A. A Direct Transfer of Layer-Area Graphene. *Appl. Phys. Lett*. **2010**, *96*, 113102.

(71) Baklanov, M. R.; Mogilnikov, K. P.; Polovinkin, V. G.; Dultsev, F. N. Determination of Pore Size Distribution in Thin Films by Ellipsometric Porosimetry. *J. Vac. Sci. Technol., B: Microelectron. Process. Phenom*. **2000**, *18*, 1385.

(72) Smilgies, D. Research Papers Scherrer Grain-Size Analysis Adapted to Grazing- Incidence Scattering with Area Detectors Research Papers. *J. Appl. Crystallogr*. **2009**, *42*, 1030−1034.

(73) Dirin, D. N.; Dreyfuss, S.; Bodnarchuk, M. I.; Nedelcu, G.; Papagiorgis, P.; Itskos, G.; Kovalenko, M. V. Lead Halide Perovskites and Other Metal Halide Complexes As Inorganic Capping Ligands for Colloidal Nanocrystals. *J. Am. Chem. Soc*. **2014**, *136*, 6550−6553.

(74) Efros, A.; Rosen, M. The Electronic Structure of Semiconductor Nanocrystals 1. *Annu. Rev. Mater. Sci*. **2000**, *30*, 475−521.

(75) Ekimov, A. I.; Hache, M. C.; Schanne-Klein, M. C.; Ricard, D.; Flytzanis, C.; Kudryavtsev, I. A.; Yazeva, T. V.; Rodina, A. V.; Efros, A. L. Absorption and Intensity-Dependent Photoluminescence Measure-ments on CdSe Quantum Dots: Assignment of the First Electronic Transitions. *J. Opt. Soc. Am. B* **1993**, *10*, 100−107.

(76) Wolcott, A.; Doyeux, V.; Nelson, C. a.; Gearba, R.; Lei, K. W.; Yager, K. G.; Dolocan, A. D.; Williams, K.; Nguyen, D.; Zhu, X. Y. Anomalously Large Polarization Effect Responsible for Excitonic Red Shifts in PbSe Quantum Dot Solids. *J. Phys. Chem. Lett*. **2011**, *2*, 795− 800.

(77) Foos, E. E. The Complex Interaction of Spectroscopic Shifts and Electronic Properties in Semiconductor Nanocrystal Films. *J. Phys. Chem. Lett*. **2013**, *4*, 625−632.

(78) Leatherdale, C.; Bawendi, M. Observation of Solvatochromism in CdSe Colloidal Quantum Dots. *Phys. Rev. B: Condens. Matter Mater. Phys.* **2001**, *63*, 1−6.

(79) Chan, E. M.; Xu, C.; Mao, A. W.; Han, G.; Owen, J. S.; Cohen, B. E.; Milliron, D. J. Reproducible, High-Throughput Synthesis of Colloidal Nanocrystals for Optimization in Multidimensional Param-eter Space. *Nano Lett*. **2010**, *10*, 1874−1885.

(80) Lambert, K.; De Geyter, B.; Moreels, I.; Hens, Z. PbTe|CdTe Core|Shell Particles by Cation Exchange, a HR-TEM Study. *Chem. Mater*. **2009**, *21*, 778−780.

(81) Ghosh Chaudhuri, R.; Paria, S. Core/shell Nanoparticles: Classes, Properties, Synthesis Mechanisms, Characterization, and Applications. *Chem. Rev*. **2012**, *112*, 2373−2433.

(82) Zhang, J.; Yang, Q.; Cao, H.; Ratcliffe, C. I.; Kingston, D.; Chen, Q. Y.; Ouyang, J.; Wu, X.; Leek, D. M.; Riehle, F. S.; et al. Bright Gradient-Alloyed CdSe X S 1− X Quantum Dots Exhibiting Cyan-Blue Emission. *Chem. Mater*. **2016**, *28*, 618−625.

(83) Li, H.; Zanella, M.; Genovese, A.; Povia, M.; Falqui, A.; Giannini, C.; Manna, L. Sequential Cation Exchange in Nanocrystals: Preservation of Crystal Phase and Formation of Metastable Phases. *Nano Lett*. **2011**, *11*, 4964−4970.

(84) Lechner, R. T.; Fritz-Popovski, G.; Yarema, M.; Heiss, W.; Hoell, A.; Schülli, T. U.; Primetzhofer, D.; Eibelhuber, M.; Paris, O. Crystal Phase Transitions in the Shell of PbS/CdS Core/Shell Nanocrystals Influences Photoluminescence Intensity. *Chem. Mater*. **2014**, *26*, 5914−5922.

(85) Manna, L.; Scher, E. C.; Alivisatos, A. P. Synthesis of Soluble and Processable Rod-, Arrow-, Teardrop-, and Tetrapod-Shaped CdSe Nanocrystals. *J. Am. Chem. Soc*. **2000**, *122*, 12700−12706.

(86) Manna, L.; Milliron, D. J.; Meisel, A.; Scher, E. C.; Alivisatos, A. P. Controlled Growth of Tetrapod-Branched Inorganic Nanocrystals. *Nat. Mater*. **2003**, *2*, 382−385.

(87) Goris, B.; Van Huis, M. A.; Bals, S.S.; Zandbergen, H. W.; Manna, L.; Van Tendeloo, G. Thermally Induced Structural and Morphological Changes of CdSe/CdS Octapods. *Small* **2012**, *8*, 937− 942.

(88) Groeneveld, E.; Witteman, L.; Lefferts, M.; Ke, X.; Bals, S.; Van Tendeloo, G.; de Mello Donega, C. Tailoring ZnSe-CdSe Colloidal Quantum Dots via Cation Exchange: From Core/Shell to Alloy Nanocrystals. *ACS Nano* **2013**, *7*, 7913−7930.

Chapter 7. Fine Tuning the Magnetic Properties of Cobalt Ferrite Thin Films by controlling nanoscale structure

7. 1 Introduction

There is great research interested in magnetic spinel ferrites (MFe_2O_4; M = Mn, Fe, Co, Ni, etc.) due to their widespread use in areas such as ferrofluids,[1-7] magnetic recording media[8-12] biomedical applications[13-18] and RF devices[19-28]. In particular, cobalt ferrite ($CoFe_2O_4$, CFO) is a hard magnetic material with a bulk coercivity of >4000 Oe and reasonably high saturation magnetization of 500 emu/cm^3, which has led to its use in magnetic recording media.[29, 30] However, its high coercivity also limits its use in other applications, especially high frequency applications, where soft ferrites are extensively used.[23-27, 31-33]

Advances in nanoscience now allow us to control a wide range of material properties through nanostructuring.[34-41] This allows us to effectively, and often selectively, tune material properties to tailor them to specific applications. Here, we apply nanostructuring techniques to the CFO material system to create a magnetically soft system, opening up further use in high frequency applications. This is accomplished by controlling magnetic domain size and structure, which determines the coercivity and remanence without significantly influencing the dynamic properties, such as the ferromagnetic resonance (FMR). We specifically investigate two methods for controlling the domain size and dipolar coupling: introducing mesoporosity and using nanocrystals as building blocks.

Introducing mesopores has been widely explored as a method to increase surface area,[40, 42-44] limit crystallite size[45-47] and tune the electric,[46, 48] magnetic[20, 34, 47] and mechanical properties[34, 42, 47, 49] in thin films. An open porous network can increase the surface area in a thin film by orders of magnitude,[40, 42] which is useful in areas where surface reactivity is important, such as

catalysis,[43, 45, 48, 50, 51] as well as areas where large interfacial areas are desired, such as pseudocapacitive energy storage.[44, 49, 52] Porosity can also control crystalline and magnetic domain size by breaking up the material and limiting domain size to be equal to or smaller than the wall thickness, or the thickness of the material between two pores.[20, 34] We have previously shown that in sol-gel derived thin films of CFO with 14-nm pores, the coercivity of the films could be tuned by changing the wall thickness, and therefore the maximum magnetic domain size. In these films, the porous structure also promoted a preference for out-of-plane magnetic orientation, which is unusual in thin films. This is thought to be due to a difference in the mechanical strain state of the system.[34] In that system as well as the work presented here, the mesoporous structure is achieved by a block copolymer templating method.

Block copolymer templating is a facile route to creating mesoporous structure in thin films.[34, 45-47, 53, 54]. In this method, an amphiphilic diblock copolymer is mixed in solution with an inorganic precursor material, such as a sol-gel solution or nanocrystals. The amphiphilic nature of the polymer induces the formation of polymer micelles such that in a polar solvent the hydrophobic block aggregates in the micelle core while the hydrophilic block interacts with the solvent keeping the micelle soluble. This mixture is then deposited onto a substrate where the polymer and inorganic material undergo evaporation induced self-assembly (EISA). This composite is then calcined to crosslink or sinter the inorganic material and thermally degrade and remove the polymer, leaving behind a robust, mesoporous film. In the case of sol-gel derived films, the films can then be crystallized at higher temperatures. The film morphology is determined by the initial organic-inorganic composite structure and can be tuned by changing the size or composition of the polymer as well as the ratio between polymer and inorganic precursor material in solution.[34, 47]

Another route to controlling domain structure is to make thin films using nanocrystals as precursor materials. Nanocrystals are attractive because they are solution-processable, highly tunable, and can be synthesized at relatively low temperatures, usually below 300˚C.[35, 36, 55-61] Below a critical size, each nanocrystal is a single crystalline domain as it is energetically unfavorable to form a grain boundary in such a small structure. Similarly, in magnetic materials, there is a critical size below which domain wall formation is unfavorable, so each nanocrystal is also a single magnetic domain.[55] In the case of CFO, it has been shown that nanocrystals have both a single crystallographic and magnetic domain when they are below 40 nm in diameter.[57] Therefore, the size of the magnetic domain can be controlled by changing the nanocrystal size, which is easily achieved synthetically.[35, 61-63] These nanocrystals with well-defined domain structure can then be deposited into thin films with magnetic properties determined by the original nanocrystal properties.

Additionally, recent work has shown that nanocrystals can be made compatible with block copolymer templating techniques leading to mesoporous, nanocrystal-based films.[53] Traditionally, nanocrystals were not well suited to this type of templating. This is due to the fact that they are generally synthesized with long organic ligands on the surface which serve to both keep the nanocrystals soluble and prevent aggregation.[35, 36, 61, 62] However, while useful, these ligands also prevent the nanocrystals from sintering to form a robust network during the annealing process causing the film to collapse upon removal of the polymer template. Recently, new ligand-stripping chemistries have been developed that create bare nanocrystals with charges on the surface that stabilize them in solution.[37, 38] These charge-stabilized nanocrystals can then be successfully templated using block copolymer–based methods. Templated nanocrystal films combine the

advantages of nanocrystals, such as domain size control and low temperature crystallization, with the benefits of structured, porous thin films.

In this work, we present wide range tunability over the magnetic properties of cobalt ferrite thin films by tuning their nanoscale architecture. We investigate films made from sol-gel methods, as well as different sizes of nanocrystals, both mesoporous and dense, and processed over a range of annealing temperatures. We find that the room temperature coercivity is tunable from 3100 Oe for dense, sol-gel derived films down to 70 Oe for mesoporous, nanocrystal-based films. Finally, we investigate the dynamic properties of these films by looking at the ferromagnetic resonance (FMR) in X-band and find that the FMR remains constant across all measureable films despite drastic differences in static magnetic properties.

7.2 Results and Discussion

The effect of mesoporosity on the properties of sol-gel derived films was investigated first. Both dense films and polymer-templated, mesoporous films were fabricated, as described above. The pore structure was investigated using top-view SEM, as seen in figure 7.1(a). The pores are seen to be circular, fairly well ordered and hexagonally packed. While top-view SEM is useful for characterizing pore structure, it cannot determine whether the polymer was indeed removed, or to what degree. In order to confirm that the polymer template was removed to leave an open porous network, ellipsometric porosimetry was used. In this technique, a small molecule, in this case toluene, is adsorbed into the pores and then desorbed out of the pores while the change in film thickness is measured ellipsometrically. The pore size distribution, shown in figure 7.1(b), was determined by fitting the adsorption and desorption isotherms using the Kelvin equation.[64] The adsorption process is a function of the pore volume while the desorption process is limited by the neck size, or the size of the tunnel connecting two pores. Therefore, the adsorption curve was used to determine that the average pore radius is 12 nm while the average neck radius is 10 nm in this sample. This correlates well to the SEM image in figure 7.1(a) in which the top view of the pores shows them to be on the order of 20 nm in diameter.

X-ray diffraction was used to confirm that the films had the desired spinel crystal structure. Representative diffractograms of both a dense and porous film, both crystallized at 500˚C, are shown in figure 7.1(c). In both samples, the films were found to have a spinel crystal structure with no impurity phases present at measureable levels. Information about average crystallite size can also be extrapolated using the Scherrer equation:

$$\tau = \frac{K\lambda}{\beta \cos\theta} \quad (1)$$

where τ is the average crystallite size, K is the shape factor, λ is the wavelength of the X-rays, β is the peak broadening, or full width at half maximum of the peak, and θ is the Bragg angle. In this work, we assume spherical domains and use a shape factor of 0.9. For the films crystallized at 500˚C, the approximate average crystalline domain size was found to be 26.2 nm for the dense film and 13.1 nm for the porous film. The estimated crystallite size in the porous film is approximately the same size as the pore walls, 10 nm, as determined by SEM. In the absence of a limiting pore structure, the crystalline domain size is determined by crystallization kinetics which is why the domains are larger in the bulk samples. This trend was found for films, regardless of crystallization temperature.

The static magnetic properties of these films was probed using two instruments: MOKE and SQUID magnetometers. These techniques measure magnetization in different ways, and on different time scales, so by comparing them, we can gain further insight into the magnetic properties of our films. In MOKE magnetometry, circularly polarized light interacts with the magnetic spins which rotates the polarization, referred to as Kerr rotation. The time constant of the measurement in this case is about 3 ms. SQUID magnetometry on the other hand is a measurement of the inductance caused by moving the sample through the center of the measurement coils. Its measurement time is longer than that of MOKE magnetometry, generally 1-10 seconds. By comparing magnetic hysteresis loops for a given sample between these two methods, we can gain valuable insight into the time dependence of properties.

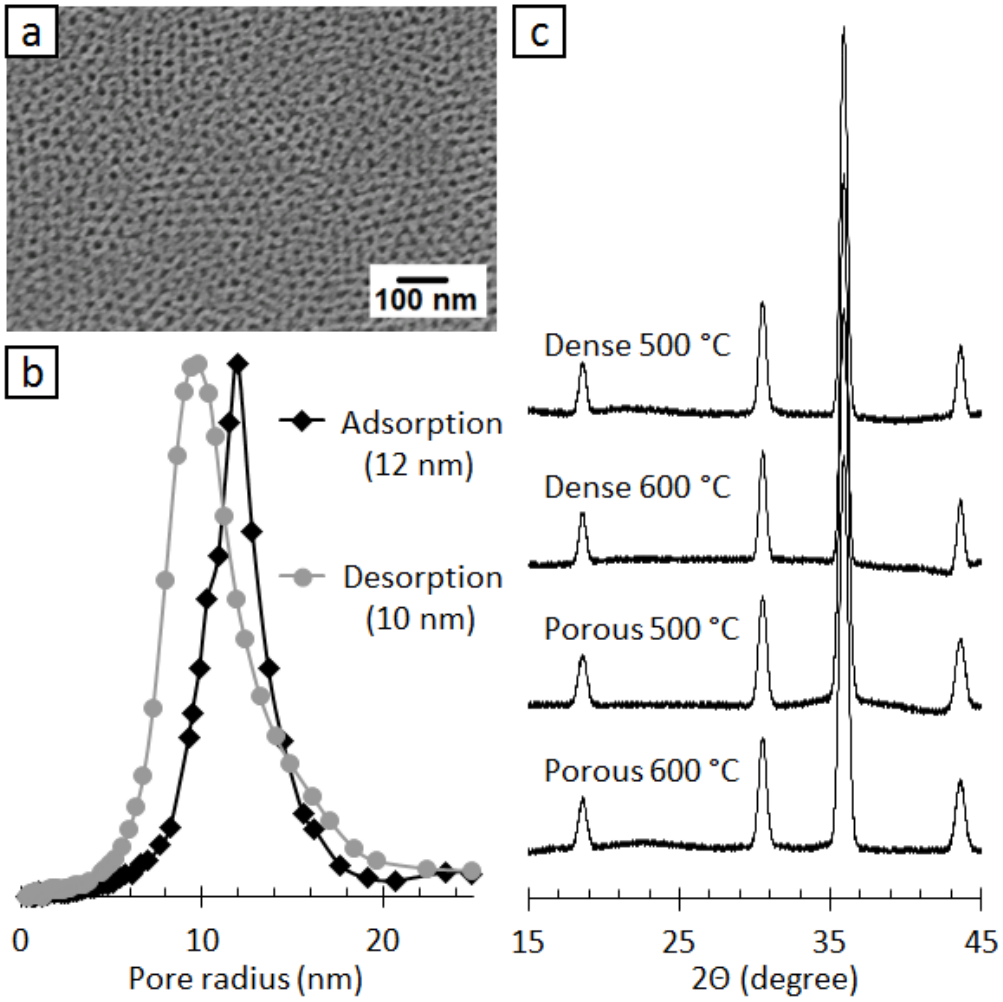

Figure 7.1 (a) Top-view SEM of a templated, sol-gel derived thin film annealed at 500˚C. (b) Pore radius distribution of a templated film annealed at 500˚C. The average pore size (black), calculated from the adsorption isotherm, is 12 nm while the average neck size (grey), from the desorption isotherm, is 10 nm. (c) X-ray diffractograms dense and porous films annealed at 500˚C and 600˚C.

Figure 7.2(a) shows the room temperature magnetic hysteresis loops for both dense and porous films as measured by MOKE magnetometry. The solid black and grey curves are dense films crystallized at 500˚C and 600˚C respectively and the corresponding dashed curves are from the respective porous films. The dense films have coercivities of 2590 Oe (annealed at 500˚C) and 3100 Oe (annealed at 600˚C) while the porous film show lower coercivities of 1960 Oe (annealed at 500˚C) and 2350 Oe (annealed at 600˚C).

The drastic lowering of the coercivity due to induced porosity is mainly attributed to the decrease in the magnetic domain size. As described above, the maximum magnetic domain size is limited by the wall thickness in porous films. The reduction in domain volume reduces the coercivity by reducing the magnetocrystalline anisotropy energy (MCA), as described in the Stoner–Wohlfarth model:[65]

$$E_{MCA} = KVsin^2\theta \quad (2)$$

Where K is a material-specific magnetocrystalline anisotropy constant, V is the domain volume and θ is the angle between an applied field and the easy axis. Coercivity is a measure of the MCA energy so by reducing domain size (V), the MCA energy and therefore coercivity are also reduced. This is also the reason that the films crystallized at 600˚C have a higher coercivity. The higher crystallization temperature causes grain growth, leading to larger domains and therefore larger MCA and higher coercive widths. It is interesting to note that grain growth also occurs in the porous films. At elevated temperatures, the CFO structure can more freely rearrange leading to films with thicker pore walls and slightly larger pores, as discussed in our previous work.[34]

In order to more fully probe the magnetic properties, magnetic hysteresis loops measured using SQUID magnetometry were collected and are presented in figure 7.2(b). Here again the coercivity is reduced from 1420 Oe in the dense film and 610 Oe in the porous film annealed at 500˚C. In

both cases, the coercivities measured using SQUID magnetometry are lower than those measured using MOKE magnetometry. The longer measurement time of SQUID magnetometry allows more time for the spins to reorient due to thermal fluctuations leading to a lower observed coercivity and remanent magnetization. Finally, whereas sample magnetization must be normalized in our MOKE measurements, SQUID magnetometry shows that there is a large difference in saturation magnetization between the samples. The dense film has a saturation magnetization of 440 emu/cm^3, which is approaching the bulk value of 485 emu/cm^3, while the porous film has a saturation magnetization of 90 emu/cm^3. This decrease can be attributed to the reduced density due to induced porosity.

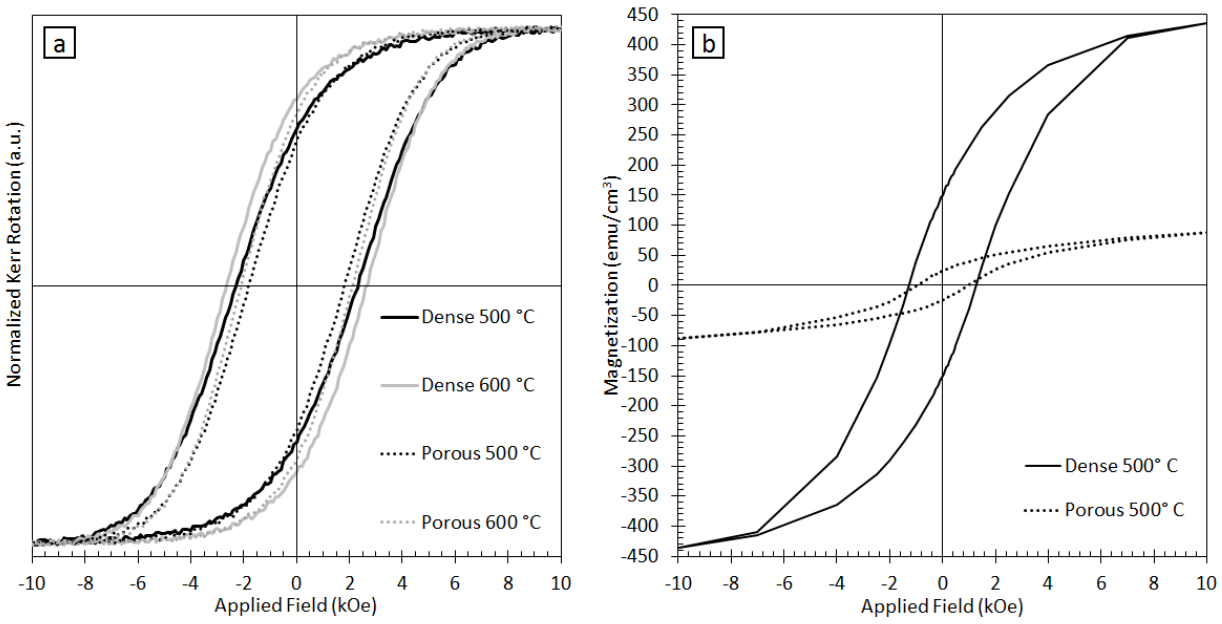

Figure 7.2 (a) Magnetic hysteresis loops for dense (solid) and porous (dashed) films annealed at 500˚C and 600˚C collected on a MOKE magnetometer and (b) magnetic hysteresis loops for films annealed at 500 ˚C collected on a SQUID magnetometer.

In addition to making mesoporous films, another route to limiting domain size is to use nanocrystals as building blocks for thin films. Nanocrystals of two different sizes were synthesized and characterized using TEM. Figure 7.3 shows micrographs of the 5-nm as-synthesized (a) and 8-nm as-synthesized (b) nanocrystals. The nanocrystals are very monodisperse in size and shape and pack hexagonally which is indicative of monodispersity in spherical nanocrystals. The spacing between the nanocrystals is due to the organic ligands on the surface which cannot be seen in TEM.[61] These ligands can then be chemically removed in a manner that leaves charges on the surface, which can stabilize the nanocrystals in solution but does not physically separate them. As expected, TEM images of the ligand-stripped nanocrystals, as shown in figure 7.3(c)–(d), show that the nanocrystals are no longer spaced apart on the grid, but instead are touching. From these micrographs it can be seen that the ligand-stripping process increases the polydispersity in size somewhat, but the average size and shape are maintained. XRD shows that both sizes of nanocrystals were synthesized in the expected spinel crystal structure and that structure is preserved through the ligand-stripping process (figure 7.3(e)–(f)).

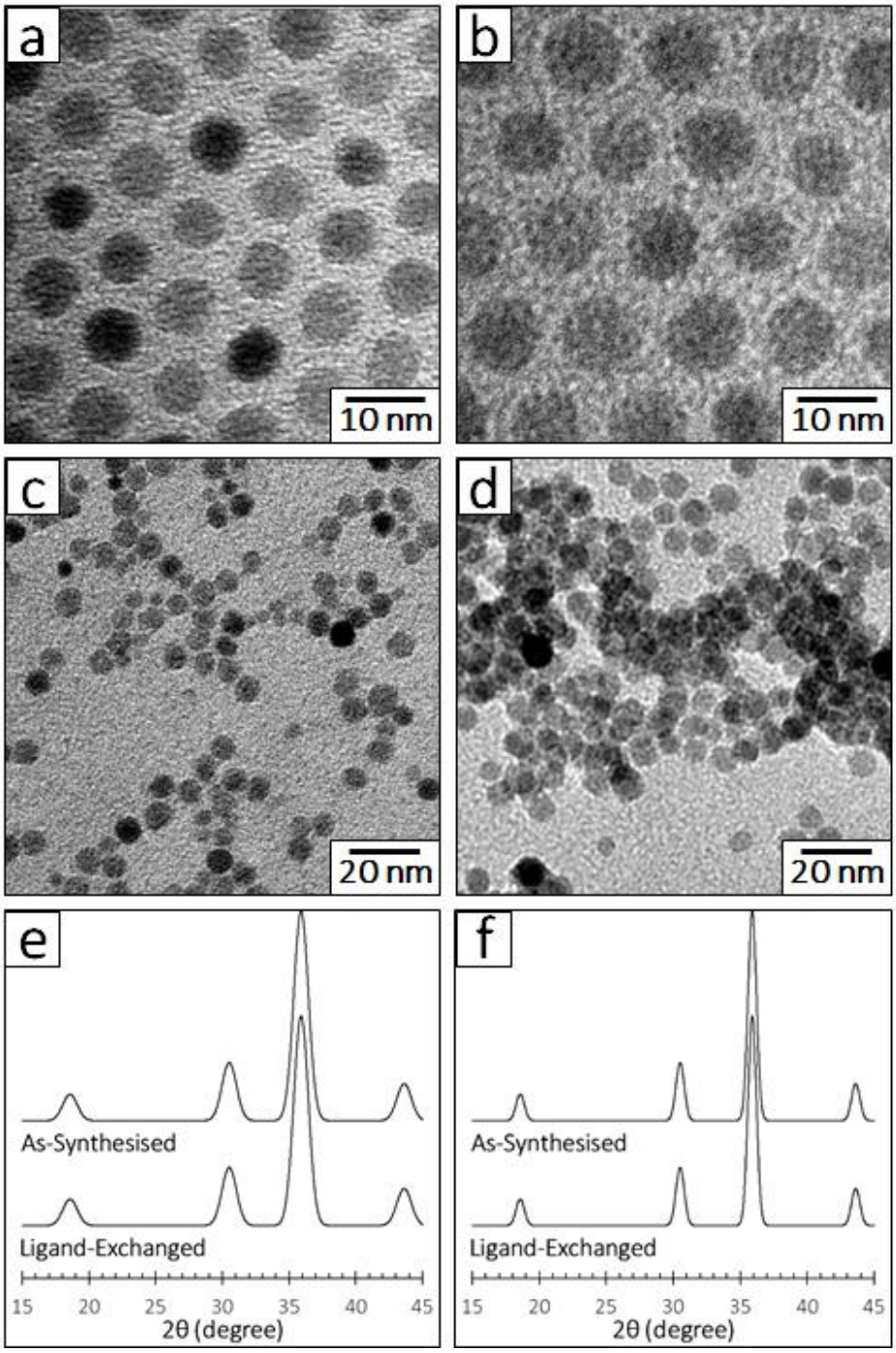

Figure 7.3 TEM images of as-synthesized 5 nm (a) and 8 nm (b) nanocrystals and ligand stripped 5 nm (c) and 8 nm (d) nanocrystals. XRD diffractograms of as synthesized and ligand stripped 5 nm (e) and 8 nm (f) nanocrystals.

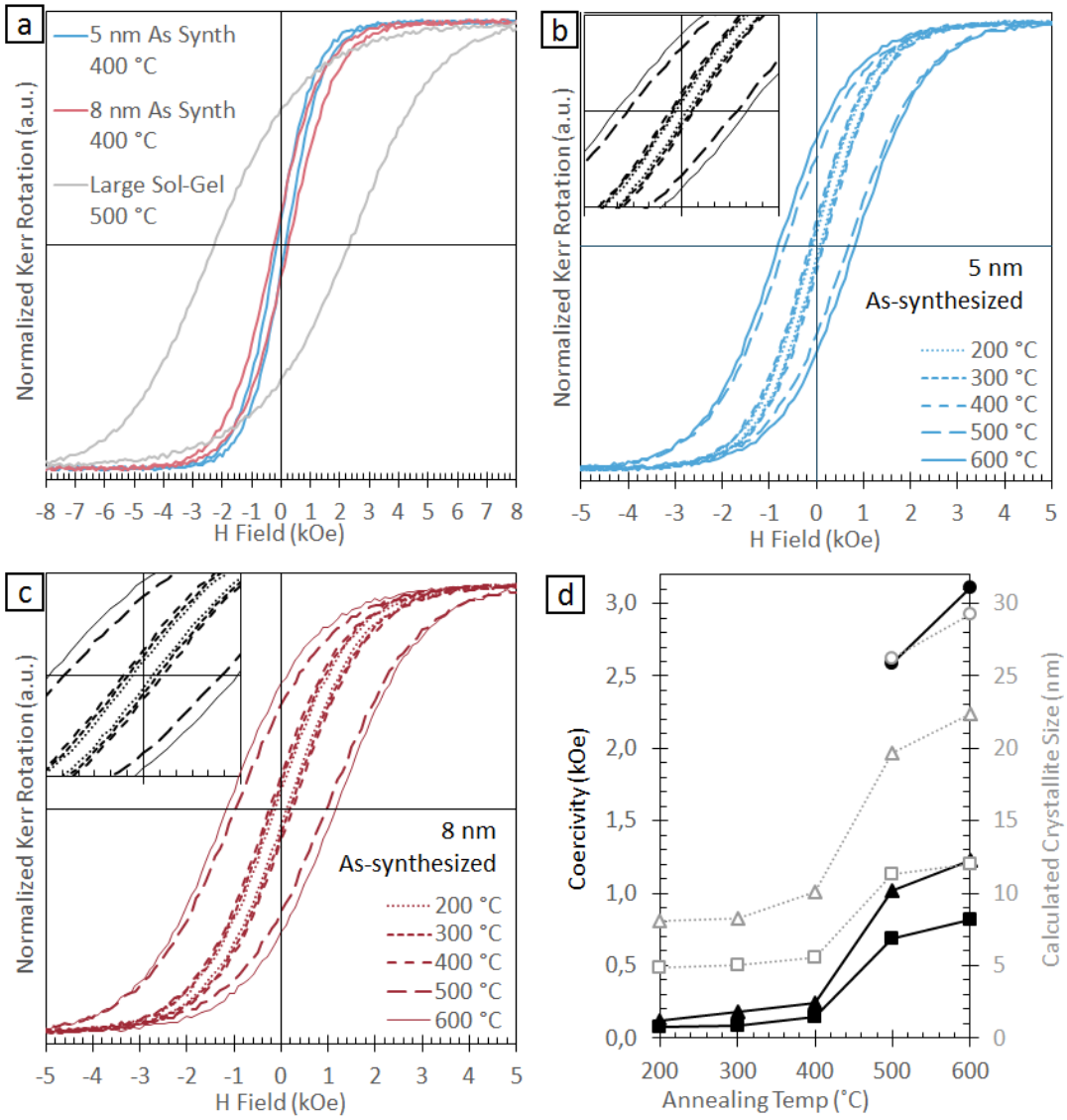

Figure 7. 4 (a) Room temperature, in plane magnetic hysteresis loops of films annealed at 400˚C made from as synthesized 5 nm nanocrystals and 8 nm nanocrystals, including data for a dense sol-gel derived film annealed at 500˚C for comparison. Magnetic hysteresis loops for films made from as synthesized 5 nm (b) and 8 nm (c) nanocrystals annealed at various temperatures. (d) Measured coercivity and crystallite size calculated from the Scherrer equation as a function of annealing temperature.

Thin films were made from both as-synthesized and ligand-stripped nanocrystals of each size. While the nanocrystals are crystalline as synthesized, the films were still annealed in order to sinter them together enough to make a mechanically robust film. Figure 7.4(a) shows representative hysteresis loops of films made from both sizes of nanocrystals both as-synthesized and ligand-stripped with data from a dense sol-gel film for comparison. The films annealed at 400˚C have coercivities of 140 Oe for the film of 5 nm nanocrystals and 210 Oe or the film 8 nm nanocrystals. For comparison, the 5-nm nanocrystal film had a coercivity of 50 Oe as measured by SQUID magnetometry.

As expected, there is very little difference between the as-synthesized and ligand-stripped nanocrystals. This suggests that despite some observed change in size dispersity as shown in figure 7.3, the ligand-stripping process has a minimal impact on the nanocrystal properties which makes it useful tool for nanocrystal processing in various situations. It also suggests that in these films, the contribution of the surface to the magnetization is minimal.

The effect of annealing temperature on the magnetic properties was also investigated and the resulting hysteresis loops are shown in figure 7.4(b)–(c). The data shown is from the films of as-synthesized nanocrystals; in each case, the ligand-free analogs were also investigated and the differences between them remained minimal. The films were annealed between 200˚C and 600˚C and for both smaller and larger nanocrystals, the coercivity increased with increasing annealing temperature. This is attributed to increased grain growth due to nanocrystal sintering at higher temperatures.

In order to characterize the effect of annealing temperature on domain size, XRD was done on all of the films and the average crystallite size was calculated using the Scherrer equation (1) as described above. The calculated crystallite sizes and observed coercivity are plotted in figure

7.4(d) as a function of annealing temperature for both sol-gel and nanocrystal-based films. For all films the calculated crystallite size and coercivity show similar trends. This is particularly noticeable in the nanocrystal-based films between 400˚C and 500˚C where there is a large jump in both values. This suggests that in that temperature range there is a point at which the nanocrystal sintering or melting occurs more rapidly. This correlation supports our conclusion that crystallite size is the primary factor in determining the coercivity.

Both inducing porosity in sol-gel derived films and using nanocrystals to make thin films have been shown to lower the coercivity of CFO thin films. In order to further tune the magnetic properties, porous, nanocrystal-based films were fabricated. It is worth noting that ligand stripping is required for the block copolymer templating process used here. Top-view SEM images shown in figure 7.5 show the pore structure in films made from 5-nm nanocrystals (a) and 8-nm nanocrystals (b). The pores in the nanocrystal-based films are larger than their sol-gel counterparts because a different, larger block copolymer was used for the nanocrystals due to the difference in solvent requirements for the two precursors. As for the sol-gel films, the templating polymer was removed via thermal annealing, as discussed below.

To investigate the open porosity of the post-annealed films, ellipsometric porosimetry was performed and the results for an example film based on 5-nm nanocrystals and annealed at 400˚C, are presented in figure 7.5(c). The porosimetry confirms that the templated nanocrystal-based films have an open pore structure with an overall porosity of 38%, an average pore radius of 14 nm and an average neck radius of 7 nm. This corresponds well to the top-view SEM images shown in figure 7.5(a). XRD was again employed to determine that the spinel structure was indeed retained during the templating process, and the resulting diffractograms are in figure 7.5(d).

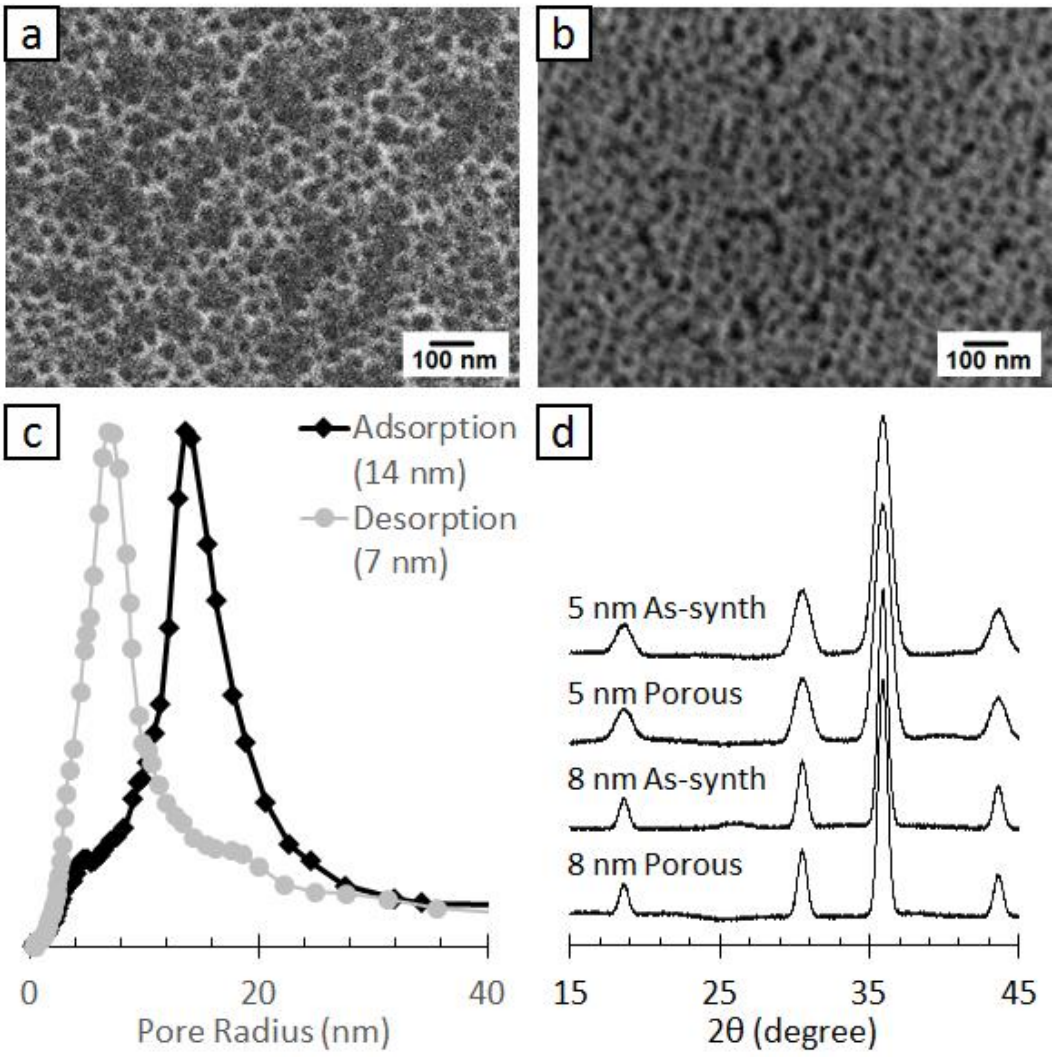

Figure 7.5: Top-view SEM images of porous films made from 5 nm (a) and 8 nm (b) nanocrystals. Pore radius distribution of a representative templated film made from 5 nm nanocrystals annealed at 400˚C. (d) X-ray diffractograms of both dense and porous nanocrystal-based films.

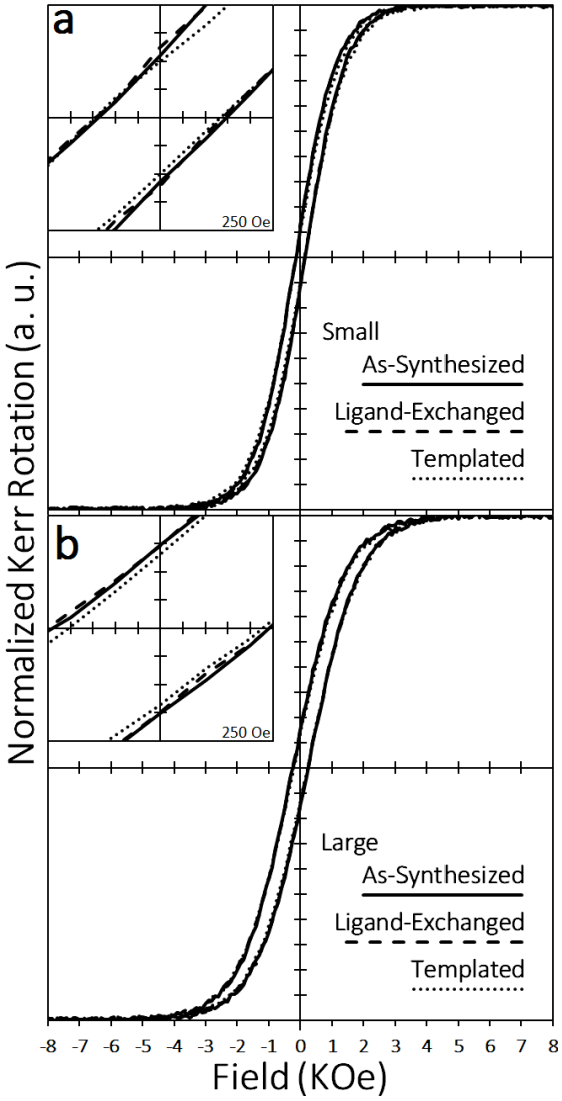

Figure 7.6 Room temperature, in plane magnetic hysteresis loops of both dense and mesoporous thin films annealed at 400˚C from 5 nm nanocrystals (a), 8 nm nanocrystals (b).

Figure 7.6 shows magnetic hysteresis loops of both dense and porous nanocrystal-based films annealed at 400˚C. In the case of these nanocrystal-based films, dense films refer to films with no polymer template, and therefore no mesopores, but these films do have some nanoporosity due to the limitation on spherical packing of the nanocrystals. As described above, the addition of mesopores to sol-gel derived films serves to limit the crystalline, and therefore magnetic, domain size, as does making nanocrystal-based films. However, if the coercivity were solely dependent on physical domain size, we would expect to see no change due to porosity in the nanocrystal-based samples, which is not the case. There is an observable decrease in coercivity of ~10 Oe due to porosity for 5-nm-nanocrystal-based films and ~40 Oe in 8-nm-nanocrystal-based films. This suggests that there is a secondary mechanism by which pores decrease magnetic coercivity, which we believe is the limiting of dipolar interactions in porous films. Spins near a pore have fewer neighboring spins with which to dipole couple, which can allow them to more easily align with the external field, hence lowering the observed coercivity.

In addition to characterizing the static magnetic properties, ferromagnetic resonance (FMR) measurements were used to explore the dynamic behavior. FMR is an absorptive phenomenon in which a magnetic material absorbs microwave radiation causing the magnetic spins to precess around the axis of an applied bias field. It is well described by the Landau–Lifshitz–Gilbert (LLG) model of precessional motion.[66] Within this model, high frequency losses are taken into account by the Gilbert damping coefficient (α). Damping is when a precessing spin stops its precession and returns to static alignment with the applied field. The peak to peak linewidth (ΔH_{pp}) is a common figure of merit because it is related to the Gilbert damping coefficient through the following relation:

$$\alpha = \frac{\gamma \Delta H_{\text{pp}}}{4\pi f'} \quad (3)$$

Where γ is the gyromagnetic ratio, which is 2.8 GHz/kOe, and f' is the measurement frequency. For most applications, losses should be minimized, so low values for α, and therefore low ΔH_{pp}, are desired.

Here, despite the large range of observed coercivities, almost all of the films showed identical room temperature FMR. In these cases the ΔH_{pp} was found to be 39 G, which corresponds to $\alpha = 0.0009$ and the center field $H_0 = 3519$ G. This suggests that while the static properties such as coercivity and remanence are dependent on domain level structure, the dynamic behavior is more a function of the material or atomic level composition.

The only films that did not show identical FMR were the sol-gel derived films and the 8-nm-nanocrystal-based films annealed at or above 500˚C, which showed no resonant behavior at the measurement frequency (X-band, 9.7 GHz). Those films have the highest coercivities, which is likely the cause of the lack of resonance. A requirement for FMR is that the sample is magnetically saturated such that all of the spins are aligned with the applied bias field. In the samples with high coercive fields, it is probable that the bias field at which FMR occurs in CFO at 9.7 GHz was insufficiently high to fully saturate the sample, thereby eliminating the resonance. It is for this reason that CFO has not been widely investigated for microwave applications where strong FMR and low losses are desired.

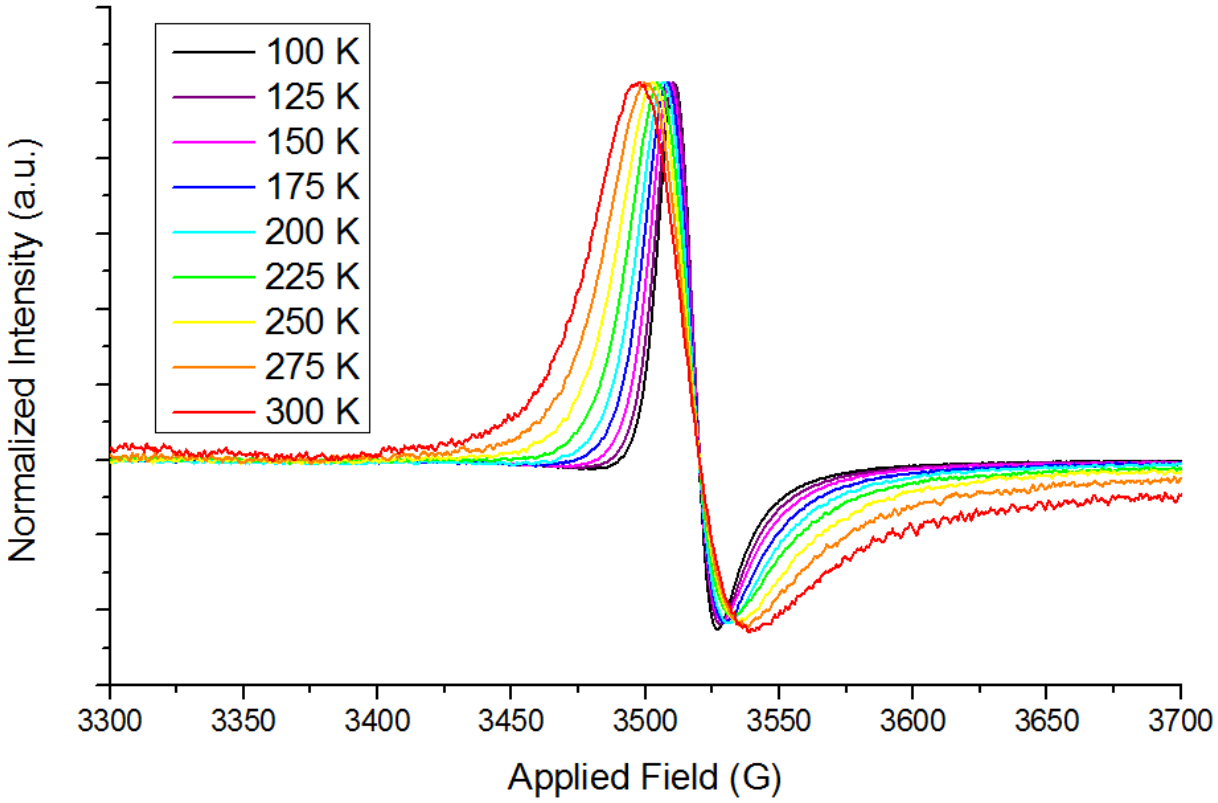

Figure 7.7 Temperature-dependent FMR spectra of a representative film made from as-synthesized 5 nm nanocrystals annealed at 400˚C.

However, the lower coercivities achieved in the nanocrystal-based films ensure that the spins are saturated thereby allowing FMR. Temperature-dependent FMR spectra, or the derivative of microwave power absorption spectra, of an example film made using 5-nm nanocrystals is presented in figure 7.7. The intensities were normalized for easier comparison, although the intensity decreased with increasing temperature which is why the data at higher temperatures appears noisier. At room temperature, the linewidth is 39 G and α is 0.0009 which is fairly low for a ferrite material at such a high frequency. Commercially produced ferrites such as lithium ferrite and nickel zinc ferrite have damping coefficients of 0.008 and 0.009 respectively.[31, 67] This suggests that nanostructured CFO is an intrinsically low-loss material which makes it promising for use in microwave applications.

The temperature dependent FMR measurements reveal that linewidth increases linearly with temperature, which is consistent with a ferromagnetic material. It has been shown that linewidths increase with increasing temperature until the blocking temperature and then decrease with further increasing temperature in the superparamagnetic regime.[59, 68, 69] The asymmetry between the positive and negative peaks of the spectra is commonly found in solid magnetic materials and is due to magnetic anisotropies and dipolar interactions within the film. This also suggests that the film is ferromagnetic in this temperature range. If the sample were above the Curie temperature and in a paramagnetic state, the magnetic anisotropies would be zero and the resulting spectra would be perfectly isotropic.[70] It is also worth noting that at higher temperatures, the absorption intensity does not return to zero immediately. This is due to non-resonant microwave absorption and has been observed both in CFO and other ferrite materials.[21, 28]

7.3 Conclusions

Here we have presented two methods for tuning the static magnetic properties of cobalt ferrite thin films: making mesoporous films and making nanocrystal-based films. By controlling the film precursor, porosity and annealing temperature, the coercivity was successfully tuned from 3100 Oe down to 70 Oe. We postulate that the major mechanism for reducing the coercivity in these samples was limiting crystalline and magnetic domain size through nanostructuring, while decreasing dipolar interactions played a secondary role. Furthermore, we have shown that despite the large range of attainable coercivities, the dynamic magnetic properties remain largely the same between samples suggesting that the static magnetic properties arise from domain level structure while the high frequency behavior is dominated by atomic level structure.

7.4 Experimental Methods

Materials.

Cobalt(II) acetylacetonate (>99%) and 1-octadecanol (97%) were purchased from Alfa Aesar. Iron(III) acetylacetonate (>99%) and benzyl ether (99%) were purchased from Acros Organics. Cobalt(II) nitrate hexahydrate (99.99%), iron(III) nitrate nonahydrate (99.999%) 1,2-hexadecanediol (technical grade, 50%) and 2-methoxyethanol (99.8%%) were purchased from Sigma-Aldrich. Poly(styrene-*b*-N,N-dimethylacrylamide) with M_n: PS(51000)-PDMA(8500), was obtained from Polymer Source. All chemicals were used without further purification.

Fabrication of sol-gel derived CFO thin films.

Sol-gel derived films were fabricated a described in our previous work[34]. $Co(NO_3)_2 \cdot 6H_2O$ (0.11 g) and $Fe(NO_3)_3 \cdot 9H_2O$ (0.11 g) were dissolved in 1 mL of 2-methoxyethanol, 1 mL of ethanol and 0.02 mL glacial acetic acid. This solution was allowed to age for 3 days with magnetic stirring at room temperature and was always found to be clear at this point. The templating polymer used to make porous structures was PEP-PEO. To make mesoporous films, 40 mg of PEP-PEO was dissolved in 1 mL of ethanol before being added to a 2-mL solution and stirred for 1 hour. Both dense and porous films were deposited via dipcoating at <20% humidity onto cleaned silicon substrates. These films were then calcined at 180˚C for 24 hours to allow for solvent removal and to crosslink the CFO to form a more rigid inorganic-organic composite. Subsequently, the films were annealed at either 500˚C or 600˚C for 5 hours to both remove the polymer template and crystallize the film. Film thickness can be fine-tuned using the rate at which the substrate is pulled out of the solution. For this work films with thicknesses of ~100 nm were studied.

Synthesis of CFO nanocrystals.

The nanocrystals were synthesized following a procedure previously published by Song *et al*. with few modifications.[35] Dibenzyl ether was used as the solvent and oxygen source, rather than phenyl ether. For the synthesis of nanocrystals with a 5-nm diameter, $Co(acac)_2$ (2 mmol, 0.5143 g), 1,2-hexadecanediol (20 mmol, 5.169 g), oleic acid (10 mL), oleylamine (10 mL) and benzyl ether (40 mL) were all heated to 140˚C under flowing argon and rapid magnetic stirring. $Fe(acac)_3$ (4 mmol, 1.413 g) well dissolved in benzyl ether (20 mL) was then injected and the mixture was then quickly heated to 240˚C where it was allowed to react for 30 minutes before being cooled down to room temperature. The product was then precipitated with ethanol via centrifugation and redispersed in hexanes three times before being redispersed in either hexanes or toluene (20 mg/mL) for storage in air.

These 5-nm nanocrystals were then used as seeds to grow nanocrystals with a diameter of 8 nm. In this synthesis, 100 mg of 5-nm nanocrystals were mixed with $Co(acac)_2$ (1 mmol, 0.257 g), $Fe(acac)_3$ (2 mmol, 0.706 g), 1-octadecanol (10 mmol, 2.7049 g), and oleic acid (5 mL), oleylamine (5 mL) under argon flow and magnetic stirring. The mixture was heated to 240˚C and allowed to react for 30 minutes before being cooled to room temperature and being washed in the same manner as for the 5-nm nanocrystals.

Ligand-stripping of CFO nanocrystals.

The ligands were stripped using a previously published procedure by Rosen *et al.* in which tetraethyloxonium tetrafluroborate (Meerwein's Salt) is used to reactively strip the native oleic acid ligands.[38] In a typical ligand-stripping procedure, 10 mg of Meerwein's Salt was dissolved in 1 mL of dry acetonitrile in a nitrogen glovebox. The solution was then removed from the glovebox and 0.2 mL of that solution was added to 2 mL of CFO nanocrystals (20 mg/mL) in a centrifuge

tube. The mixture was vortexed for approximately 30 seconds, 5 mL of chloroform was added, and it was centrifuged at 4000 RPM for 5 minutes. Any nanocrystals left in solution were assumed to be incompletely exchanged and the supernatant was discarded although most of the nanocrystals had precipitated. The precipitate was then dissolved in either DMF or NMP, often a 1:1 ratio with a total volume of 1 mL. The ligand-stripped nanocrystals were then stable in solution for weeks and stored in air.

Fabrication of nanocrystal-based thin films.

Nanocrystal-based films were deposited by dipcoating and it was found that the relative humidity did not have a large impact on film quality, so it was not strictly controlled, although most films were pulled at humidity levels between 20–40%. Here, we refer to films cast without a block copolymer templating agent as dense nanocrystal films and those with a templating agent as porous films. Dense films of as-synthesized nanocrystals (with ligand) were pulled from the initial 20 mg/mL solution in hexanes and the ligand-stripped nanocrystal films were pulled from solutions in 1:1 DMF:NMP. It was found that the nanocrystals were more stable in DMF, but DMF alone does not wet substrates well, making it difficult to produce quality films.

Mesoporous nanocrystal films were made using poly(styrene-*b*-*N*,*N*-dimethylacrylamide), (PS-PDMA) as the templating agent. In a typical synthesis, 20 mg of PS-PDMA was added to 1 mL of DMF and mixed on a rotary mixer at room temperature until dissolved (~1 hour). 1 mL of the ligand-stripped nanocrystal solution was then added to the polymer solution and the mixture was sonicated for 10 minutes. The solution was then left gently mixing on a rotary mixer until deposited. It is worth noting that all of the films here were deposited within 5 hours of initially dissolving the polymer. Films deposited over a day after the polymer was dissolved were found to be of low quality. Both dense and porous films were then annealed for 4 hours at annealing

temperatures from 200–600˚C. For the porous films, temperatures at or above 400˚C were required to remove the polymer template.

Characterization.

A JEOL JSM-6700F field emission scanning electron microscope (FE-SEM) was used to characterize the microstructure of the films. An FEI T12 Quick CryoEM and CryoET transmission electron microscope (TEM) operating at 300 kV was used to characterize the nanocrystal size and shape. Ellipsometric porosimetry was performed on a PS-1100 instrument from Semilab using toluene as the adsorbate at room temperature. A UV-visible CCD detector adapted to a grating spectrograph analyzes the signal reflected by the sample. The light source is a 75-W Hamamatsu Xenon lamp and measurements were performed in the spectral range from 1.24–4.5 eV. Data analysis was performed using the associated SEA software.

The static magnetic characterization was done using both a magnetooptical kerr effect magnetometer (MOKE) and a Quantum Design MPMS superconducting quantum interference device (SQUID) magnetometer. The homebuilt MOKE system uses a 620-nm laser, a photoelastic modulator modulating the beam at 60 Hz and a lock-in detector set to that frequency. All measurements were done in transverse mode measuring in-plane magnetization. X-ray diffraction patterns were the result of 2D grazing incidence wide angle X-ray scattering experiments (GIWAXS) performed at the Stanford Synchrotron Radiation Lightsource (SSRL). These experiments were carried out using beamline 11-3. The resulting 2D images were integrated to create the 1D patterns presented here. FMR spectra were collected using a Bruker EMX X-band EPR spectrometer operating at 9.72 GHz.

7.5 References

(1) Krishna Surendra, M.; Annapoorani, S.; Ansar, E.; Harikrishna Varma, P. R.; Ramachandra Rao, M. S., Magnetic Hyperthermia Studies on Water-Soluble Polyacrylic Acid-Coated Cobalt Ferrite Nanoparticles. *J. Nanopart. Res.* **2014**, *16*, 1-14.

(2) Kamali, S.; Pouryazdan, M.; Ghafari, M.; Itou, M.; Rahman, M.; Stroeve, P.; Hahn, H.; Sakurai, Y., Magnetization and Stability Study of a Cobalt-Ferrite-Based Ferrofluid. *Journal of Magnetism and Magnetic Materials* **2016**, *404*, 143-147.

(3) Andreu, I.; Natividad, E.; Ravagli, C.; Castro, M.; Baldi, G., Heating Ability of Cobalt Ferrite Nanoparticles Showing Dynamic And Interaction Effects. *RSC Advances* **2014**, *4*, 28968-28977.

(4) Chand, M.; Kumar, S.; Shankar, A.; Porwal, R.; Pant, R. P., The Size Induced Effect on Rheological Properties of Co-Ferrite based Ferrofluid. *Journal of Non-Crystalline Solids* **2013**, *361*, 38-42.

(5) Lisjak, D.; Jenus, P.; Drofenik, M., Formation of Columnar Structures by the Magnetically Directed Assembly of Cobalt Ferrite Nanoparticles. *Magnetics, IEEE Transactions on* **2012**, *48*, 3303-3306.

(6) Nabeel Rashin, M.; Hemalatha, J., Magnetic and Ultrasonic Studies on Stable Cobalt Ferrite Magnetic Nanofluid. *Ultrasonics* **2014**, *54*, 834-840.

(7) Lacroix, L.-M.; Malaki, R. B.; Carrey, J.; Lachaize, S.; Respaud, M.; Goya, G. F.; Chaudret, B., Magnetic Hyperthermia in Single-Domain Monodisperse FeCo Nanoparticles: Evidences for Stoner–Wohlfarth Behavior and Large Losses. *Journal of Applied Physics* **2009**, *105*, 023911.

(8) Hu, W.; Zou, L.; Chen, R.; Xie, W.; Chen, X.; Qin, N.; Li, S.; Yang, G.; Bao, D. Resistive Switching Properties and Physical Mechanism of Cobalt Ferrite Thin Films. *Applied Physics Letters* **2014**, *104*, 143502.

(9) Jiang, C.; Wu, L.; Wei, W.; Dong, C.; Yao, J. The Resistive Switching Memory of $CoFe_2O_4$ Thin Film using Nanoporous Alumina Template. *Nanoscale Res Lett* **2014**, *9*, 1-5.

(10) Matzen, S.; Moussy, J.-B.; Mattana, R.; Bouzehouane, K.; Deranlot, C.; Petroff, F. Nanomagnetism of Cobalt Ferrite-Based Spin Filters Probed by Spin-Polarized Tunneling. *Applied Physics Letters* **2012**, *101*, 042409.

(11) Ramos, A. V.; Guittet, M.-J.; Moussy, J.-B.; Mattana, R.; Deranlot, C.; Petroff, F.; Gatel, C. Room Temperature Spin Filtering in Epitaxial Cobalt-Ferrite Tunnel Barriers. *Applied Physics Letters* **2007**, *91*, 122107.

(12) Takahashi, Y. K.; Kasai, S.; Furubayashi, T.; Mitani, S.; Inomata, K.; Hono, K., High Spin-Filter Efficiency in a Co Ferrite Fabricated by a Thermal Oxidation. *Applied Physics Letters* **2010**, *96*, 072512.

(13) Sanpo, N.; Berndt, C. C.; Wen, C.; Wang, J., Transition Metal-Substituted Cobalt Ferrite Nanoparticles for Biomedical Applications. *Acta Biomaterialia* **2013**, *9*, 5830-5837.

(14) Amiri, S.; Shokrollahi, H., The Role of Cobalt Ferrite Magnetic Nanoparticles in Medical Science. *Materials Science and Engineering: C* **2013**, *33*, 1-8.

(15) Berensmeier, S., Magnetic Particles for the Separation and Purification of Nucleic Acids. *Applied Microbiology and Biotechnology* **2006**, *73*, 495-504.

(16) Joshi, H. M.; Lin, Y. P.; Aslam, M.; Prasad, P. V.; Schultz-Sikma, E. A.; Edelman, R.; Meade, T.; Dravid, V. P., Effects of Shape and Size of Cobalt Ferrite Nanostructures on

their MRI Contrast and Thermal Activation. *Journal of Physical Chemistry C* **2009**, *113*, 17761-17767.

(17) Pershina, A. G.; Sazonov, A. E.; Ogorodova, L. M., Investigation of the Interaction between DNA and Cobalt Ferrite Nanoparticles by FTIR Spectroscopy. *Russian Journal of Bioorganic Chemistry* **2009**, *35*, 607-613.

(18) Yoo, D.; Lee, J.-H.; Shin, T.-H.; Cheon, J., Theranostic Magnetic Nanoparticles. *Accounts of Chemical Research* **2011**, *44*, 863-874.

(19) Hannour, A.; Vincent, D.; Kahlouche, F.; Tchangoulian, A.; Neveu, S.; Dupuis, V., Self-Biased Cobalt Ferrite Nanocomposites for Microwave Applications. *Journal of Magnetism and Magnetic Materials* **2014**, *353*, 29-33.

(20) Li, G.-M.; Wang, L.-C.; Xu, Y., Templated Synthesis of Highly Ordered Mesoporous Cobalt Ferrite and its Microwave Absorption Properties. *Chinese Physics B* **2014**, *23*, 088105.

(21) Mata-Zamora, M. E.; Montiel, H.; Alvarez, G.; Saniger, J. M.; Zamorano, R.; Valenzuela, R., Microwave Non-Resonant Absorption in Fine Cobalt Ferrite Particles. *Journal of Magnetism and Magnetic Materials* **2007**, *316*, e532-e534.

(22) Sharma, D.; Khare, N., Single Phase Cobalt Ferrite Thin Films for Tunable Microwave Filter. *AIP Conference Proceedings* **2015**, *1665*, 080010.

(23) Popov, M. A.; Zavislyak, I. V.; Murthy, D. V. B.; Srinivasan, G., Dielectric Resonance in Nickel Ferrite for K and Ka-Band Filters. *Microwave and Optical Technology Letters* **2014**, *56*, 814-818.

(24) Lagarkov, A. N.; Rozanov, K. N., High-Frequency Behavior of Magnetic Composites. *Journal of Magnetism and Magnetic Materials* **2009**, *321*, 2082-2092.

(25) Schloemann, E., Advances in Ferrite Microwave Materials and Devices. *Journal of Magnetism and Magnetic Materials* **2000**, *209*, 15-20.

(26) Ö zgür, Ü .; Alivov, Y.; Morkoç, H., Microwave Ferrites, Part 1: Fundamental Properties. *J Mater Sci: Mater Electron* **2009**, *20*, 789-834.

(27) Popov, M. A.; Murthy, D. V. B.; Zavislyak, I. V.; Srinivasan, G. Magnetic field tunable 18–36 GHz dielectric bandpass filter *Electronics Letters*, **2012**, *48*, 98-99.

(28) Fannin, P. C.; Marin, C. N.; Malaescu, I.; Stefu, N.; Vlazan, P.; Novaconi, S.; Sfirloaga, P.; Popescu, S.; Couper, C., Microwave absorbent properties of nanosized cobalt ferrite powders prepared by coprecipitation and subjected to different thermal treatments. *Materials & Design* **2011**, *32*, 1600-1604.

(29) Yin, J.; Ding, J.; Liu, B.; Miao, X.; Chen, J., Nanocrystalline Co-ferrite Films with High Perpendicular Coercivity. *Applied Physics Letters* **2006**, *88*, 162502.

(30) Dhakal, T.; Mukherjee, D.; Hyde, R.; Mukherjee, P.; Phan, M. H.; Srikanth, H.; Witanachchi, S., Magnetic Anisotropy and Field Switching in Cobalt Ferrite Thin Films Deposited by Pulsed Laser Ablation. *Journal of Applied Physics* **2010**, *107*, 053914.

(31) Cadieu, F. J.; Rani, R.; Mendoza, W.; Peng, B.; Shaheen, S. A.; Hurben, M. J.; Patton, C. E., Static Magnetic and Microwave Properties of Li-Ferrite Films Prepared by Pulsed Laser Deposition. *Journal of Applied Physics* **1997**, *81*, 4801-4803.

(32) Verma, A.; Alam, M. I.; Chatterjee, R.; Goel, T. C.; Mendiratta, R. G., Development of a New Soft Ferrite Core for Power Applications. *Journal of Magnetism and Magnetic Materials* **2006**, *300*, 500-505.

(33) Harris, V. G.; Geiler, A.; Chen, Y.; Yoon, S. D.; Wu, M.; Yang, A.; Chen, Z.; He, P.; Parimi, P. V.; Zuo, X.; Patton, C. E.; Abe, M.; Acher, O.; Vittoria, C., Recent Advances in

Processing and Applications of Microwave Ferrites. *Journal of Magnetism and Magnetic Materials* **2009**, *321*, 2035-2047.

(34) Quickel, T. E.; Le, V. H.; Brezesinski, T.; Tolbert, S. H., On the Correlation between Nanoscale Structure and Magnetic Properties in Ordered Mesoporous Cobalt Ferrite (CoFe2O4) Thin Films. *Nano Letters* **2010**, *10*, 2982-2988.

(35) Song, Q.; Zhang, Z. J., Shape Control and Associated Magnetic Properties of Spinel Cobalt Ferrite Nanocrystals. *Journal of the American Chemical Society* **2004**, *126*, 6164-6168.

(36) Peddis, D.; Orrù, F.; Ardu, A.; Cannas, C.; Musinu, A.; Piccaluga, G., Interparticle Interactions and Magnetic Anisotropy in Cobalt Ferrite Nanoparticles: Influence of Molecular Coating. *Chemistry of Materials* **2012**, *24*, 1062-1071.

(37) Dong, A.; Ye, X.; Chen, J.; Kang, Y.; Gordon, T.; Kikkawa, J. M.; Murray, C. B., A Generalized Ligand-Exchange Strategy Enabling Sequential Surface Functionalization of Colloidal Nanocrystals. *Journal of the American Chemical Society* **2011**, *133*, 998-1006.

(38) Rosen, E. L.; Buonsanti, R.; Llordes, A.; Sawvel, A. M.; Milliron, D. J.; Helms, B. A., Exceptionally Mild Reactive Stripping of Native Ligands from Nanocrystal Surfaces by Using Meerwein's Salt. *Angewandte Chemie International Edition* **2012**, *51*, 684-689.

(39) Jing, P.; Du, J.; Jin, C.; Wang, J.; Pan, L.; Li, J.; Liu, Q., Improved Coercivity and Considerable Saturation Magnetization of Cobalt Ferrite ($CoFe_2O_4$) Nanoribbons Synthesized by Electrospinning. *J Mater Sci* **2016**, *51*, 885-892.

(40) Innocenzi, P.; Malfatti, L., Mesoporous Thin Films: Properties and Applications. *Chemical Society Reviews* **2013**, *42*, 4198-4216.

(41) Kao, J.; Bai, P.; Lucas, J. M.; Alivisatos, A. P.; Xu, T., Size-Dependent Assemblies of Nanoparticle Mixtures in Thin Films. *Journal of the American Chemical Society* **2013**, *135*, 1680-1683.

(42) Boissiere, C.; Grosso, D.; Lepoutre, S.; Nicole, L.; Bruneau, A. B.; Sanchez, C., Porosity and Mechanical Properties of Mesoporous Thin Films Assessed by Environmental Ellipsometric Porosimetry. *Langmuir* **2005**, *21*, 12362-12371.

(43) Hamd, W.; Cobo, S.; Fize, J.; Baldinozzi, G.; Schwartz, W.; Reymermier, M.; Pereira, A.; Fontecave, M.; Artero, V.; Laberty-Robert, C.; Sanchez, C., Mesoporous α-Fe_2O_3 Thin Films Synthesized via the Sol-Gel Process for Light-Driven Water Oxidation. *Physical Chemistry Chemical Physics* **2012**, *14*, 13224-13232.

(44) Rauda, I. E.; Augustyn, V.; Dunn, B.; Tolbert, S. H., Enhancing Pseudocapacitive Charge Storage in Polymer Templated Mesoporous Materials. *Accounts of Chemical Research* **2013**, *46*, 1113-1124.

(45) Ortel, E.; Reier, T.; Strasser, P.; Kraehnert, R., Mesoporous IrO2 Films Templated by PEO-PB-PEO Block-Copolymers: Self-Assembly, Crystallization Behavior, and Electrocatalytic Performance. *Chemistry of Materials* **2011**, *23*, 3201-3209.

(46) Fang, J.; Kang, C. B.; Huang, Y.; Tolbert, S. H.; Pilon, L., Thermal Conductivity of Ordered Mesoporous Nanocrystalline Silicon Thin Films Made from Magnesium Reduction of Polymer-Templated Silica. *The Journal of Physical Chemistry C* **2012**, *116*, 12926-12933.

(47) Quickel, T. E.; Schelhas, L. T.; Farrell, R. A.; Petkov, N.; Le, V. H.; Tolbert, S. H., Mesoporous Bismuth Ferrite with Amplified Magnetoelectric Coupling and Electric Field-Induced Ferrimagnetism. *Nat Commun* **2015**, *6*, 6562.

(48) Hartmann, P.; Brezesinski, T.; Sann, J.; Lotnyk, A.; Eufinger, J.-P.; Kienle, L.; Janek, J., Defect Chemistry of Oxide Nanomaterials with High Surface Area: Ordered Mesoporous Thin Films of the Oxygen Storage Catalyst CeO2–ZrO2. *ACS Nano* **2013**, *7*, 2999-3013.

(49) Brezesinski, T.; Wang, J.; Senter, R.; Brezesinski, K.; Dunn, B.; Tolbert, S. H., On the Correlation Between Mechanical Flexibility, Nanoscale Structure, and Charge Storage in Periodic Mesoporous CeO2 Thin Films. *ACS Nano* **2010**, *4*, 967-977.

(50) Detsi, E.; Cook, J. B.; Lesel, B. K.; Turner, C. L.; Liang, Y.-L.; Robbennolt, S.; Tolbert, S. H., Mesoporous $Ni_{60}Fe_{30}Mn_{10}$-Alloy Based Metal/Metal Oxide Composite Thick Films as Highly Active and Robust Oxygen Evolution Catalysts. *Energy & Environmental Science* **2016**, *9*, 540-549.

(51) Rosen, J.; Hutchings, G. S.; Jiao, F., Ordered Mesoporous Cobalt Oxide as Highly Efficient Oxygen Evolution Catalyst. *Journal of the American Chemical Society* **2013**, *135*, 4516-4521.

(52) Brezesinski, K.; Wang, J.; Haetge, J.; Reitz, C.; Steinmueller, S. O.; Tolbert, S. H.; Smarsly, B. M.; Dunn, B.; Brezesinski, T., Pseudocapacitive Contributions to Charge Storage in Highly Ordered Mesoporous Group V Transition Metal Oxides with Iso-Oriented Layered Nanocrystalline Domains. *Journal of the American Chemical Society* **2010**, *132*, 6982-6990.

(53) Rauda, I. E.; Buonsanti, R.; Saldarriaga-Lopez, L. C.; Benjauthrit, K.; Schelhas, L. T.; Stefik, M.; Augustyn, V.; Ko, J.; Dunn, B.; Wiesner, U.; Milliron, D. J.; Tolbert, S. H., General Method for the Synthesis of Hierarchical Nanocrystal-Based Mesoporous Materials. *ACS Nano* **2012**, *6*, 6386-6399.

(54) Hsueh, H.-Y.; Yao, C.-T.; Ho, R.-M., Well-Ordered Nanohybrids and Nanoporous Materials from Gyroid Block Copolymer Templates. *Chemical Society Reviews* **2015**, *44*, 1974-2018.

(55) Chen, C.-C.; Herhold, A. B.; Johnson, C. S.; Alivisatos, A. P., Size Dependence of Structural Metastability in Semiconductor Nanocrystals. *Science* **1997**, *276*, 398-401.

(56) Shafi, K. V. P. M.; Gedanken, A.; Prozorov, R.; Balogh, J., Sonochemical Preparation and Size-Dependent Properties of Nanostructured CoFe2O4 Particles. *Chemistry of Materials* **1998**, *10*, 3445-3450.

(57) Chinnasamy, C. N.; Jeyadevan, B.; Shinoda, K.; Tohji, K.; Djayaprawira, D. J.; Takahashi, M.; Joseyphus, R. J.; Narayanasamy, A., Unusually High Coercivity and Critical Single-Ddomain Size of Nearly Monodispersed $CoFe_2O_4$ Nanoparticles. *Applied Physics Letters* **2003**, *83*, 2862-2864.

(58) Yin, Y.; Alivisatos, A. P., Colloidal Nanocrystal Synthesis and the Organic-Inorganic Interface. *Nature* **2005**, *437*, 664-670.

(59) Xuebo, C.; Li, G., Spindly Cobalt Ferrite Nnanocrystals: Preparation, Characterization and Magnetic Properties. *Nanotechnology* **2005**, *16*, 180.

(60) Lee, D. C.; Smith, D. K.; Heitsch, A. T.; Korgel, B. A., Colloidal Magnetic Nanocrystals: Synthesis, Properties and Applications. *Annual Reports Section "C" (Physical Chemistry)* **2007**, *103*, 351-402.

(61) Verma, S.; Pravarthana, D., One-Pot Synthesis of Highly Monodispersed Ferrite Nanocrystals: Surface Characterization and Magnetic Properties. *Langmuir* **2011**, *27*, 13189-13197.

(62) López-Ortega, A.; Lottini, E.; Fernández, C. d. J.; Sangregorio, C., Exploring the Magnetic Properties of Cobalt-Ferrite Nanoparticles for the Development of a Rare-Earth-Free Permanent Magnet. *Chemistry of Materials* **2015**, *27*, 4048-4056.

(63) Geng, B. Q.; Ma, Y. Q.; Xu, S. T.; Xu, Y. F.; Sun, X.; Dai, Z. X.; Zheng, G. H., High magnetic performance of cobalt ferrite and anomalous magnetizing behavior of CoFe2/oxide derived from ferrite. *Ceramics International* **2016**, *42*, 317-324.

(64) Haynes, J. M., Pore size analysis according to the Kelvin equation. *Matériaux et Construction* **1973**, *6*, 209-213.

(65) Stoner, E. C.; Wohlfarth, E. P., A Mechanism of Magnetic Hysteresis in Heterogeneous Alloys. *Philosophical Transactions of the Royal Society of London A: Mathematical, Physical and Engineering Sciences* **1948**, *240*, 599-642.

(66) Gilbert, T. L., A phenomenological theory of damping in ferromagnetic materials. *Magnetics, IEEE Transactions on* **2004**, *40*, 3443-3449.

(67) Montiel, H.; Alvarez, G.; Gutiérrez, M. P.; Zamorano, R.; Valenzuela, R., Microwave absorption in Ni–Zn ferrites through the Curie transition. *Journal of Alloys and Compounds* **2004**, *369*, 141-143.

(68) Hochepied, J. F.; Pileni, M. P., Ferromagnetic resonance of nonstoichiometric zinc ferrite and cobalt-doped zinc ferrite nanoparticles. *Journal of Magnetism and Magnetic Materials* **2001**, *231*, 45-52.

(69) Singh, J.; Dixit, G.; Srivastava, R. C.; Kumar, H.; Agrawal, H. M.; Chand, P., Magnetic resonance in superparamagnetic zinc ferrite. *Bull Mater Sci* **2013**, *36*, 751-754.

(70) Flores-Arias, Y.; Vázquez-Victorio, G.; Ortega-Zempoalteca, R.; Acevedo-Salas, U.; Ammar, S.; Valenzuela, R., Magnetic phase transitions in ferrite nanoparticles characterized by electron spin resonance. *Journal of Applied Physics* **2015**, *117*, 17A503.